CHARACTERISATION OF TITANIUM ALLOY PROCESSED BY CONSTRAINED BENDING AND STRAIGHTENING SEVERE PLASTIC DEFORMATION

WAMBURA MWIRYENYI MWITA

A THESIS SUBMITTED TO THE UNIVERSITY OF JOHANNESBURG

IN FULFILMENT OF THE DEGREE OF DOCTOR OF PHILOSOPHY (PhD)

IN
MECHANICAL ENGINEERING SCIENCE

THE FACULTY OF ENGINEERING AND THE BUILT ENVIRONMENT

SUPERVISOR: PROF. E.T. AKINLABI

FEBRUARY, 2020

DECLARATION

I, Wambura Mwiryenyi MWITA, declare that the content of this thesis represents my own work; and that the thesis has not previously been submitted for academic examination for any qualification at any institution. To the best of my knowledge, it contains no copy or paraphrase of work published by another person, except where duly acknowledged in the text. Furthermore, it represents my own opinions and not necessarily those of the University of Johannesburg.

Signed **Date** **25th February 2020**

DEDICATION

This work is dedicated to my wife Janet, my daughters Paulina and Erica, my son Elisha and last but not least to my mother, Ghati. Their prayers, material support and encouragement have counted a lot towards the completion of this piece of work.

ACKNOWLEDGEMENTS

Glory and Praise must go to the Almighty God for having allowed the completion of this work. I am deeply indebted to my supervisor Professor Esther Titilayo Akinlabi of the Department of Mechanical Engineering Science, the University of Johannesburg for her oversight in the completion of this work. My heart-felt appreciation goes to her for the close supervision, guidance, as well as the financial and material support she provided to me, whenever I was in need. I am grateful to the followings individuals for their technical assistance with this work: Mr. Kelvin K. Mogano from B1-208 Lab of Metallurgy for demonstrating sample preparation and tests; Mr. Walter Dott, from B3-116 Lab of Machine shop for machining tensile test samples; Mr. Michael Phiri from B4-115 Lab of Manufacturing Engineering, He assisted with the fabrication of the CBS tool, My colleague Dr. Fredrick M. Mwema, who did the coordination and supply of metallurgical consumable materials.

My special appreciation is extended to all the staff and my fellow students in the department for their team work and various supports during my study. Lastly but not least, I am grateful to the University of Johannesburg for the Global Excellence Stature (GES) funding support that enabled me to accomplish this research.

ABSTRACT

Most Severe Plastic Deformation (SPD) processes lack both the capability for continuous process and the homogeneity of tailored material properties in processed samples. These challenges have limited the adaptation of SPD technology to process titanium alloys for biomedical and structural applications. This thesis presents microstructural and mechanical characterization of Ti6Al4V titanium alloy processed by a Constrained Bending and Straightening (CBS) SPD technique. The proposed CBS method was intended for a continuous process of titanium sheets with improved magnitude and homogeneity of the entailed strain, hardness and tensile properties.

The CBS process tool was designed and fabricated in the University of Johannesburg workshop. The tool was used to process Titanium Alloy Grade 5 (Ti6Al4V) sheets at a combination of (2, 4, 6) passes (N) and (6 mm, 12 mm) feeds (F) designated as N2F6, N4F6, N6F6, N2F12, N4F12 and N6F12. Sub-samples were cut from the processed sheets. The samples were prepared, and their respective microstructural analysis, hardness and tensile tests were performed. A numerical model for the CBS process was built and simulated with ABAQUS Standard Finite Element Analysis (FEA) method. The model was used to predict the magnitude and the homogenity of the Effective Plastic (EP) strain, the tensile yield strength and the hardness of the material. The simulation results were validated with the experimental data. The experimental results showed that

comparing with the As Received (AR) samples, the processed samples showed a decrease in the average grain size from 10μm to 3μm, together with the formation of new finer subgrains. The tensile strength, the yield strength and the hardness of the material increased by 29.3%, 33.5% and 24.4%, respectively. The values of these material properties at the F6 feed were higher than those at the F12 feed.

The simulated results showed that the maximum mean EP strain of 2.87 induced in the material correlated with the highest strain homogeneity that corresponded to the lowest Coefficient of strain Variation (CV) of 18.9%. A comparison of the results from both methods on the yield strength and the hardness showed a direct correlation at the N2 and the N4 passes. A relative inverse correlation was observed at the N6 pass due to the saturation of the material hardening and the onset of yielding. Results from this study have quantitatively shown that the CBS method performed well the intended work. However, this method needs desirable improvement at a commercial level before it is viable as an alternative method for the continuous production of the titanium alloy sheets enhanced with the homogeneous microstructural and mechanical properties.

TABLE OF CONTENTS

LIST OF FIGURES

LIST OF TABLES

LIST OF PUBLICATIONS

Journal articles

1. W. M. Mwita and E. T. Akinlabi, "Numerical prediction of tensile yield strength and micro hardness of Ti6Al4V alloy processed by constrained bending and straightening severe plastic deformation," *Mater. Res. Express*, vol. 6, no. 10, p. 106560, Aug. 2019. doi: 10.1088/2053-1591/ab39a9.

2. W. M. Mwita and E. T. Akinlabi, "Bending Forces and Hardness Properties of Ti6Al4V Alloy Processed by Constrained Bending and Straightening Severe Plastic Deformation," in *Advances in Material Sciences and Engineering. Lecture Notes in Mechanical Engineering*, 1st ed., M. Awang, S. Emamian, and F. Yusof, Eds. Singapore: Springer-Singapore, 2020, pp. 389–398. doi: 10.1007/978-981-13-8297-0_41.

Conference proceedings

1. W. Mwita, E. Akinlabi, and K. Sanusi, "Constrained bending and straightening-a proposed method for severe plastic deformation of metals," *IOP Conf. Ser. Mater. Sci. Eng.*, vol. 423, pp. 1–6, Nov. 2018.
   doi: 10.1088/1757-899X/423/1/012169.
   Presented at:
   3rd International Seminar on Advances in Materials Science and Engineering (ISAMSE) Nanyang, Singapore. Jun 22-24, 2018.

2. W.M. Mwita and E.T. Akinlabi,
   "Numerical investigation on strain properties of Ti6Al4V alloy processed by

constrained bending and straightening severe plastic deformation" *ASME 2019 International Mechanical Engineering Congress and Exposition, 2020,* p. V012T10A024. doi:10.1115/IMECE2019-11163
Presented at:
ASME 2019 International Mechanical Engineering Congress and Exposition IMECE2019, November 11-14, 2019, Salt Lake City, Utah, USA.

3. K.O. Sanusi, E.T. Akinlabi, and W.M. Mwita,
"Accumulative Roll Bonding (ARB) Process for Effective Biomedical NiTi Alloys," in *Volume 3: Biomedical and Biotechnology Engineering*, 2017, p. V003T04A059. doi: 10.1115/IMECE2017-71299.
Presented at:
American Society of Mechanical Engineers-International Mechanical Engineering Congress & Exploitation (ASME-IMECE)-2017, Tampa Convention Center, Tampa Florida USA November 3-9, 2017.

LIST OF ABBREVIATIONS

ABBREVIATIONS	DEFINITIONS
AR	As Received
ARB	Accumulative Roll Bonding
ASR	Asymmetric Rolling
BC	Boundary Condition
BCC	Body Centered Cubic
BMD	Bending Moment Diagram
CBS	Constrained Bending and Straightening
CGP	Constrained Groove Pressing
CGP-CR	Constrained Groove Pressing-Cross Rotation
CP Ti	Commercial Pure Titanium
CV	Coefficient of strain Variation
DISC	Discharge
ECAP	Equal Channel Angle Pressing
ECAP-C	Equal Channel Angle Pressing-Conform
EDS	Electron Diffraction Spectrometer
EP	Equivalent Plastic
FBD	Free Body Diagram
FC	Force of Constraining
FCC	Face Centered Cubic
GP	Groove Pressing
HCP	Hexagonal Close Packed
HPT	High Pressure Torsion
HV	Vicker's Hardness

ABBREVIATIONS	DEFINITIONS
I-ECAP	Incremental Equal Channel Angular Press
MDF	Multi Directional Forging
NT	Normal-Transversal
OPM	Optical Microscope
RCS	Repetitive Corrugation and Straightening
RN	Rolling-Normal
RT	Rolling-Transversal
SE	Super Elasticity
SEM	Scanning Electron Microscope
SFD	Shear Force Diagram
SMA	Shape Memory Alloy
SME	Shape Memory Effect
SPD	Severe Plastic Deformation
SR	Symmetric Rolling
SYM	Symmetry
TE	Twist Extrusion
XRD	X-Ray Diffractometer

NOMENCLATURE

SYMBOLS	DESCRIPTIONS	UNITS (SI)
A_s	Shear area	m^2
A_t	Tensile area	m^2
B	Full width at half maximum peak (FWHM)	Rad
b	Burger's vector, length, width	m
C_i	i^{th} Cycle of bending-straightening strokes	-
D	Die size, length	m
d	Grain size	m
E	Young's modulus	N/m^2
ε	Axial strain	m/m
ε_{en}	Engineering strain	-
eF	Fracture elongation	-
ε_m	Mean strain	-
eP	Percentage elongation	-
ε_p	Plastic strain	-
ε_{pci}	Effective plastics (EP) strain per i^{th}- cycle	-
ε_{pNj}	Effective plastics (EP) strain per j^{th}- pass	-
ε_{tr}	True strain	-
F	Feed length	m
f	Volume fraction of cell wall	-
FC	Constraining force	N
G	Shear modulus	N/m^2
h	Height , length	m
H	Height, length	m

SYMBOLS	DESCRIPTIONS	UNITS (SI)
I	Second moment of area	m^4
k	Material property	m
K	Scherrer's constant	-
l	Dislocation path, Length	m
L	Sample length	m
l_{gf}	Gauge length of a tensile sample after fracture	m
l_{go}	Initial gauge length of a tensile sample	m
M	Bending moment, torque	Nm
m	Factor of safety	-
MA	Mechanical Advantage	-
M_{max}	Maximum bending moment	Nm
M_T	Taylor factor	-
N	Number of pass	-
n	Strain hardening coefficient	-
ŋ	Efficiency	-
p	Pressure	N/m^2
Q	Bending force	N
r	Radius	m
R	Reaction force	N
Sb	Bending stress	N/m^2
Sb_{max}	Maximum bending stress	N/m^2
S_{en}	Engineering stress	N/m^2
SF	Fracture stress	N/m^2
S_o	Material stress coefficient	N/m^2
Ss	Shear stress	m^2

SYMBOLS	DESCRIPTIONS	UNITS (SI)
ST	Tensile Strength/tensile ultimate strength	N
S_{tr}	True stress	N/m^2
SY	Yield stress/plastic flow stress	N/m^2
T	Temperature	K
t	Thickness	m
Ti	Titanium	-
u, v ,x	Length	m
V	Shear force	N
w	Width	m
Z	Section modulus	m^3
α-Ti	Alpha phase of titanium	-
β	Angle of twist of die	Rad
B-Ti	Beta phase of titanium	-
γ	Shear strain	m/m
θ	Angle of shear, diffraction	Rad
λ	Wave length	m
v	Poison ratio	-
ρ	Dislocations density	m^{-2}
τ	Shear stress	N/m^2
μ	Coefficient of friction	-
ω	Rotational speed	Rad/s
Φ	Angle of die	Rad
δ%	Percentage increase of yield strength and hardness values based on AR samples	-
Δ%	Percentage variation of results between experimental and simulated model	-

GLOSSARY OF TERMS

Glossary terms	Definitions
Alpha-titanium	Titanium phase with HCP lattice structure
Apparent shear angle	The angle at a given position with respect to the perpendicular to the surface of the sheet before rolling
Bending/straightening height (h) In CBS	The height moved by bender and straightener during bending and straightening strokes respectively
Beta transus temperature	Is the critical temperature at which alpha titanium transforms to beta titanium upon heating
Beta-titanium	Titanium phase with BCC lattice structure
Bio implants	These are artificial devices placed in the body in order to perform treatment, assist or completely replace biological structures e.g. orthodontic guide wires, spinal cord disc stabilizing plates.
Biocompatibility	Capability of bio material, structure or implant to coexist and perform its duties without causing any adverse effect to the cells, tissues and organs of the host body.
Biomedical materials	These are materials used for making implants and prostheses (artificial organs) e.g. titanium alloys and stainless steels.
Boundary condition (BCs) in FEA	BCs are sets of known constraints/conditions for an FEA model. They can be force, moment rotational and translational displacement, temperature etc.

Burger's vector	Defines the magnitude and direction of the lattice distortion due to a dislocation in the lattice structure
CBS Cycle (C)	A CBS cycle C consists of bending-straightening strokes.
CBS Pass (N)	A CBS pass N is completed when a cycle C for bending-straightening is performed entirely over the sample length at a preset feed length.
Coefficient of strain variation (CV)	CV is a strain homogeneity measuring criterion defined as the ratio between the standard deviation of the strain value to the mean strain value. The lower the CV implies the higher the strain homogeneity and vice versa.
Constrained bending and straightening (CBS)	CBS SPD involves imposing simple shear strains in material by successful bending and straightening of the material in a constrained state at a predetermined feed length.
Continuous process	Is a non-discrete process that can manufacture bulk samples of material efficiently in a short time
Corrosion resistance	Ability of material to resist reaction with environmental adverse agents such as moisture, chemicals and oxygen.
CP titanium	This is commercial pure titanium with more than 98% purity
Crystallite	Is the smallest unit of grain
Crystallite mean size (D)	Is the average volume or area crystallite size

Deformation-elastic	A recoverable deformation of material after removal of the load
Deformation-plastic	This is a non-recoverable/permanent deformation of material after removal of the load
Dislocation	A dislocation is a defect in the crystal structure that may be due to the abnormality of the atomic positions
Dislocation density	Is the number of dislocations per unit volume of the crystalline material
Dislocation-edge	An edge/line dislocation forms when an extra plane of atoms is inserted in the crystalline material. In this case the Burgers vector is perpendicular to the dislocation line.
Dislocation-screw	Screwed dislocations result when the dislocations move perpendicular to the direction of the shear stress. In this case, the Burgers vector is parallel to the dislocation line.
Ductility of material	Ability of material to undergo plastic deformation before it fractures e.g. mild steel is more ductile than Ti6Al4V alloy.
Effective plastic (EP) strain	EP strain is the Von Mises equivalent plastic strain induced in material when that material undergoes plastic deformation.
Element	Elements are the smallest bodies discretized from the finite element main model. Connected elements build up the model.
Engineering strain,	This is the ratio of change in the dimension of the body

(ε_{en})	to its original dimension
Engineering stress (S_{en})	This is the applied load divided by the original cross section area of the member
Factor of safety (m)	The ratio of strength of the material to the applied load
Feed (F) of CBS	A feed F in CBS is the distance/velocity the sample moves after each successful bending-straightening cycle in the rolling direction
Flow stress	Flow stress is the instantaneous value of the stress required to continue plastically deforming the material. It is approximated to the yield stress of the material.
Fracture elongation (eF)	Fracture/total elongation is defined as the percentage by which the material can be stretched before it completely breaks.
Fracture stress (SF)	Fracture stress is the instantaneous stress value at fracture-usually lower than the tensile strength
Gauge length of the tensile test sample (l_g)	This is the effective thinner part of the tensile test specimen for tensile deformation
Grain	A grain consists of crystals arranged in a definite pattern and orientation.
Grain boundary	Is the interface region between two or more neighboring grains
Grain size	This is the average diameter of the grain based on either its volume or area.
Hardness	Hardness is the ability of the material to resist indentation/penetration by other materials.
Lattice strain fields	These result from the displacement of atoms from their

	regular positions in the lattice structure due to induced dislocations and plastic deformation. Lattice strain fields can be tensile or compressive.
Lattice structure	This describes the orderly arrangement of atoms in crystalline solids.
Low angle (LAGB) and high angle grain (HAGB) boundary	These are the average distribution of mis-orientation angles between neighboring grains measured along the grain boundaries. LAGB< 15^{o} and HAGB >15^{o}
Major diameter of thread (d)	The outer diameter of the bolt thread
Nipple	Male pipe joint
Node	Nodes are used as connectors of elements that build up the model. Nodes act as joints for the elements.
Percentage elongation (eP)	Percentage elongation is a measure of a tensile test sample material's ductility, defined as the ratio of increase of gauge length to the original gauge length.
Phase of material	That part of the material with homogeneous physical and chemical characteristics.
Poison ratio	The ratio between the lateral strain to the longitudinal strain
Repetitive corrugation and straightening (RCS)	RCS is SPD where simple shear strains are induced in a material via repeated bending and straightening load.
Severe plastic deformation (SPD**)**	SPD involves imposing large plastic strains in material by a hydrostatic load with insignificant change of material geometrical dimensions.

Shape memory effect (SME)	SME is the property of a material, in which it recovers from load induced residual strains and remembers its shape upon unloading and heating.
Shear-pure	Pure shear is shearing of the body without it being associated with any bending phenomenon. It involves no rigid body rotation.
Shear-simple	Simple shear is a deformation of the body in which parallel planes in the body remain parallel, while maintaining a constant distance relative to each other-even after deformation. It involves rigid body rotation.
Slip plastic deformation	Sliding of crystal blocks of atoms over one another along definite crystallographic planes that are known as slip planes.
Socket	Female pipe joint
Springback	Resistance of material to bending
Strain (ε)	The ratio of change in the dimension of the body to its original dimension e.g. axial and shear strain.
Strain hardening exponent (n)	Material property factor that characterizes hardening behaviour of material during hot or cold working.
Strain homogeneity	This is a property of even distribution of strain in a material in terms of magnitude and orientation.
Strain propagation in CBS	This is imposing strain in the sample after a CBS bending-straightening cycle C, is propagated entirely over the sample length at a preset feed length.
Strain superposition in CBS	Resultant effective plastic strain after C cycle is propagated entirely over the sample.

Strength coefficient ($S_{o)}$	This is a material property that characterizes the strengthening behaviour of a material
Stress (S)	Stress is the ratio of applied force to the area of action
Supper elasticity (SE)	SE is the property when the material is loaded at austenitic temperature. It can recover large residual strains up to 8% upon removal of the load.
Tensile strength (ST)	This is the maximum/ultimate strength attained by a material before yielding to fracture
Thread pitch (*l*)	The axial length moved by a thread in one rotation
Thread tap	A tool for making threads
Titanium alloy	A combination of titanium with other elements to form titanium alloys e.g. Ti6Al4V and Ti-6Al-7Nb
Titanium alloy stabilizers	Stabilizers are elements added to a titanium alloy to stabilize in either the alpha phase (e.g. Al,O,C) or the beta phase (e.g. V, Mo, Ta).
True strain (ε_{tr})	Is the ratio of instantaneous change in the dimension of the body to its initial size
True stress (S_{tr})	This is the applied load divided by the instantaneous cross section area of the member
Twinning plastic deformation	Involves a portion of the crystal blocks of atoms that are moved on one side of the plane to form a mirror of the atoms on the other side of the plane. The mirror plane is known as the twinning plane.
Ultrafine and nano grain structures	Ultrafine grain structure has average grain size of greater than 100nm and less than 1000nm; while the nano size structure has an average grain size of less

	than100nm.
Unit cell	The unit cell is the basic unit of atomic order repeating itself in the crystal structure.
Wear resistance	This is the ability of a material to resist sliding contact material removal in different environmental conditions.
Yield strength (SY)	Yield strength is the maximum strength of material in the elastic range approximated to the proof stress at 0.2% of plastic strain.

CHAPTER ONE: INTRODUCTION

1.1 Background of the study

Recent studies have shown that titanium and its alloys have significantly gained application in biomedical, aerospace and automotive engineering [1][2][3][4]. These materials are preferred to other alloys due to their competitive properties, such as a high strength to weight ratio, relatively good corrosion resistance, low stiffness and good biocompatibility. However titanium and its alloys have exhibited low strength, hardness and poor wear resistance that may lead to in-service failure of the structures and the bio implants [5]. The performance and reliability of these materials' structures are dependent on the intrinsic and artificially enhanced functional properties by specific applied manufacturing processes. The functional properties include; strength, hardness and fine grained microstructure.

Severe plastic deformation (SPD) is among the advanced methods applied to process and enhance titanium alloys with improved functional properties for structural and biomedical application. Repetitive corrugation and straightening (RCS) is one of the severe plastic deformation processes that have been used to manufacture ultrafine grain structured titanium sheets with improved microstructural and mechanical properties [6][7].

1.2 Problem statement

Most SPD technology processes lack both the capability of continuous production and the homogeneity of material properties enhanced in processed metallic sheet samples. The processes are still characterized as discrete processes; and they are limited to small size samples of metals and alloys. These have been among the major challenges of SPD technology to be implemented and to process titanium alloys on the industrial scale. More research is still needed to improve the SPD technology for the continuous processing of bulk titanium alloy samples with improved magnitude and homogeneity of the enhanced properties for structural and biomedical applications.

1.3 Study Objectives

1.3.1 Aim of the study

The aim of this study is to investigate the mechanical and microstructural properties of Ti6Al4V alloy sheets processed by the constrained bending and straightening (CBS) severe plastic deformation (SPD) technique. The CBS processes is intended to continuous process and enhance the Ti6Al4V alloy with improved magnitude and homogeneity of strain, tensile strength, hardness and microstructure.

1.3.2 Specific Objectives

Specific objectives of this study are:

(i) To design and fabricate a CBS processing tool;

(ii) To perform the CBS processing on Ti6Al4V sheet samples;

(iii) To analyze the microstructure of the processed samples;

(iv) To determine the tensile properties of the processed samples

(v) To determine the hardness properties of the processed samples;

(vi) To develop a numerical model for the CBS process that predicts the magnitude and the homogeneity of the induced strain;

(vii) To apply the model to predict the tensile yield strength and the hardness of CBS processed Ti6Al4V samples.

1.4 Hypothesis statement

This study investigates the capability of the proposed CBS SPD method to process and enhance Ti6Al4V alloy sheets with improved microstructural and mechanical properties. Using experimental and numerical methods, it is expected that the CBS method will improve the evolving microstructure, the homogeneity and the magnitude of the induced strain, hardness and the tensile strength of the CBS processed Ti6Al4V sheet samples at the selected number of passes and feed lengths.

1.5 Significance of the study

The findings of this study will impact on the followings:

(i) CBS is aimed to be an alternative continuous SPD method for Ti6Al4V sheets to be enhanced with improved homogeneous properties;

(ii) Enhanced material properties will improve the performance and the reliability of Ti6Al4V alloy for biomedical and structural application;

(iii) The rresults from this research will provide CBS performance parameters for effective material properties

(iv) The use of the CBS technique will lead to the production of light-weight and stronger titanium alloys preferred for biomedical, aerospace and automotive applications.

(v) It is expected that in the future CBS will be extended to process other metallic materials.

(vi) The results will add knowledge and skills to academics, researchers, technologists' manufacturers, the general society and the nation at large in the areas of materials processing and manufacturing.

1.6 Limitations of the study

The results from this study were based on the following conditions: The standard material investigated was 2mm thick Ti6Al4V alloy sheets processed by CBS. Feeding, bending

and straightening of the sample were done manually. A hydraulic jack of 10 tons capacity was used as a source of force for the bending and straightening.

1.7 Scope of the thesis

This thesis covers the characterization of the mechanical and microstructural properties of Ti6Al4V alloy processed by constrained bending and straightening (CBS) severe plastic deformation. Chapter One covers the study background, where the application of titanium alloys and the significance of severe plastic deformation are briefly highlighted. Furthermore, the chapter covers the research problem, the study objectives, the hypothesis and the expected research outcomes. Chapter Two consists of the detailed literature review on selected titanium alloys, their competitive properties, as well as their application in biomedical, aerospace and automotive engineering.

Chapter Two has an overview on the various severe plastic deformation methods, their performance and the drawbacks specifically on titanium alloys. A detailed description of the CBS SPD method is also presented. Chapter Three presents the methodology applied to achieve the research objectives; and it consists of the design and the fabrication of CBS physical model, the procedures for: processing samples with CBS, tensile, hardness and microstructural analysis. Chapter Three also includes a numerical modelling of the CBS process. Chapter Four covers the results presented in various tabular and graphical

forms. It also contains a detailed discussion of both the experimental and simulation results. Chapter Five contains the main conclusions made from the study, as well as the recommendations for future work. The references and appendices are presented at the end of the thesis.

CHAPTER TWO: LITERATURE REVIEW

2.1 Scope and focus of the literature review

The literature review focuses on the competitive properties and the drawbacks of titanium alloys for biomedical, automobile and aerospace applications. The various severe plastic deformation techniques reported in the literature for processing titanium alloys with enhanced mechanical and microstructure properties were also discussed. Each technique was discussed by focusing on the working principle, the induced strain theoretical formulas, the performance (in this review, this was based on the capability of continuous processing and homogeneity of the induced strain), as well as the respective associated drawbacks. A proposed CBS SPD method, its working principle and the key features of this method were highlighted. Lastly, conclusive remarks on the literature review were summarized.

2.2 Titanium and its alloys

Titanium ore was first discovered in 1891 in a Cornish sand beach by an English chemist and mineralogist, William Gregor [1]. It is the fourth most abundant structural metal in the earth's crust (0.57%) by weight, after aluminum (8.23%), iron (5.63%), and magnesium (2.33%) respectively. The main ores of titanium are rutile with 95% of TiO_2 and ilmenite ($FeTiO_3$) with 50%-65% of TiO_2 [2]. Pure titanium has an average melting point of 1675^{o}C, a density of 4500 kg/m^3, elastic stiffness of about 120 GPa, thereby

giving it a high strength to weight ratio. The formation of a chemically inert oxide on its surface makes it an excellent corrosion resistant compound. These are among the competing properties that have made titanium and its alloys a choice for various structural and biomedical applications. The phase state of titanium and its alloys is dependent on the thermal-mechanical processes performed, and on the alloying elements in the material. These alloys exist mainly in the alpha phase with a hexagonal close packed (HCP) lattice structure; or in the beta phase with a body centered cubic (BCC) lattice structure, or in a mixture of both alpha and beta phases. HCP and BCC lattice structured unit cells are shown in figure 2.1(a) and (b) respectively. A Scanning Electron Microscopic image of T6Al4V alpha-beta titanium is shown in figure 2.2.

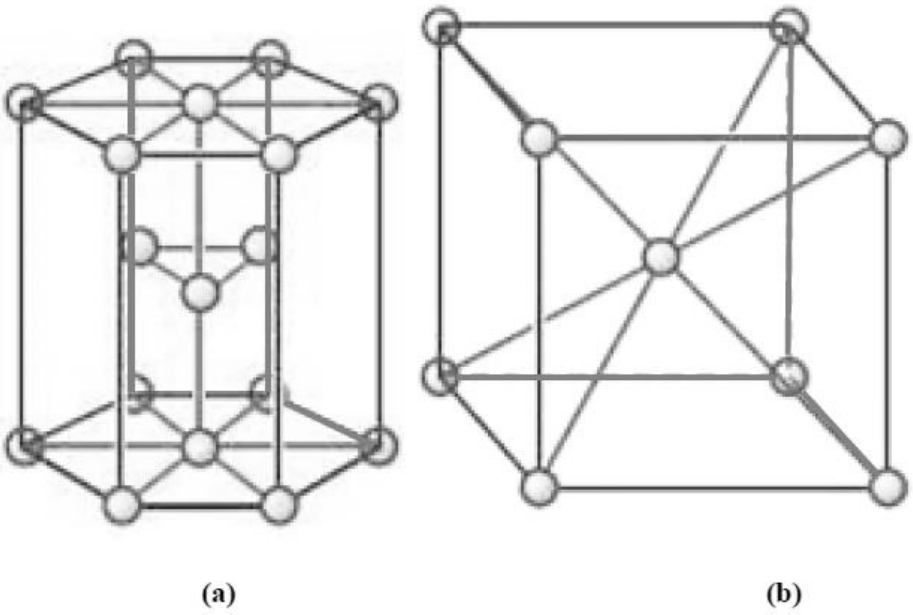

Figure 2.1: (a) HCP and (b) BCC crystal lattice structures[2]

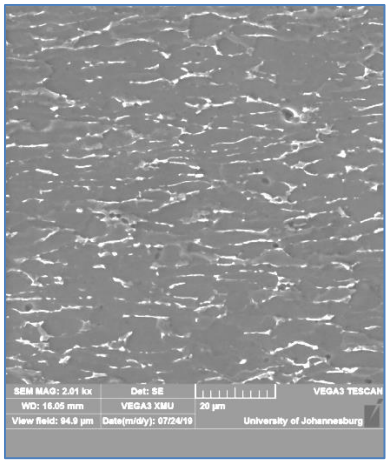

Figure 2.2: SEM image of Ti6Al4V alloy with alpha (grey) and beta (white)) phases[8]

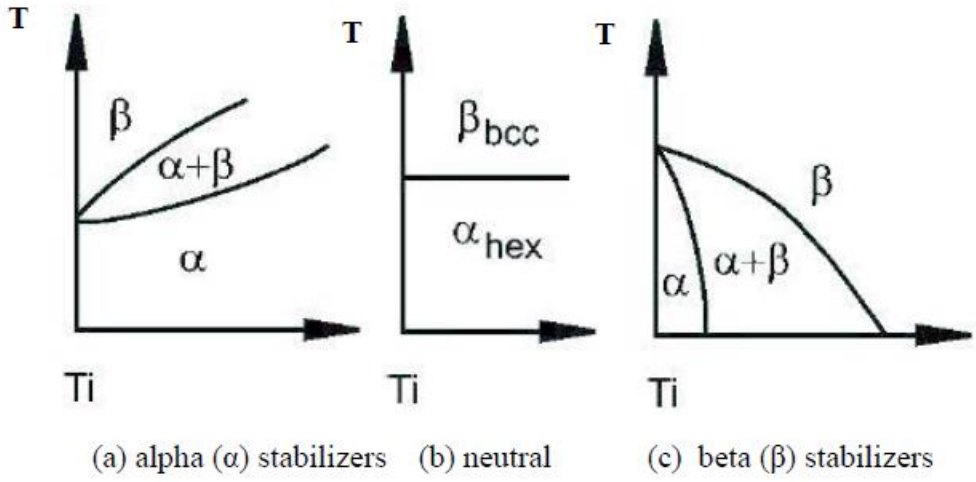

Figure 2.3: Temperature (T) versus stabilizers concentration phase diagrams for HCP-alpha and BCC-beta titanium alloy (Ti)[2]

The transformation from the alpha to the beta phase during heating is dependent on the material temperature condition known as beta-transus temperature. The average beta-transus temperature for pure titanium is 885^{o}C [2]. Certain alloying elements are added to

stabilize alpha phase at high temperatures, as shown in figure 2.3 (a). The alpha phase titanium is stable below the beta-transus temperature while the beta phase is stable above the beta-transus up to the melting temperature in figure 2.3 (b). The beta phase can be stabilized at lower temperatures by adding some elements, as shown in figure 2.3 (c). Aluminum (Al), Oxygen (O), Carbon (C) and Nitrogen (N) are used as alpha stabilizers; while elements such as Vanadium (V), Iron (Fe), Molybdenum (Mo), Nickel (Ni), Chromium (Cr), Tantalum (Ta) and Niobium (Nb) are used as beta phase stabilizers at lower temperatures [2].

Commercially pure titanium (CP Ti) is an example of the alpha phase titanium. Depending on the quantity of added interstitial oxygen element, this material is further divided into four grades namely; Grade1, 2, 3 and 4 [2][9]. The tensile and yield strength of the material increases with the grade number. The ductility of the material decreases with the grade number; therefore CP Ti Grade1 is relatively most ductile, followed by CP Ti Grades 2, 3 and 4, respectively. Biomedical and structural application of CP Ti titanium will be briefly discussed in the next sub-chapter.

Ti6Al4V is one of the titanium alloys that exhibit both the alpha and the beta phases at room temperature. This can be achieved by the addition of 10%-20% of beta stabilizers to the alloy. Aluminum element is added to stabilize the alpha phase, to harden and improve

the strength of the alloy. Vanadium is added to stabilize the beta phase, to improve ductility and the material's formability.

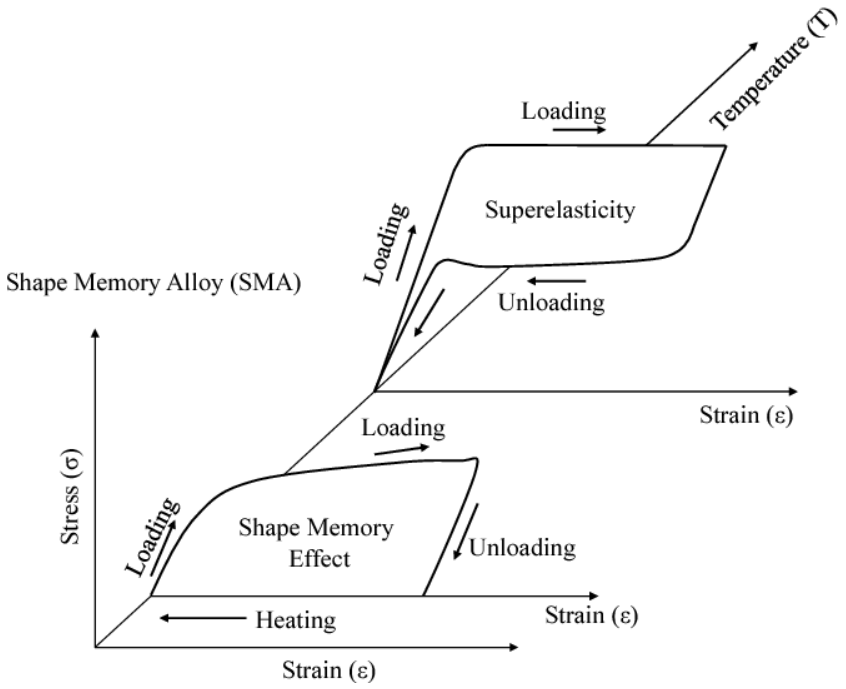

Figure 2.4: SME and SE of NiTi alloy[10]

Another group of titanium alloys is known as titanium based shape memory alloys. An example of these alloys is the NiTi alloy. The NiTi alloy has two additional unique properties, namely the Shape Memory Effect (SME) and Super-Elasticity (SE), as shown in Figure 2.4. In SME, after the material is deformed at a low temperature, and the subsequent removal of the load, the material recovers a large residual strain (up to 8%), upon heated to the austenite finish temperature via martensite-austenite phase

transformation. In SE, the material, when loaded at the austenite finish temperature, it may deform beyond the elastic strain but it recovers the strain completely upon removal of the load. These unique material properties have made titanium shape memory alloys competitive materials for biomedical and structural application as briefly discussed in the next sub-chapter.

2.3 Application of titanium and its alloys

The use of titanium and its alloys as biomedical materials has been increasing significantly. Biomedical materials are those materials used in biomedical engineering for making prostheses and implants[11][12]. The requirements for biomedical materials include; high static and fatigue strength, excellent corrosion and wear resistance, together with a low modulus of elasticity close to that of bone [2][13]. These materials should have good ductility, biocompatibility and be free from toxic elements, such as Vanadium and Tin.

Traditionally, stainless steel (SS), Cobalt Chromium (CoCr) and Titanium (Ti) alloys have been the main metal alloys used for biomedical implants [14]. However SS and CoCr alloys have relatively a higher elastic modulus than that of a host's cortical bones. This can lead to high stress shields along implant-body contact and the release of adverse Cr ions to the host body.

Titanium and its alloys are preferred, rather than SS and CoCr alloys, based on their relatively excellent corrosion resistance, low elastic modulus (about 120 GPa), relatively close to that of the bone (30 GPa), and good biocompatibility. Biomedical Ti alloys include commercially purity titanium (CP Ti), Ti6A14V and NiTi. CP Ti is preferred for low strength application in cardiovascular implants such as artificial valves and stents. Ti6A4V is preferred for high static and fatigue strength application in orthopaedic implants such as bone plates, hip joint stem, craniofacial plate and plate screws [1][5]. Non-toxic titanium alloys, with lower stiffness than CP Ti and Ti6A14V alloys have been developed for bio implants. Examples are: Ti6AlNb, Ti13Nb13Zr and Ti12Mo6Zr2Fe [1][13].

The Shape Memory Effect (SME) and Super-Elasticity (SE) unique properties of the NiTi alloy make this material applicable for producing bio implants for instance in dentistry for teeth holding and filling wire. Furthermore, the alloy is used for spinal implants where the SME property is exploited for spinal disc stabilization and the orthopaedic joining of fractured bones [15].

Based on their high specific strength, good resistance to heat, corrosion resistance, embrittlement at low temperature, and thermal expansion, titanium alloys are competitive materials for aerospace engineering. CP Ti is used for nacelle at the engine entry and hot

air and water pipes. Alloys, such as Ti6Al4V, Ti6Al2Sn4Zr2Mo, Ti-8AlMoV, Ti15V3Cr3Su3Al and Ti10V2Fe3Al are used for making air frames, blades for turbines, compressors and fans, landing gears and drive shafts [2][4]. Titanium alloys are also competitive materials in automotive engineering for making valves, valve springs, suspension springs, connecting rods exhaust pipes, propelling shafts and body panels. Furthermore, the alloys are also used for making military vehicles, tanks and armors [3].

A list of commonly used alpha, beta and alpha-beta titanium alloys for structural and biomedical applications is presented in Table 2.1.

Table 2.1: Alpha, beta and alpha-beta titanium alloys [2][3][13][16]

Alloy	**Alloy type**	**Alloy**	**Alloy type**
CP-Ti, Grades:1, 2, 3 and 4	α	Ti-10V-2Fe-3Al	Near β
Ti-5Al-2.5Sn	α	Ti-15V-3Cr-3Su-3Al	β
Ti-8Al-1Mo-1V	Near α	Ti-13V-11Cr-3Al	β
Ti-6Al-2Sn-4Zr-2Mo	Near α	Ti-13Nb-13Zr	β
Ti-5Al-2Sn-2Zr-4Cr-4Mo	α + β	Ti-12Mo-6Zr-2Fe	β
Ti-6Al-2Sn-4Zr-6Mo	α + β	Ti-15Mo	β
Ti-8Mn	α + β	Ti-15Mo-3Nb	β
Ti-5Al-2.5Fe	α + β	Ti-16Nb-10Hf	β
Ti-6Al-7Nb	α + β	Ti-15Mo-5Zr-3Al	β
Ti-4Al-3Mo-1V	α + β	Ti-15Mo-2.8Nb-0.2Si-0.26O	β
Ti-6Al-4V	α + β	Ti-35Nb-7Zr-5Ta	β
Ti-4Al-6V-2Sn	α + β	Ti-29Nb-13Ta-4.6Zr	β

Although titanium alloys are competitive and preferable materials for structural and biomedical engineering applications, the choice of these alloys is hindered by the relatively high costs associated with their manufacturing processes. This is due to the fact that these alloys are very reactive to other elements such as hydrogen and oxygen. Ore purification, casting and welding processes performed on these alloys should be done at a highly isolated environment free of contaminants [17][18]. Furthermore, these alloys have low ductility; they are hard to machine; and that leads to significant tool wear. Nevertheless, there is a need for efficient manufacturing processes to enhance these alloys with the desired properties.

The SPD process is currently among the advanced techniques applied to enhance titanium alloys with ultrafine/nano microstructure and improved tensile strength and hardness [19][20][21]. Performance and challenges of the SPD on the titanium alloys are discussed in detail in the forthcoming subchapters. The next sub-chapter discusses the fundamentals of plastic deformation of metals, when subjected to loads of magnitudes that are beyond the elastic limit.

2.4 Plastic deformation of metals

Metals, like other materials, when subjected to sufficient loads undergo deformation in the form of axial or shear strains. The applied load may be in the form of tensile,

compression, bending and torsion, or a combination of these. When these materials are subjected to the load below the elastic limit, they recover the induced deformation upon removal of the load. The recoverable type of deformation is known as elastic deformation. This behaviour in materials is mathematically well described by Hooke's Law. On the other hand if the applied load is higher than the elastic limit, the materials do not recover the induced deformation upon the removal of the applied load. This unrecoverable deformation of the material is called plastic (also known as permanent) deformation. Elastic deformation stretches the inter-atomic bonds away from their equilibrium radius of separation, without sufficient energy to break the inter-atomic bonds.

Plastic deformation to some extent breaks the inter-atomic bonds; and therefore, involves the rearrangement of atoms in a solid material. The plastic deformation is a result of the movement of high density dislocations, due to the applied load in the plastic range. Two main types of plastic deformation may occur in the material; these are slip and twining as illustrated in Figure 2.5 (a) - (c). Slip plastic deformation involves sliding of the crystal blocks of atoms over one another along definite crystallographic planes, known as slip planes. Slipping occurs by motion of dislocations when the applied shear load exceeds the critical value. Each atom in a crystal moves same distance along the slip plane; while the crystal orientation remains unchanged. The slip plane is generally the one with the

greatest atomic density; and the slip direction is the closely packed direction within the slip plane.

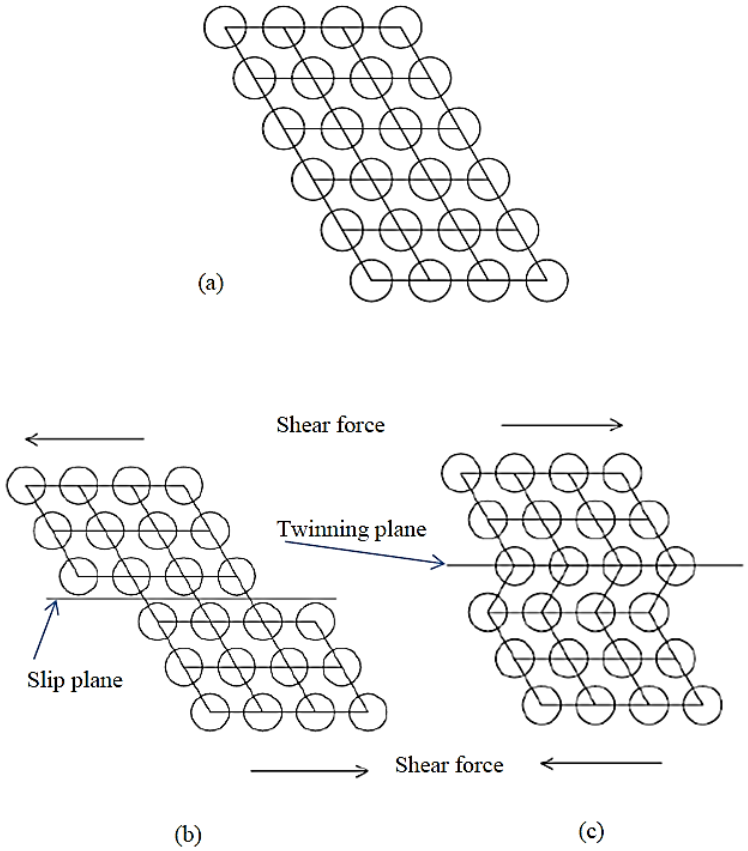

Figure 2.5: Plastic deformation of a crystal lattice structure: (a) un-deformed crystal (b) slip deformation in which the atoms in the lattice are moved to new positions (c); and twinning deformation, in which the atoms move and form a mirror image on the opposite side of the twinning plane

Twining refers to plastic deformation that occurs when the applied shear stress causes a portion of the crystal blocks of atoms to shift out of position and assume new orientations. The atoms are moved to form a mirror image of the atoms of the other side of the plane, known as the twinning plane. The twinned lattice is the mirror image of the

parent crystal. The main role of the twinning deformation is that it can cause changes in plane orientation; so that further slip can occur. Slip deformation mostly occurs in face centered cubic (FCC) metals; while twinning deformation occurs mostly in BCC and HCP metals.

In slip plastic deformation, the orientation of the crystal atoms on either side of the slip plane remains unchanged; while twinning deformation results in the reorientation of the atomic direction across the twinning plane. Twinning occurs at low temperatures and high rates of shear and shock loading where there are few slip systems restricting slip deformation. The magnitude of slip deformation is relatively higher (in exact atomic spacing) than twinning deformation (in less than interatomic spacing). Plastic deformation in metals can lead to their phase transformation; A good example is stress induced phase transformation exhibited by shape memory alloys [22][23].

2.5 Severe Plastic Deformation (SPD) Strengthening

2.5.1 Principle of SPD

An SPD is a process whereby a material is subjected to a hydrostatic stress state. As a result, plastic strains are induced in the material sample in the form of pure or simple shear, without any significant changes in its overall dimensions. The basic principle of SPD is illustrated in Figure 2.6. A two dimensional (2D) body is hydrostatically loaded. In practical terms, the plastic strains can be induced in a material by tension,

compression, bending, torsion, or a combination of these four loads. The applied hydrostatic load can develop dislocations in the lattice structure resulting in the formation of the plastic strains in the material.

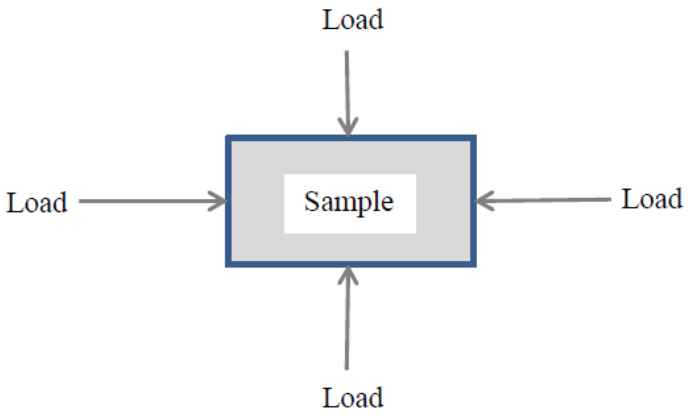

Figure 2.6: Hydrostatically loaded 2D body

Dislocations are line defects in a material's crystal- lattice structure. The defects are characterized by abrupt changes in the regular ordering of the atoms in the crystal. Irregular ordering of atoms can be due to introduced extra planes of atoms, or due to the loss of planes of atoms in the crystal. Two parameters are used to represent a dislocation; the direction of the dislocation line *l*, and the Burger's vector *b* that defines the magnitude and the direction of the lattice distortion due to a dislocation in the lattice structure. Dislocations can be in the form of edge, also known as line dislocations, screw, or a combination of them both. Indeed, most dislocations are probably a hybrid of the edge and screw forms. Figure 2.7 represents an edge dislocation in which the defective

points produced in the lattice structure by the dislocation, lie along a line. The dislocation is propagated across the crystal by slipping along one atomic plane after another, together with the breaking of a small fraction of inter-atomic bonds in the immediate vicinity of the dislocation line.

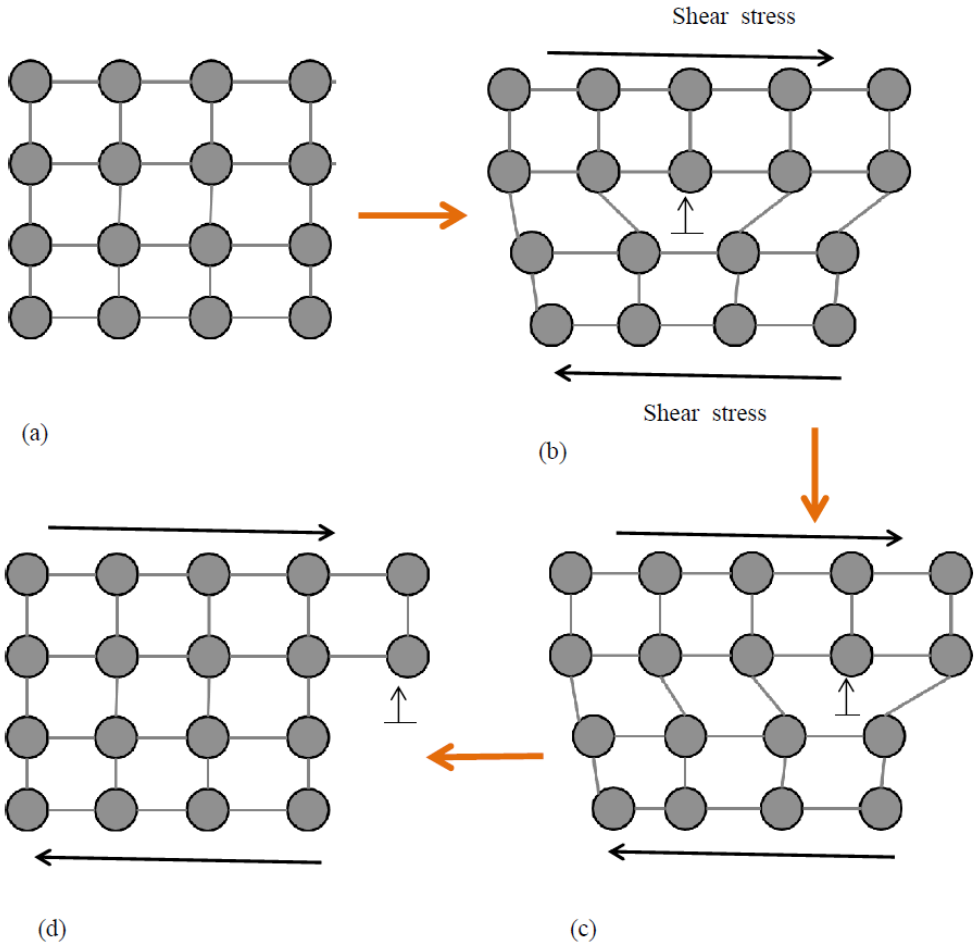

Figure 2.7: Edge dislocation: (a) defect-free crystal; (b) a crystal with line defect (dislocation) shown with a small arrow; (c)-(d) movement of dislocation in the crystal with the applied stress

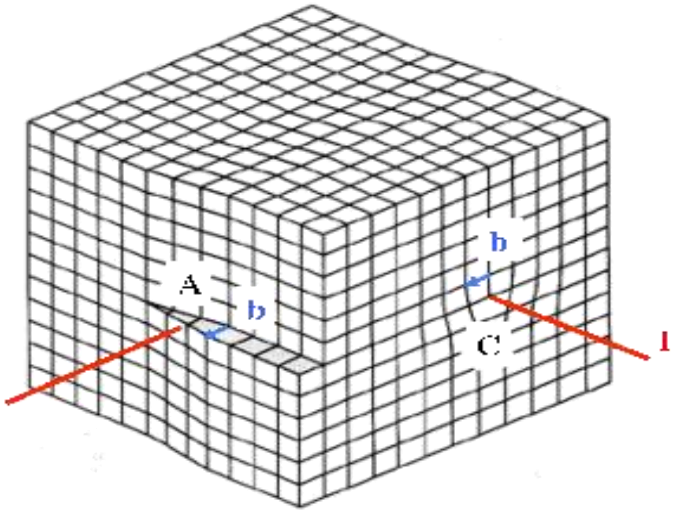

Figure 2.8: Screw dislocation on face A and edge dislocation on face C, with respective direction of dislocation line l and Burger's vector b [24]

The direction of dislocation motion is parallel to the shear stress. The Burger's vector is perpendicular to the dislocation line. In screw dislocation, as shown in Figure 2.8, the dislocations move perpendicular to the direction of the shear stress. In this case, the Burger's vector is parallel to the dislocation line. In most metallic materials, the magnitude of the Burger's vector for a dislocation is of a magnitude equal to the interatomic spacing of the material crystal lattice; since a single dislocation would offset the crystal lattice by one closely packed crystallographic spacing unit.

Dislocations can greatly affect the material properties. Since the quantity of the induced dislocations density and their movement increase with the increase of applied stress/strains, ultimately their impeded movement can result in the material's

microstructure grain refinement and improved tensile strength and hardness properties [14][25]. An equivalent strain of 3.5 and above, is sufficient to produce an ultrafine grain in the material [26]. Various models have been developed on mechanisms of strengthening metals with SPD. The main two models, namely the dislocation density strengthening model and grain boundary strengthening model were selected; and will be discussed in detail in the forthcoming sub-chapters.

2.5.2 Dislocation density strengthening model

This strengthening model assumes that increased dislocations due to material deformation are mainly stored in the grains. As the material is plastically loaded, the bonds surrounding the dislocations are elastically strained by the defect, when compared with the bonds between the constituents of the regular crystal lattice. Therefore, these bonds break at relatively lower stresses, thereby leading to plastic deformation. The strained bonds around a dislocation are characterized by the lattice strain fields; in which there are compressive strained bonds directly next to an edge dislocation and tensile strained bonds beyond the end of an edge dislocation. The strained bonds form compressive strain fields and tensile strain fields, respectively. The dislocations strain fields obey similar laws of attraction and repulsion; in order to relieve the overall strain, the compressive strains are attracted to the tensile strains, and vice versa. Ultimately, the material becomes saturated with dislocations; and more dislocations are prevented from motion and nucleating.

This resistance to the formation and the motion of dislocations manifests itself, as a resistance to plastic deformation. Eventually, the higher stress is required to overcome the strain-field interactions and further plastic deformation, therefore the yield strength of the material increases; while the ductility decreases.

The process of plastic deformation associated with dislocation movement in metals was studied extensively by Mecking and Kocks [27]. The results of their work on SPD of FCC polycrystalline metals showed good proportionality between the flow stress and the square-root of the dislocation density.

Estrin and Kubin [28] observed the macroscopic non uniformity of strain hardening on metals under slip plastic deformation. Estrin et al [29] proposed a dislocation density strengthening and hardening model on the cell-forming of crystalline materials at large strains. The cell-wall volume fraction was found to decrease, as a function of strain; furthermore, the predicted dislocation density agreed well with the experimental measurements. The volume average generated dislocation density ρ_i stored in grains is dependent on the mean free path for the dislocation movement l, the Burger's vector b and the strain ε. It is given by Equation 2.1 [30] as:

$$\rho_i = (blk_2)^{-1} - ((blk_2)^{-1} - \rho_0)e^{-k_2\varepsilon} \qquad 2.1$$

ρ_o is the initial dislocation density stored in grains; and k_2 is material constant.

The total dislocation density in the grain and the grain boundaries-ρ_t is represented in Figure 2.9; and it is given by Equation 2.2 [30] as:

$$\rho_t = \varepsilon(bl)^{-1} \quad 2.2$$

The shear stress increment, due to the dislocation density increase is given by Equation 2.3 as applied by Ashby [31] and Taylor [32] as follows:

$$\Delta\tau = \alpha_1 Gb\sqrt{\rho_i} \quad 2.3$$

$\Delta\tau$ = shear stress increment, α_1 = constant = 0.3, G = the shear modulus.

The relation between shear stress, shear strain, equivalent stress and equivalent strain can be given by Equation 2.4 as:

$$\frac{dS}{d\tau} = \frac{d\gamma}{d\varepsilon} = M_T \quad 2.4$$

M_T = Taylor factor

The increment of the flow stress ΔSY is given by Equation 2.5 [32] as:

$$\Delta SY = \Delta\tau M_T = \alpha M_T G\sqrt{\frac{b\varepsilon}{l}} \quad 2.5$$

Quantitatively, the equivalent yield stress of the material, using the dislocation-dislocation interaction model, is given by Equation 2.6 as:

$$SY(\varepsilon) = S_o + \alpha M_T Gb\sqrt{\rho_i(\varepsilon)} \quad 2.6$$

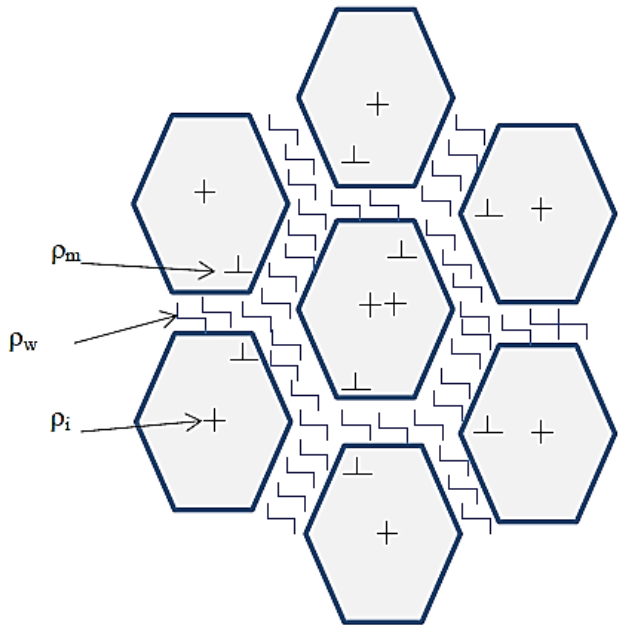

Figure 2.9: Schematic representation of the dislocation density for a polycrystalline material; dislocations in cell wall (ρ_w); dislocations in cell interior (ρ_i); and mobile dislocations (ρ_m)

The first term in the right hand side of the above equation is the initial strength; while the second term is the equivalent stress increment due to the dislocation density increase. Two common mathematical (empirical) relations of the work hardening phenomenon are used; Holloman's and Ludwig's equations are power law relationships between the stress and the plastic strain. The Holloman's equation relates the stress and the induced EP strain. The relation is given by Equation 2.7 as:

$$S = S_o \varepsilon_p^n \qquad 2.7$$

Where, S = stress, S_o = the strength coefficient, ε_p = the EP strain and n = the material property known as the strain hardening coefficient. The Ludwig's Equation 2.8 is the power law equation that includes the yield strength *SY*; and it considers the plastic strain *(ε_o)*, due to the prior deformation of the material.

$$S = SY + S_o\left(\varepsilon_o + \varepsilon_p\right)^n \qquad 2.8$$

2.5.3 Grain boundary strengthening model

In this model, SPD strengthening of metals is achieved through grain refinement. Reducing the grain size from coarse to fine grains results in more grain boundary surface area; and hence more grain boundaries which limit the lengths and the motions of dislocations. The limited movement of the dislocations strengthens the material by requiring a larger force to deform it. In this case the dislocations are stored in cell walls/grain boundaries and in grains (Figure 2.9); however, this model is strongly material dependent. Grain subdivision/fragmentation during SPD occurs, as a result of the dislocation cell formation via the accumulation of the mis-orientation between the neighbouring dislocation cells. Initially, the SPD introduces a very high dislocation density in the material, which results in intra granular structure of thick walled cells of grain boundaries with low angles ($<15^o$) of misalignment known as low angle grain boundaries (LAGBs). Increasing the strain decreases the cell walls' thickness, whereby the cells transform into fine grains; and the walls become non-equilibrium grain

boundaries with high angles (>15^{o}) of misalignment. These are known as high angle grain boundaries, (HAGBs) [33]. LAGBs and HAGBs grains are illustrated in Figure 2.10.

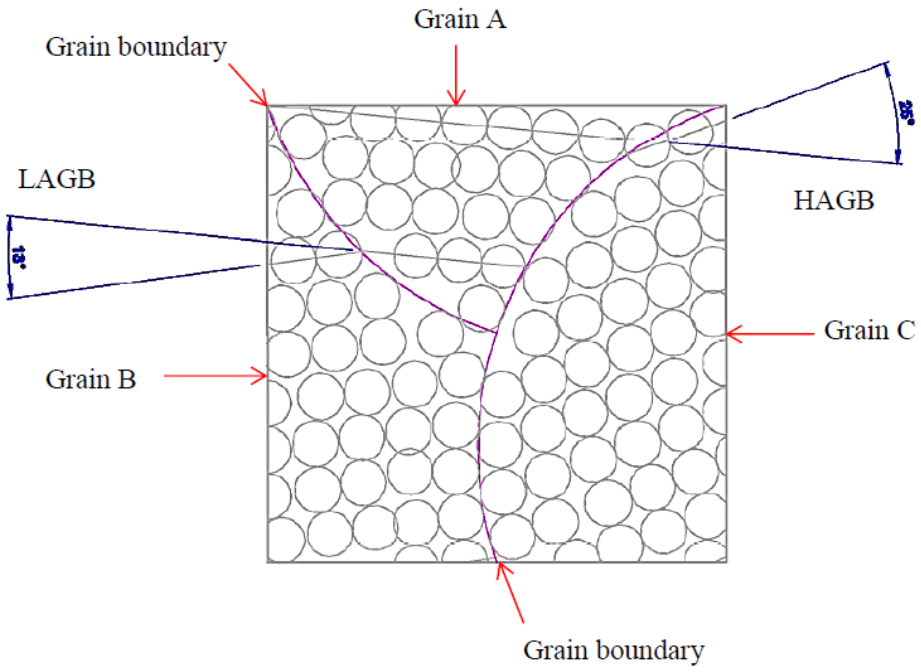

Figure 2.10: Low (LAGB) and high (HAGB) angle misalignment grain boundaries

Jiang et al [34] studied a dislocation density model that predicts the flow stress-grain size relation of polycrystalline metals. Their results agreed well with the Hall-Petch equation; and they showed that the flow stress depends on the densities of the statistically stored dislocation and the geometrically necessary dislocation. Based on the work models of Estrin and coworkers [29][35] [36], the total dislocation density in the cell interior and in the cell boundaries ρ_t is related to the dislocation cell size, according to Equation 2.9 as:

$$d = \frac{k}{\sqrt{\rho_t}} \tag{2.9}$$

Where, d = the average dislocation cell/grain size, k = the material proportionality constant. The total dislocation density is further defined by Equation 2.10 as:

$$\rho_t = f\rho_w + \rho_i(1 - f) \tag{2.10}$$

f = volume fraction of the cell walls, which decreases with the thinning of the cell walls due to the increased strain, while ρ_w and ρ_i are the dislocation densities in the cell walls and in the cell interiors, respectively. Equation 2.9 shows that the grain refinement is not an infinite process; as it would reach a steady state at a particular steady state dislocation density value. This condition is assumed; if the mechanism of grain subdivision via dislocation cell formation controls the grain refinement. The minimum achievable grain size d_{min} is determined by Equation 2.11 as:

$$\frac{d_{min}}{b} = kM_T\beta\frac{G}{S_m} \tag{2.11}$$

Where, S_m = the highest possible stress, β = a numerical constant, G = the shear modulus, b = the Burger's vector, M_T = the Tailor factor and k = the material constant.

The Hall-Petch equation predicts the relationship between the yield strength and the average grain size of the material [37], as given by Equation 2.12 as:

$$SY = S_o + \frac{k}{\sqrt{d}} \tag{2.12}$$

SY = the yield stress, S_o = the material initial stress for the dislocation movement, k = the material dependent coefficient and d = the average grain diameter.

2.6 Processes of severe plastic deformation

2.6.1 High Pressure Torsion (HPT)

The HPT is the SPD process whereby the material sample is constrained; and it is held between the upper and the lower anvils. One of the anvils rotates under a high pressure in GPa. Consequently the material is imposed with torsional plastic shear strains. The working principle of the HPT is represented in Figure 2.11.

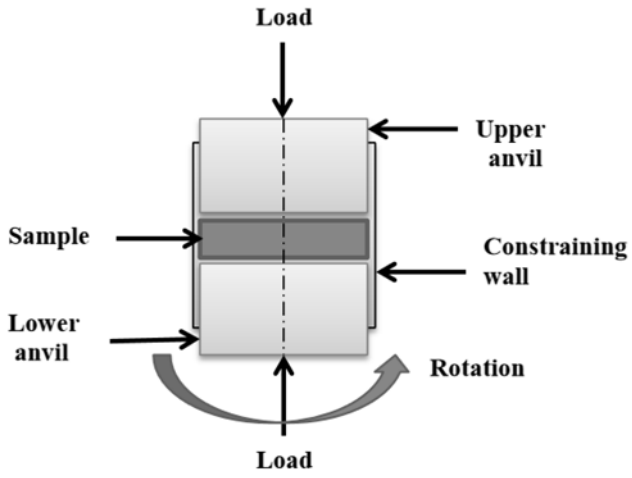

Figure 2.11: The principle of the HPT process [38]

Material is deformed plastically by pure shear, due to surface frictional forces. The effective plastic strain induced in a cylindrical sample by HPT is given by Equation 2.13 [36] as:

$$\varepsilon_p = N\frac{2}{\sqrt{3}}\frac{\pi r}{t} \qquad 2.13$$

Where, r = the radius of sample/length from the sample axis; t = thickness of sample; and N = number of passes (complete torsional rotations). Other factors influencing the microstructure and the homogeneity of the induced properties in material are: the magnitude of the applied pressure; the friction on the contact surfaces, and the process temperature [19][39]. Regardless of the number of passes performed, Equation 2.13 shows that the induced strain decreases from the outer circle radius r, towards the centre of the sample. Also the strain decreases with the increase of the sample thickness, *t*. Variation of strain with sample radius and thickness result in the deformation heterogeneity and the limited size of the processed samples.

Extensive research work has demonstrated the capability of HPT technique to process fine grained microstructure titanium alloys with entailed desirable microstructural and mechanical properties. The HPT entailed mechanical properties include the tensile strength and the hardness [25][40]. Valiev and Smirnov [41] performed HPT at 10 rotations, 4 GPa on Ti6Al4V alloy; and they reported that the average hardness (HV) increased from 300 of the AR samples to 450, with lack of homogeneity. The alloy alpha and beta particles had average grain sizes (nm) of 300 and 80 respectively. Wang et al. [42] worked on the hardness homogeneity of CP Ti processed by HPT. Their results

showed a mean grain size of 105nm at 6GPa pressure; and 20 turns were achieved. The processed samples showed the hardness inhomogeneity that to some extent decreased with the increase of turns of the HPT process.

Todaka et al. [43] studied the hardening properties of the HPT processed CP Ti. , A range of grain sizes of 100 - 200nm were observed in the material; and the hardness of the material increased with the decrease in the grain size. Nie et al. [44] studied the corrosion properties of HPT formed CP Ti; and they reported to have achieved a fine grain size of 110nm from coarse grain size of 10μm. Their study found that the hardness and the corrosion resistance increased with a decrease in the grain size.

Zhilyaev et al [45] studied the microstructural and the micro hardness of annealed CP Ti; and they then processed it by HPT. Their study found that the microstructural average grain size of the processed samples was less than 200nm; while the hardness of the material decreased at an annealing temperature greater than 600^{o}C. A study done by Figueiredo and Langdon [46] found that HPT deformed CP Ti at a pressure of 8 GPa formed a fine grained microstructure and ω-HCP phase with improved hardness. It was observed that the hardness and the hear strain at the disc centre were lower than that at the outer edges.

Experimental and numerical works have shown that the HPT is one of the most effective SPD techniques to enhance metal with grain refinement and improved strength. This is attributed by HPT being a true hydrostatic stress state process. However the process can produce samples of limited size and geometries with reduced ductility. The method can process discs of lengths up to 10mm and diameters up 20mm. Furthermore, the process is associated with strain and microstructural in homogeneities along with the sample radius towards the disc centre [11].

Improved models with good results have been developed on HPT continuous processing of larger samples, these include Continuous-HPT [47] and Incremental-HPT [48]. The HPT method is still at the experimental stage; and has it has not yet been implemented at the industrial level of continuous production.

2.6.2 Equal Channel Angle Pressing (ECAP)

The ECAP is a process whereby a billet (sample) is repeatedly inserted in a die which contains two channels with equal cross sections intersecting at an angle ϕ. A schematic diagram for the ECAP process is shown in Figure 2.12. The intersecting angle ϕ ranges from 90^{o} to $157.5^{o.}$ [49]. In ECAP process, the mode of material deformation is simple shear; as it is pressed and changes its direction through the die.

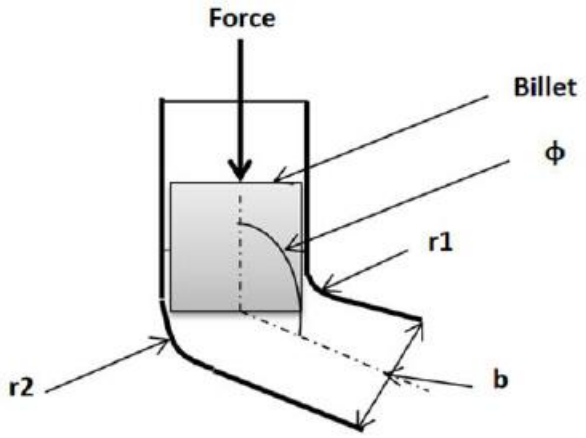

Figure 2.12: Principle of ECAP process

The EP strain induced in the billet by the ECAP is given by Equation 2.14 [36] as:

$$\varepsilon_p = N\frac{2}{\sqrt{3}}Cot\frac{\Phi}{2} \qquad 2.14$$

$\boldsymbol{\Phi}$= the included angle of the die axes, N = the number of passes. Other parameters that affect the induced EP strain are the inner radius r_1, the outer radius r_2, the die width b, the value of the pressing load, the contact friction between the billet and the die and the pressing temperature [50][51][52]. There is EP strain in-homogeneity in the ECAP pressed billets mainly attributed to firstly the difference of the material flow velocities along the inner and outer radii of the die. Secondly, the abrupt change of hydrostatic stress from the compression to tension state; as the material enters and leaves the shear plane respectively.

Application of the ECAP method to improve mechanical properties of the titanium alloys has been reported. Semenova et al. [53] performed ECAP at 4 passes on Ti6Al4V and reported that the tensile strength (MPa) increased from 970 to 1100 and failure elongation (%) decreased from 17 to 11. In the same article and on same material they performed ECAP+Extrusion at 2 passes and found that the tensile strength (MPa) increased to 1300 and failure elongation (%) decreased from 16 to 8. In both cases the alpha particle average grain size decreased from a range of 3µm-8µm for the as received (AR) samples to 200nm - 400nm.

Mendes et al. [54] studied microstructure, strength and corrosion resistance of CP Ti processed by ECAP and found that average grain size of 500nm was observed in the material, optimum strength and ductility was at a combination of ECAP 4 passes and cold rolling. Ultra-fine grain CP Ti had 115% tensile strength higher than coarse grain one. There was no difference of corrosion resistance between coarse and ultra-fine grain material. Greger et al. [55] reported that ECAP formed CP Ti had a grain size of 250-300nm with increase of yield stress from 350-550 MPa, tensile strength from 450-650 MPa.

Polyakov et al [56] performed effect of combined ECAP and Drawing on CP Ti fatigue strength and biocompatibility, results showed that ECAP formed material had a grain size

of 200nm with tensile strength of 1400 MPa, endurance limit higher than coarse grain sample by 50% with better osseo-integration biocompatibility. ECAP-Conform and Incremental Equal channel Angular Press (I-ECAP) [56] models were develop for continuous processing of metals with ultrafine/nano microstructure.

A study was done by Gzyl et al. [21] on producing high strength metals using I-ECAP. The method was derived from ECAP but with reduced friction and possibility to produce long billets such as bars and plates. The authors processed Ti grade 4 with I-ECAP, the average grain size of 700nm and an increase of tensile yield stress from 470-805 MPa were achieved.

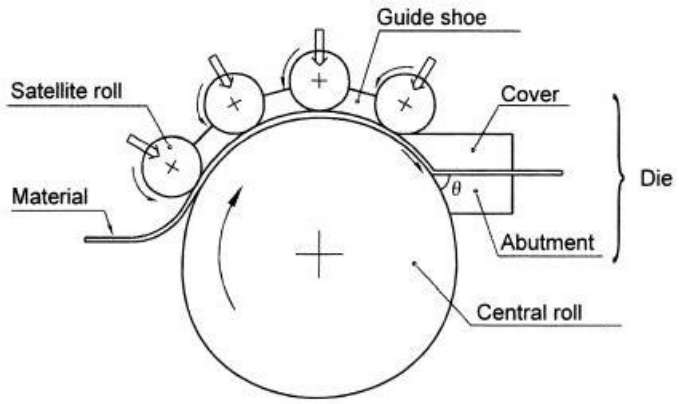

Figure 2.13: Principle of Con-shearing process[36]

Con-shearing is another SPD method that basically works on the ECAP principle. It was aimed to provide continuous processing of ultrafine grain long samples [36]. As shown in Figure 2.13 it consists of a center roll and satellite rolls rotating in opposite directions about their central axes. Rotating rolls drive the sample through the die at an angle θ. The equal channel die induce plastic shear strains in the sample without significant change in its geometric dimensions.

The ECAP method provides a true hydrostatic stress state without significantly changing the billet dimensions, which is a desirable condition for any SPD process. However this process needs relatively large forces to press the sample through the die. It has also been characterized with shear strain inhomogeneity in the billets. More research is required to investigate the effects of parameters such as the die shape and the pressing rate on the microstructural properties. The process has not yet been implemented at the industrial scale of continuous process of the bulk metal billets [57].

2.6.3 Accumulative Roll Bonding (ARB)

The ARB is the SPD process, whereby the material is first rolled on a rolling machine then cut into two pieces, the pieces are cleaned, stacked and rolled again (see Figure 2.14). The ARB process cycle can be repeated infinitely to achieve large amount EP strain.

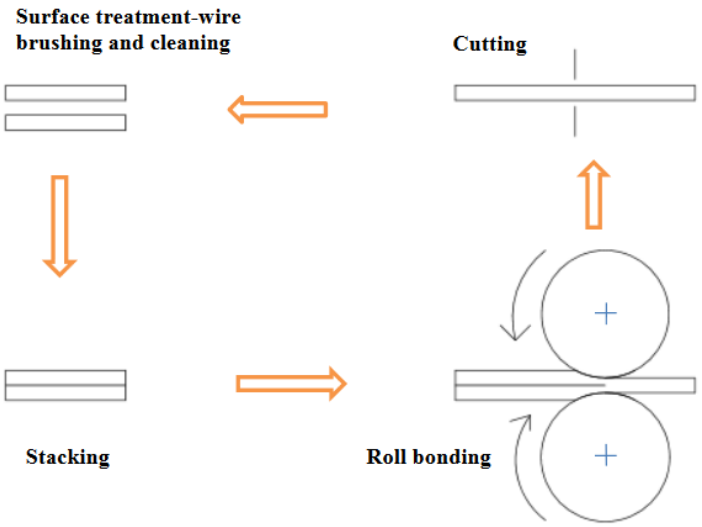

Figure 2.14: Principle of ARB process[58]

The EP shear strain induced in the rolled sample is calculated by Equation 2.15 [59] as:

$$\varepsilon_p = N\frac{2}{\sqrt{3}}ln\frac{t_1}{t_2} \qquad 2.15$$

Where, t_1 and t_2 = the thicknesses of the sample before and after rolling respectively, and N = the number of passes. The EP strain is dependent on the initial-after rolling thickness reduction ratio and the number of passes performed N. The quality of surface treatment, the rolling temperature, the rolling force, the size and the speed of rolls affect the induced strain [60]. A thickness ratio of 35% - 50% is recommended in each pass [59][61]. Simultaneously, the ARB induces the EP strain and does bonding of the stacked layers.

For better bonding and deformation of the material, the ARB process should be performed at the elevated temperature below that of the recrystallization [62][63]. Compared with ECAP, HPT and conventional rolling processes, the ARB has an additional mode of plastic deformation with redundant shear strain imposed on material.

The use of ARB SPD to improve the titanium alloy microstructural grain refinement, tensile and hardness properties has been reported by various authors. Tsuji et al [60] performed the ARB process on titanium added interstitial free (IF) steel for structural application. The samples were rolled at a temperature of 773K, strain rate 46/s at 7 passes. Results showed that the average grain size was reduced from 27μm to 420nm, the tensile strength increased from 280 MPa to 870 MPa. The elongation decreased from 57% to 9%.

Kitahara et al [64] studied fatigue properties of CP Ti worked by ARB at 6 passes. Results showed the microstructural average grain size of 89nm. As the number of roll passes was increased, the tensile strength increased by 100% to 850 MPa, with the decreased fatigue crack propagation rate. Fattah-alhosseini et al. [65] investigated the microstructural and mechanical properties of CP Ti processed by ARB at room temperature for six passes. The results showed the grain refinement from 45μm to 90nm,

the yield stress and tensile strength increased from 284 MPa and 799 MPa to 415 MPa and 989 MPa respectively.

The use of ARB to manufacture laminated metal composites has also been reported. Romberg et al [66] produced Ti/Al bimetallic laminates using the ARB with intermediate heating at 773K for 90minutes. The results showed that the produced composite laminates had improved in tensile yield strength from 350 MPa to 450 MPa and bonding strength due to imposed fine grain and hardness. This was only achieved by the reduced rolling thickness ratio, both increased rate of strain hardening and the roll speed.

Du et al. [67] produced Ti/Al composite laminates using a hot pressing followed by multi pass hot rolling at 773K. The laminates showed strong bonding with Ti-Al interface layers of nano scale thickness. The strength properties of Ti/Al composites depended on volume fractions of Ti and were in a good combination of strength and ductility. Other works on the use of the ARB method that enhanced ultra-fine grain and improved tensile strength of the laminates have been reported [63][68][69].

The ARB process can be implemented on a conventional roll facility for continuous production of ultrafine grain bulky metal sheets. The serious drawbacks of the ARB process are the edge cracks and the fracture of the samples with reduced ductility at

higher passes [59]. These are caused by excessive EP strain induced in the material noting that the rolling is not a true hydrostatic process. The process is characterized by unreliable bonded layers' interfacial strength, waste of material and grain contamination during cutting-stacking-rolling cycle.

2.6.4 Asymmetric Rolling (ASR)

The ASR is an SPD process whereby material sheets are rolled with rolls of different rotational speeds [70]. Difference of rolls' rotational speeds can be achieved by using rolls with either different diameter sizes or different frictional properties.

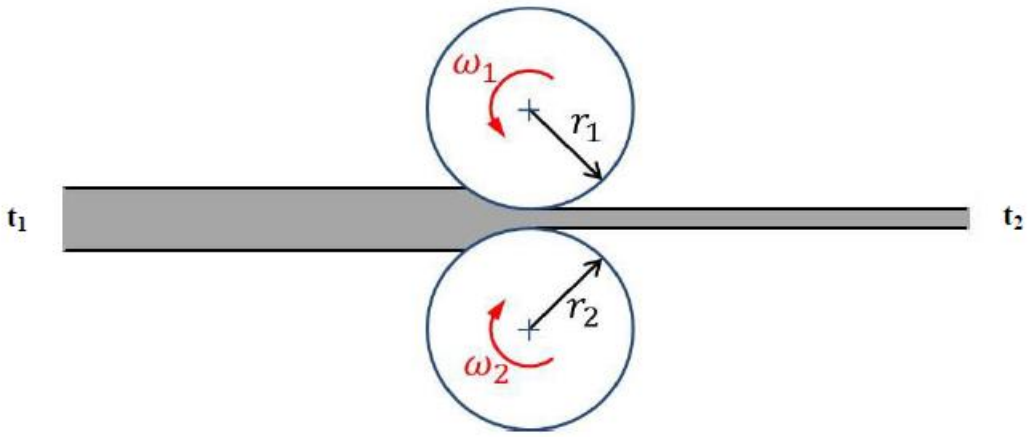

Figure 2.15: Principle of the ASR process

The principle of the ASR process is shown in Figure 2.15. Based on Roumina and Sinclair [71], unequal rotational speeds imposed on the upper and the lower surfaces of sheet results to shifting of the neutral points (the points on the upper and the lower

surface where the sheet velocity equals the roll velocity). This phenomenon results in imposition of high shear strain in the material. Comparing to a conventional symmetric rolling (SR), the ASR has the advantage of reduced rolling force and torque. Also a quasi-uniform shear strain across the sheet thickness can be achieved at certain parameters.

The EP strain induced in the ASR rolled sample is determined by Equation 2.16 [61] as:

$$\varepsilon_p = N\frac{2}{\sqrt{3}}\sqrt{1+\left[\frac{(1-r)^2}{(2r-r^2)}tan\theta\right]^2}\, ln\frac{1}{1-r} \qquad 2.16$$

Where, $r = 1-\frac{t_2}{t_1}$, t_1, t_2 = the sample thicknesses before and after the rolling pass respectively, θ = the apparent shear angle.

Equation 2.16 consists of two strain components i.e. the shear strain and the normal strain. Chao et al. [72] conducted a comparison study between ASR and SR on the microstructural and the textural characteristics of the Ti6Al4V alloy. Results of their study showed that ASR processed samples had higher grain refinement with equiaxed structure and mean grain size of 180nm compared to SR processed samples. The reason attributed to the grain refinement was due to the higher equivalent plastic strain induced in the material by the ASR method. Furthermore, the results showed that the basal

textural direction was displaced from the normal towards the rolling direction. This was different from the textures induced by SR process.

The roll speed ratio, force and material temperature condition determine the effectiveness of this process [73],[74]. Zhiming Li et al. [75] combined asymmetric rolling (ASR) and symmetric rolling (SR) on CP Ti grade 2 at room temperature. Results showed that for ASR; the average grain size of processed samples was 130nm, tensile strength of the AR samples and the processed samples were 470 MPa and 780 MPa respectively. For combined ASR and SR processes; the average grain size was 80nm, the tensile strength improved from 470 MPa for the AR samples to 920 MPa.

Yu et al. [76] performed ARB then ASR on AA1050/AA 6061 aluminum composite laminates to study the interface bonding strength. Their results showed that the mean equivalent strain at peak value corresponded to the maximum metallic laminates interface bond strength at a rolling speed ratio of 1.2. The ASR method has proved to enhance diffusion bonding of metal laminates with improved interface bond. Possibility of this process to be implemented and performed on a conventional rolling facility makes it potential for continuous processing of fine grained structure bulk metal sheets.

2.6.5 Twist Extrusion (TE)

Twist extrusion was introduced by Beygelzimer, YY and co-workers in 1999 [77]. It is an SPD process in which material sample is hydrostatically compressed with a plastic flow through a die of two prisms separated by a twisted section. As the sample is compressed through the die, it is induced with plastic shear strains with insignificant change of its dimensions. The working principle of the TE process is represented in Figure 2.16.

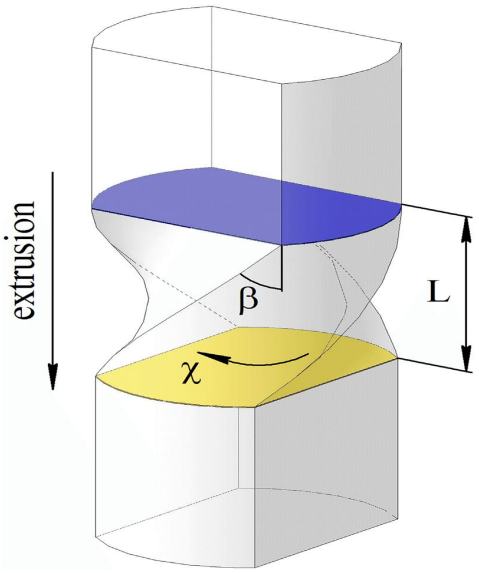

Figure 2.16: Principle of TE process die angle β, twist-channel length L, and twist angle χ [78]

The low and high effective plastic (EP) strains induced in the sample under the TE process are given by Equations 2.17 and 2.18 [79] as:

$$\varepsilon_p^l = 0.4 + 0.1tan\beta \qquad 2.17$$

$$\varepsilon_p^u = N\frac{2}{\sqrt{3}}tan\beta \qquad 2.18$$

N, β are the number of passes and the die angle, (twist line slope angle) respectively. Advantages of the TE method are that, extruded sample reduce in porosity defects, the process can be applied to extrude hollow and solid rectangular sections. Also it is capable of processing samples with improved isotropic and homogeneous deformation by turning the sample at $45^o/90^o$ for each of the consecutive passes performed. Turning the sample is best alternated in clockwise and anticlockwise directions. Processing of ultrafine/nano grain metals with TE process has been reported on different metal alloys. Examples are titanium [78][79][80], steel[81], copper [82] and aluminium [83]. TE processed samples have been characterized with loss of ductility and inhomogeneity of properties across the sample section, for instance deformation along the centre was found lower compared to that away from the die centre axis. However deformation homogeneity can improve with increasing the number of process passes [84].

2.6.6 Multi Directional Forging (MDF)

Multidirectional or multiaxial forging is an SPD process in which the material sample is subjected to a series of hydrostatic compressive loads without any changing in the geometrical dimensions. The load is applied on the sample in turn along its three principles X-Y-Z axes. This is achieved by rotating the sample by 90^o angle after each loading step. A complete MDF pass is achieved after the sample has been loaded in each

of the three axes. Multi passes are performed on the sample to achieve more EP strain, fine grained microstructure and improved tensile strength and hardness of the material.

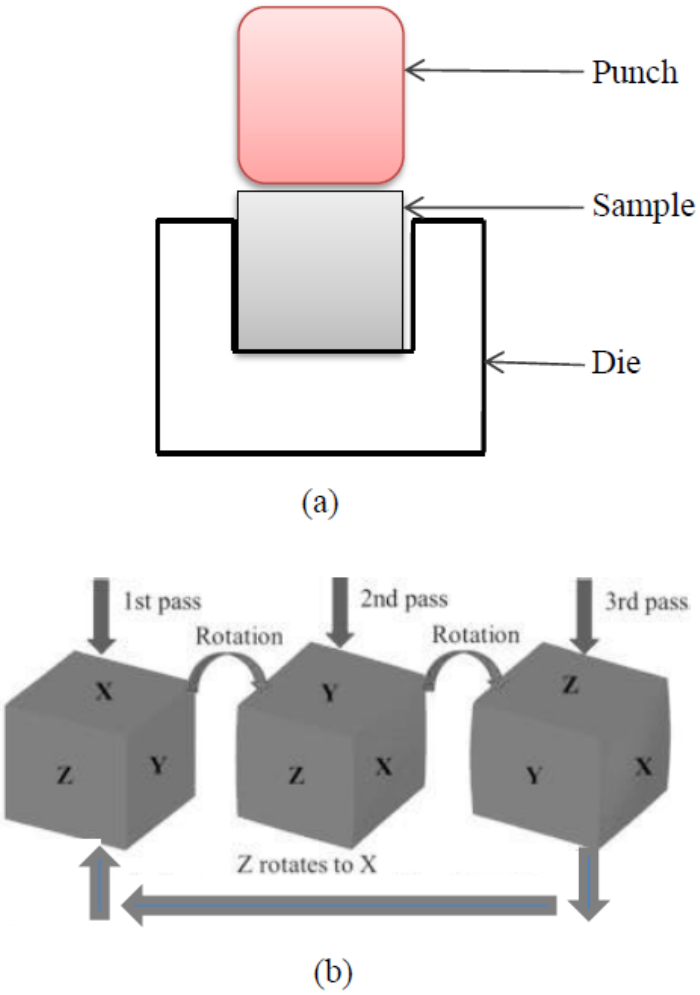

Figure 2.17: Principle of the MDF process[85][86]

The principle of the MDF is represented in Figure 2.17 (a). It consists of a punch, sample and a die. A sample is alternatively rotated after each successful compressive hammering

as shown in Figure 2.17 (b). The EP strain induced in the sample processed by the MDF is determined by Equation 2.19 [87] as:

$$\varepsilon_p = N\frac{2}{\sqrt{3}} ln\frac{h}{w} \qquad 2.19$$

Where, N, h and w, are the number of passes, the thicknesses of the sample before and after deformation, respectively. The use of MDF to produce different metal alloys with ultrafine grain microstructure and improved strength and hardness is widely reported in the literature [87][85][86]. Salishchev et al.[88] studied mechanical and microstructural properties of Ti6Al4V alloy performed with MDF at 20^{o}C-500^{o}C temperature range. Results showed the grain refinement from 10μm to 0.4 μm, increase of tensile and fatigue strengths (MPa) from 1050 and 580 to 1300 and 690 respectively. It was found that the strength values decreased with increasing the deformation temperature.

Ansarian et al.[89] performed MDF on CP Ti at room and 220^{o}C temperatures for a maximum of 6 passes. Results showed that both the tensile and shear strengths of the material increased with increasing the number of passes and reducing the pressing temperature. The average microstructural grain size was reduced from 64μm to 1μm. Miura et al.[90] performed the MDF on CP Ti at room temperature, processed samples showed a maximum increase of tensile strength to 710 MPa at 21% ductility with the average grain size of 400nm. The main drawback of the MDF process is the

inhomogeneity of the induced EP strain across the sample. However the strain homogeneity can be improved by application of lubricants to reduce friction between the sample and the die contacts, and increase the number of process passes. In practice the MDF is performed at elevated temperature less than 0.5 of the material melting temperature. Raising the material temperature may result to dynamic recrystallization and grain growth of refined grains.

2.6.7 Repetitive Corrugation and Straightening (RCS)

The RCS is an SPD process whereby, simple shear strains are induced in material via the bending deformation mode [91]. The RCS is performed by corrugating and flattening material with rotating rolls for a continuous process, or with pressing dies for a discontinuous process. Schematic diagrams for continuous and discontinuous RCS processes are presented in Figure 2.18 (a) and (b) respectively. Similar to HPT, ECAP and ARB processes, the RCS process can induce a large amount of plastic strains to the material with insignificant change in its geometric dimensions. There are mainly three types of die profiles that are so far used in the RCS method, these are: the Vee-groove, Flat-groove and the Semi-circular groove [92][93][94]. The profiles of these dies are represented in Figure 2.19. The equation for the EP strain induced in the material under the RCS depends on the die profile used. The Von Misses EP strain for the RCS Semi-circular die is determined by Equation 2.20 [92] as:

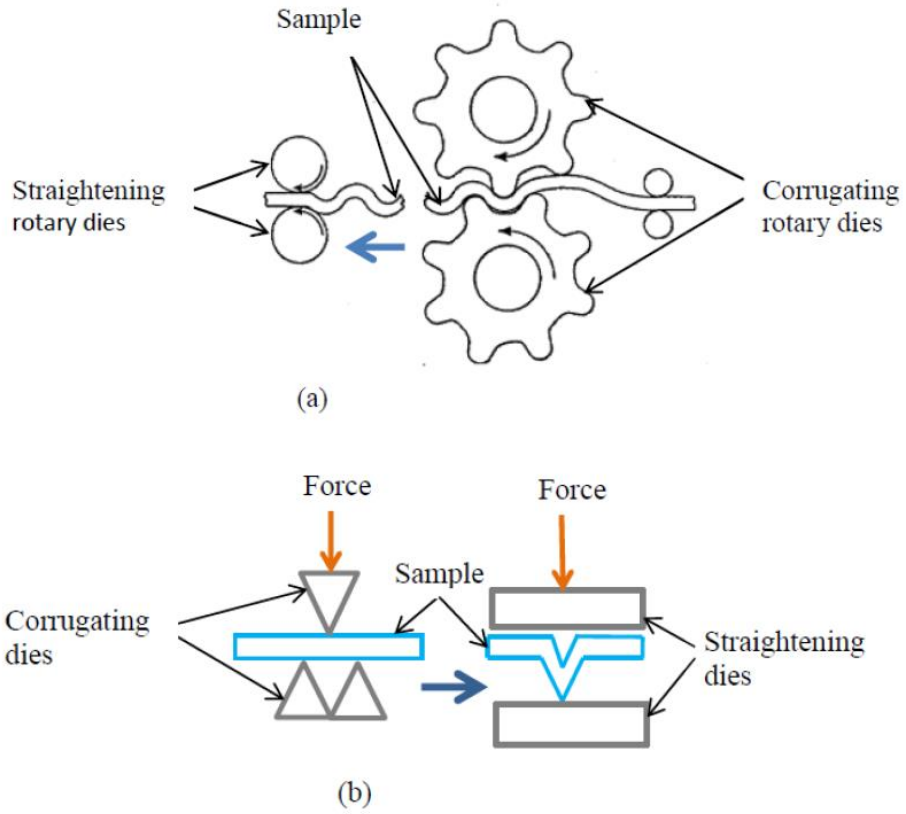

Figure 2.18: Principle of RCS process (a) Continuous corrugating and flattening rolling (CSR) process (b) discontinuous groove pressing (GP) and flattening process [36]

$$\varepsilon_p = N\frac{4}{\sqrt{3}} ln\left(\frac{r+t}{r+0.5t}\right) \qquad 2.20$$

r = radius of the corrugating surface, t = thickness of sample and N = number of passes performed. For the Vee-groove and the Flat groove dies, the Von Misses EP strain is given in [7] [92] [95] by Equation 2.21as:

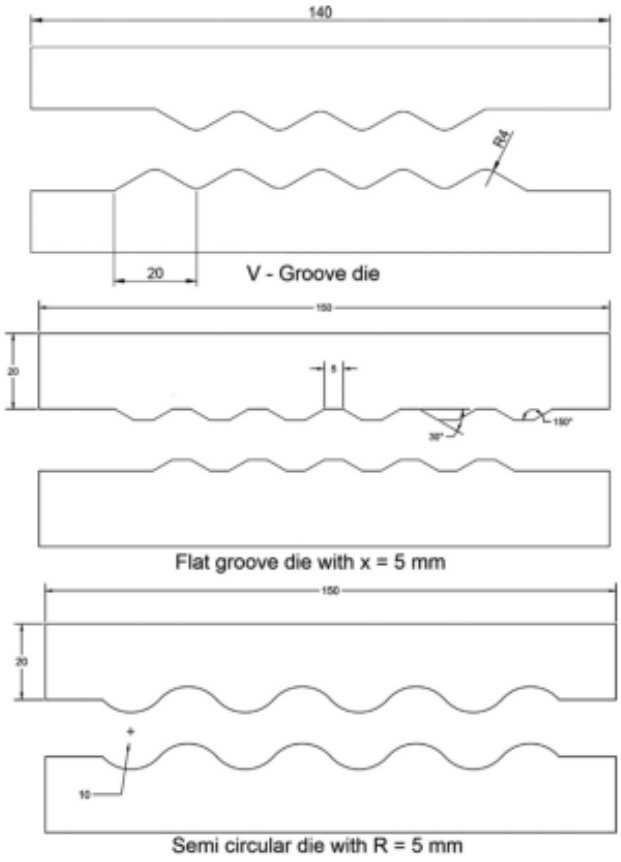

Figure 2.19: Vee, Flat and Semi-circular groove dies profiles used by Thangapandian et al. [92]

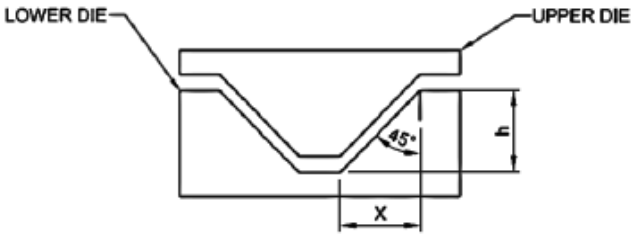

Figure 2.20: Detailed geometry of a pair of the flat groove dies

$$\varepsilon_p = N\frac{2}{\sqrt{3}}\gamma \quad (2.21)$$

$$\gamma = \gamma_{xy} = \frac{x}{h} \quad (2.22)$$

x= groove height of the die (as shown in Figure 2.20), h = the width of the die = sheet thickness t, and γ = the resulting engineering shear strain. The contact angle between the bender and the open die is optimally made equals to 45^o for pure shear, therefore γ = x/h=1. Equations 2.20 and 2.21 can determine the EP strain in the material in most deformed area. However, the material deformation is not homogeneous; therefore, the equations cannot be used to predict the average EP strain in the material.

Bending strain characteristics of material under discontinuous and continuous RCS processes are illustrated using Figure 2.21 (a) and (b) respectively. In each case a deformed sample is shown in un-corrugated, corrugated and straightened states. In the corrugated state, the shaded regions of the sample are the most deformed part while the un-shaded regions are the least or non-deformed part. During straightening back to flat state, additional strain is induced to the deformed region while the horizontal unshaded region remaining relatively un-deformed. This uneven deformation of material results to inhomogeneous strain distribution and can persist even after several RCS passes [96]. Other techniques have been developed and applied to improve deformation homogeneity and strain distribution in materials processed by RCS discontinuous method. One of these

techniques is the use of spacer bar that is alternatingly placed at the ends of the sample in each of successive pressing and flattening pass.

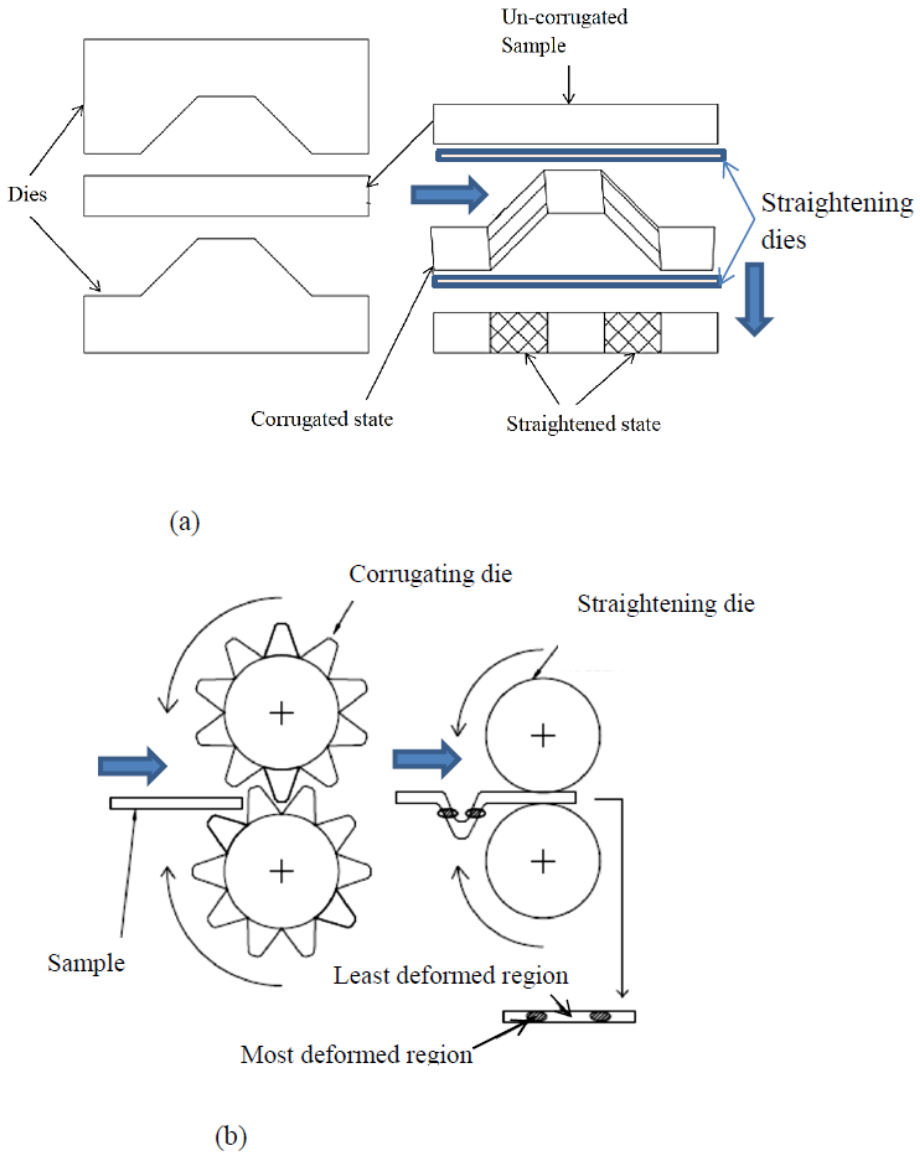

Figure 2.21: RCS bending deformation behaviour (a) Discontinuous process (b) Continuous process

This method is also known as Constrained Groove Pressing (CGP), a schematic diagram for CGP processes pressing and flattening dies are presented in Figure 2.22 (a) and (b) respectively. Advantages of the CGP over the Groove Pressing (GP) are that apart from improved CGP induced strain homogeneity; the sample is constrained from expansion during pressing and flattening, hence increasing the EP strain in the material without significant change of its dimensions.

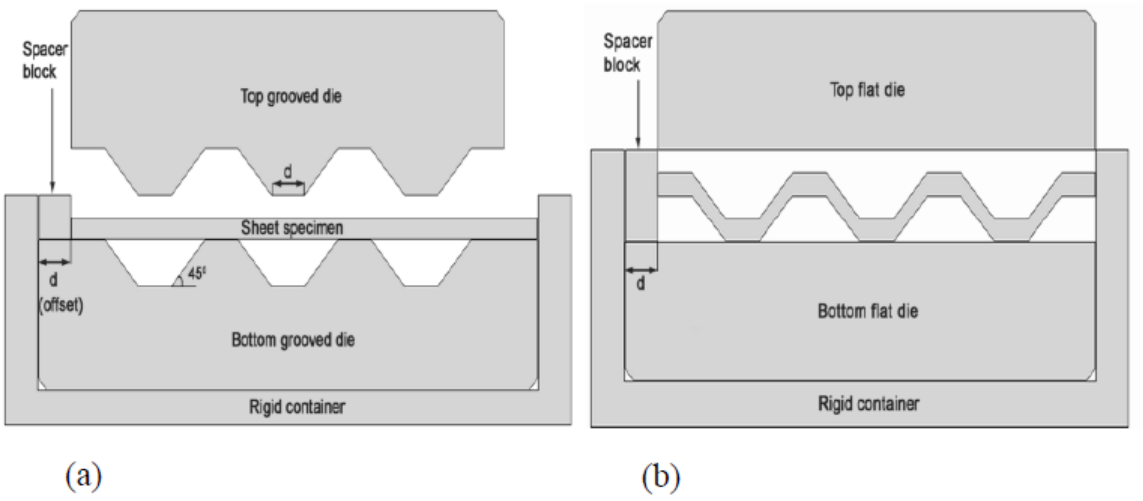

Figure 2.22: CGP (a) pressing dies (b) flattening dies [7]

Another technique applied for improving deformation and strain homogeneity is rotating the sample by $90^{o}/180^{o}$ angle after each of successive pressing and flattening pass. This technique is also known as Constrained Groove Pressing-Cross Rotation (CGP-CR). A schematic diagram for a complete CGP-CR pass process route is shown in Figure 2.23.

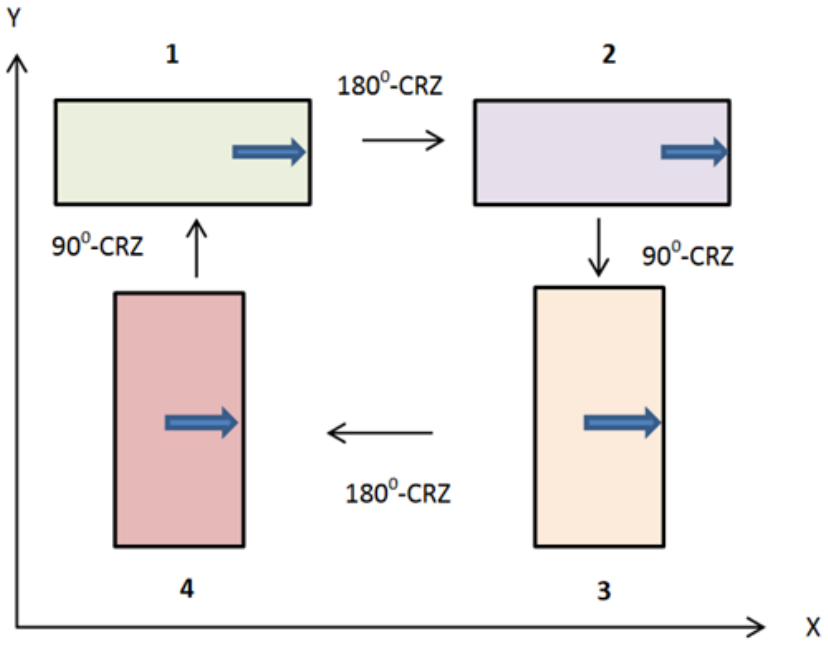

Figure 2.23: A complete pass for CGP-CR process route with four steps on a sample rotated about the z -axis in the x-rolling direction

In a CGP-CR process pass, four pairs of bending and flattening steps are performed on the sample, each pair on 0^o, 180^o, 90^o and 180^o successive rotation of the sample about the axis normal to the X-Y plane. Firstly, the sample undergoes bending and flattening. Secondly it is rotated 180^o then undergoes bending and flattening. Thirdly the sample is rotated 90^o then performed bending and flattening. Fourthly it is rotated 180^o then performed bending and flattening. The process can be performed for more than pass. Application of the RCS SPD method to process ultrafine grain metallic sheets has been reported by various authors. Thirugnanam et al.[6] studied the bioactivity of grain refined

CP Ti of size (100 mm x 60 mm x 2 mm) sheets processed by the GP method up to 3 passes before any cracks initiated. The results showed that an average grain refinement from 50μm of AR material to 3μm was achieved. The material yield and tensile strengths (SY and ST) increased from 325 MPa and 455 MPa to maxima of 432 MPa and 537 MPa respectively at 2 pass. The hardness increased from 125 HV for the AR material to 203 HV at 2 passes. The GP processed Ti sheets showed an improved bioactivity for bone implant applications. The GP was associated with the deformation and the strain inhomogeneity.

Kumar et al [7] studied the CP Ti (130 mm x 20 mm x 2 mm) sheets processed by CGP process at 300^{o}C temperature up to 8 passes, before cracks initiated. The results showed that the grains' average size was refined from 40μm of the AR material to 500nm. The material yield and tensile strengths (SY and ST) increased from 323 MPa and 452 MPa to 466 MPa and 519 MPa respectively. Hardness increased from 125 HV for the AR material to 208 HV at 8 passes. Analysis of the microstructure showed that there were still deformation heterogeneities and localized strain inhomogeneity in the specimen during each pass.

However, the CGP showed better results than GP. Other works have shown metallic sheets other than CP Ti processed with CGP with ultrafine grain refinement and

improved mechanical properties [94][97]. Numerical investigations have been reported on the deformation inhomogeneity exhibited by RCS processed samples. Ghazani and Vadj [93] did simulation work on the deformation behaviour of Al-Mag alloy processed by CGP. The results in Figure 2.24 (a) show that the material in the first stage pressed state, the regions represented by letter C (indicated in red colour) were the most deformed parts with higher induced plastic strain and the regions represented by letter D (indicated in blue colour) were the least deformed parts with the least induced strain.

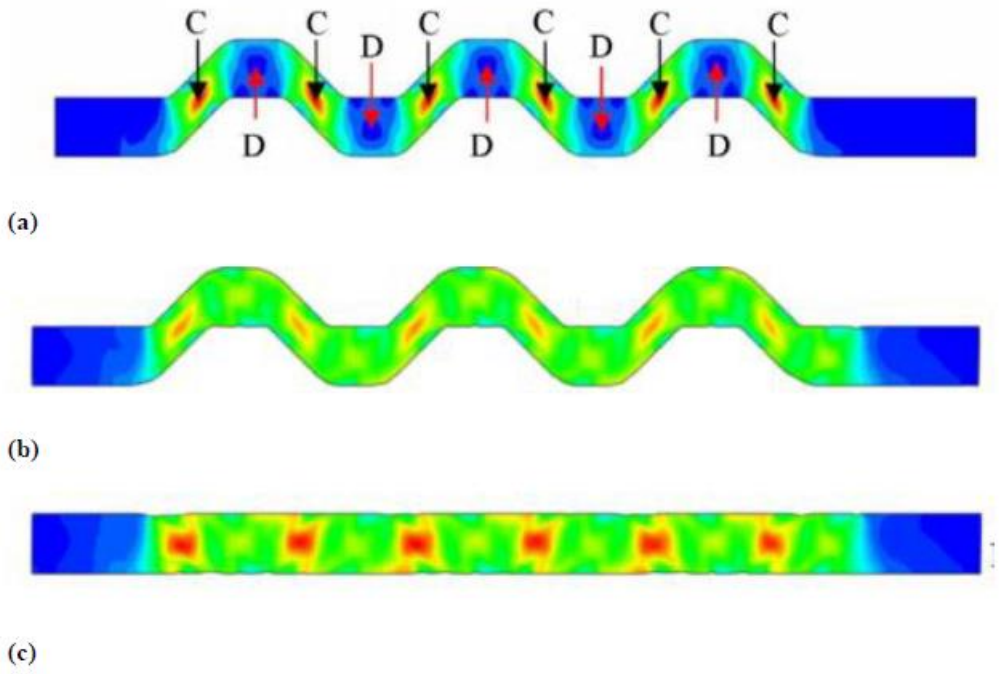

Figure 2.24: CGP (a) First pressing (b) Fifth pressing and (c) Fifth flattening [93]

Improved strain homogeneity by cross-rotation of the sample at the 5th pressing and flattening is shown in Figure 2.24 (b) and (c), respectively. However, there is still some strain inhomogeneity observed in the material in the flattened state. Khodabakhshi et al. [97] both experimented and simulated the low carbon steel sheets processed by the CGP-CR at 2 passes. The results in Figure 2.25 (a)-(h) showed that the average grain size decreased from 30μm of the AR samples to 250nm at 2 passes; the yield strength increased from 218 MPa to 426 MPa at 1pass. The hardness increased from 97 HV to 176HV at 2 passes. The equivalent plastic strain increased with the number of passes. However, the equivalent strain distribution in the processed sheet was inhomogeneous even after multiple process passes. The CGP-CR process was found to have better strain homogeneity and superior mechanical properties than CGP.

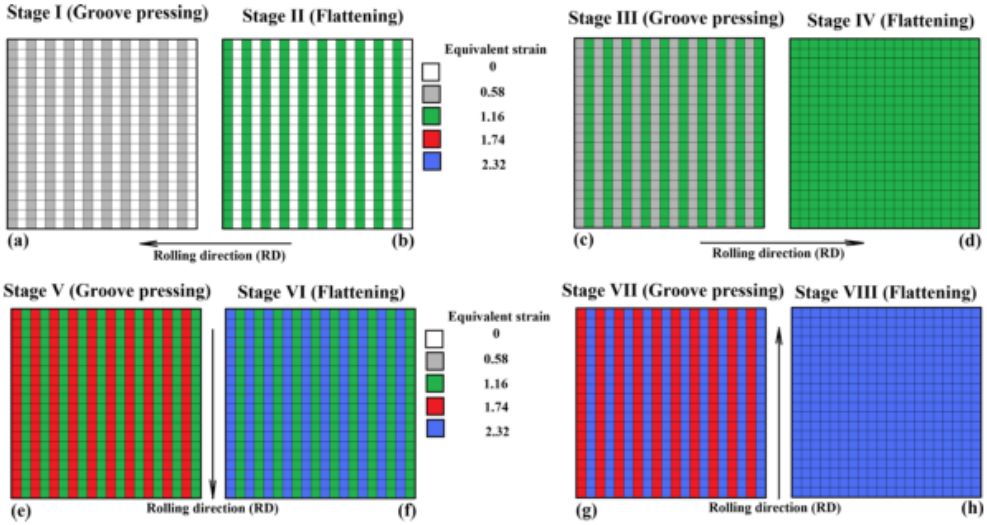

Figure 2.25: Four (a-h) steps of bending and flattening route for a CGP-CR pass [97]

The die profile used in RCS process determines the microstructural and the mechanical properties of the processed material. Thangapandian et al.[92], investigated the effect of the GP die profile on 3 mm thick Al-Mg alloy sheets. These authors used three types of dies: a Semicircular of radius, r = 5 mm, Flat-groove of width x = 5 mm, and Vee-groove of height h = 4 mm. The dies' profiles and sizes can be recalled from Figure 2.19. The results showed that Semicircular die processed sheets withstood 15 passes without cracking; with the lowest ductility reduction of 31%. The samples exhibited higher strain homogeneity than those deformed with Flat-groove die but with lower strain homogeneity than the Vee-groove die. The grain refinement improved from 45 μm of the AR material to 20μm. The maximum strength of 173 MPa was reached at 6 passes. Rate of hardness value with number of passes was slightly lower than those of the Vee-groove and the Flat-groove dies deformed samples.

Flat-groove die processed sheets withstood 8 passes before cracking. Those sheet samples had the highest ductility reduction of 66%, with the least strain homogeneity. The average grain size reduced from 40μm of the AR material to 28μm. A maximum strength of 175 MPa was achieved at 6 passes. The rate of hardness values with number of passes was average, when compared with the samples processed with Vee-groove and Semicircular dies. Vee-groove die processed samples withstood 4 passes before cracking with a ductility reduction of 63%. The samples exhibited the highest strain homogeneity

with an average grain refinement from 40µm of the AR material to 22µm. The maximum strength of 170 MPa was reached at 2 passes. The rate of hardness values with number of passes was slightly higher than those of the samples processed by Flat-groove and Semicircular dies. However it was found that the Vee-groove dies' sharp edges impart damage and stress concentrations to the material, which results in early crack formation and fracture of the samples. The study concluded that a Semicircular die showed the optimal strain homogeneity, high ductility and less material cracks. Its weakness was the low rate of hardness and strength with the number of passes. The Flat groove die showed the highest rate of hardness and strength with the number of passes, with moderate crack formation in the material. The Vee-groove die was characterized by the formation of cracks and stress concentrations that reduced the material's strength under static and fatigue loads.

2.6.8 Constrained Bending and Straightening (CBS)

The CBS SPD process was proposed and applied in this study for the continuous production of the Ti6Al4V alloy sheets. The CBS technique basically evolved from the RCS process; and it was aimed to enhance the Ti6Al4V alloy sheets with improved magnitude and homogeneity of the strain, tensile strength and hardness of the material. The principle of the CBS process with a Flat groove bending die is represented by a schematic diagram in Figure 2.26 (a).

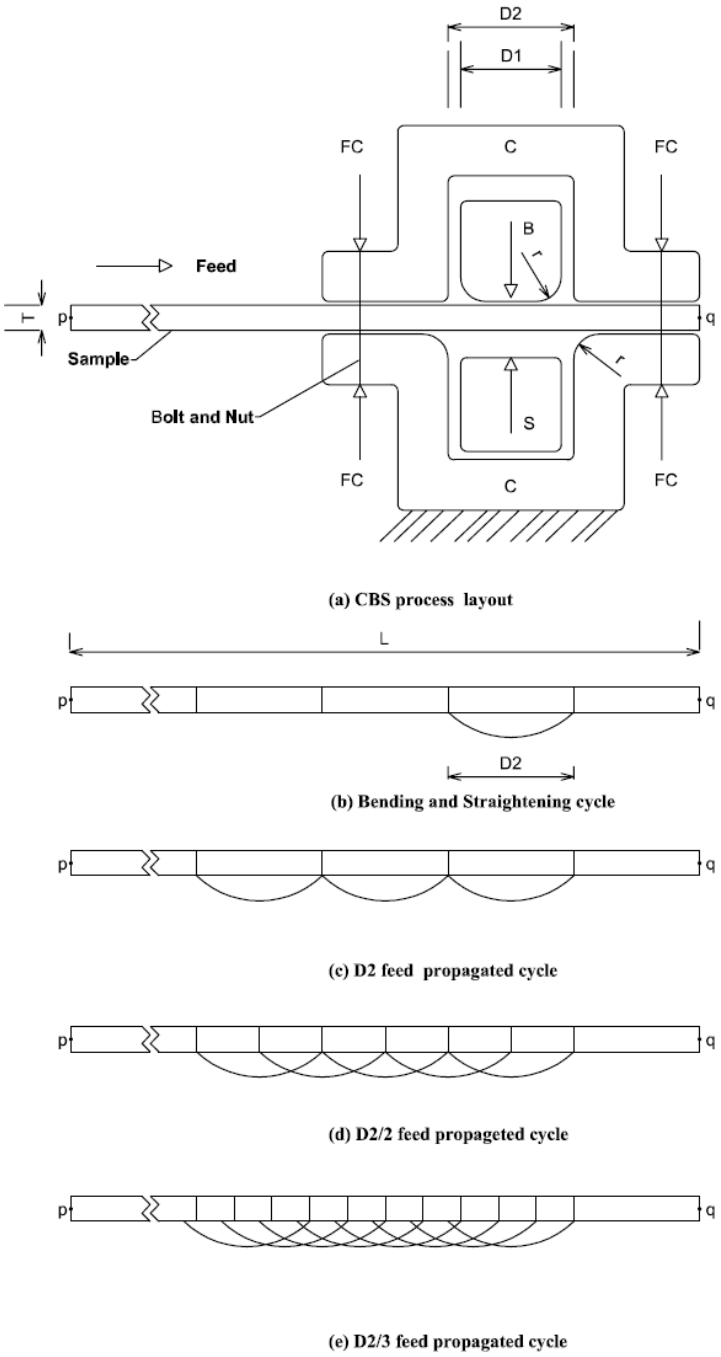

Figure 2.26: (a) Layout of flat bending die CBS tool (b) CBS bending-straightening cycle, C_i (c) propagated cycle at F = D2, (d) at F=D2/2 and (e) at F= D2/3

The processing tool consists of a bending bar B of size D1, straightening bar S and open die of size D2. Alternatively, the bending die profile can be round as shown in Figure 2.27. Bending and straightening bars move the maximum height equal to the sheet thickness T in a vertical direction. The tool has a pair of constraining brackets C used for holding the sheet in a constrained state by applying the constraining force FC. In this case the lower constraining bracket also acts as a die. One CBS cycle denoted as C_i consists of a pair of bending-straightening strokes.

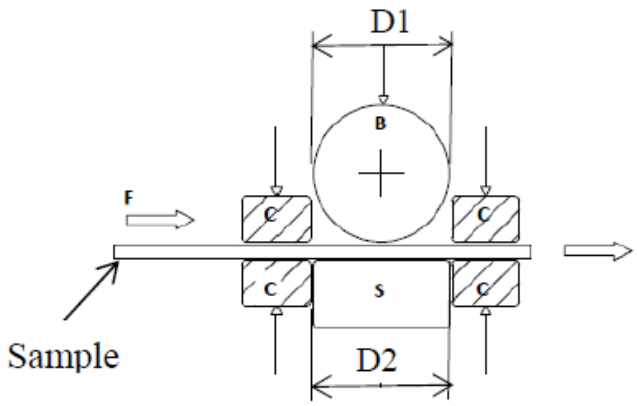

Figure 2.27: Layout of a circular bending die CBS tool

The CBS process has a feed system to move the sheet sample forward at a selected feed length F after each successful bending and straightening cycle C_i. A sheet sample of length L_{pq} and thickness T subjected to one bending and straightening cycle C_1 with an induced number of bending curves is shown in Figure 2.26 (b). A complete CBS pass, N is performed after C_1 is propagated over the entire sample length L_{pq} at a specified feed length F. The number of bending curves for the CBS processed samples, are then

propagated at D2, D2/2 and D2/3 feeds are shown in Figure 2.26 (c), (d) and (e), respectively. The number of bending curves over the length L_{pq} depends on the feed length F, between successive bending and the number of bending-straightening passes, N performed. Magnitude and homogeneity of EP strain induced in material sample are directly proportional to the number of induced CBS bending curves. The resultant EP strain induced per pass is obtained by the super-positioning of the EP strains of the propagated cycles. It can be observed from Figure 2.26 (c)-(e) that the feed length of D2 has fewer bending curves hence it will induce lower homogeneity and magnitude of the EP strain in material.

It is anticipated that the magnitude and the homogeneity of the EP strain will increase with the increase of the number of passes N at the lowered feed length F. Therefore a feed length of D2/3 will have more bending curves; and hence, will induce higher strain homogeneity and magnitude in the material than the D2/2 and D2 feeds. To increase the number of passes N, the bending-straightening cycle C_i is propagated repeatedly on the sheet at the specified feed F. The average EP strain induced in the sample under the CBS process for the Semi-circular, Flat-groove and the Vee-groove dies can be determined by modifying Equations 2.20 and 2.21, respectively. For a circular bending die the average EP strain is determined by Equation 2.23 as:

$$\varepsilon_p = N\frac{D}{F}\frac{4}{k\sqrt{3}}ln\left(\frac{r+t}{r+0.5t}\right) \qquad 2.23$$

For the Flat-groove and the Vee-groove dies, the average EP strain is determined by Equation 2.24 as:

$$\varepsilon_p = N\frac{D}{F}\frac{2}{k\sqrt{3}} \qquad 2.24$$

D = *D2* = the length of the open die, *r* = *D1/2* the radius of the bender, *t* = the thickness of the sample; and *N* = the number of passes, *F* = the feed length.The ratio *D/F* accounts for the die size and the feed length on the EP strain. The factor *k* accounts for the effectiveness of the dies and the non-linearity due to the number of passes performed. In this study, the value of *k* was estimated by using the simulation results in Chapter Four.

Potentials of the CBS process as an alternative SPD method are: Motions and forces for feeding, bending, straightening and number of passes can be predetermined and controlled. As a result, the process has the capability of continuously processing metal sheets with improved magnitude and the homogeneity of mechanical and microstructural properties. The method is viable to be automated and be adapted to process bulk samples of unlimited length. The CBS dies can be arranged in series to increase effectiveness of the process, the geometry of the CBS dies can be redesigned and then be applied to process bars of round section. Furthermore, it can be integrated in series with other SPD processes. Like most of the other SPD processes the CBS process does not emit any harmful gases; therefore it is an environmentally friendly process.

In this study, a preliminary analytical investigation was done on the application of CBS to improve the strain and the tensile yield strength of Ti6Al4V sheets [98]. Analytical investigation considered the samples processed by CBS with circular bending die, as shown in Figure 2.27 at 1, 2, 3, 4 passes (N) combined with 2 mm, 3 mm, 6 mm feeds (F). The analytical results showed that the EP strain increased with the number of passes at the lowered feed length. The EP strain at N4 pass was 300% higher than that at N1 pass. The EP strain at 2 mm feed was 200% higher than that at 6mm feed. The highest yield strength of 1302.6 MPa was achieved at 2 mm feed, which was 6.4% higher than the strength at N1 pass.

An experimental work was performed on the hardness and the bending forces of Ti6Al4V sheets processed by CBS of 20 mm diameter circular die [99] . The samples were annealed at 550^{o}C temperature; and they were then processed at 1, 2 passes (N) combined with 5 mm, 10 mm and 20 mm feeds (F). The results showed that at 2 passes, the average bending force at 10 mm feed was 18296 N. That was slightly higher than 17593 N at 20 mm feed; then it relatively decreased to 17917 N at 5 mm feed. The material maximum increase of average hardness was 16.3% at 2 passes and 10 mm feed over that of annealed samples. The hardness reached a saturation point and relatively decreased at the 5 mm feed level compared with that at 10 mm feed. However, the samples processed at 5 mm as the lowest feed and 2-pass had the highest hardness

homogeneity, when compared with the samples processed at 10 mm and 20 mm feeds. A number of annealed samples developed cracks at N2 passes. This could have been attributed to the contamination of atmospheric air to the sheet samples during the annealing process.

To avoid this, in the later experimental work, the Ti6Al4V sheet samples were not annealed prior to CBS process. Furthermore the results showed that the sheets samples processed by CBS with the bending die diameter of 20 mm exhibited low hardness homogeneity. The results in [98][99] showed that the CBS with a Semi-circular (round) bending die gave the lower values of EP strain; hence they showed lower strength and hardness values compared with the CBS with Flat groove bending dies. Therefore, later experimental and simulations work in this study were focused on the CBS with the Flat groove bending dies of sizes less than 20 mm.

2.7 Conclusive remarks

The following conclusive remarks from the literature review were made:

(i) Titanium alloys have excellent corrosion resistance, good biocompatibility, low elastic moduli and a high strength to weight ratio. These unique properties make these alloys superior to stainless steel and cobalt chromium alloys for bio implants and structural applications.

(ii) Titanium alloys have exhibited low strength and poor wear resistance. Therefore, there is a need for efficient material processing techniques to enhance these alloys with improved magnitude and homogeneity of their enhanced properties.

(iii) Surface hardening such as nitriding can improve the wear resistance of titanium alloys; however, the coating may lack thickness uniformity; and it degrades with time, leading to corrosion and the wearing of the implants and other structures made thereof.

(iv) Extensive research done at the experimental level has shown that the SPD technology is effective in processing; and it enhances the titanium alloys with desirable properties for biomedical and structural applications

(v) Most SPD technology processes are limited to sample size and geometry; consequently, they have not yet been adapted for the continuous processing of bulk samples,

(vi) Uneven deformation of the processed samples is another serious drawback of most SPD processes, including RCS. This can result in the inhomogeneity of the enhanced properties, such as strain, microstructure and strength.

(vii) Currently there is no work reported in the literature on the use of RCS and related techniques (GP, CGP and CGP-CR) to process and characterize the microstructural and the mechanical properties of the Ti6Al4V alloy.

The current research focuses on characterizing Ti6Al4V sheets processed with constrained bending and straightening (CBS). The CBS is a continuous process intended to improve the microstructural grain refinement, the homogeneity and the magnitude of the tensile strength and hardness of the material. The CBS is a modified RCS method in which improved homogeneity and magnitude of material properties are dependent on the number of passes N and on the feed length F. The following Chapter 3 covers the methodology of the study, in which a detailed account is given on the CBS tool fabrication, material test procedures and the development of a numerical model.

CHAPTER THREE: METHODOLOGY

3.1 Introduction

This chapter covers a detailed description of the methods used to achieve the research objectives and these are presented in the flow chart in Figure 3.1.

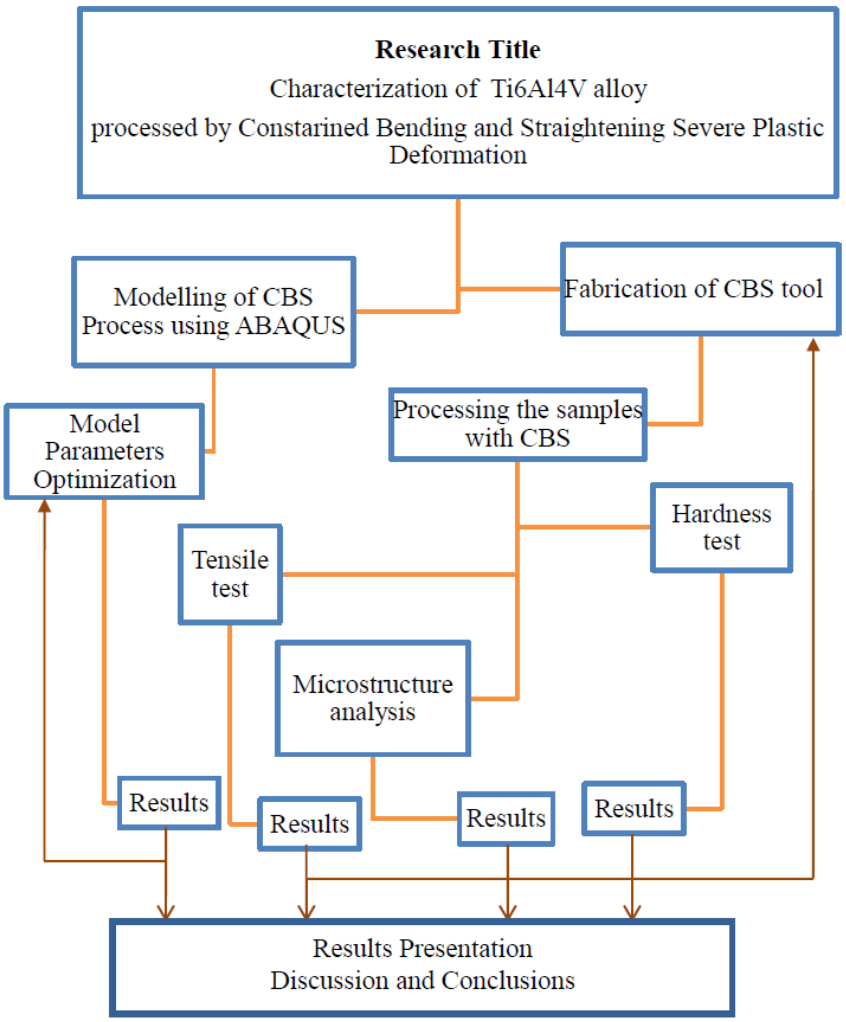

Figure 3.1: Methodological flow chart

The chart consists of a list and the sequential flow of experimental and simulation activities done to realize the study objectives. The details were given on the main parts of the CBS tool, the material selection of the parts, sizing, fabrication and performing the CBS process on Ti6Al4V sheets. It also covers the specific procedures for sample preparation, tensile, hardness test and microstructural analysis. The tools, the equipment used and the investigated parameters are specified. The chapter also includes procedures for the development of a numerical model, which was used to predict the magnitude and the homogeneity of the EP strain, the tensile yield strength and the hardness of the CBS processed samples. The model was simulated with the ABAQUS FEA software. The optimization of the model parameters involved the continuous selection of process parameters that could enhance the CBS with better performance. The parameters included were: the die geometry, size, feed lengths and the number of passes.

3.2 Fabrication of the Constrained Bending and straightening processing tool

3.2.1 CBS tool functional parts and material specifications

The CBS tool was designed and fabricated based on the working principle shown in Figure 2.26. The tool size of the bender *D1* = 8 mm and length of open die *D2* = 12 mm. A 3D sketch of the tool drawn by CAD is shown in Figure 3.2 (a). Sub-assemblies of the tool's parts and hydraulic jack are presented in Figure 3.2 (b) and (c), respectively. The

tool consists of the frame of elliptical base flat bars welded on two reinforced vertical flat bars.

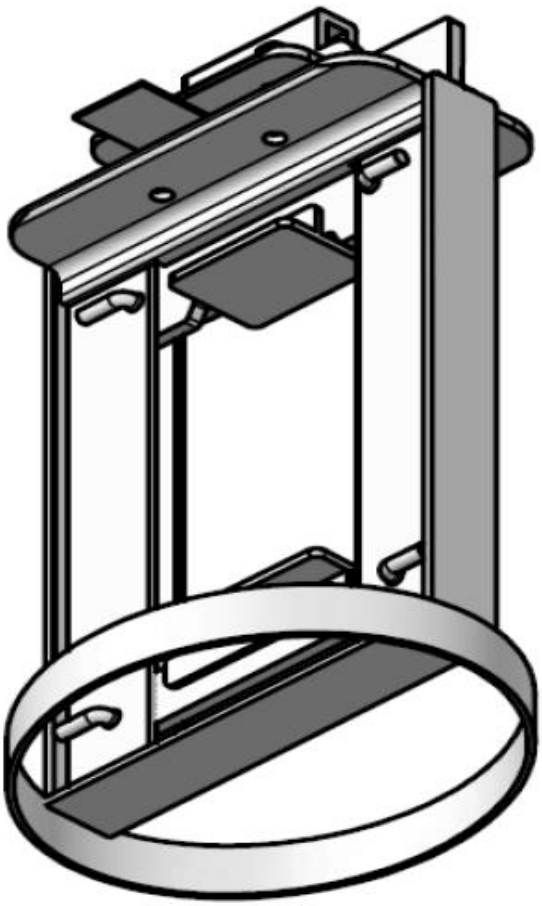

(a)

It has the bender, upper, lower constraining brackets and straightener. It also has the upper and lower jack supporters and four bolts and nuts for constraining the sample during the bending and straightening cycles.

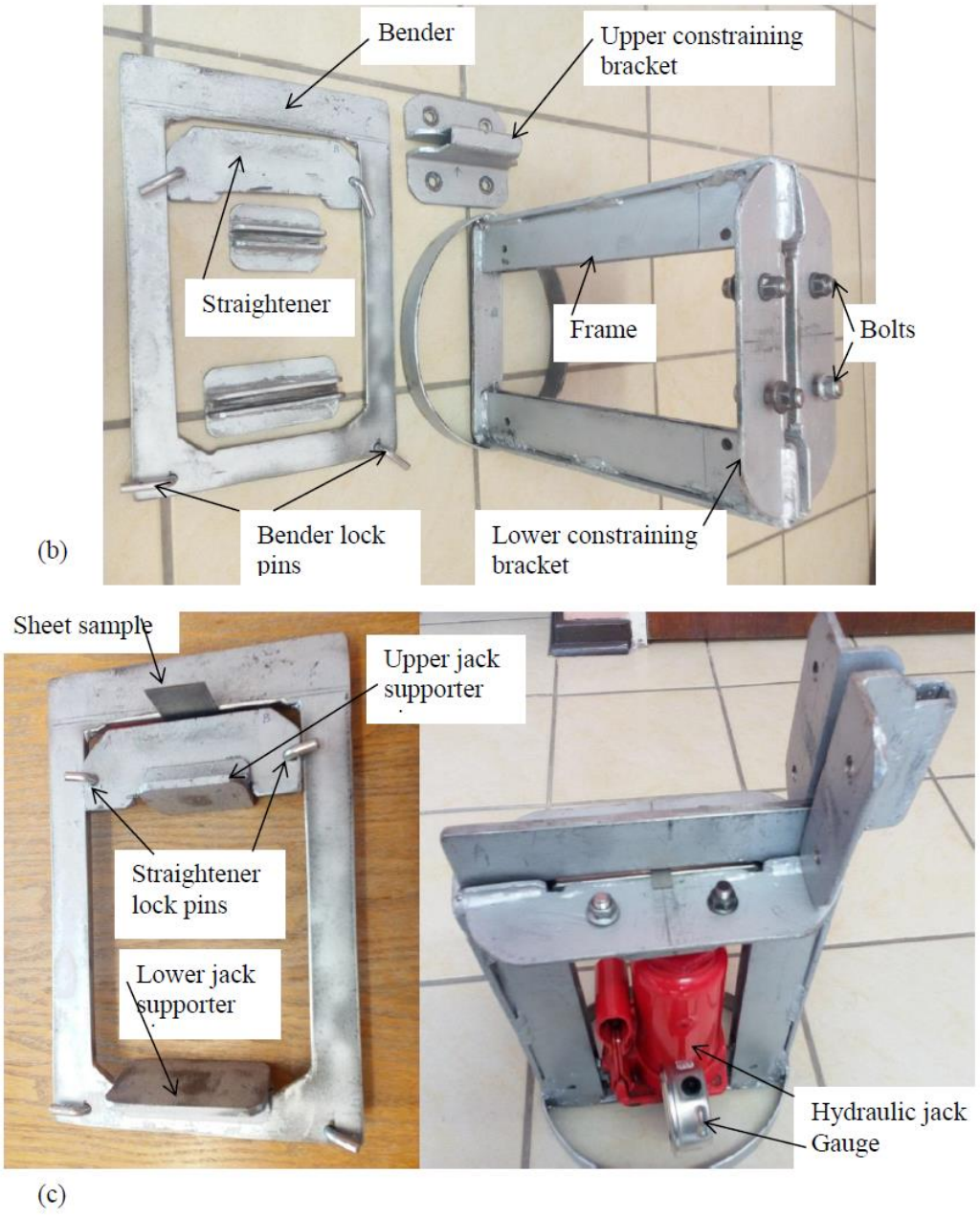

Figure 3.2: CBS process tool: (a) 3D sketch of the tool (b) Tool's parts sub-assembly (c) Tool and jack assembly

A hydraulic jack with a pressure reading gauge was attached to the CBS tool to provide bending and straightening pressing forces on the Ti6Al4V samples sheets. The purpose of attaching a hydraulic jack with a hydraulic pressure gauge was to read the pressing force exerted by the jack. The gauge initially reads the pressure, which was later multiplied by the piston area, in order to give the bending force.

There are four lock pins; and each pair of the two pins is alternatively used for locking the straightener and the bender on the frame during bending and straightening respectively. Therefore, an activated jack could provide either bending or straightening forces by locking either the straightener, or the bender, respectively on the frame. The constraining brackets were used to hold the sample during the bending by four (4) nuts tightened on their respective bolts. Feeding of the sample was done by loosening the nuts on the bolts and pressing and sliding the sample at a specified feed length.

3.2.2 Geometric size and material selection for the CBS tool parts

Materials for tool parts were selected based on their strength to carry the required load, availability and affordability. The frame, bender, straightener, constraining brackets, jack supporters and lock pins were all made of structural steels purchased from local suppliers. The size of each part was estimated by comparing the material strength with the maximum applied load. A detail of the design calculations used to determine the part's

sizes is given in the following paragraphs in this sub-chapter. Selected materials, standards/specifications, strength and quantity of parts for the tool are presented in Table 3.1.

Table 3.1: Parts and material specifications

Part	**Standard/ Geometry**	**Material**	**Specification / Dimension**	**Strength (MPa)**		**Quantity**
				σ_{UTS}	σ_Y	
Bender	Plate	Steel EN10025 -S275JR[	8 mm thick	480	350	1
Straightener	Plate	Steel EN10025 -S275JR	8 mm thick	480	350	1
Constraining Brackets	Angle section	Steel EN10025 -S355JR[	6 mm thick	430	275	2
Frame	Plate	Steel EN10025 -S355JR[	5 mm thick	430	275	1
Jack Supporters		Steel EN10025 -S355JR[	5 mm thick	430	275	2
Lock pins		Steel EN10025 -S355JR	8 mm Dia.	430	275	4
Bolts and Nut	Grade 8.8	Steel	Grade 8.8 M10x40mmx 1.25	830	600	4
Hydraulic Jack			10Tones			1
Pressure Gauge	Model No:G2517 L		6000psi (41.37 MPa)			1

The loading conditions for the bender and the straightener members are shown in Figure 3.3 (a). For simplicity, the dominant loads on the members are taken as a concentrated bending load and a straightening load, respectively.

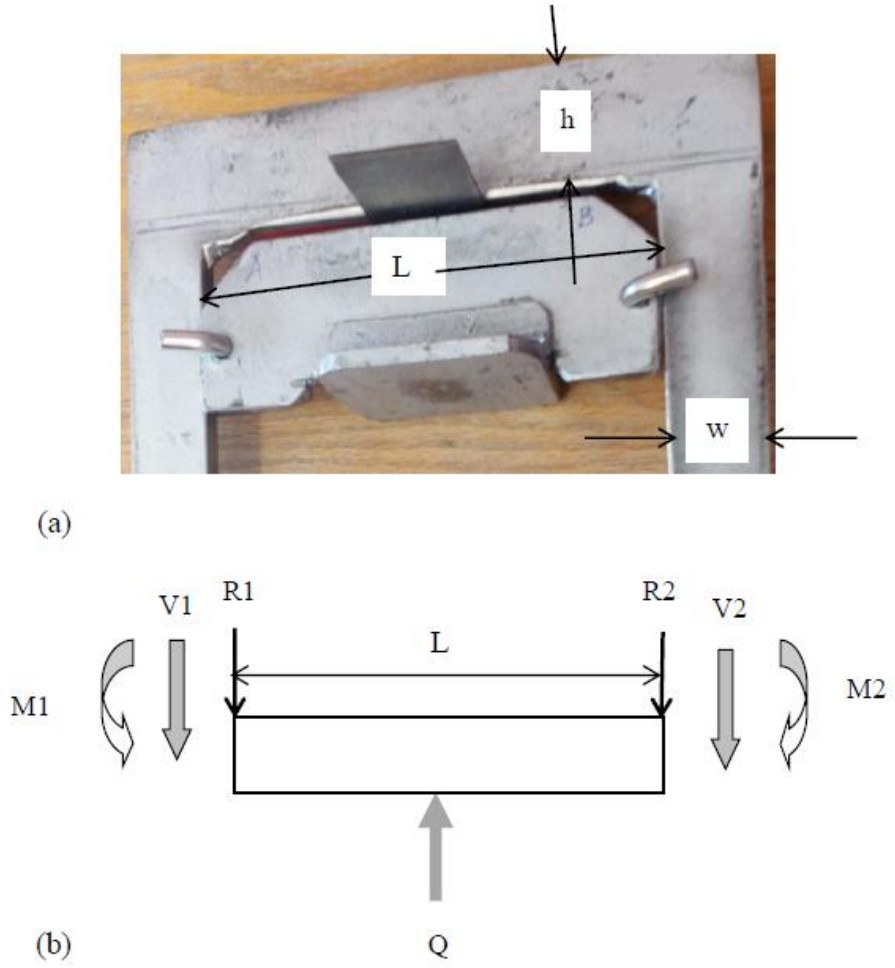

Figure 3.3: Bender and straightener; (a) loading condition layout ;(b) free body diagram

The loads are due to the bending and straightening forces Q exerted by the hydraulic jack on the sheet sample. Tensile and shear loads were also considered on the bender arms.

Since both parts are made of the same material, the design calculations for the bender were assumed also to satisfy the straightener. Therefore, for simplicity, the size calculations for the straightener were skipped. The theoretical bending force Q_{th} required to bend the sheet was estimated by using Equation 3.1 [101] as:

$$Q_{th} = ST\frac{Wkt^2}{D} \qquad 3.1$$

ST, *t*=2 mm, *W*=42 mm and D=*D2*=12 mm are sample material ultimate tensile strength (*ST*=950 Mpa for Ti6Al4V), thickness, width and length of open die, respectively. The factor *k* depends on the die profile, *k* = 0.3, 0.7 and 1.3 for *V*-die, whipping die and *U* -die , respectively. In this study the value of *k* = 0.7 was used. Substituting the respective values of these parameters in Equation 3.1 gave the theoretical bending force as Q_{th} = 9310 N. Considering a factor of safety of m = 1.4 on the force results to mQ_{th} =13034 N.

An experimental method was used to determine the average bending and straightening force *Q*. The procedures of determining *Q* are covered in section 3.2.3; and the results showed that Q =19237 N. Therefore, 19237 N was selected as the design-bending load for sizing the CBS tool parts. A factor of safety of *m* =1.4 was multiplied by the experimental force *Q*, to account for any possible variation of the bending and straightening forces and the material properties.

The selected effective dimensions of the bender and straightener were: length L = 170 mm, thickness b = 8 mm, and height h = 42 mm. The material selected was steel EN 10025-S275JR of yield strength 350MPa [102]. Based on these dimensions, the applied loads were compared with the material strength, as follows. The bender's ends were considered rigidly fixed from rotation, as shown by the free body diagram (FBD) in Figure 3.3 (b). The FBD shows the applied and reaction forces and the moments on the bender. These are the bending force *Q*, the reaction forces; *R1, R2,* the shear forces *V1, V2* and the moments *M1, M2*. Since the bending load induces bending stress in the member mainly in the longitudinal direction, the bender was treated as a rectangular beam with fixed ends loaded in bending with a concentrated force *Q* at the middle. The maximum bending stress in the bender is given by using Equation 3.2 as:

$$Sb_{max} = \frac{M_{max}}{Z} \tag{3.2}$$

Sb_{max} = maximum bending stress, M_{max}= maximum bending moment in the bender, Z = section modulus. For the fixed ends body loaded in bending with a concentrated force *Q* at the middle, taking a factor of safety for the load *Q* as *m* =1.4; the maximum bending moment M_{max} =1.4QL/8 [103][104], for a rectangular section, Z = I/(h/2) = (bh^3/12)(2/h). Therefore, the maximum bending stress at the outer point in the middle of the bender is given by Equation 3.3 as:

$$Sb_{max} = \frac{8.4}{8}\frac{QL}{bh^2} \tag{3.3}$$

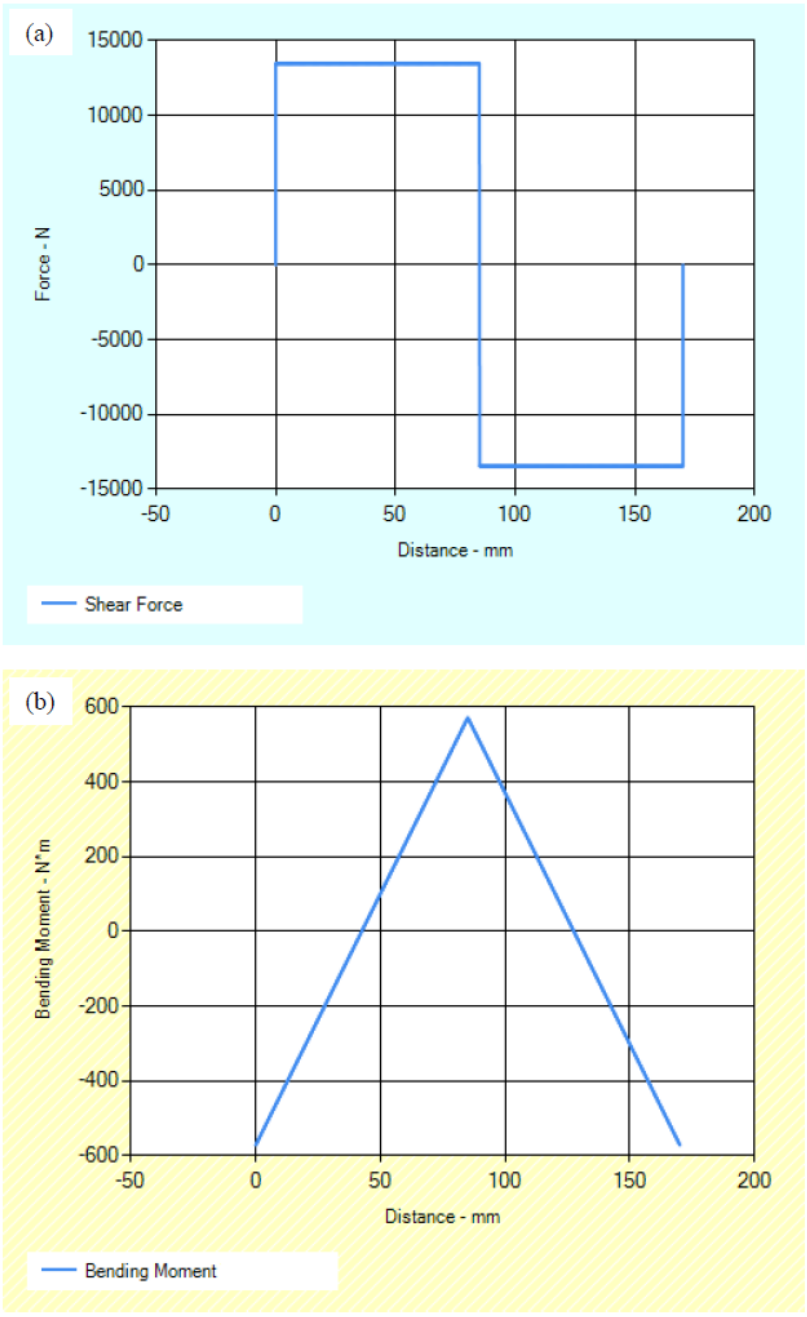

Figure 3.4: Load distribution on the bender (a) shear force diagram (b) bending moment diagram

Substituting the known values for *Q*, *L*, *b*, and *h* in Equation 3.3 gives $Sb_{,max}$= 243.3 MPa, which is less than the yield strength of the material (350 MPa). The shear and bending moment diagrams for the bender based on a factor of safety *m* = 1.4, are presented in Figure 3.4(a) and (b) respectively. The load diagrams show that the reaction forces *R1=R2* = 13466 N, shear forces *V1=V2* = 13466 N. Reaction moments *M1=M2* = -572.3 Nm, the maximum bending moment M_{max} = 572.3 Nm and occurs at the centre of the bender. The tensile stress in the bender arm is given by Equation 3.4 as:

$$St = m\frac{Q}{A_t} \qquad 3.4$$

Q = total tensile force on the bender, *m* =1.5 factor of safety, A_t = total tensile area = 2*bw* for two arms of the bender where *w* = 30 mm. Equation 3.4 can also be used to determine the direct shear stress in the bender arms. Substituting the values for *m*, *Q*, *b* and *w* in Equation 3.4 gives *St* = 60.1 MPa which is less than both the material yield strength (350 MPa) and the permissible shear yield strength (taken as 0.58 of the tensile yield strength).

The layout and loading conditions for both upper and lower constraining brackets are shown in Figure 3.5 (a). The dominant load on both brackets is taken as concentrated bending loads. The loads are induced by the hydraulic jack during bending and straightening of the sheet. Observation on the loading layout shows that the upper constraining bracket and bolts are more likely to fail during straightening than during the bending step; therefore the selection of the brackets size and bolts were done, based on

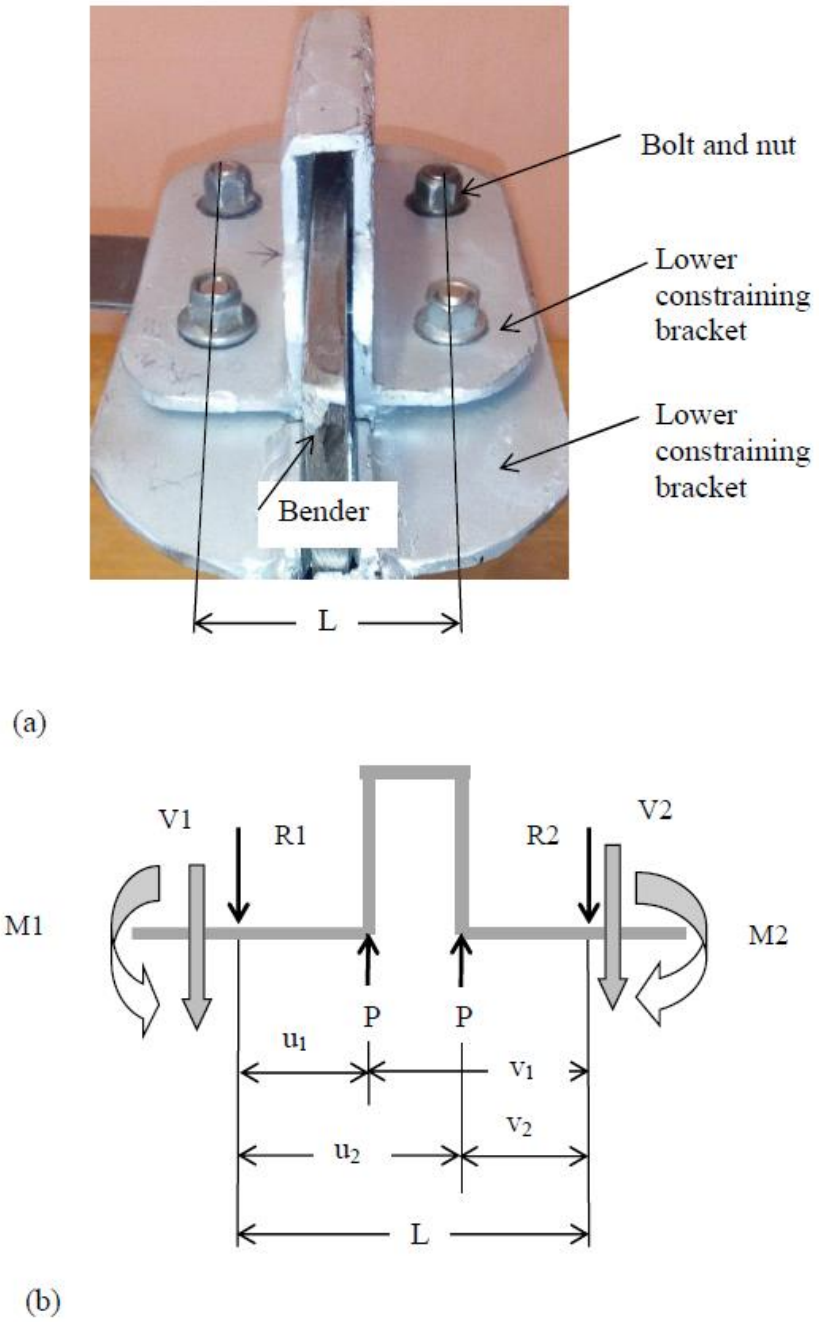

Figure 3.5: Constraining brackets (a) layout loading conditions (b) free body diagram

the straightening stage. Both upper and lower brackets were made of the same material therefore calculation for the upper bracket was assumed to satisfy the lower bracket also. The effective dimensions of the constraining brackets were selected as follows: The effective length between bolt centres L = 65 mm, was measured in the rolling direction.

The effective overall width of the bracket b = 128 mm measured in the transverse direction and the plate thickness height h = 6 mm. The proposed material was steel EN 10025-S355JR angle section of yield strength 275MPa [102]. The detailed dimensions of the angle sections can also be found in[105]. Based on these dimensions, the applied loads were compared with the material strength, as follows. Since the loading condition shows that induced bending stress in the brackets is mainly in the longitudinal direction, the brackets were considered as a rectangular beam, with rigidly fixed ends from motion by the bolts, as shown in the free body diagram (FBD) in Figure 3.5 (b).

The FBD shows the applied and the reaction forces and moments on the bender. These are the applied bending forces each of magnitude P, the reaction forces $R1$, $R2$ shear forces $V1$, $V2$ and the moments $M1$, $M2$. The fixed ends bracket was loaded in bending with two concentrated forces, each of magnitude P acting vertically upward. Noting that $2P = Q$ as a total concentrated force acting on the bracket, the maximum bending stress in the bracket was determined by Equation 3.5 as:

$$Sb_{max} = \frac{M_{max}}{Z} \quad 3.5$$

Sb_{max} = the maximum bending stress, M_{max} = the maximum bending moment and Z = the section modulus. For the fixed ends member loaded in bending with two concentrated forces each of magnitude P, taking a factor of safety for the load P as m =1.4, the maximum bending moment is given in by Equation 3.6 [103][104] as:

$$M_{max} = \frac{1.4P}{L^2}(u_1 v_{1+}^2 u_2 v_2^2) \quad 3.6$$

Where, u, v are the lengths from the point of load application to the left and the right end of the beam respectively. For rectangular solid section Z = I/(h/2) = (bh^3/12)(2/h). The maximum bending stress at the end outer point on the bracket is given by Equation 3.7 as:

$$Sb_{max} = \frac{8.4P}{bh^2L^2}(u_1 v_{1+}^2 u_2 v_2^2) \quad 3.7$$

Referring to the bracket loading FBD, the values for u_1, v_1, u_2 and v_2 were taken as: 25 mm, 40 mm, 40 mm and 25 mm, respectively. Substituting the known values in Equation 3.7 gives the maximum bending stress as 269.7 MPa, which is slightly less than the yield strength (275 MPa) of the proposed material for the constraining brackets. Shear and bending moment distribution diagrams for the constraining bracket based on a factor of safety m =1.4; and these are presented in Figure 3.6 (a) and (b), respectively.

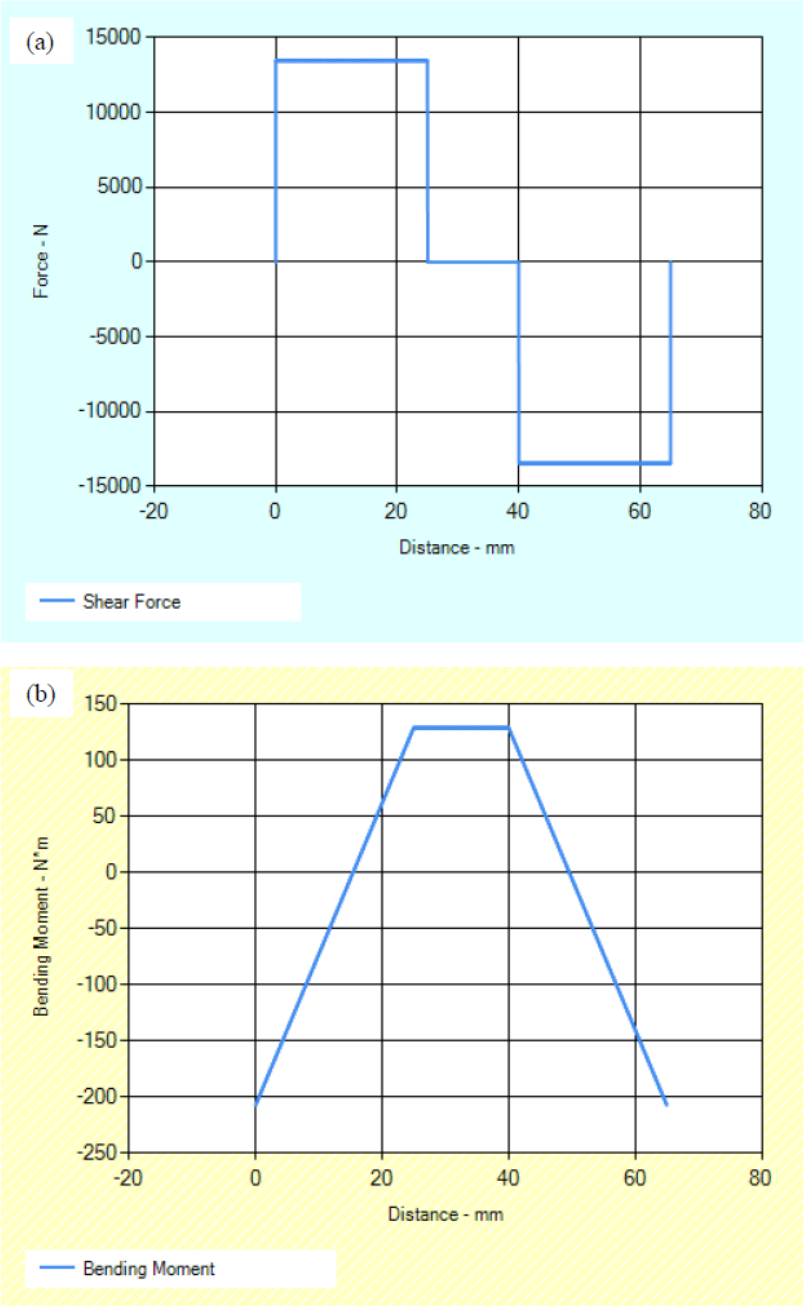

Figure 3.6: Load distribution on the constraining bracket (a) shear force diagram (b) bending moment diagram

The Load diagrams show that the reaction forces *R1=R2*= 13465.9 N, shear forces *V1=V2*= 13465.9 N. The reaction moments *M1=M2* = -207.2 Nm, maximum bending moment M_{max} = -207.2 Nm; and it occurs at the ends of the bracket.

The lock pins were loaded under shear and the shear stress in the pins was determined by Equation 3.8 as:

$$Ss = m\frac{Q}{2A_s} \tag{3.8}$$

Where m =1.4 factor of safety, $Q = 2P$ total shearing force on the pins, $2A_s$ = total shear area for 2 pins locked during bending or constraining. The material selected for the pins was Steel EN10025-S355JR of yield strength *SY* = 275 MPa. The shear strength of the pin was taken as 0.58*SY*=160 MPa; and it was equated to the load S_S. Substituting values of S_S, m and Q, in Equation 3.8, gives A_s = 84 mm^2. The selected diameter of the lock pin was 8mm.

The main load considered in the bolts was the tensile force Q, as a result of the bending and straightening force Q transmitted to the bolted brackets. The selected material for the bolts and nuts was steel Grade 8.8 with a yield strength *SY* of 600 MPa [102]. The tensile stress in the bolts was given by Equation 3.9 as:

$$St = m\frac{Q}{A_t} \tag{3.9}$$

Q = 2P= the total tensile force on the bracket, m =1.5 = factor of safety, 4A_t = total tensile area for 4 bolts. Substituting values of Q, m and the tensile yield strength SY in Equation 3.9 gives the minimum required tensile area for each bolt as 12 mm^2. Four bolts of standard size M10 x 40 mm x 1.25 mm (nominal diameter x length x pitch) [106] and nuts were selected. Each bolt with a nominal diameter of 10mm has a tensile area of 61.2 mm^2. After all the parts' sizes and quantities were determined, their respective engineering drawings were prepared by using CAD software. The detailed and assembly drawings can be found in Appendix A.

Plates, angle sections and steel bolts were purchased from the local retailers. Plates and angle sections were cut according to the part dimensions specified in the drawings. The tool was fabricated and assembled in Manufacturing Workshop in the Mechanical Engineering Science Department at the University of Johannesburg. The cost estimates for the CBS process tool are presented in Appendix E.

3.2.3 Assembly of the pressure gauge on the hydraulic jack

A 10 ton hydraulic bottle jack attached to a 6000 psi pressure gauge-model no G2517L was used in this study. The jack and the pressure gauge were bought separately; and the assembly of the two parts was done in the workshop. Before the gauge was attached to the jack, the jack parts were dismantled, as may be seen in Figure 3.7, by unscrewing the

housing top nut using a pipe wrench. The reservoir cylinder, large cylinder, large piston, inlet and discharge ball valves were taken out.

Figure 3.7: Parts of a dismantled jack

A sketch for the sectional view of the jack is shown in Figure 3.8. On the milling machine, a hole of 6 mm diameter was drilled vertically to a depth of 15 mm. Another hole of the same size was drilled on the base of the jack horizontally, until it coincided with the vertical hole, the hole was meant to connect the hydraulic fluid flowing from the

discharge valve to the reading gauge. An 11 mm drill bit was used to bore the horizontal hole.

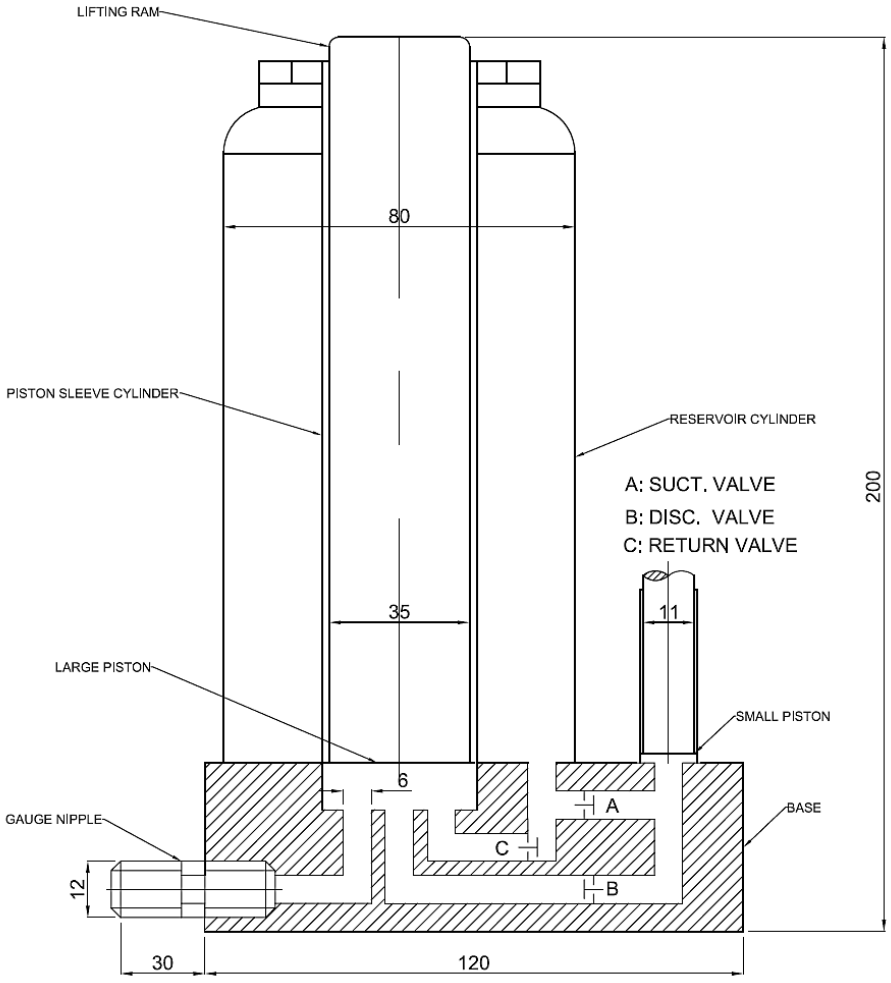

Figure 3.8: Sectional view of the jack (all dimensions in mm)

A standard N410-3 NPT¼ thread tap in Figure 3.9 was purchased and used for threading the drilled hole. The recommended drill hole for the purchased thread tap was 11.11 mm.

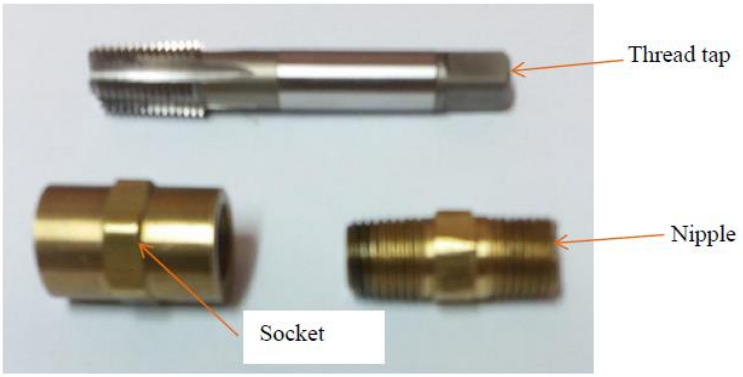

Figure 3.9: Thread tap , nipple and socket

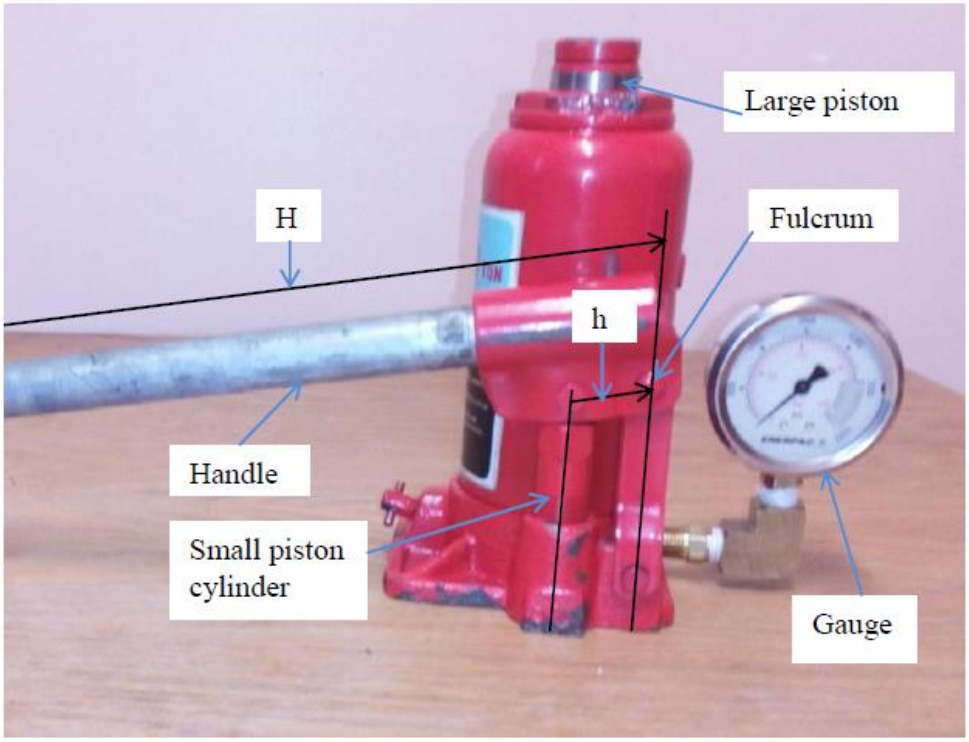

Figure 3.10: Assembled jack, pressure gauge and handle

The gauge was fixed on the jack with a pair of ½ inch size nipple and socket. The jack was re-assembled with inlet and discharge ball valves, large piston, large cylinder and the reservoir cylinder. A complete assembly of the jack is shown in Figure 3.10.

In order to increase the mechanical advantage (leverage) of the jack system, and thereby minimizing the effort to operate the jack manually, a handle of considerable length was used. It was considered that the effective length of the handle to the fulcrum be *H*, the length from small piston to the fulcrum *h*, diameter of large piston d_2, diameter of small piston d_1 and the efficiency of the system η. The total mechanical advantage MA_t can be determined by the product of mechanical advantage due to the lever, and the mechanical advantage due to the jack hydraulic system, by Equation 3.10 as:

$$MA_t = \frac{Load}{Effort} = \frac{H}{h}\frac{d_2^2}{d_1^2}\eta \qquad 3.10$$

The measurement showed that: H = 477 mm, h = 27 mm, d_2 = 35 mm and d_1 = 11mm, the efficiency for system was taken as ŋ = 0.9 (ranges from 90%-95%) to account for frictional losses. Substituting the known values in Equation 3.10 gives MA_t =170. Therefore, Equation 3.10 for the MA_t gives the relationship between the required effort force on the handle and the respective output load by a factor of 170. Note that the maximum bending force produced by the jack was not to exceed its 10 tons (98000 N) capacity.

An experiment was performed to estimate the constraining force exerted by the bolts on the sheet sample. Figure 3.11 shows the layout of the test, where the constraining was done by tightening the nut with a spanner of length h, which was found to rotate approximately one revolution. The effort force *E* applied on the spanner was measured by a spring balance attached to the spanner. The axial constraining force in the bolt FC was determined by equation 3.11 [106][107] as:

$$FC = \frac{2M}{d_m}\left(\frac{\pi d - \mu l Sec\alpha}{l + \pi\mu d Sec\alpha}\right)\text{ŋ} \qquad 3.11$$

M = torque applied on the spanner = *Eh*

Measured values of E and h were 19.6 N and 0.16 m, respectively

l = pitch of thread =0.00125 m

d_m = mean diameter of thread, $d_m = d - l/2 = 0.009375$ m

d = major diameter of thread = 10 mm

α = half of thread angle, for hexagonal thread $(60^o/2) = 30^o$

μ = coefficient of friction between the steel bolt and the nut threads contact surface = 0.3

ŋ = efficiency of the thread taken as 50% for the non-lubricated threads

Substituting the values for *M, d,* α, μ and *l* gives constraining force on each bolt FC= 423.5 N. The average bending force Q produced by the jack with large piston diameter d_2 on the sample during the bending or straightening was given by the product of pressure and area by Equation 3.12 as:

$$Q = p\frac{\pi d_2^2}{4} \qquad 3.12$$

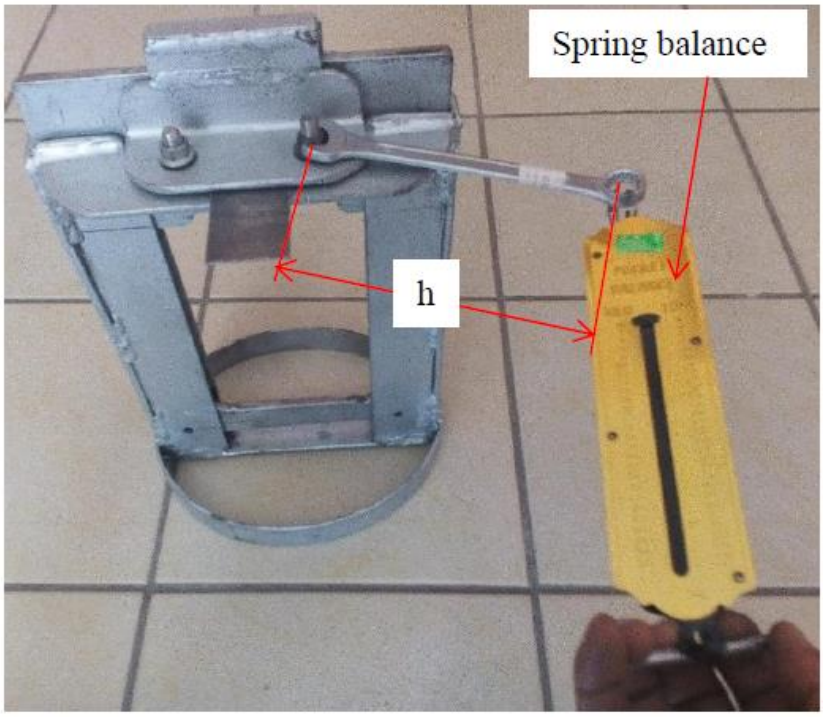

Figure 3.11: Measurement of constraining force

Whereby, p = the gauge reading pressure (psi) transmitted equally in the hydraulic system. Testing of the tool showed that the average measured value of pressure p for bending and straightening was 2900 psi, where 1psi = 0.0068947 MPa. Substituting the values for p and d_2 = 35 mm in Equation 3.12 gives Q = 19237 N. Therefore, the experimental average of the bending and the straightening force was 19237 N.

3.3 Processing of the samples with the CBS tool

Ti6Al4V alloy sheets of 2 mm thickness were supplied by Titanium A2Z South Africa. The material composition and the tensile properties are presented in Table 3.2. The received sheets were cut into sub-size samples, each with cubic nominal dimensions (length x width x thickness) of 152 mm x 42 mm x 2 mm, respectively.

Table 3.2: Ti6Al4V alloy material properties

Ti6Al4V-ASTM B265, Grade5. Chemical composition: C(0.02), Fe(0.12), N(0.018,) O(0.1), H(0.003), Al(5.9),V(4.1), Others(<0.4) and Ti(balance).	
Yield strength, SY (MPa)	Max 886
Tensile strength, ST (MPa)	Max 950
% Elongation	10-13
Thickness of sheets (mm)	2

A total of 21 sheet samples were cut by using the diamond SiC disc on a Mecatome T300 machine. Figure 3.12 represents the sheet sample configured in three directional axes, namely the rolling (R), normal (N) and transverse (T). Eighteen (18) samples were prepared and successfully deformed with the CBS process i.e. three samples for each of N = 2, 4, 6 (denoted as N2, N4, N6) passes combined at F = 12 mm, 6 mm (denoted as F6, F12) feed lengths respectively.

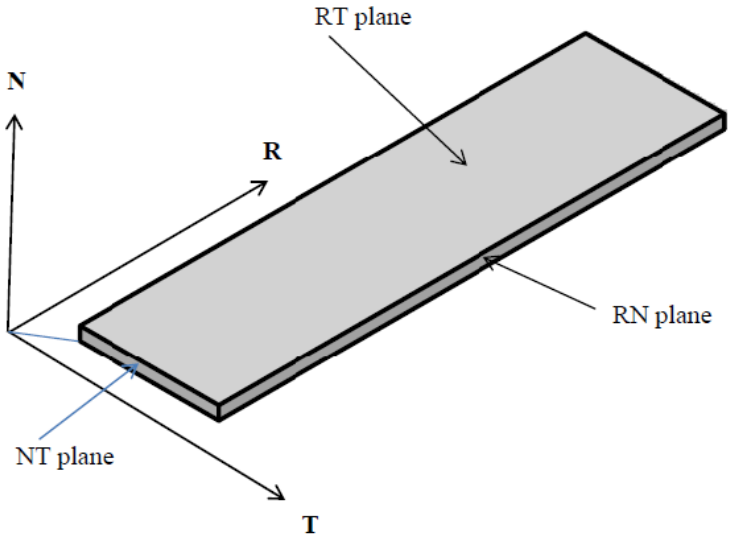

Figure 3.12: A sheet sample represented in rolling (R), normal (N) and transverse (T) directions

Detailed breakdown of the number of samples processed, combination of number of passes N with feed lengths F and notation of samples are given in Table 3.3. Three of the received samples were not deformed for the purpose of being a reference material; hence, here these were referred to as received samples (AR).

Table 3.3: Details of processed samples

Number of pass, N	Feed, F(mm)	Notation of samples	No of samples	Remark
-	-	AR	3	Each group of samples produced sub samples for tensile, hardness and microstructure analysis
2	6	N2F6	3	
4	6	N4F6	3	
6	6	N6F6	3	
2	12	N4F12	3	
4	12	N6F12	3	
6	12	N6F12	3	

A picture layout of the CBS process is presented in Figure 3.13. The process was performed on the samples at room temperature. For each pass and feed length specified in Table 3.3, the samples were equally deformed with the average force of 19237 N at an

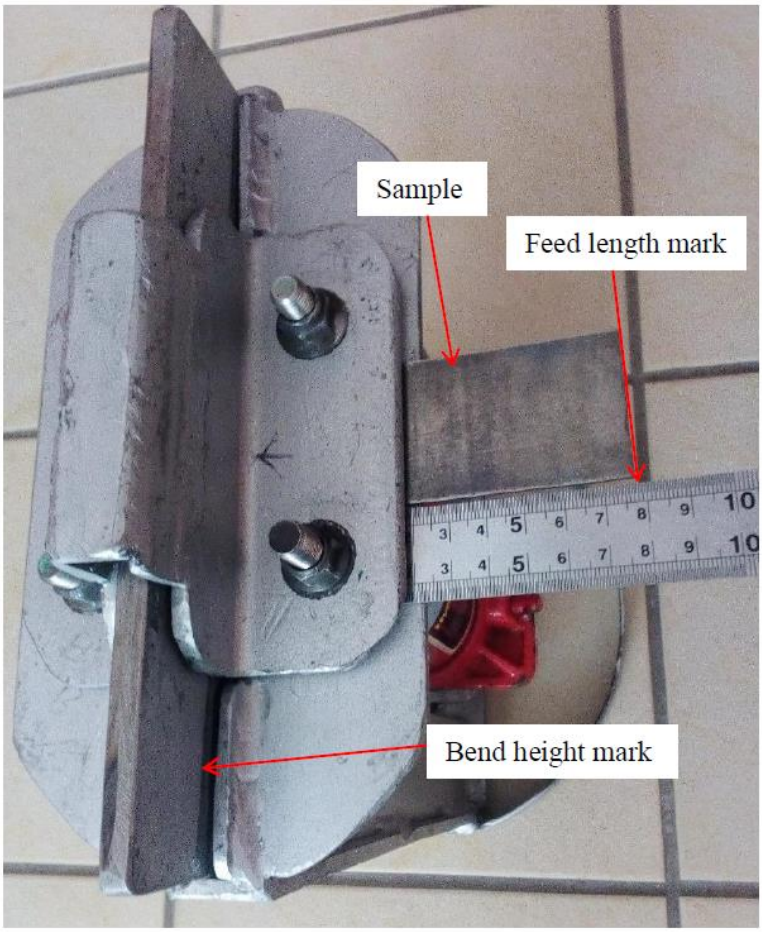

Figure 3.13: Layout of the CBS process

average velocity of 0.2 mm/s; and the average deformation velocity was determined by taking the ratio of bending depth of 2 mm to the average deformation time of 10s.

Samples were deformed at the plastic bending depth of 2 mm; since it is recommended that the bending depth should not exceed the sample thickness. The bending depth on the sample could be determined by measuring the height of the groove perpendicular to the sample surface along the curvature centre.

Figure 3.14: (a) Sheet sample in bending state (b) Fractured sample

Figure 3.14 (a) and (b) shows the samples after the bending and fracture states, respectively. In order to reduce the feed forces and the contact friction forces during feeding of the sample, each successive feed was preceded by loosening the bolts to enhance the un-constraining of the sample. After feeding, the sample at the specified

feed, the bolts were tightened gain in order to enhance the constraining of the sample. The feed length was measured with a steel ruler.

The number of the CBS passes N, on the sample was increased by performing repeated bending-straightening cycles over the length of the sample, at the specified feed length F. An attempt to perform the CBS process on sheet samples at 4 mm (F4) feed length resulted in cracking and fracture of the samples in early 1st (N1) and 2nd (N2) passes. Therefore, the experimental results at F4 feed were not included in this study. However, the effect of the CBS process on the strain magnitude and the homogeneity in the samples at F4 feed length were included in the numerically simulated model.

Figure 3.15: Measurement of samples' dimensions with a Vernier caliper

Measurements on the length (L), width (W) and thickness (T) of the samples were taken before and after the CBS process was performed; and a digital Vernier caliper (see Figure 3.15) was used for this measurement.

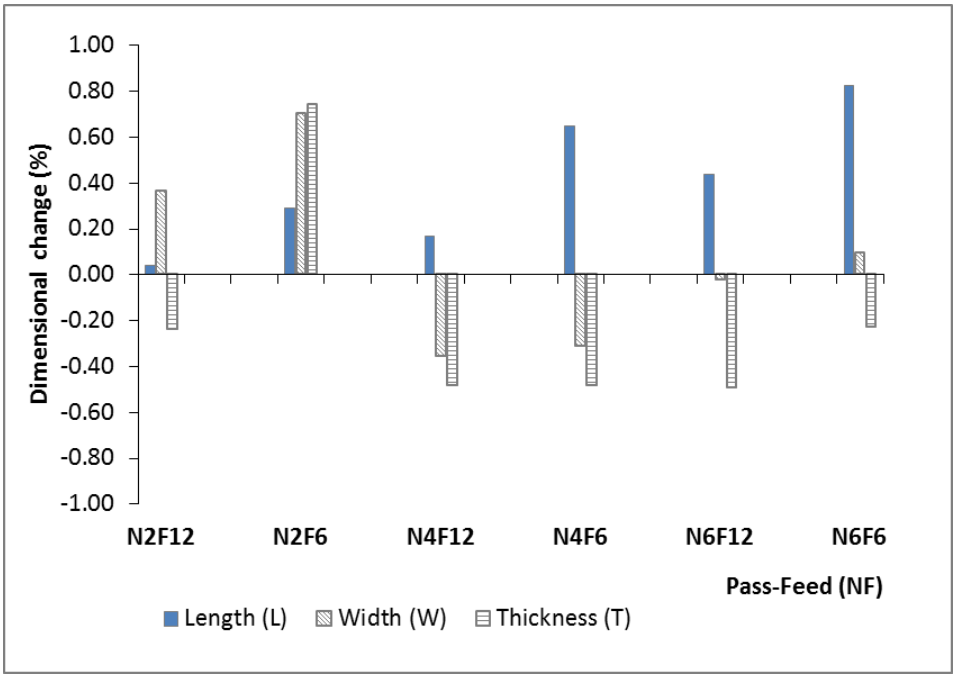

Figure 3.16: Average percentage dimensional changes versus number of pass-feed (NF) of processed samples

The objective of measuring the dimensions was to observe any sample dimensional change after the CBS process had been performed. The average samples' percentage of dimensional changes after the process were calculated, plotted and presented in Figure 3.16. The results showed that the lowest and highest changes of length were 0.04% and 0.82% at N2F12 and N6F6 respectively. The change of length was proportional to the

number of passes; and this was higher at F6 feed than F12 feed in all the passes. The reason for this could be due to the higher bending curves that induce more elongation at F6 feed than those achieved at the F12 feed. The highest and lowest changes of width were 0.70% at N2F6 and 0.02% at N6F12.

However, the measurements showed random decrease and increase of changes of width dimensions. Average change of samples' thickness was; -0.24% at N2F12, 0.21% at N2F6, -0.48% at N4F12, -0.48% at N4F6, -0.50% at N6F12 and -0.23% at N6F6. Mostly the samples showed a slight decrease of thickness after the CBS process. In conclusion, the samples' length, width and thickness dimensional changes of less than 1% were considered as insignificant. An insignificant dimensional change is one of the desirable conditions to severe plastic deformation.

In this study, the used CBS tool's parameters namely; motion and forces for feeding, bending and straightening were operated and controlled manually. This could have reduced the process continuity. Automating the operation of these steps could improve continuity and efficiency of the process. The processed samples were then prepared for the tensile test, the hardness test and the microstructural analysis as discussed in the next sub-chapters.

3.4 Tensile test

Tensile test sample dimensions were determined, according to the ASTM-E8M standards [108]. The transverse section of the test samples lies in the NT plane (refer to Figure 3.12). A total of twenty one (21) tensile test samples were machined. Each sample with a gauge length of 25 mm measured along the rolling direction, width 6 mm and thickness 2 mm. The detailed dimensions of the test sample are given in Figure 3.17.

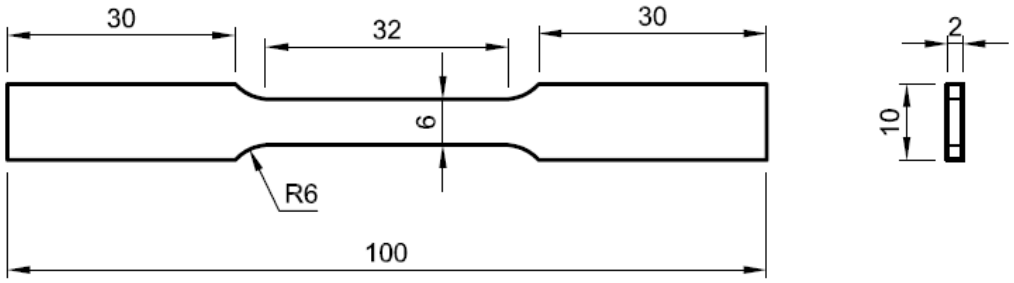

Figure 3.17: Tensile test sample standard dimensions (all dimensions in mm)

The samples were fractured by a tensile load on the Zwick/Roell Z250 tensile test machine at a cross head speed of 5mm/min and $0.003s^{-1}$ strain rate. Figure 3.18 (a) and (b) shows some tensile test samples before and after fracture, respectively. For each pass number-feed length (NF) category of samples, the average results for engineering tensile stress-strain were plotted. Tensile strength (ST), yield strength (SY), stress at fracture (SF), percentage elongation (eP) and fracture elongation (eF) were determined. Values of ST, SF and eF were determined from the test data and the stress-strain curves plotted accordingly.

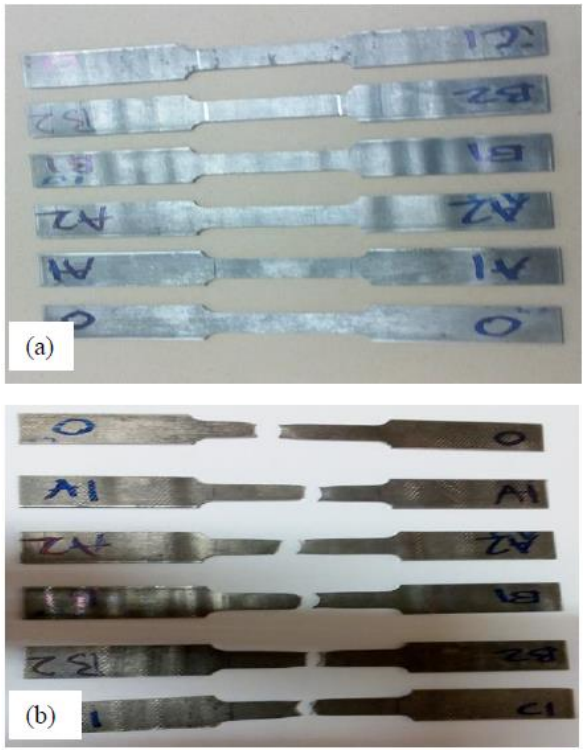

Figure 3.18: Tensile test samples (a) before fracture (b) after fracture

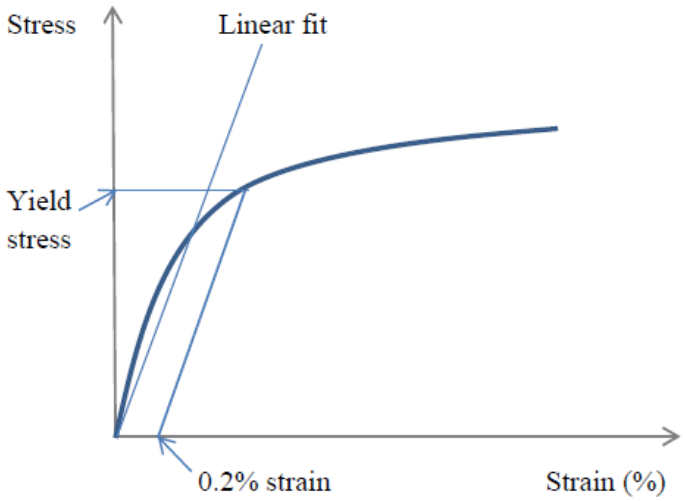

Figure 3.19: Measurement of proof yield strength from the stress-strain curve

The proof yield stress *SY* was determined by using the plotted stress-strain curve, based on the 0.2% plastic yield strain, as illustrated in Figure 3.19. First, the linear fit of the curve was determined; and the 0.2% strain point was marked on the strain axis. A line was drawn from the point parallel to the linear fit line, until intersected with the stress-strain curve. Another line was drawn from the point of intersection and projected to the stress axis to give the yield stress. The samples' percentage elongations (eP) were determined by Equation 3.13; as the ratio of the increase of the gauge length at fracture to the initial gauge length.

$$eP = \frac{l_{gf} - l_{go}}{l_{go}} 100 \qquad 3.13$$

l_{go} and l_{gf} are sample gauge lengths before and after fracture respectively. The following relationships were used between the engineering stress (S_{en}) - strain (ε_{en}) and the true stress (S_{tr}) - strain (ε_{tr}) as shown by Equations 3.14 and 3.15 respectively [107] as:

$$S_{tr} = S_{en}(1 + \varepsilon_{en}) \qquad 3.14$$

$$\varepsilon_{tr} = ln(1 + \varepsilon_{en}) \qquad 3.15$$

The tensile test results at various passes (N)-feed (F) for tensile strength, yield strength percentage elongation (eP) and fracture elongation (eF) were presented; and they will be discussed in detail in Chapter 4.

3.5 Hardness test

Samples processed with CBS method were prepared for the hardness test. During the CBS process, the bending of the samples was considered plane strain, in which the strains on the NT planes along the T direction were found to be constant. Therefore, a hardness investigation was considered on the RT and RN planes. From each category of the NF processed samples, two sub-size samples, each of length 15 mm, were cut from the RT plane and RN plane, respectively. Figure 3.20 shows the planes on which the samples were cut as indicated in blue and orange coloured line respectively.

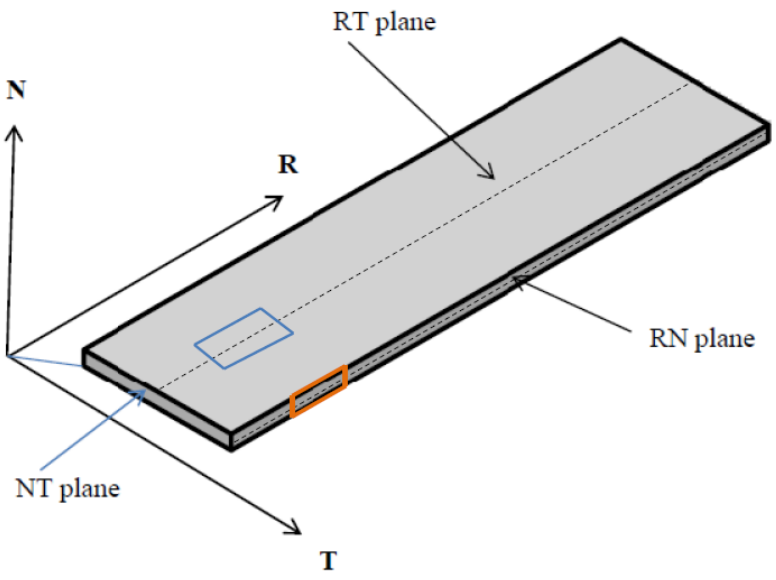

Figure 3.20: RT and RN planes considered for samples hardness test

Mounting, grinding and polishing of the samples were done, according to the ASTM-E03 standards [109]. The samples were hot mounted on the Struers mounting machine.

Polyfast resin was used at a pressure of 350 Bar, at a heating temperature of 180^0C, with heating and cooling times of 3 and 2 minutes, respectively. One set of mounted samples that were cut from the RN and RT planes is shown in Figure 3.21.

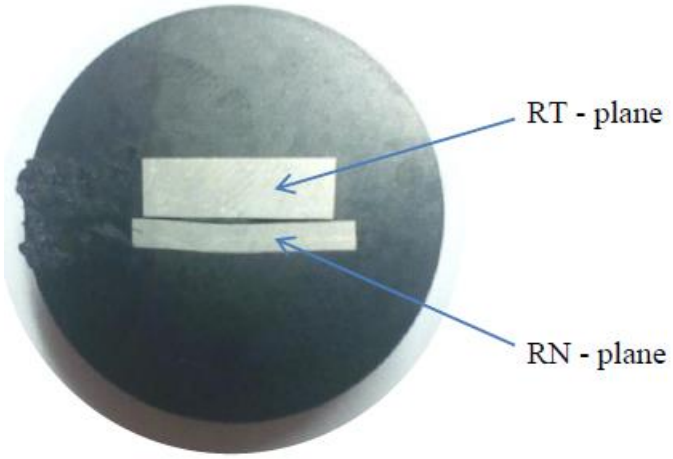

Figure 3.21: Mounted samples cut from RN and RT planes

With a force of 25 N at a speed of 200 rpm, the mounted samples were then plane ground with #320, #800 and #1200 SiC sand papers followed by fine grinding with MD Largo disc and diamond suspension lubricant for 5 minutes. The samples were then polished with MD Chem disc and OPS solution lubricant, with a force of 20 N at a speed of 150 rpm for 5 minutes. A Vickers hardness (HV) test was conducted, according to the ASTM-E92 standards [110]. Vickers micro hardness along the sample's centre line were determined at intervals of 1 mm using a digital hardness tester, at 9.8 N (1kgf) indentation load and 15s dwell time with 0.03% error. The indenter made of diamond had a square-base pyramidal geometry with an included angle of 136^o. The machine made

indentations on the sample, whose sizes were measured by using an optical microscope. The Vickers's hardness (HV) values were determined by Equation 3.16 as:

$$HV = \frac{1.8544Q}{\left(\frac{d_1 + d_2}{2}\right)^2} \qquad 3.16$$

Q, d_1 and d_2 are indentation load (kgf), first and second diagonal lengths (μm) of the indenter penetration, respectively. For each feed length F and pass N, the hardness values of samples were determined and then averaged. Hardness test results versus pass (N)-feed (F) values were presented; and these will be discussed in Chapter 4.

3.6 Microstructural analysis

After the hardness test, the indentations were removed by grinding the samples with #1200 SiC sand paper, MD Largo disc and diamond suspension; then they were polished with MD-Chem disc and OPS solution. The polished samples were etched, according to the ASTM-E407 [111] standard guides. Kroll's etchant, with a volume ratio of 94% -H_2O (water), 4% -HNO_3 (nitric acid) and 2%-HF (hydrofluoric acid) was used. The polished samples were immersed in the etchant for 30 seconds. Based on the ASTM-E112 [112] standards, the micro grain structure and the morphology of the etched samples were characterized by using the Olympus BX61M optical microscope (OPM) and the Vega3 Tescan Scanning Electron Microscope (SEM) at 20 kV accelerating voltage. The SEM equipment was equipped with the Electron Diffraction Spectrometer (EDS) that was used

to study the elemental composition and the quantification in the AR and the processed samples. X-Ray Diffraction (XRD) detector was used to characterize the CBS processed samples on Ti6Al4V alloy phases and their composition. The crystallite mean size and the lattice strain in the processed material were characterized, based on the Williamson-Hall method. Rigaku Altima-IV X-Ray Diffractometer (XRD) with Cu-K_α radiation with a wave length (λ) of 0.154056nm was used. The diffractometer with K_β filter worked at a scanning rate of 1.00 (deg)/min, step width of 0.01 (deg) in a scan range of 5 (deg)-90(deg). The samples were scanned at 40 kV, 30 mA.

The X-Ray Diffraction (XRD) is associated with how atomic planes in crystals tend to reflect X-ray beams at certain angles of incidence. The XRD technique is widely used to determine: the average spacing distances between the planes of atoms in crystals, crystal and grain size and texture (orientation), different phases and the structure of the materials. It is also used to measure the internal stresses and strains in the crystallite. The principle of the XRD was mathematically defined by the Bragg's Law, as represented by Equation 3.17 as:

$$n\lambda = 2dSin\theta \quad 3.17$$

n, λ, d and θ are the integral constant, the wave length of the incidence X-ray beam, the distance between the atomic planes in a crystal and the angle of incidence, respectively.

The crystallite mean size *D* was related to Bragg's diffraction angle θ by Scherrer's Equation 3.18 [113] as:

$$B(2\theta) = \frac{K\lambda}{DCos\theta} \quad 3.18$$

B(2θ) = full width at half maximum peak (FWHM) (radians)

K = 0.9, known as the Scherrer's constant

θ = the peak position angle (radians)

λ = 0.15406nm, the wave length of X-ray beam

D = the crystallite size (nm)

Scherrer's equation provides only the lower bound to the crystallite size, since it considers mainly the contribution of the crystallite size to the peak broadening. The Williamson-Hall method [114],[115] considers the size and the internal strain contributions to the peak broadening and both the size and the strain are mutually independent of each other. The resultant width of the peak is given by Equations 3.19 - 3.21 as:

$$B_t(2\theta) = B_s + B_\varepsilon \quad 3.19$$

Substituting the expressions for B_s, and B_ε gives:

$$B_t(2\theta) = \frac{K\lambda}{DCos\theta} + 4\varepsilon Tan\theta \quad 3.20$$

$$B_t(2\theta)Cos\theta = \frac{K\lambda}{D} + 4\varepsilon Sin\theta \quad 3.21$$

$$\varepsilon = \frac{B_t(2\theta)Cos\theta}{4}, \quad B_t(2\theta) = FWHM \qquad 3.22$$

The values of the strain ε and the total width of the peak B_t can be deduced from Equation 3.21 as shown by Equation 3.22: The results of the microstructural analyses are presented and discussed in Chapter 4.

3.7 Numerical modelling and simulation

3.7.1 Description of the numerical method and the model

In this study, the purpose of performing a numerical investigation was to have results from a different approach that later would be compared with their experimental counter-parts for the consistence of the study's findings. The Finite Element Analysis (FEA) was used to investigate the performance of the CBS on Ti6Al4V sheets enhanced properties. The use of the FEA method was considered to be cost and time effective; as it reduces the number of physical prototypes that need to be built, and the experiments to be performed over the entire cycle of the product's design, test and optimization [116].

The FEA is well applied in the manufacturing, automotive and aerospace industries. As a numerical method, the FEA gives the approximate solutions by solving a set of differential equations for the elements discretized from the model and interconnected with the joints called the nodes. Elemental solutions are assembled to obtain solutions for

a complete model. The accuracy of solved variable depends on the expression of the variable in the form of linear, quadratic and cubic equations. ABAQUS Standard FEA Version 6.18 software was chosen and used to develop and simulate the CBS model for a number of reasons; ABAQUS is widely preferred; it is available in academia; it is easy to learn. Furthermore, the software has a wide variety of material, elements modelling and it can be customized to solve a particular problem [97].

A goodly number of experimental and simulation work on the performance of RCS and related processes on metal sheets have been reported in the literature by various authors [93][97][117]. These authors have reported the significant strain inhomogeneity observed in the samples; however, no other experimental or numerical work, on the use of the RCS method to process and characterize the Ti6AL4V alloy has been reported in the literature. This motivated the development of a numerical model that predicted how the number of passes N and the feed length F affect the magnitude and the homogeneity of the EP strain, the tensile yield strength and the hardness of the processed samples.

The homogeneity of the induced EP strain was quantified by using the coefficient of strain variation (CV) parameter. The values of the tensile yield strength and the hardness of the material samples were estimated by using the flow stress power law equation. The numerical model was validated by comparing the tensile yield strength and the hardness

simulation results with their experimental counter-parts. Furthermore, a comparison of the model's results with other experimental and simulation works in the literature will be done in Chapter 4. The details of the model's development and simulation are given in the forthcoming sub-chapters.

3.7.2 Development of the numerical model

The model was developed from the CBS basic working principle, whose simplified layout is shown in Figure 3.22. A numerical model consists of the bender B, the straightener S, as well as the upper and lower constraining brackets C and the sheet sample. The lower constraining bracket also acted as an open die. Both the bender and the straightener were assigned a vertical displacement of 2 mm, during the bending and straightening strokes respectively.

During the bending stroke, the constrained force FC in the brackets was taken as 500 N, this value resulted from the upscale of 423 N, as estimated by Equation 3.11. The selected constraining force was in the range of 0-5% of the sample material's ultimate tensile strength. During the straightening stroke, the brackets' holding force on the sheet sample is enhanced by fixing both brackets from rotational and translational motions. Feeding of the sample was enhanced by the propagation of bending-straightening cycles over the entire length L_{pq}.

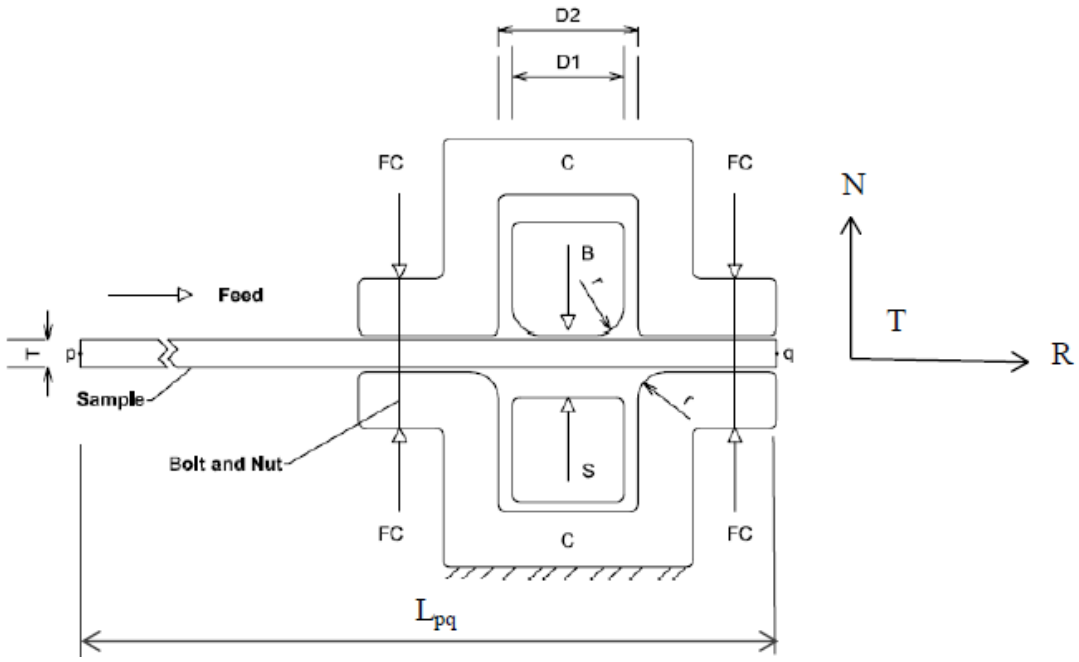

Figure 3.22: CBS numerical model base

The model parts' geometric dimensional parameters are as follows: the size of the bender D1= 8 mm, the length of open die (in this case is the lower constraining bracket) D2=12 mm. The surface radius of the bender and the open die r = 2 mm. The sheet sample's length x width x thickness (mm^3) were 100 x 42 x 2. The model was simulated at N2, N4, N6 passes; and each set was combined with F4, F6, F12, respectively. The combinations were designated as N2F4, N4F4, N6F4, N2F6, N4F6 N6F6, N2F12, N4F12 and N6F12 respectively.

The following assumptions were made and apply to the CBS model:

- In each of the CBS cycles, both the bending and the straightening strokes were maintained at 2 mm, that is to say a bender and straightener move a vertical distance of 2mm during the bending and the straightening strokes, respectively.
- In each of the CBS passes N, a cycle was propagated on the sample length at a constant specified feed length; therefore, the specified feed length F remained unchanged during propagation.
- The bending and the straightening rates in each pass remained constant at 0.2 mm/s.

Based on these stated assumptions, it was deduced that the bending and straightening cycles over the sample length were repeating; and they were symmetrical. Therefore, the simulation of the bending-straightening was considered on a model of reduced length from 100 mm to 22 mm. The strain distribution on the normal-transverse (NT) planes along the transverse (T) axis were constant; hence, bending of the sample was treated as a plane strain. The model then was simplified from R-N-T axes-three dimensional (3D) to the rolling direction-normal (RN) axes-of a two dimensional (2D) plane strain. A reduced size model is presented in Figure 3.23. The sheet sample was treated as an elastic-plastic deformable body; while the bender, the straightener and the constraining brackets were treated as non-deformable bodies. The sample was discretized with a total

of 280 elements of mesh size 0.4 mm, 342 nodes; and the element type was CPE4R (4-node bilinear plane strain quadrilateral reduced integration).

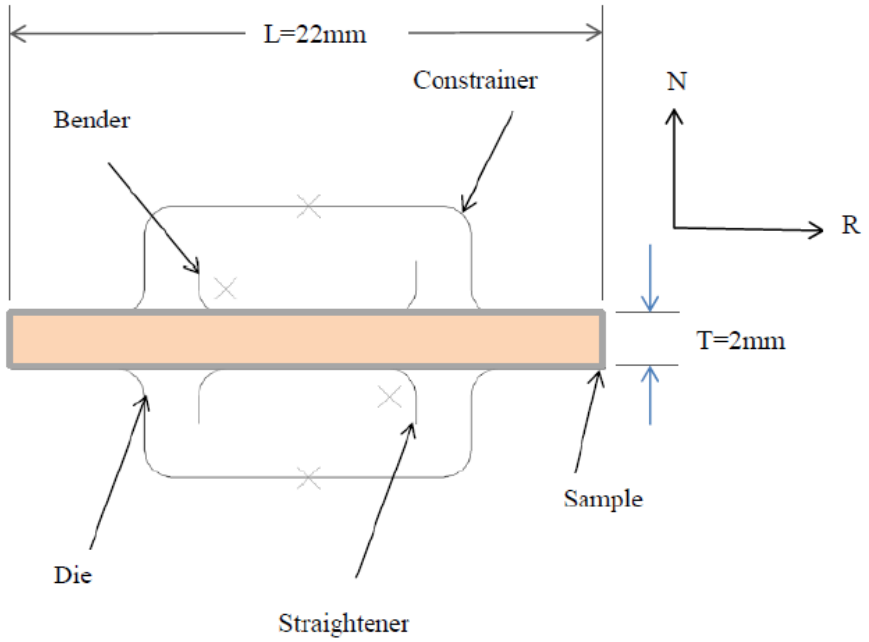

Figure 3.23: Reduced size CBS simulation model

The number of elements and nodes generated on other parts were, respectively: the bender (29, 30), the straightener (29, 30), the upper constrainer (71, 72) and the lower constrainer/die (71, 72). The parts were assigned an element mesh size of 0.4 mm. The contact friction μ, between the sheet and other metals was taken as 0.1 within 0.05-0.1 for the cold forming of metals [19,21]. The tensile yield strength and the Young's modulus of Ti6Al4V alloy were SY=850 MPa and E=115 GPa, respectively; while the poison ratio ν = 0.34. The bender, straightener, upper and lower constrainers (dies) were each made of structural steel with Young's modulus E of 210 GPa and the poison ratio ν = 0.3.

The boundary conditions and simulation steps for the CBS model were generated; they are represented by the block diagram in Figure 3.24.

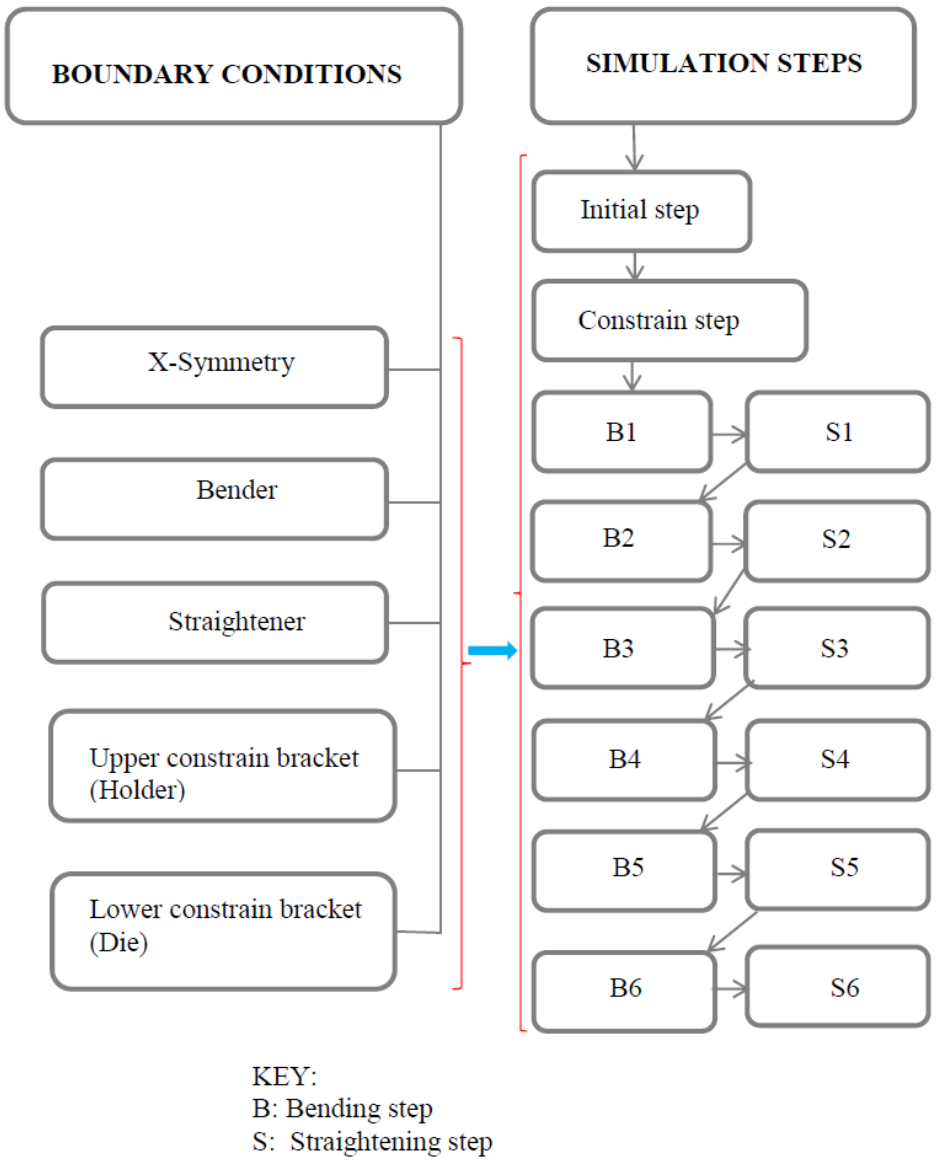

Figure 3.24: List of the CBS model boundary conditions and simulation steps

A total of five (5) boundary conditions were generated to describe the motions and the positions of the model parts in the executed steps. These are the sample's ends symmetric (X-sym), the bender, the straightener, the upper constrain bracket and the lower constrain bracket (die). A total of fourteen (14) steps were generated; and these are the initial step and constraining step. Other steps are the B1-B6 bending steps and the S1-S6 straightening steps.

The X-symmetrical boundary condition was defined as the sample was restricted from the translational motion along X-axis, the rotational motions about both Y and Z-axes. In a constraining step, a force of 500 N was applied on each side of the upper constrain bracket to hold the sample. This was followed by the bending step, in which the bender was given a downward displacement of -2 mm.

In each of the straightening step, the upper constrain bracket was fixed from all rotational and translational motion; and the straightener was given an upward displacement of 2 mm. The lower constraining bracket (die) was fixed from translational and rotational motion in all bending-straightening steps. The simulated magnitude and distribution of the effective plastic (EP) strain for the 1^{st}, 2^{nd}, 4^{th} and 6^{th} CBS bending-straightened cycles over the 22 mm length are presented in Figure 4.12-Figure 4.16 in Chapter 4.

The Nodal EP strain values for the 2nd, 4th and 6th cycles were extracted. The nodal mean EP strain values per cycle number (ε_{pci}) were determined, as the sum of the nodal EP strain values from bottom row vertically to top row divided by the total number of nodes in the rows (nr). Six (6) nodes were counted on six (6) rows, from the bottom row to the top row. Each set of cycle values was propagated on the 100 mm sample length at 12 mm, 6 mm and 4 mm feeds, in order to give the EP strain at N2F12, N4F12, N6F12, N2F6, N4F6, N6F6, N2F4, N4F4 and N6F4. After propagation, the EP strain values were superposed to give the resultant EP strain values per pass (ε_{pNj}) for the total model length of 100 mm. The cycle strains (ε_{pci}) propagation and superposition on the sample at the feed length F, are represented by a schematic diagram in Figure 3.25.

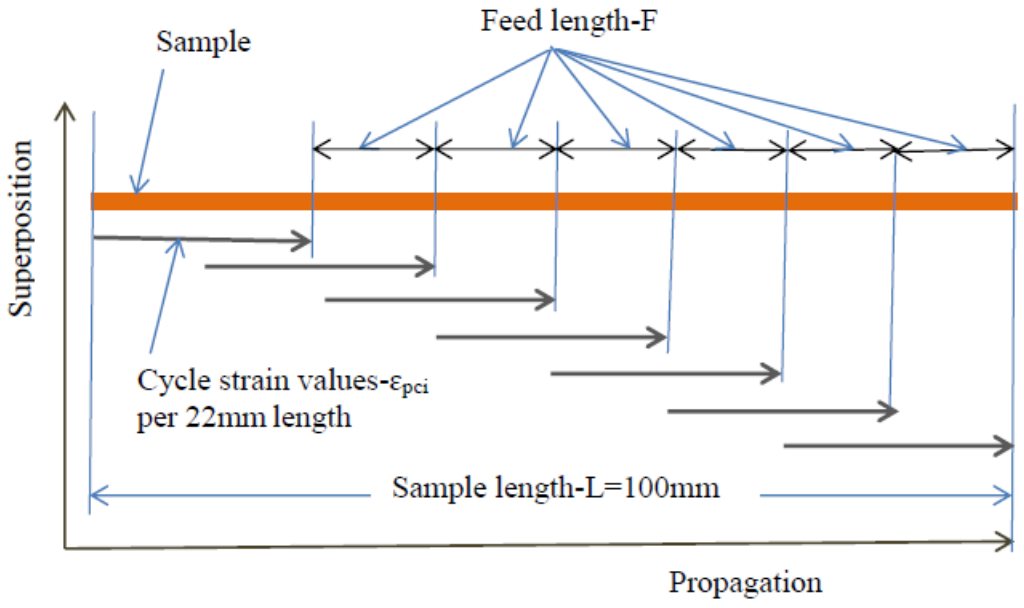

Figure 3.25: A schematic diagram for EP strain propagation and superposition

The EP strain homogeneity was defined by the coefficient of EP strain variation (CV), in which the lower the CV value, the higher is the homogeneity of the induced strain. The CV was determined by using Equation 3.23 as:

$$CV = \frac{S}{\varepsilon_m} x100\% \qquad 3.23$$

S = the standard deviation of the EP strain defined by Equation 3.24 as:

$$S = \sqrt{\frac{\sum_{j=1}^{n}\left(\varepsilon_{pNj}-\varepsilon_m\right)^2}{n-1}} \qquad 3.24$$

$$\varepsilon_m = \frac{\sum_{j=1}^{n} \varepsilon_{pNj}}{n} \qquad 3.25$$

ε_m and n are the mean EP strain per N^{th} pass and the total number of strain values per N^{th} pass on the specified sample length, respectively.

In the plastic deformation of a material, the flow stress is the instantaneous value of the plastic stress required to keep the material flowing. The flow stress is approximated to the true tensile yield strength of the material, as a function of the plastic strain during the strain hardening-strengthening processes.The true yield stress was estimated; as the flow stress determined by the Holloman's Power Law Equation 2.7 , here recalled as Equation 3.26:

$$SY = S_o \varepsilon_p^n \quad 3.26$$

ε_p = ε_m true effective/equivalent plastic (EP) strain induced in material, S_o = material property known as the strength coefficient; and n = the strain hardening exponent. Various researchers have reported on the investigation of the strength coefficient S_o and the strain hardening exponent n values for the Ti6Al4V alloy. For instance, Rajendran et al. [20] developed a model based on the Ramberg and Osgood flow rule model [119] on the strength coefficients of isobaric metallic materials. Gupta et al. [18] developed a model on the strain hardening properties of Ti6Al4V alloy sheets under prior heat treatment and cold working. Based on these models, the values for the strength coefficient S_o and the strain hardening exponent n for the Ti6Al4V alloy, were selected as S_o=1200 MPa and n = 0.045. The hardness of the material was estimated and determined by Equation 3.27 [120] as:

$$HV = \frac{SY}{2.8} = \frac{S_o}{2.8} \varepsilon_p^n \quad 3.27$$

The simulated results for the magnitudes and homogeneity of induced EP strain, hardness and yield strength of material at N2F12, N4F12, N6F12, N2F6, N4F6, N6F6, N2F4, N4F4 and N6F4 are presented and will be discussed in Chapter 4. The numerical model results were validated by a comparison between the simulated tensile yield strength and

the hardness values with experimental true tensile yield stress and hardness counter-parts, as will be discussed in Chapter 4.

3.8 Summary

This methodology chapter has covered the methods and procedures required to achieve the study objectives. It has all the details on material selection, design and the fabrication of the CBS tool. The specific procedures and equipment needed for: the material samples' processing with CBS, the samples microstructural analysis, the tensile and the hardness tests were explained. The chapter also includes the steps of a numerical model's development and simulation. The results for the microstructural analysis, the tensile values, the hardness tests and the numerical modelling will be presented and discussed in Chapter 4.

CHAPTER FOUR: RESULTS AND DISCUSSION

4.1 Introduction

This chapter covers a detailed discussion of the results from various tests carried out in the study. The results from the microstructural analysis, the hardness test, the tensile test and the numerical model simulation are presented in various forms; and they will be discussed in depth. Each category of results was covered in its separate sub-chapter.

4.2 Microstructural analysis

In this section, the results for the microstructural characteristics of the samples processed by the CBS method at selected pass-feed (NF) are presented. The microstructural properties of the samples were studied on the longitudinal (RN) and the top (RT) planes. Where R, N and T are the rolling, normal and transverse directional axes, respectively. Microstructural characterization was done, where the samples' grain structural, morphology and size were studied with an Optical Microscope (OPM) and a Scanning Electron Microscope (SEM). The grain size was measured by taking the average size for the grains considered across the microstructural image. The AR and the processed samples' elemental detection and composition were analyzed by using the Electron Diffraction Spectrometer (EDS). An X-Ray Diffraction Spectrometer (XRD) was used to analyze the evolution of: the material phases and their compositions, the crystallite size and the lattice strain versus the CBS processed pass-feed (NF).

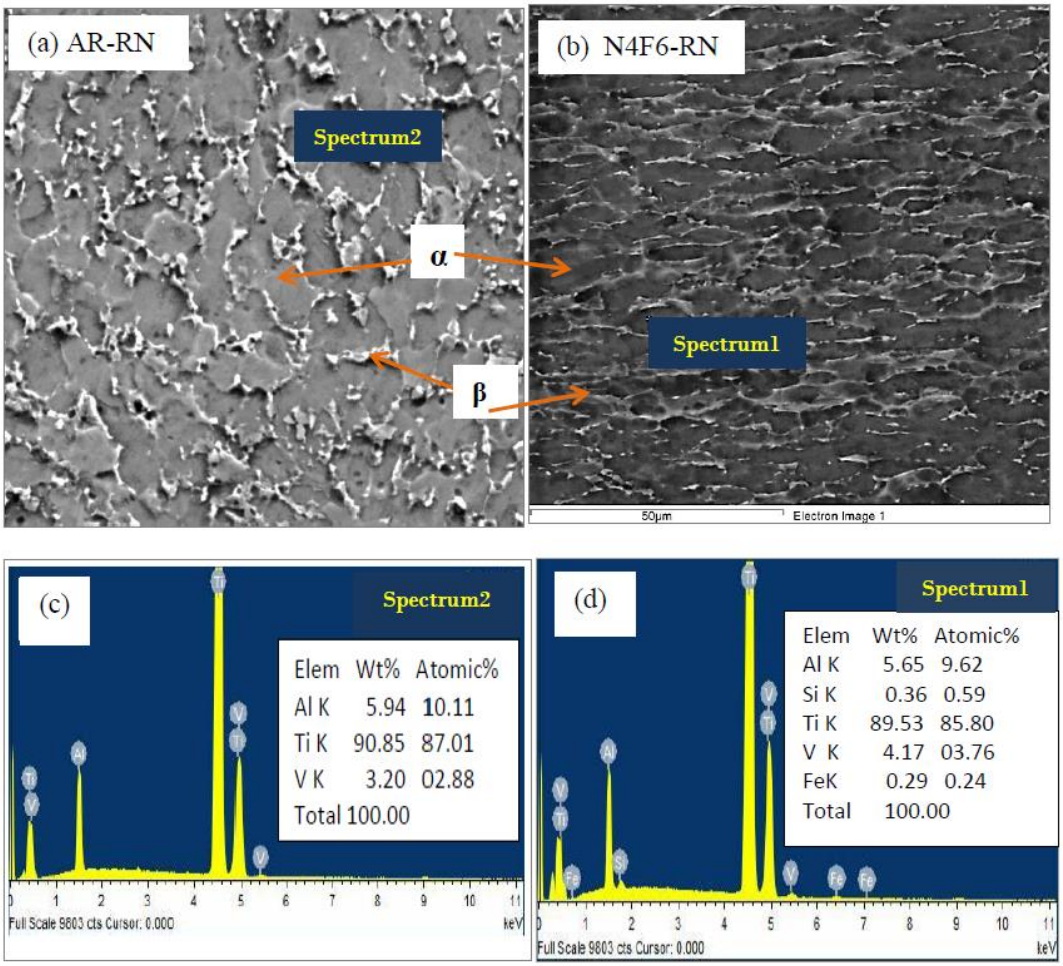

Figure 4.1: (a) SEM image of AR sample (b) SEM image of sample processed at N4F6(c) EDS elemental composition of AR sample (d) elemental composition of sample processed at N4F6

The SEM images and the EDS elemental compositions for the AR samples and the N4F6 processed samples, respectively, are presented in Figure 4.1(a) - (d). The results in Figure 4.1(a) and (c) showed that the AR samples consisted of titanium with both alpha and beta phases. The EDS spectrum showed that the samples had titanium (Ti) as a major constituent element, together with aluminum (Al) and vanadium (V) as the major

alloying elements. Elemental mapping from one of the AR samples is shown in Figure 4.2. The elemental mapping showed the distribution of Ti, Al and V as the major elements in the Ti6Al4V alloy used in this study.

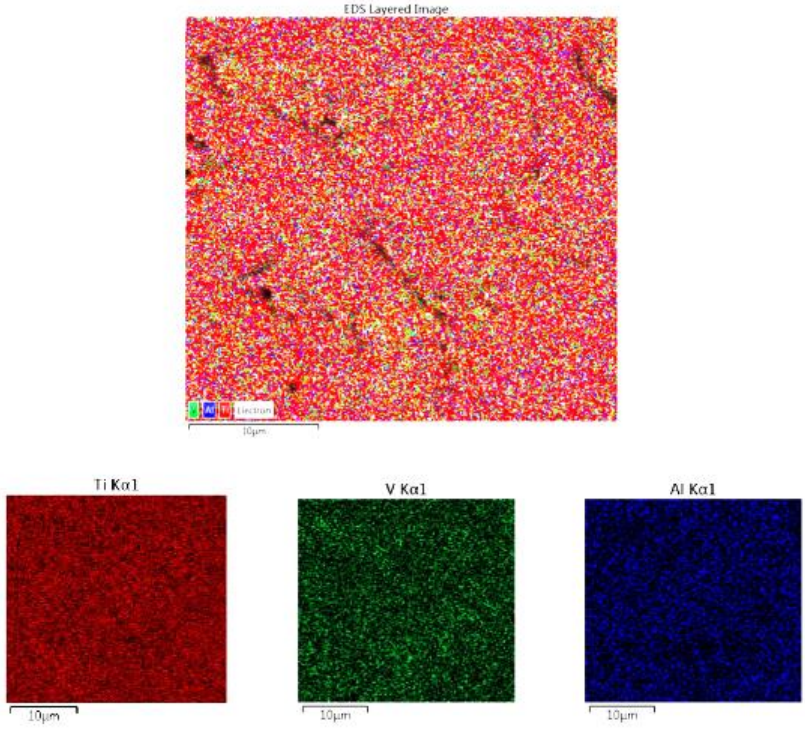

Figure 4.2: EDS elemental mapping for the AR sample

The results for the sample processed at N4F6, together with the elemental composition shown in Figure 4.1(b) and (d) respectively, showed that as the samples were processed with the CBS method, they underwent a significant evolution of their microstructural properties and material phases. The evolution of the microstructure and the phases, together with the number of pass-feeds will be discussed in the forthcoming sections.

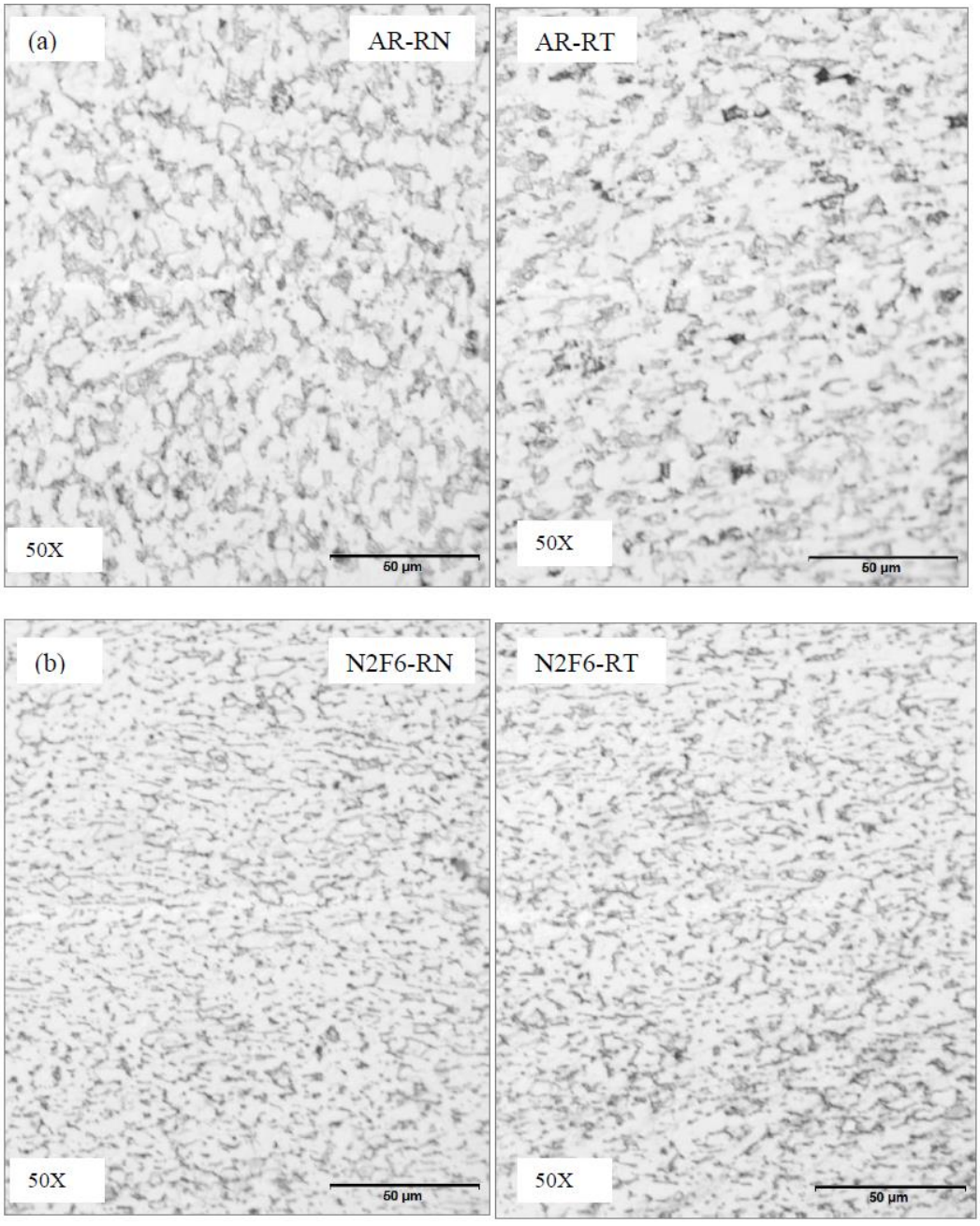
(a)
AR-RN
50X
60 µm
AR-RT
50X
60 µm
(b)
N2F6-RN
50X
60 µm
N2F6-RT
50X
50 µm

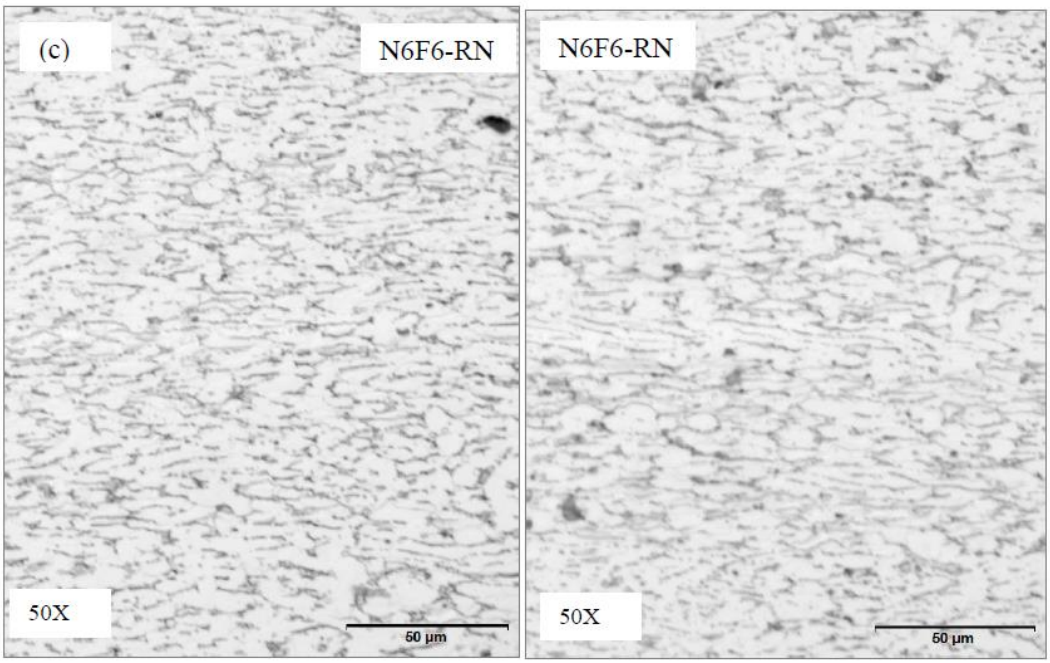

Figure 4.3: OPM images of the samples (a) AR (b) processed at N2F6 (c) processed at N6F6

Selected OPM and SEM microstructural images for the AR samples and for the samples processed at the N2 and N6 passes are presented in Figure 4.3 - Figure 4.6. A complete list of the OPM and the SEM microstructural images for the AR samples and the samples processed at N2F6, N4F6, N6F6, N2F12, N4F12 and N6F12 is given in Appendix B. SEM and OPM images showed that their microstructure on RN and RT planes for the AR samples and samples processed at the same pass-feed (NF); and they had a close similarity of particle/grain size and structure. A comparison made between the microstructural OPM and SEM images of the same sample showed a direct correlation on grain structure and refinement versus the number of pass (N) and feed (F) values.

The SEM images in Figure 4.5 (a) for the microstructure of the AR sample show that initially, the sample had alpha and beta titanium phases, shown with grey and white colours respectively. The alpha particles had a homogeneous equiaxed structure with an average size of 10.5µm. The intergranular beta particles had an average length and thickness of 10µm and 4µm, respectively. Initially, both the alpha and the beta particles showed a distribution with random orientations. The SEM images for the microstructure of the samples processed at N2F6 and N6F6 in Figure 4.5 (b) and (c), respectively showed that both the alpha and the beta grain sizes reduced with the number of passes, N relative to those of the AR samples.

The results showed that the samples processed at N6F6 had more homogeneous grain distribution than the samples processed at N2F6. At N6F6, the alpha phase particles had transformed to elongated (columnar) structure with sub-particles of an average thickness of 3µm. The intergranular beta phase transformed to smaller sized particles, with an average thickness of 1.5µm and a length of 5µm. The reduction of alpha and beta particles was an evidence for the grain refinement that could enhance the improvement in the material hardness and the tensile strength.

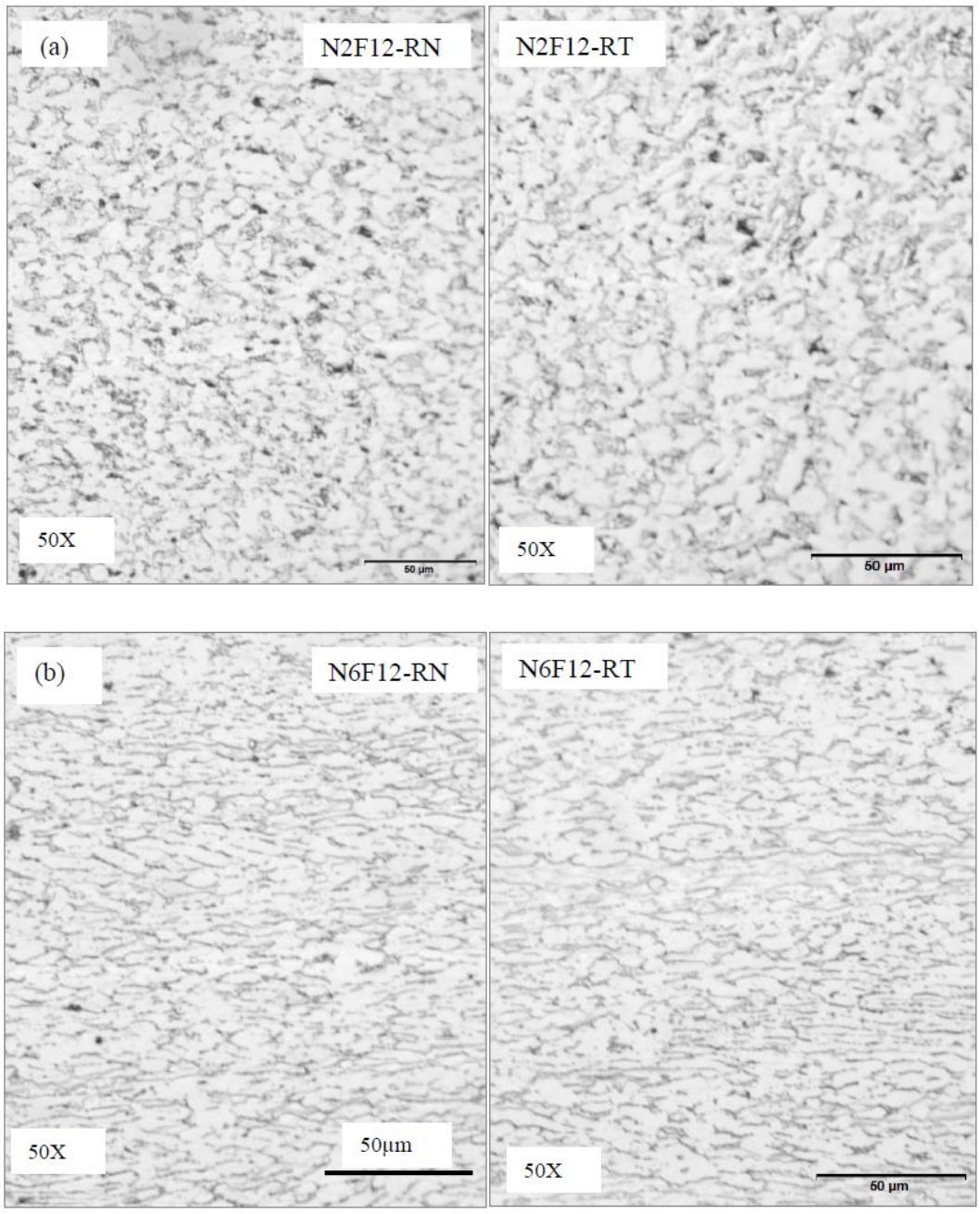

Figure 4.4: OPM images of the samples processed at (a) N2F12 (b) N6F12

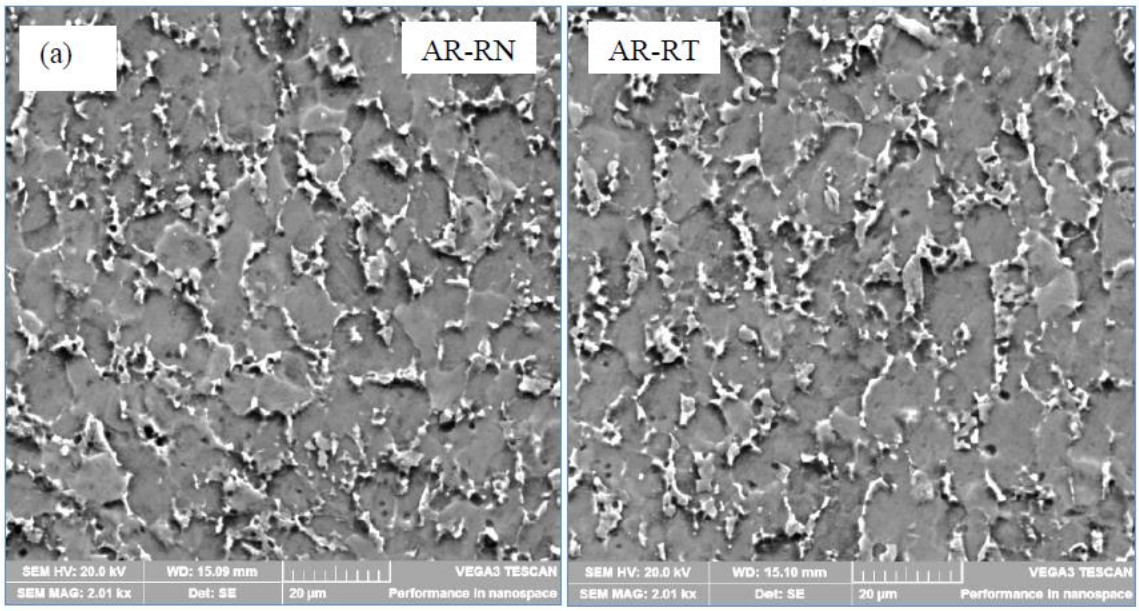
(a)
AR-RN
SEM HV: 20.0 kV
WD: 15.09 mm
VEGA3 TESCAN
SEM MAG: 2.01 kx
Det: SE
20 µm
Performance In nanospace
AR-RT
SEM HV: 20.0 kV
WD: 15.10 mm
VEGA3 TESCAN
SEM MAG: 2.01 kx
Det: SE
20 µm
Performance In nanospace

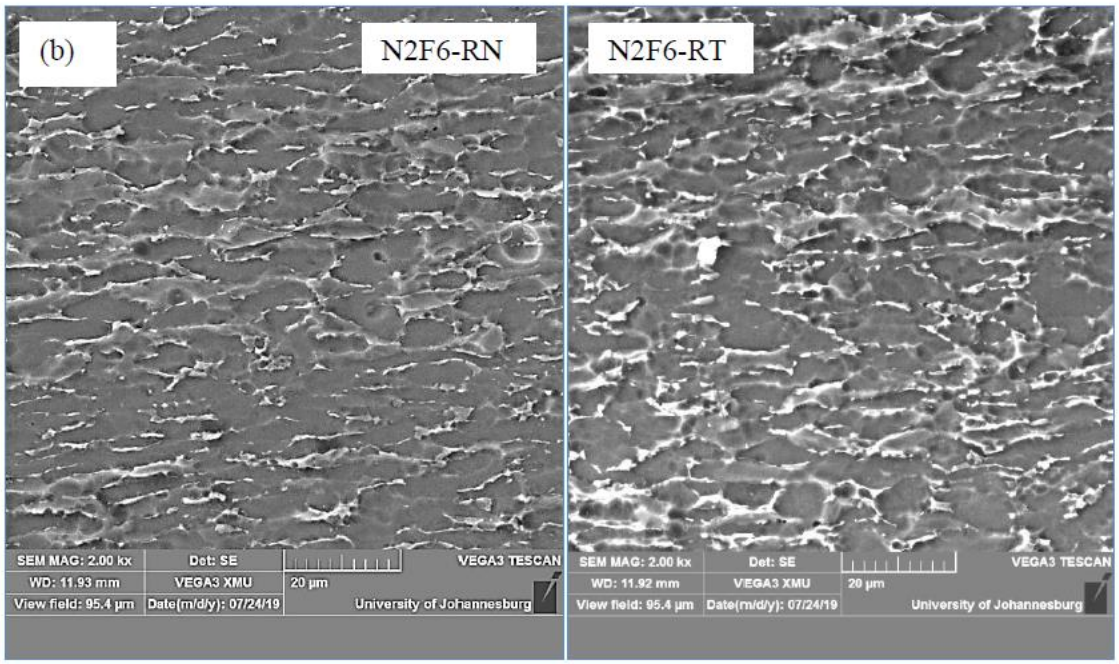
(b)
N2F6-RN
SEM MAG: 2.00 kx
Det: SE
VEGA3 TESCAN
WD: 11.93 mm
VEGA3 XMU
20 µm
View field: 95.4 µm
Date(m/d/y): 07/24/19
University of Johannesburg
N2F6-RT
SEM MAG: 2.00 kx
Det: SE
VEGA3 TESCAN
WD: 11.92 mm
VEGA3 XMU
20 µm
View field: 95.4 µm
Date(m/d/y): 07/24/19
University of Johannesburg

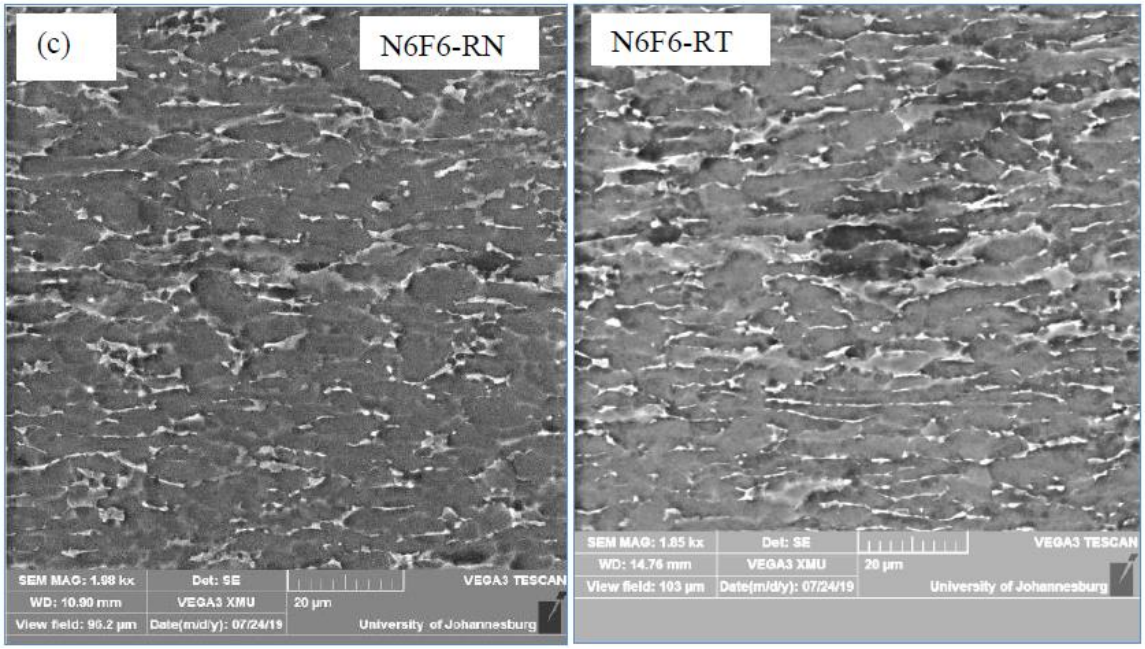

Figure 4.5: SEM images of the samples (a) AR (b) processed at N2F6 (c) processed at N6F6

The SEM images of the microstructure for the samples processed at N2F12 and N6F12 are presented in Figure 4.6 (a) and (b), respectively. The increase in the pass number from N2 to N6, resulted in the reduction of both alpha and beta particles sizes, as compared with those of the AR samples. Those samples processed at N6F12 exhibited more homogeneous grain distribution than the samples processed at N2F12. At N6F12, the alpha phase particles were characterized with an elongated structure, with an average thickness of 5µm. The intergranular beta phase transformed to a smaller size and elongated particles, with an average thickness of 1µm and a length of 7µm.

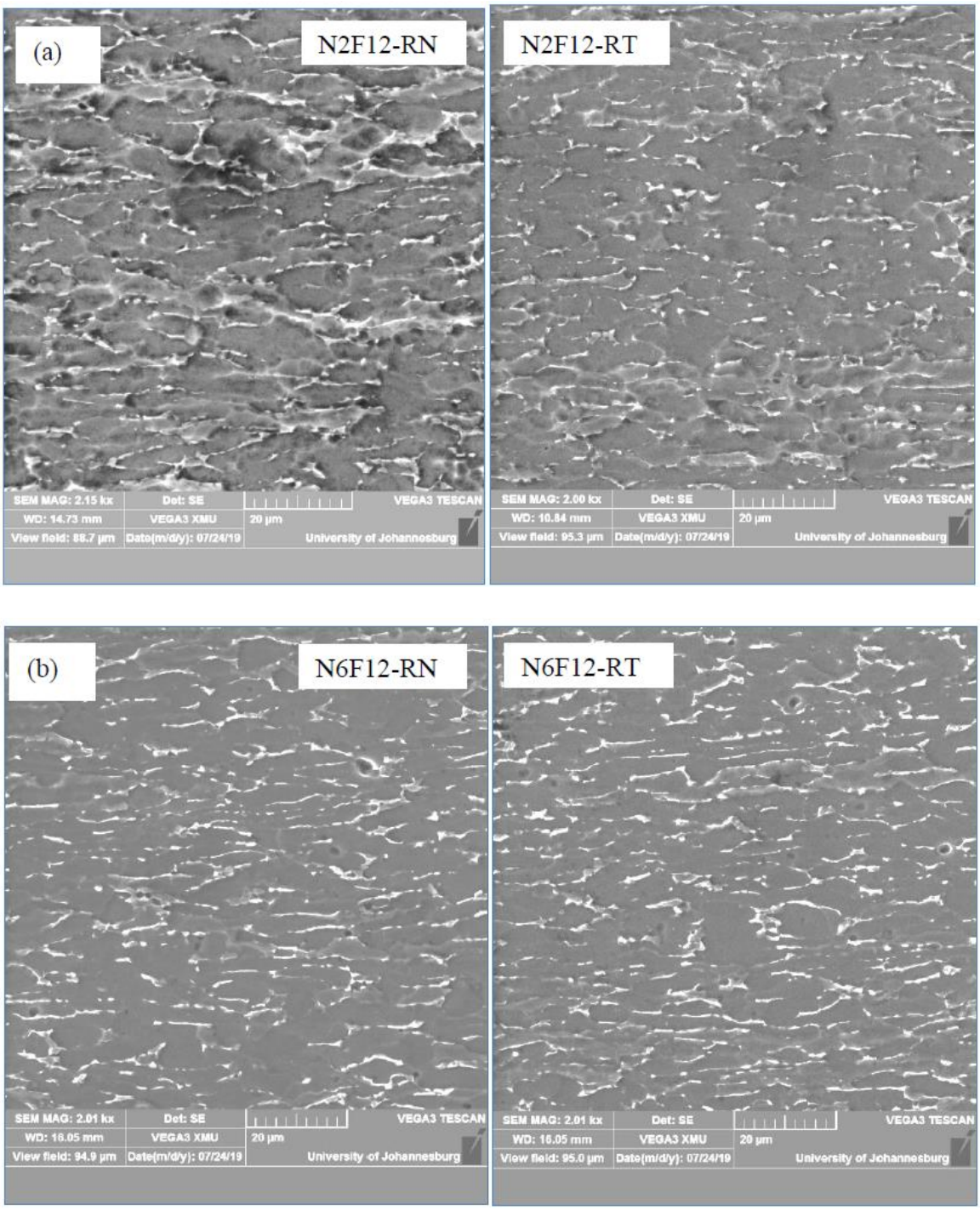

Figure 4.6: SEM images of the samples processed at (a) N2F12 (b) N6F12

The reduction of the alpha and the beta particles' sizes indicated that the CBS process had enhanced the material microstructural grain refinement attributed to the dislocations and the plastic strains induced in the processed samples. The grain refinement and the dislocations entanglement had made a potential contribution to the improvement of the material hardness and to the tensile strength.

Samples processed at F6 feed (N2F6, N4F6, N6F6) and those processed at F12 feed (N2F12, N4F12, N6F12) showed a relatively lower microstructural homogeneity compared with that of the AR samples. However, the samples processed at F6 feed showed a better microstructural homogeneity and grain refinement than those processed at F12 feed. The reason could be, at F6 feed, a greater number of overlapped bending curves with more plastic strain were induced in the material compared with the samples processed at F12 feed.

Selected data for the XRD spectra intensities versus the diffraction angles were determined. The data for the AR samples and the samples processed by the CBS at N6F6 and N6F12 were extracted, plotted and presented in Figure 4.7 (a)-(c), respectively. The AR samples had higher intensities and narrower peaks than those of the samples processed at N6F6 and N6F12.

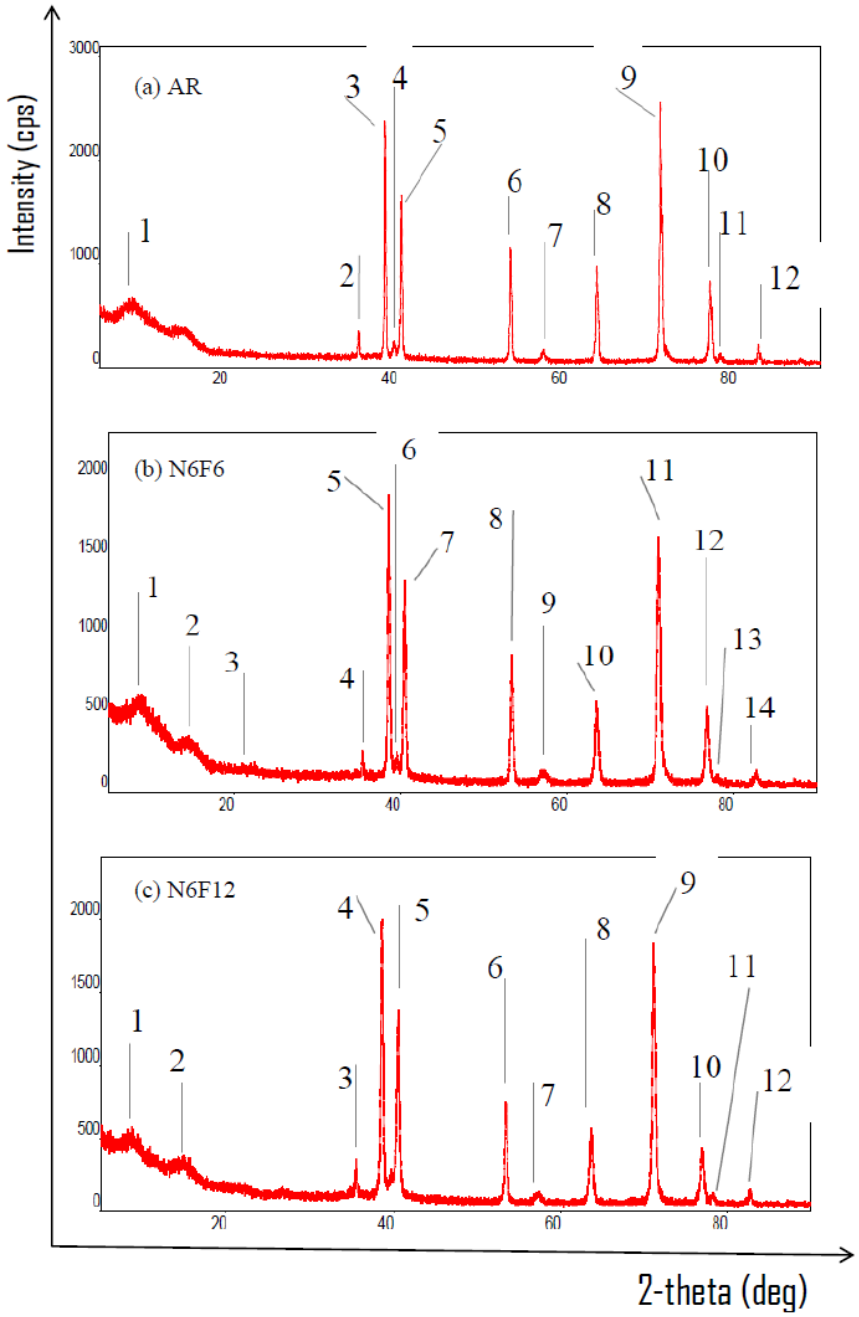

Figure 4.7: XRD spectra intensities versus diffraction angles (a) AR samples (b) samples processed at N6F6 (c) samples processed at N6F12

The samples processed at N6F6 and N6F12 had broader and shorter spectra peaks, as compared with those of the AR samples. The samples processed at the N6F6 had the shortest and broadest peaks, followed by those of the samples processed at N6F12. The widening and shortening of the spectra peaks could have been due to dislocations, plastic strains induced in the material by the CBS process and the microstructural grain refinement[115][121]. The number assigned to each of the diffraction peaks in Figure 4.7 represents the Ti6Al4V alloy, detected material phases. The details of the material phases for the AR samples, the samples processed at N6F6 and N6F12 are fed in Table 4.1-Table 4.3 respectively.

Table 4.1: Phases detected in the AR samples

No	Phases detected for AR samples
1	Unknown
2	alpha-Ti(1,0,0),alpha-Al2.1 Ti2.9(1,0,0)
3	alpha-Ti(0,0,2),alpha-Al2.1 Ti2.9(0,0,2)
4	omega-Ti0.84 V0.16(1,0,1),beta-Ti(1,1,0),Aluminum Vanadium(1,1,2)
5	alpha-Ti(1,0,1),alpha-Al2.1 Ti2.9(1,0,1)
6	alpha-Ti(1,0,2),alpha-Al2.1 Ti2.9(1,0,2)
7	omega-Ti0.84 V0.16(2,0,1),beta-Ti(2,0,0)
8	alpha-Ti(1,1,0),alpha-Al2.1 Ti2.9(1,1,0),Aluminum Vanadium(2,1,3)
9	alpha-Ti(1,0,3),omega-Ti0.84 V0.16(2,1,1),alpha-Al2.1 Ti2.9(1,0,3)
10	alpha-Ti(1,1,2),alpha-Al2.1 Ti2.9(1,1,2),Aluminum Vanadium(1,1,6)
11	alpha-Ti(2,0,1),alpha-Al2.1 Ti2.9(2,0,1)
12	alpha-Ti(0,0,4),alpha-Al2.1 Ti2.9(0,0,4)

The results showed that the main phases evolved were alpha-titanium, alpha-aluminum titanium, omega-vanadium titanium, aluminium iron titanium, and aluminum vanadium

and beta titanium. The percentage composition of each phase slightly varied with the number of performed CBS pass-feeds (NF), as shown in Table 4.4. The percentage of the alpha phase increased from that of the AR samples, 72.78% to 88.18% and 88.52% for samples processed at N6F6 and N6F12, respectively. The percentage of the beta phase decreased from that of the AR samples, 7.18% to 0.4% and 4.9% for those samples processed at N6F6 and N6F12, respectively.

Table 4.2: Phases detected in the samples processed at N6F6

No	Phases detected for N6F6 samples
1	Unknown
2	Unknown
3	Aluminum Iron Titanium(1,0,0),Aluminum Titanium(0,0,2)
4	Titanium, syn(1,0,0),omega-Ti8.86 V1.14(1,0,0)
5	Titanium, syn(0,0,2),omega-Ti8.86 V1.14(0,0,2)
6	Aluminum Titanium(1,1,2),beta-Ti(1,1,0)
7	Titanium, syn(1,0,1),omega-Ti8.86 V1.14(1,0,1),Aluminum Iron Titanium(1,1,1)
8	Titanium, syn(1,0,2),omega-Ti8.86 V1.14(1,0,2)
9	beta-Ti(2,0,0)
10	Titanium, syn(1,1,0),omega-Ti8.86 V1.14(1,1,0),Aluminum Titanium(2,1,3)
11	Titanium, syn(1,0,3),omega-Ti8.86 V1.14(1,0,3)
12	Titanium, syn(1,1,2),omega-Ti8.86 V1.14(1,1,2)
13	Titanium, syn(2,0,1),omega-Ti8.86 V1.14(2,0,1),Aluminum Iron Titanium(3,1,0)
14	Titanium, syn(0,0,4),omega-Ti8.86 V1.14(0,0,4),Aluminum Iron Titanium(3,1,1),Aluminum Titanium(3,1,2)

Table 4.3: Phases detected in the samples processed at N6F12

No	Phases detected for N6F12 samples
1	Unknown
2	Aluminum Titanium(2,0,0)
3	Titanium, syn(1,0,0),Titanium Vanadium(1,0,0)
4	Titanium, syn(0,0,2),Titanium Vanadium(0,0,2),beta-Ti(1,1,0),Aluminum Titanium(3,1,1)
5	Titanium, syn(1,0,1),Titanium Vanadium(1,0,1),Aluminum Iron Titanium(1,1,1)
6	Titanium, syn(1,0,2),Titanium Vanadium(1,0,2),Aluminum Titanium(2,2,1)
7	Aluminum Titanium(7,1,0)
8	Titanium, syn(1,1,0),Titanium Vanadium(1,1,0),Aluminum Titanium(5,1,2)
9	Titanium, syn(1,0,3),Titanium Vanadium(1,0,3)
10	Titanium, syn(1,1,2),Titanium Vanadium(1,1,2),Aluminum Titanium(4,0,3)
11	Titanium, syn(2,0,1),Aluminum Iron Titanium(3,1,0),Aluminum Titanium(3,1,3)
12	Titanium, syn(0,0,4),Titanium Vanadium(0,0,4),beta-Ti(2,2,0),Aluminum Iron Titanium(3,1,1),Aluminum Titanium(6,2,2)

Table 4.4: Phase percentage versus the CBS pass-feed (NF)

Phase name	AR	N6F6	N6F12
Alpha titanium	72.78	88.18	88.52
Omega-vanadium titanium (TiV)	6.56	1.25	0.44
Aluminum iron titanium (Al-Fe-Ti)	0.97	5.08	2.30
Alpha-aluminum titanium (TiAl)	12.49	5.08	3.84
Beta titanium	7.18	0.4	4.9
Aluminum vanadium	0.9	0	0
Unknown	0	0	0
Total	100.9	99.99	100

Table 4.5: Mean crystallite size and lattice strain for alpha and beta Ti versus the CBS pass-feed

Sample	**Mean crystallite size (nm)**		**Lattice strain (%)**	
	Alpha-Ti	Beta-Ti	Alpha-Ti	Beta-Ti
AR	47.43	13.6	0.12	0.2
N6F6	22.2	10.6	0.24	0.26
N6F12	24.51	26.8	0.13	0.22

The crystallite mean size and the lattice strain versus the pass-feed (NF) for the alpha-phase and the beta-phase titanium were determined and presented in Table 4.5. The crystallite size (nm) of both the alpha and the beta titanium decreased from those of the AR samples, 47.43 and 13.6 to 22.2 and 10.6 at N6F6 respectively. Their mean sizes (nm) at N6F12 were respectively 24.51 and 26.8. Their lattice strain (%) increased from those of the AR samples, 0.12 and 0.2 to 0.24 and 0.26 at N6F6, respectively. The lattice strains (%) for alpha and beta titanium at N6F12 were respectively 0.13 and 0.22.

The results showed that the samples processed at N6F6 had a higher crystallite mean size and lattice strain than those of the samples processed at N6F12. The decrease of the crystallite mean size and the increase of the lattice strain relative to that of the AR samples was due to the dislocations and the strains induced in the samples by the CBS. The decrease of the crystallite mean size and the increase in the lattice strain could have enhanced both the grain refinement and the dislocation strengthening mechanisms that

resulted in the increase of the material hardness and the tensile strength [33][113] [115].

To conclude this subchapter on microstructural analysis, initially Ti6Al4V AR samples had equiaxed alpha and intergranular beta phase particles. The alpha particles had an average size of 10.5µm. The beta particles had an average length and thickness of 10µm and 4µm, respectively. The CBS processed samples at N6F6 had elongated alpha particles, with an average size of 3µm. The intergranular beta particles transformed to an elongated structure with an average length and thickness of 5µm and 1.5µm, respectively. The microstructure of the samples processed at N6F12 consisted of alpha particles with an average size of 5µm and beta particles with an average size of 1µm.

Samples processed at N6F6 had better microstructural homogeneity, higher gain size reduction and lattice strain than those of the samples processed at N6F12. The reduced alpha and beta particle sizes implied grain refinement due to dislocations and strains induced in the CBS processed samples. The microstructural grain refinement and the induced dislocations were a potential to improve the material hardness and the tensile strength by both the grain refinement and the dislocation strengthening mechanisms.

4.3 Hardness profiling

The results for the hardness tests of Ti6Al4V alloy sheet samples processed with CBS at N2F6, N4F6, N6F6, N2F12, N4F12 and N6F12 are presented and discussed in this sub-chapter. The hardness properties were investigated on two planes of the samples; as it was described in Figure 3.20. The investigated planes were the RN longitudinal (RN) and the top (RT) planes. The hardness measured values can be found in Appendix C2. The average hardness properties (HV) versus the pass-feed (NF) are presented in Figure 4.8 (a). The results for the hardness distribution versus the sample length for each pass-feed (NF) are shown in Figure 4.8 (b). The results in Figure 4.8 (a) showed that the average hardness values of CBS processed samples were higher than those of the AR samples; and the hardness increased with the number of passes performed.

For all passes and feeds performed, the average hardness values on samples' RT planes were slightly higher than those on the RN planes. The slight difference of the average hardness could have been attributed to the RT plane being in close contact with the dies; hence, suffered with higher contact stress and strain compared with the RN plane. The results showed that for all the N2, N4, N6 passes performed, the average hardness of the samples processed at F6 feed were higher than those of the samples processed at F12 feed.

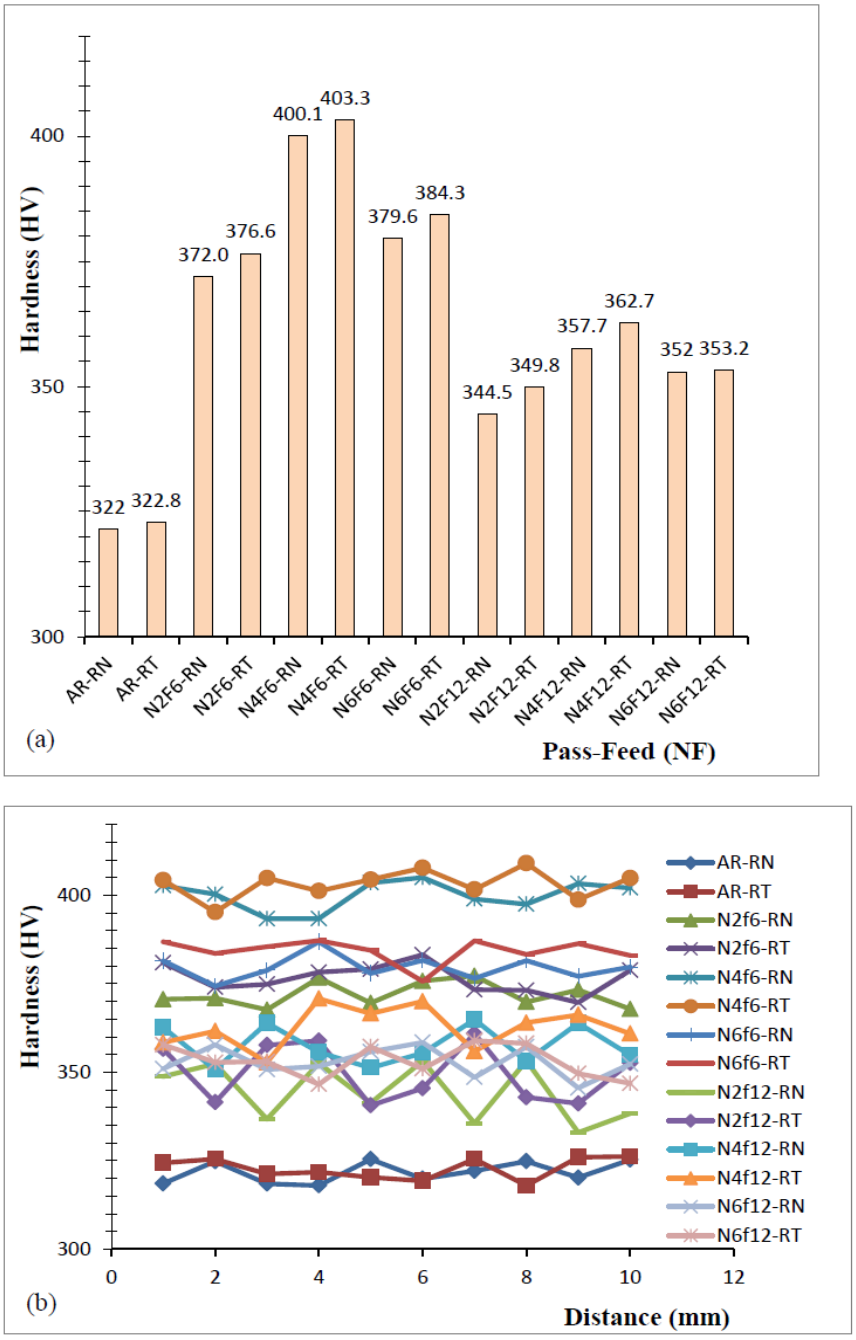

Figure 4.8: Hardness test results (a) average harness (HV) versus pass-feed (NF) (b) hardness distribution versus the sample length for each pass-feed (NF)

This could have been attributed to a higher number of bending curves with the higher EP strain and hardness values induced in the samples processed at F6 feed compared with those of the samples processed at the F12 feed.

The average hardness values (HV) for the samples processed at the F6 feed on the (RN, RT) planes, respectively were: N2 (372, 377), N4 (400.1, 403.3) and N6 (379.6, 384.3). The average hardness values (HV) for those samples processed at the F12 feed on (RN, RT) planes, respectively were: N2 (344.5, 349.8), N4 (357.7, 362.7) and N6 (352.6, 353.2). The maximum increase in the average hardness (HV) was from those of the AR samples (322, 322.8) to those of the processed samples at N4F6 (400.1, 403.3). The increase was about 24.4%. The increase in the hardness was a result of the dislocations movement acting as a hair doer, specializing in the impediment during the plastic deformation of the material by the CBS process.

The strengthening mechanism was mainly strain hardening due to dislocations interaction [27][29]. Considering both F6 and F12 feeds, results showed that the average hardness values of the AR samples increased significantly to those of the samples processed up to N4 pass, afterwards, the average hardness values of the samples processed at N6 pass were relatively lower than those of the samples processed at the N4 pass. The reason for this drop of hardness could have been caused by the saturation of the material strain

hardening at the N4 pass, due to the high rate of dislocations annihilation, followed by the initiation of the material excessive yielding at the N6 pass. The hardening limit of titanium and other alloys processed by RCS related SPD processes has been reported widely in the literature [6] [7] [94] [97].

Strengthening of the material with SPD involves increasing the dislocations accompanied by accumulated plastic strains in the material. There is an optimal number of dislocations in the material that could enhance the maximum strengthening. A lower or higher number of dislocations than the optimal number results in the material softening [29][34][36][49].

The results for the hardness distribution versus the sample length are shown in Figure 4.8 (b). The hardness distribution showed that the CBS processed samples exhibited no metallurgical notch; the relative standard variation of the hardness values for each of the CBS processed samples was below 10%. The samples showed fairly even hardness profile which can be attributed to the hardness homogeneity enhanced in the samples by the CBS process. However, the values of the feed length and the number of pass were influential to the hardness homogeneity as will be discussed in the next paragraphs.

The AR samples had smooth hardness distribution curves on both the RN and the RT planes; therefore, the AR samples exhibited better homogenous hardness properties than

did the processed ones. The CBS processed samples were characterized by wavy hardness distribution curves, which implied the presence of hardness in-homogeneity. However, the hardness homogeneity slightly improved with the number of processed passes; and the hardness homogeneity of the samples processed at N6 was relatively higher than those of the samples processed at N4 and N2, respectively. The feed length F was shown to have a significant impact on the hardness magnitude and homogeneity.

The samples processed at the F6 feed showed relatively smoother hardness distribution curves, with better homogeneity than the samples processed at the F12 feed. The samples processed at the F6 feed could induce a higher number of overlapping bending curves in the material, which resulted in higher strain and hardness homogeneity than those of the samples processed at the F12 feed.

A comparison was made between the hardness induced in Ti6Al4V by the CBS at the 6 mm feed (4 pass, 322 - 400.1 HV) with that due to: the HPT by Valiev and Smirnov [41] (10 pass, 300 - 450 HV) and Cold work at 5% compression step by Kulkarni et al. [122] (5 pass, 336-375 HV).

To summarize the hardness results, Ti6Al4V alloy sheets samples were processed with the CBS technique at N2, N4, N6 passes each combined with F6, F12 feeds. The samples hardness properties (HV) versus the pass-feed (NF) were investigated on the longitudinal

(RN) and the top (RT) planes. The results showed that the micro hardness of the CBS processed samples improved significantly compared with that of the AR samples. For all the passes and feeds performed, the average hardness values on samples' RT planes were slightly higher than those on the RN planes. The average hardness (HV) of the material increased with the number of passes performed at N2, N4, N6. The average hardness values (HV) of material samples processed at F6 feed were higher than those of the samples processed at the F12 feed. The CBS process at F6 feed introduced more bending curves with more hardness in the material, when compared with the samples processed at the F12 feed.

The maximum increase of average hardness (HV) of 24.4% was achieved at N4F6 pass-feed. The increase of hardness was a result of the dislocations interaction and the impediment-strengthening mechanism. The average hardness values of the samples processed at N6 pass were relatively lower than those processed at the N4 pass at both the F6 and the F12 feeds. The reason for the drop in hardness after the N4 pass could be due to the material hardening saturation at N4 pass caused by the dislocation annihilation and the onset of material yielding at N6 pass. The hardness homogeneity of the CBS processed samples was highly dependent on the feed length; and it slightly improved with the number of passes N2, N4, N6 performed. The hardness homogeneity of the samples processed at the F6 feed was higher than that of the samples processed at the F12 feed.

4.4 Tensile behaviour

Ti6Al4V alloy sheet samples processed with CBS at N2F6, N4F6, N6F6, N2F12, N4F12 and N6F12 pass-feed were subjected to tensile loads to fracture. The tensile test was performed to investigate the following parameters: tensile strength *ST*, yield strength *SY*, fracture stress SF, percentage elongation eP and the fracture elongation eF. Samples' average tensile test results were plotted and their respective engineering stress-strain curves are presented in Figure 4.9.

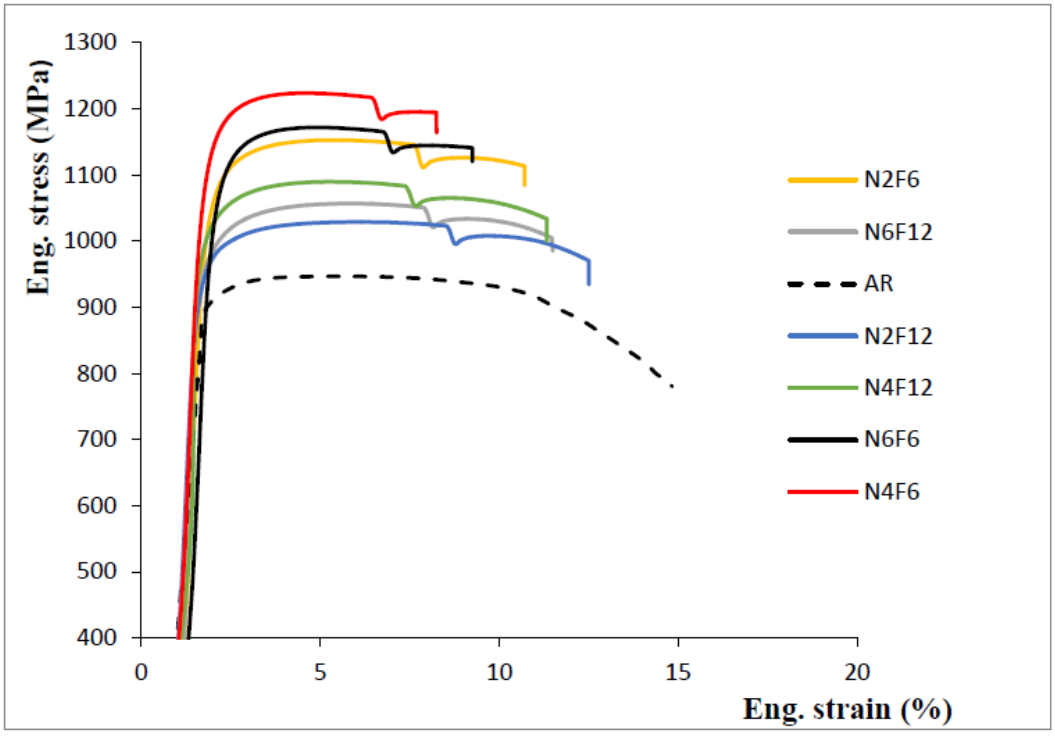

Figure 4.9: Engineering stress-strain curves for the samples' average tensile results

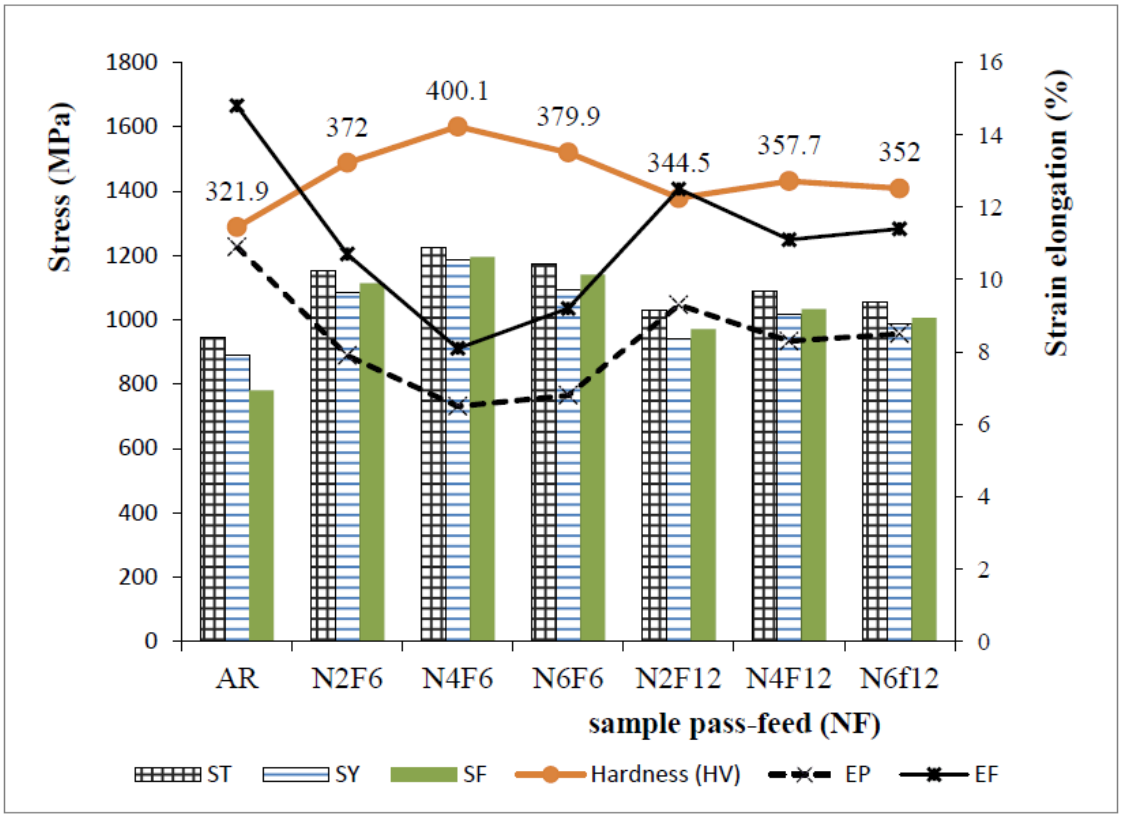

Figure 4.10: Tensile strength (ST) yield strength (SY), hardness (HV), percentage elongation (eP) and fracture elongation (eF) versus pass-feed (NF)

The average values for the tensile strength (*ST*), the yield strength (*SY*), the hardness, percentage elongation (*eP*) and the fracture elongation (*eF*) versus the pass-feed (NF) were determined from the strass-strain curves, summarized and plotted in Figure 4.10. The tensile test results and stress-strain curves for the samples at various pass-feed (NF) can be found in Appendix C1 and C3 respectively. The experimental hardness results were added to Figure 4.10 to study a correlation of the results between the tensile

strength, the ductility and the micro hardness enhanced in the samples versus the performed number of the CBS passes-feeds (NF) values. The results for the tensile strength of the tested samples showed that the tensile strength, *ST* (MPa) of the samples processed at the F6 feed increased with the number of passes from the AR samples (946.9); to (1153) at N2F6, (1223.9) at N4F6 and (1172.5) at N6F6. In this case, the maximum increase of the tensile strength was 29.3% at N4F6The samples processed at F12 feed showed that the tensile strength, *ST* (MPa) increased with the number of passes from the AR samples (946.9); to (1028.6) at N2F12, (1090) at N4F12 and (1056.9) at N6F12. In this category, the highest increase of the tensile strength was 11.6% at N4F12.

The results for the yield strength, *SY* showed that the tensile yield strength, *SY* (MPa) of the samples processed at F6 feed also increased with the number of passes from the AR samples (890), to: (1085.7) at N2F6, (1188) at N4F6 and (1093.4) at N6F6. In this case, the maximum increase of the tensile yield strength was 33.5% at N4F6. The samples processed at the F12 feed showed that the tensile yield strength, *SY* (MPa) increased with the number of passes from the AR samples (890), to: (941.2) at N2F12, (1015) at N4F12 and (986) at N6F12. In this case, the highest increase of the tensile yield strength was 14% at N4F12.

The results for the tensile fracture stress *SF*, showed that the fracture stress (MPa) of the samples processed at F6 feed also increased with the number of passes from the AR samples (780), to: (1113.6) at N2F6, (1194.5) at N4F6 and (1141) at N6F6. The fracture stress *FS* (MPa) of the samples processed at F12 feed increased with the number of passes from the AR samples (780), to: (970.3) at N2F12, (1033.7) at N4F12 and (1005) at N6F12. The improved tensile strength of the CBS processed samples was achieved mainly by the strain hardening effect and the grain refinement, as a result of the dislocations motion and the entanglement in the material during the plastic deformation. The strengthening modes were dislocation interaction and the grain boundary strengthening [27][29].

The results showed that for all the N2, N4, N6 passes performed, the values of the tensile strength *ST*, the yield strength *SY* and the stress at fracture *SF* for the samples processed at the F6 feed were higher than those for the samples processed at the F12 feed. The reason could have been that the number of bending curves induced in the samples processed at F6 feed was greater than that induced in the samples processed at the F12 feed. More bending curves induced in the material resulted in the higher EP strain, hardness and strengthening of the material. The values of the tensile strength *ST*, the yield strength *SY* and the stress at fracture *SF* for the samples processed at the N6F6 were lower than their counter-parts for the samples processed at N4F6. The drop in the

material strength could be due to the saturation of the material strengthening achieved at N4 pass, which was followed by the onset of the yielding at the N6 pass.

The results for the tensile and the hardness tests presented in Figure 4.10 showed a direct correlation. The results showed that the values for the tensile, the yield, the fracture stresses and the hardness increased directly with the number of passes. Furthermore the values for the tensile and the hardness of the samples processed at the F6 feed were higher than their counter-parts for the samples processed at F12 feed.

The samples processed by the CBS exhibited a reduction of ductility compared with those of the AR samples. Considering the F6 feed length, the percentage elongation eP and the fracture elongation eF (%), respectively reduced from those of the AR samples (10.9, 14.8), to: (7.9, 10.7) at N2F6, (6.5, 8.1) at N4F6 and (6.8, 9.2) at N6F6. At the F12 feed, the samples' *eP* (%) and *eF* (%) reduced from those of the AR samples (10.9, 14.8), to: (9.3, 12.5) at N2F12, (8.3, 11.1) at N4F12 and (8.5, 11.4) at N6F12 respectively.

The results for the CBS processed Ti6Al4V alloy were compared with those by other SPD processes based on the number of pass N, increased engineering tensile strength (MPa) and the decreased fracture elongation (%), respectively. These are: CBS (2, 946.9 -1153, 14.8-10.7), CBS (4, 946.9-1224, 14.8-8.1), CBS (6, 946.9-1172.5, 14.8-9.2). Cold work at 5% step by Kulkarni et al. [122], (5, 1292-1500, 25). MDF by Salishchev et al.

[88] (6, 1050-1300, 9-7). Cold work at 3% step by Gupta et al. [18] (5, 900-1153, 17.5-6). CTD by Ma et al. [123] (8.5, 819-1068, 0.57-0.3). ECAP by Semenova et al. [53] (4, 970-1100, 17-11), ECAP+ Extrusion by Semenova et al. [53] (2, 940-1300, 16-8). The comparison is summarized in Table 4.6.

Table 4.6: A comparison between CBS and other SPD processes on Ti6Al4V enhanced tensile strength, hardness and ductility

Process	**Pass N**	**Eng.Tensile Strength ST (MPa)**	**Hardness (HV)**	**Elongation fracture eF (%)**	**Ref.**
Cold work at 5% compression step	5	1292-1500	336-375	25	[122]
MDF cold work	6	1050-1300	-	9-7	[88]
HPT-4GPa	10	-	300-450	-	[41]
Heat treated and Cold worked at 3% compression step	5	900-1153	-	17.5-6	[18]
CTD	8.5	819-1068	-	0.57-0.3	[123]
ECAP	4	970-1100	-	17-11	[53]
ECAP+Extrusion	2	940-1300	-	16-8	[53]
CBS at 6mm feed as compared with the AR samples	2	946.9-1153	322-372	14.8-10.7	Current Work
	4	946.9-1224	322-400.1	14.8-8.1	
	6	946.9-1172.5	322-379.9	14.8-9.2	

To summarize the tensile results, the use of the CBS process significantly improved the tensile and the yield strength of Ti6Al4V sheet samples. The strength properties depended on the number of passes N and the feed length F. The maximum increase of the

material tensile tensile and the yield strengths were 29.3% and 33.5%, respectively at N4F6. The values for the tensile strength, the yield strength and the fracture stress showed a direct correlation with the hardness values. That is to say, both the tensile strengths and the hardness properties increased simultaneously.

The improvement in the samples' tensile and hardness properties directly resulted in the reduced material ductility. The CBS processed samples exhibited a reduction in their ductility, as compared with the AR samples. The lowest values (%) for eP, eF of (6.5, 8.1) were shown by the samples processed at N4F6; and the highest values for eP, eF of (9.3, 12.5) were shown by the samples processed at N2F12. These ductility properties were relatively lower when compared with (10.9, 148) of the AR samples.

Recalling that the CBS process was performed on the material at room temperature, it is well known that the Ti6Al4V alloy specifically when deformed at low temperature has a high bending resistance, known as spring back. The effect of the material high spring back, the geometrical dimensions of the bender, the straightener and the die are the main factors that could have influenced the performance of the fabricated CBS tool and the Ti6Al4V alloy's enhanced tensile properties.

4.5 Numerical simulation

This sub-chapter covers the results for a numerical model developed and simulated with the ABAQUS FEA tool. The simulated model was used to predict the performance of the CBS process, specifically on the magnitude and the homogeneity of the EP strain, the tensile yield strength and the hardness of the Ti6Al4V alloy sheets at various pass-feeds (NF). Prior to simulation, the model samples were designated based on the CBS number of passes N and feed length F as: N2F4, N4F4, N6F4, N2F6, N4F6, N6F6, N2F12, N4F12 and N6F12. The coefficient of the strain variation (CV) was used to quantify the strain homogeneity in simulated sheet samples. The simulated results for the CV (homogeneity), the magnitude and distribution of the EP strain, the tensile yield strength and the hardness of Ti6Al4V alloy sheets at various pass-feed (NF) were plotted, presented and will be discussed in the next paragraphs.

The results for the EP strain values for the 1^{st} cycle of bending and straightening extracted from the model of length 22 mm and plotted are shown in Figure 4.11. The results showed that the distribution of the mean EP strain for the 1^{st} cycle is highly non-homogeneous. The non-homogeneous distribution of EP strain can result in the non-homogeneous microstructural, tensile strength and hardness properties in the material.

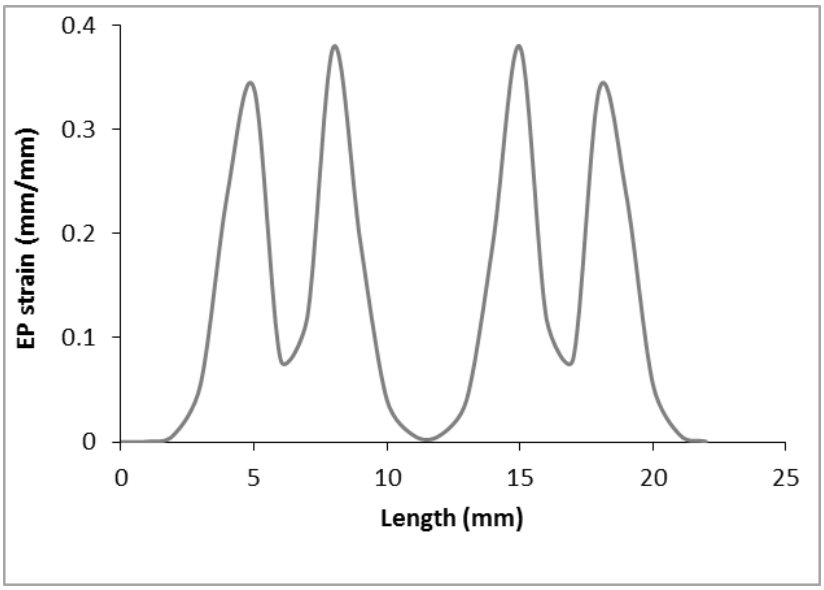

Figure 4.11: A plot of the mean EP strain distribution versus the model length for the 1st cycle bending-straightening

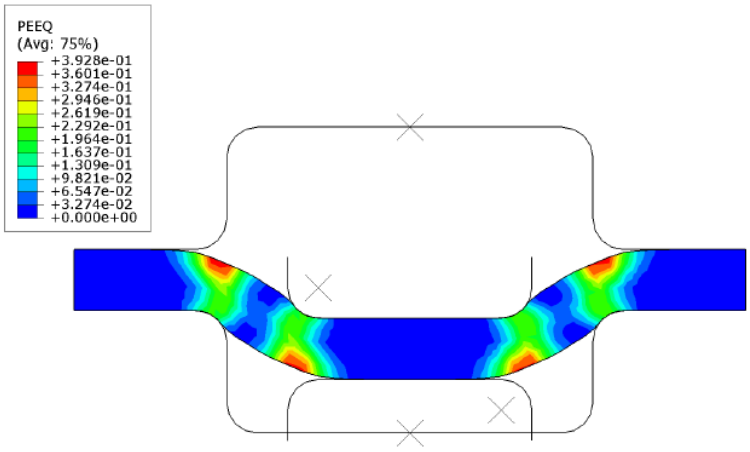

Figure 4.12: EP strain distribution after the initial bending

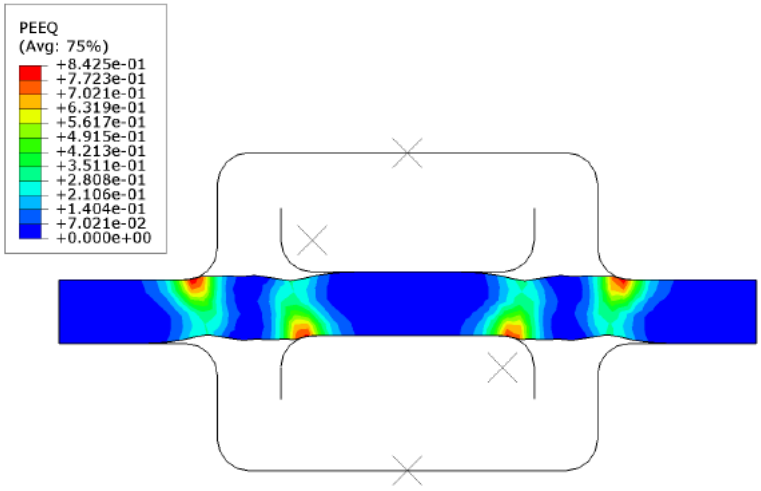

Figure 4.13: EP strain distribution in the sample after the 1st cycle bending-straightening

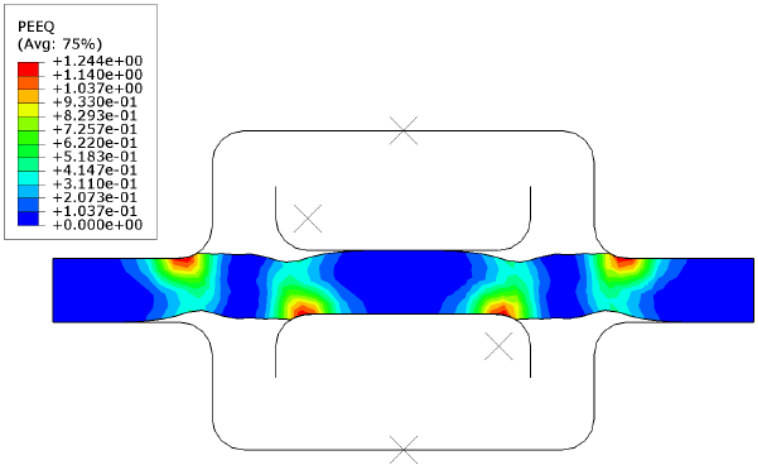

Figure 4.14: EP strain distribution after the 2nd cycle

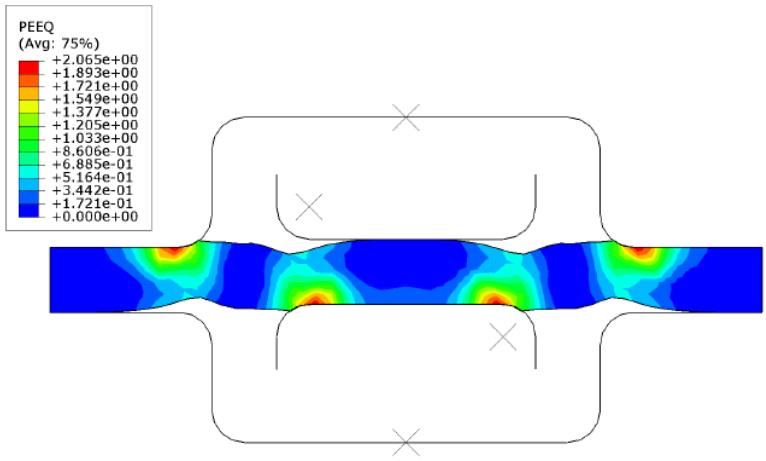

Figure 4.15: EP strain distribution in the sample after the 4th cycle

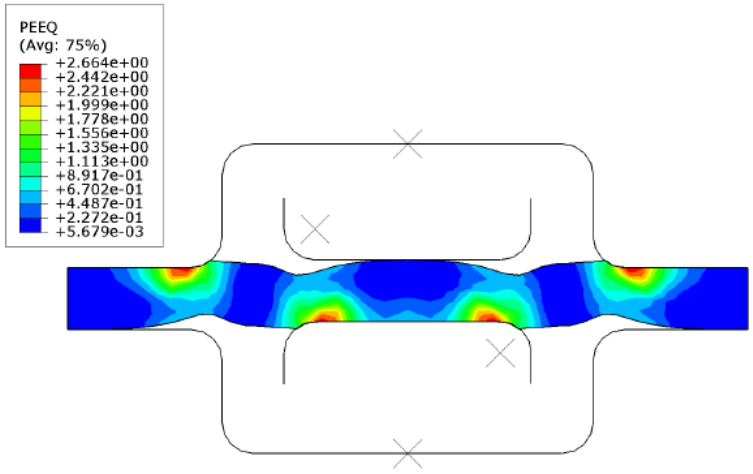

Figure 4.16: EP strain distribution in the sample after the 6th cycle

The simulated results for the distribution and the magnitude of the EP strain for the 1st, 2nd, 4th and 6th CBS bending-straightening cycles over the 22 mm length are presented in Figure 4.12 - Figure 4.16. The results showed that there was a non-homogeneous

distribution of the EP strain in the samples. Comparing the EP strain at the 6th cycle (Figure 4.16) with that at the 1st cycle (Figure 4.13), the results showed that the EP strain homogeneity slightly improved by increasing the number of cycles. The maximum induced EP strain increased from 0.84 at the 1st cycle to 2.66 at the 6th cycle. The mmagnitude and the homogeneity of the EP strain in the Ti6Al4V simulated samples were improved by propagating the 2nd, 4th and 6th cycles over the entire 100 mm sample length at N4, F6, F12 feeds.

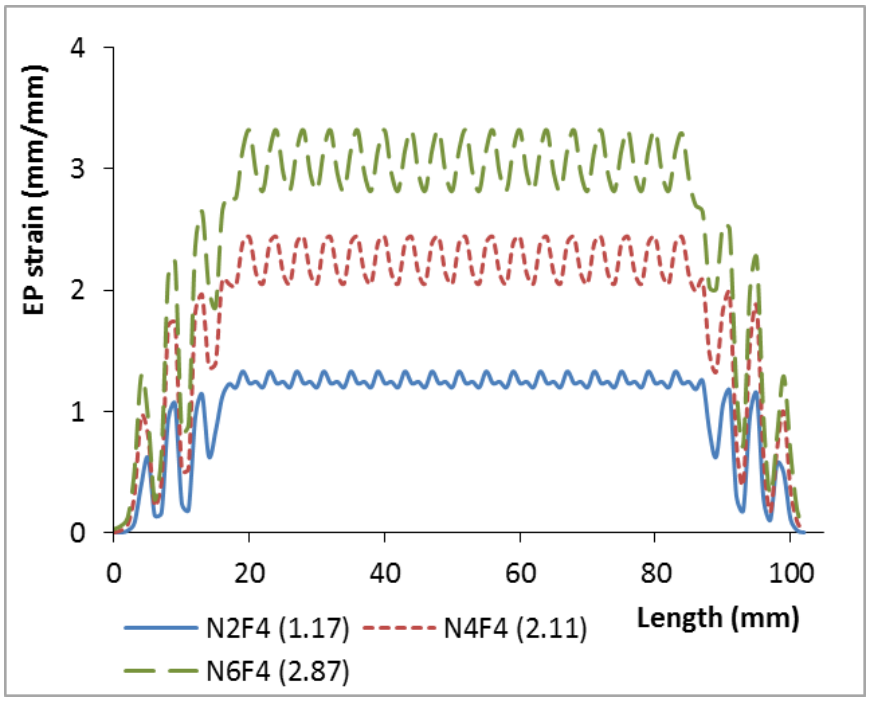

Figure 4.17: EP strain distribution versus the sample length at the F4 feed

The simulated results for the magnitude and distribution of the induced EP strain are presented in Figure 4.17 - Figure 4.19, as they were published in [8]. The values for the mean EP strain ε_m were included in brackets next to each of the curve's legends. The mean EP strain values simulated at F4 feed (1.17, 2.11, 2.87) in Figure 4.17 were the highest, followed by those simulated at the F6 feed (0.81, 1.43, 1.95) in Figure 4.18. For the N2, N4 and N6 passes, respectively, the simulated values for the mean EP strain at F12 feed (0.41, 0.73, 0.99) in Figure 4.19 were the lowest compared with those simulated at the F6 and F4 feeds. Reducing the feed length from F12 to F4 increased the number of effective bending curves and the EP strain in the sample.

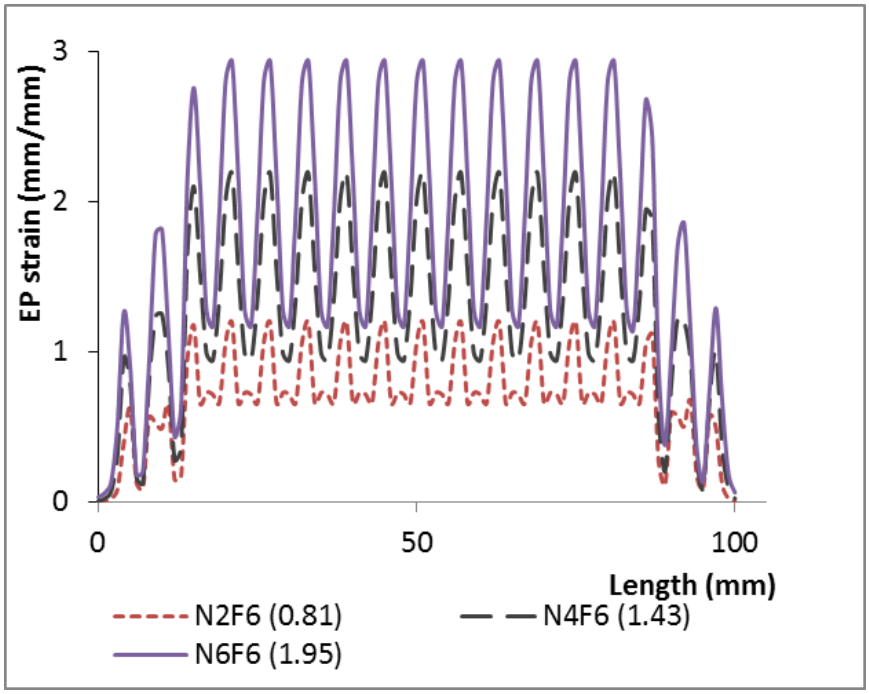

Figure 4.18: EP strain distribution versus sample length at F6 feed

The simulated results for the mean EP strain increased with the number of the CBS passes, the values for the mean EP strain at N6 were the highest followed by those values simulated at N4 and N2, respectively. When considering the simulated results at all the passes N and the feeds F, the results showed a significant variation of the EP strain between the sample's ends and its mid- span. The samples exhibited the lower EP strain values towards the end points compared with those in the mid span.

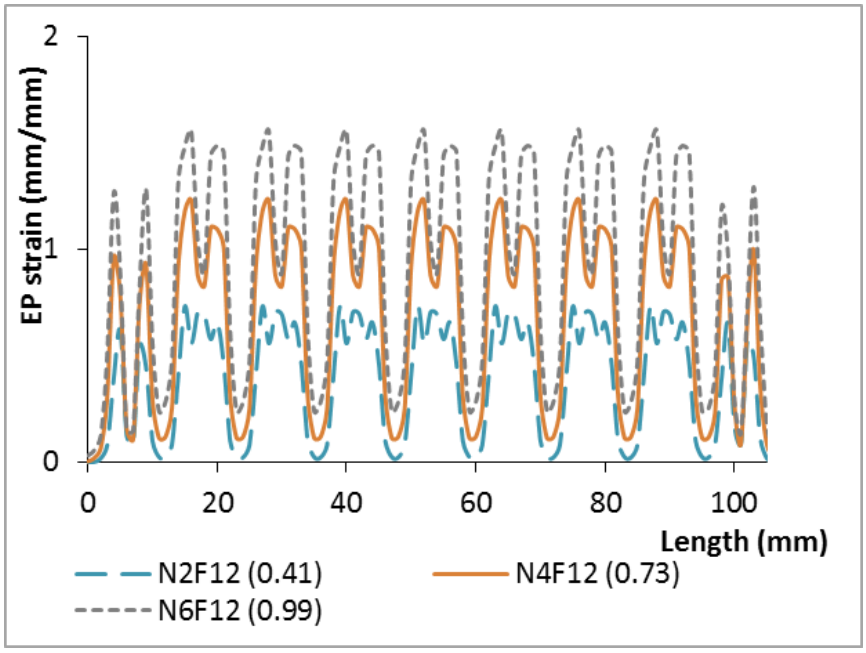

Figure 4.19: EP strain distribution versus the sample length at the F12 feed

The lower EP strain at the sample ends was attributed to the lower number of bending curves induced in the sample's ends by the CBS process, which resulted in a lower

induced EP strain. The effective factor *k* for the mean EP strain induced in the material by a Flat-groove CBS die was estimated by using the simulated EP strain results. Recalling Equation 2.24, whereby the die size *D* is replaced by the length of the open die *D2*. The parameters *F*, *N*, and ε_p stand for the feed length, the number of passes, and the EP strain, respectively.

$$k = N\frac{D2}{F\varepsilon_p}\frac{2}{\sqrt{3}} \qquad 4.1$$

The values of the factor k were determined by substituting the known values of *D2*, *F*, *N*, and $\varepsilon_p = \varepsilon_m$ in Equation 4.1.

The values of the factor *k* that had been determined at N2F4, N4F4, N6F4, N2F6, N4F6, N6F6, N2F12, N4F12 and N6F12 pass-feeds were tabulated and presented in Table 4.7. The value of *k* ranged from 5.6 to 7.2, with a mean of *k* = 6.4. The results showed that in each of the F4, F6 and F12 feeds, the factor *k* slightly increased with the number of passes N. The variation of *k* could be due to the non-linear behaviour of the evolution of the EP strain with respect to the number of CBS passes performed.

Table 4.7: Variation of the factor k with pass-feed (NF)

k	5.9	6.5	7.2	5.7	6.5	7.1	5.6	6.3	6.9
Pass-Feed (NF)	N2F4	N4F4	N6F4	N2F6	N4F6	N6F6	N2F12	N4F12	N6F12

The simulated results for the coefficient of variation (CV) of the EP strain versus the pass-feed (NF) were plotted and presented in Figure 4.20. The results showed that the CV was highly dependent on the feed length, and was slightly dependent on the number of the CBS passes. The highest value for the CV was 68.5%; and it corresponded with the lowest mean EP strain of 0.41 at N2F12.

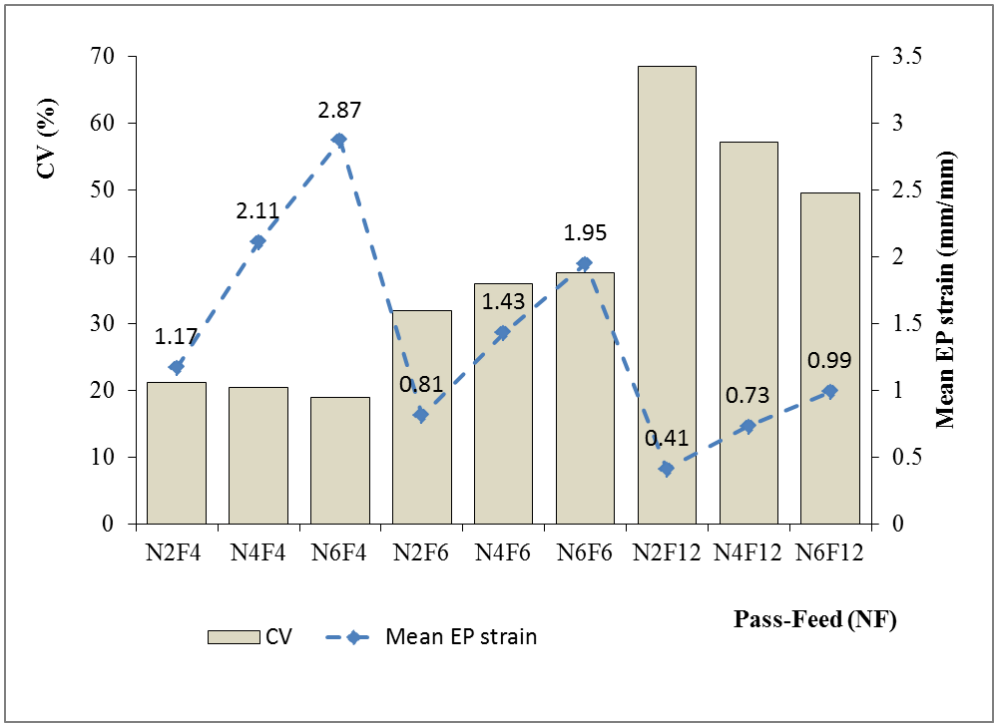

Figure 4.20: CV and the mean EP strain versus the pass-feed (NF)

The CV decreased with the number of passes to 57.2% at N4F12 and 49.5% at N6F12, respectively. The lowest value for the CV was 18.9%; and it corresponded with the highest mean EP strain of 2.87 at N6F4. The CV was slightly higher; 21.1% at N2F4 and

20.4% at N4F4, respectively. Unlike with F4 and F12 feeds, the simulated value for the CV at F6 feed slightly increased with the number of passes N. The value for the CV increased from 31.9% at N2F6 to 36% at N4F6 and 37.6% at N6F6, respectively. The lower value of the CV implied the higher magnitude and homogeneity of the strain induced in the simulated sample. The lowest value of the CV for the samples processed at the F4 feed, followed by those at F6 and F12 feeds, respectively correlated with the highest homogeneity and magnitude of the EP strain for the samples simulated at the F4 feed, followed by those at the F6 and F12 feeds, respectively.

Table 4.8: A comparison between the CBS and other RCS -related methods on the induced mean EP strain

Process	**Material**	**Pass N**	**Mean EP strain**	**CV (%)**	**Ref.**
GP	Al	2	1.16	-	[118]
		4	2.31	-	
GP	Al-1%Mg	2	0.47	98	[93]
		4	0.90	55	
RCS	Low Carbon Steel	2	1.07	-	[117]
CGP		2	1.12	-	
CGP-CR	Low C. Steel	2	1.1	14	[97]
		4	2.1	8	
CBS at 4mm feed	Ti6Al4V	2	1.17	21.1	Current Work
		4	2.11	20.4	
		6	2.87	18.9	

The simulated results for the magnitude and homogeneity of the EP strain in the CBS processed samples were relatively higher than those of the samples processed by other

RCS-related SPD processes. The comparison was based on the RCS-related SPD processes reported by Ghazani and Vajd [93], Khodabakhshi et al. [97], Solhjoei et al. [117] and Javanroodi et al. [118] on the induced EP strain and the CV at various passes as presented in Table 4.8. The simulated results for the material true yield stress versus the pass-feed (NF) were plotted, as shown in Figure 4.21. The results at the F4 feed showed that the simulated yield stress (MPa) increased from 1208.5 at N2F4, to: 1241.0 at N4F4 and 1258.3 at N6F4.

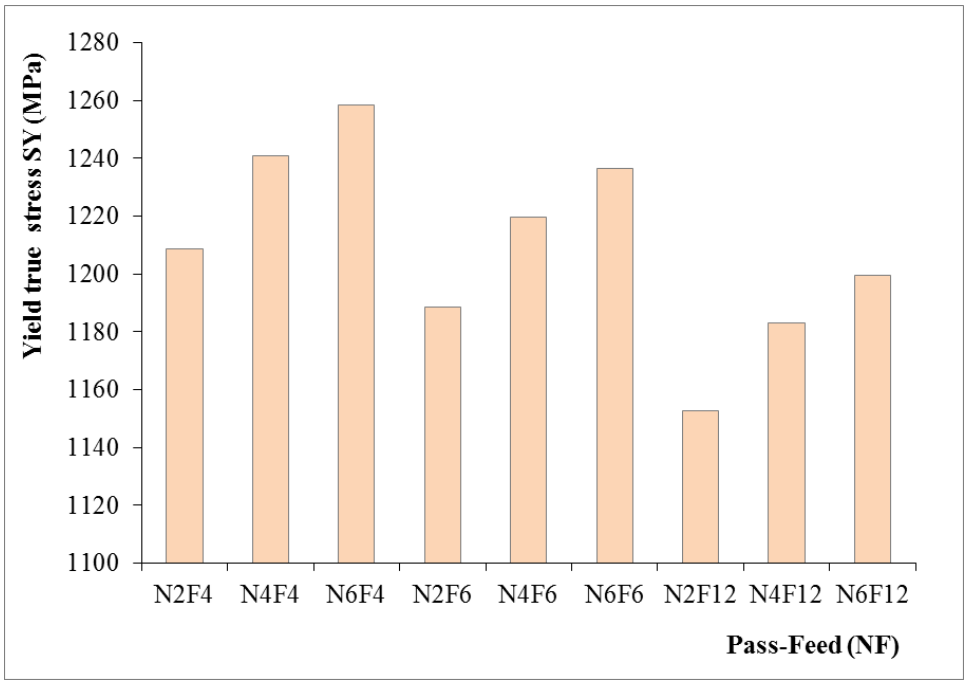

Figure 4.21: Simulated true yield stress versus pass-feed (NF)

The results at the F6 feed showed that the simulated yield stress (MPa) increased from 1188.7 at N2F6, to: 1219.4 at N4F6 and 1236.6 at N6F6. At the F12 feed, the simulated yield stress (MPa) increased from 1152.8 at N2F12, to: 1183.1 at N4F12 and 1199.4 at N6F12. The simulated true yield stress increased with the number of passes; and the yield strength values at the F4 feed were the highest, followed by those at the F6 and F12 feeds, respectively.

The experimental results for the material true yield stress versus the pass-feed (NF) were determined by converting the values for the engineering stress/strain to the true stress/strain by using Equations 3.14 and 3.15 respectively. At the F6 feed, the experimental true yield stress (MPa) increased from that of the AR samples 905, to: 1109 at N2F6, 1216.6 at N4F6 and 1118.4 at N6F6. The results at the F12 feed showed that the experimental true yield stress (MPa) increased from that of the AR samples 905, to: 957.5 at N2F12, 1036.9 at N4F12 and 1005.5 at N6F12.

The simulated results for the material hardness (HV) versus the pass-feed (NF) were plotted, as shown in Figure 4.22. The simulated results at the F4 feed showed that the hardness values (HV) increased from 431.6 at N2F4, to: 443.2 at N4F4 and 449.4 at N6F4. The simulated results at the F6 feed showed that the hardness values (HV) increased from 424.5 at N2F6, to: 435.3 at N4F6 and 441.6 at N6F6.

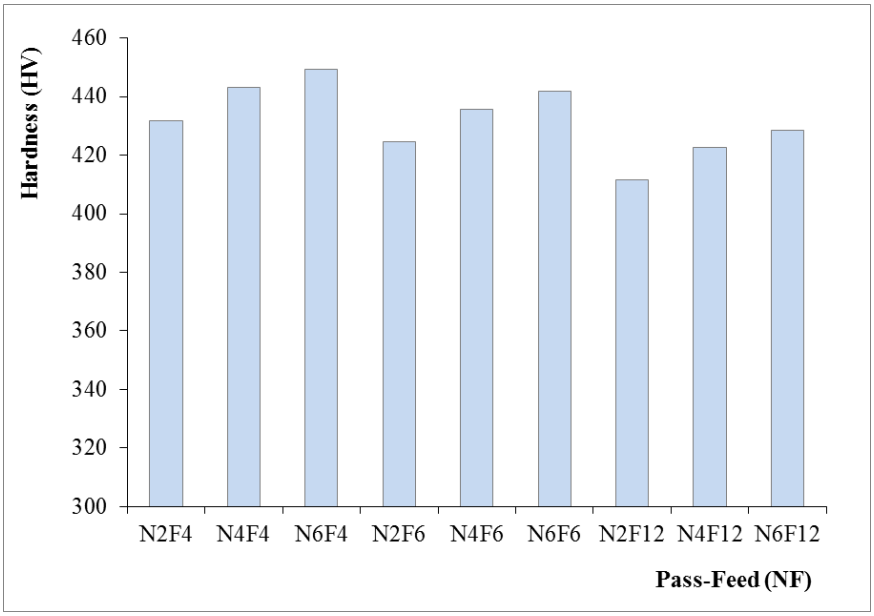

Figure 4.22: Simulated micro hardness (HV) versus pass-feed (NF)

The results at the F12 feed showed that the hardness values (HV) increased from 411.7 at N2F12, to: 422.5 at N4F12 and 428.3 at N6F12. The simulated hardness values increased with the number of passes; and the hardness values at the F4 feed were the highest, followed by those at the F6 and F12 feeds, respectively. For comparison purposes, the experimental average hardness (HV) results at various pass-feeds (NF) are recalled as being: AR (322), N2F6 (372), N4F6 (400.1), N6F6 (379.9), N2F12 (344.5), N4F12 (357.7) and N6F12 (352), respectively. The results from the experimental and the simulation methods are summarized, as shown in Table 4.9. The table consists of the values for the true tensile yield stress, the hardness, as well as their respective percentage increases.

Table 4.9: Summary of experimental and simulation results on true yield stress and hardness

	True yield stress , *SY* (MPa)					**Hardness (HV)**				
Sample	**Experimental**		**Simulated**			**Experimental**		**Simulated**		
	SY	δ%	*SY*	δ%	Δ%	Hardness	δ %	Hardness	δ%	Δ%
AR	905	-	-	-	-	322	-	-	-	-
N2F4	-	-	1208.5	33.5	-	-	-	431.6	34	-
N4F4	-	-	1241	37.1	-	-	-	443.2	37.6	-
N6F4	-	-	1258.3	39	-	-	-	449.4	39.5	-
N2F6	1109	22.5	1188.6	31.3	7.2	372	15.5	424.5	31.8	14.2
N4F6	1216.6	34.4	1219.5	34.8	0.3	400.1	24.3	435.5	35.2	8.8
N6F6	1118.4	23.5	1236.6	36.6	10.6	379.9	18	441.6	37.1	16.2
N2F12	957.6	5.8	1152.8	27.4	20.4	344.5	6.9	411.7	27.9	19.5
N4F12	1036.9	14.6	1183.1	30.7	14.1	357.7	11.1	422.5	31.2	18.1
N6F12	1005.5	11.1	1199.5	32.5	19.3	352	9.3	428.3	33	21.6

δ% represents percentage increases of yield strength and hardness values based on the AR samples. Δ% represents percentage variation of results between experimental and the simulated model.

4.6 Validation of the numerical model

A numerical model was validated by comparing the simulated results with the experimental results for the yield stress and the hardness at F6 and F12 feeds, as shown in Figure 4.23 and Figure 4.24, respectively.

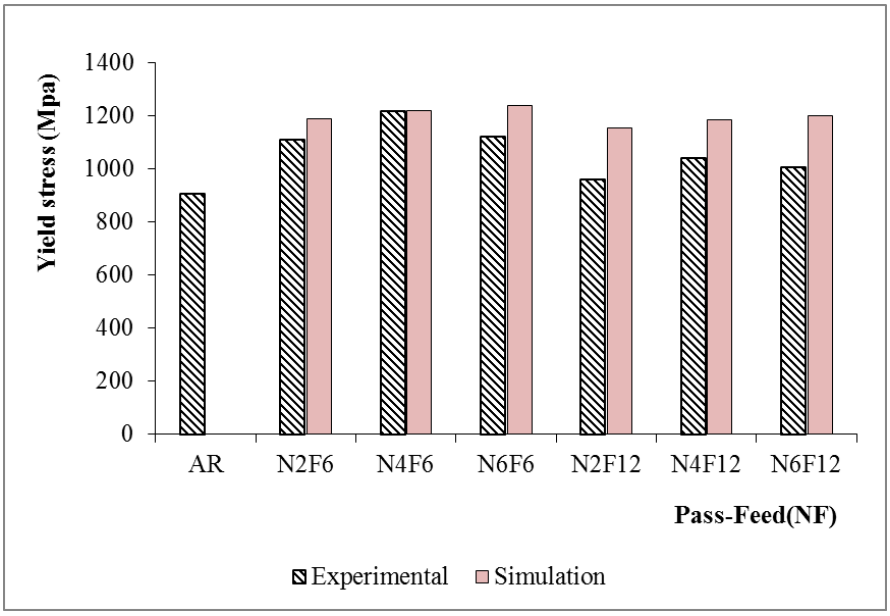

Figure 4.23: Experimental and simulated results for the yield stress at the F6 and F12 feeds

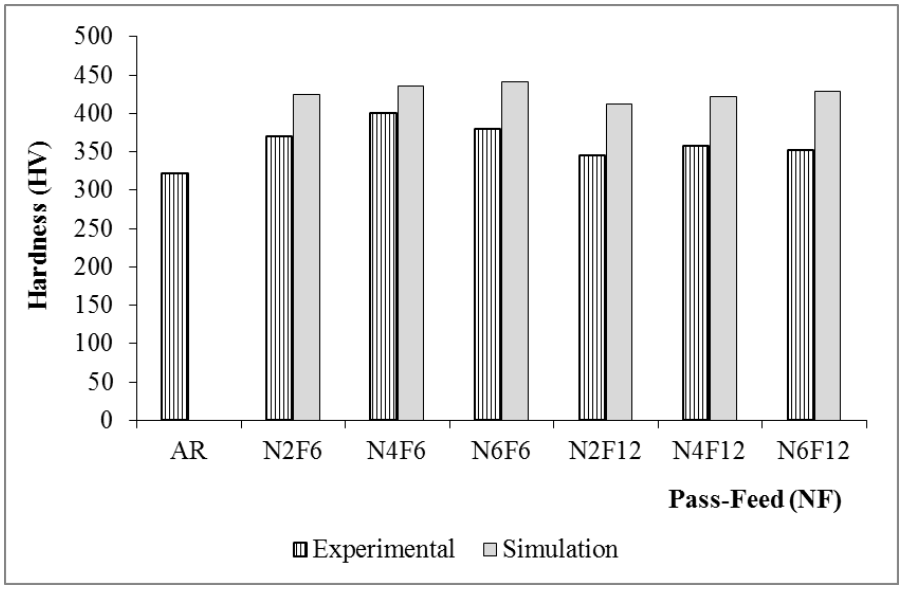

Figure 4.24: Experimental and simulated results for the hardness at the F6 and F12 feeds

In this study, the experimental tensile and the hardness results for the samples processed at F4 feed were not included. The reason was that the samples processed by the CBS at the F4 feed developed cracks and fractured in the early passes. A comparison of the experimental and the simulation results showed that there was a direct correlation between the experimental and the simulated results on the tensile yield stress and the hardness. The results from both of these methods at F6 and F12 feeds showed increased tensile yield strength and hardness values with N2, N4 and N6 passes above that of the AR samples.

The results from both methods showed that the values for the yield stress and the hardness at the F6 feed were higher than their counter-parts at the F12 feed. The experimental values for the yield stress and the hardness at the N6 pass were lower than their simulated counter-parts at the N4 pass. The drop in the material strength and hardness after the N4 pass could have been caused by the material strain hardening limit, followed by the fracture yielding at the N6 pass. This resulted in highest variations between the experimental and the simulated results for yield strength and hardness as 20% and 21.7% respectively. The numerical model could not predict the material hardening limit and the onset of the excessive yielding at N6 pass.

To conclude this sub-chapter, the results for a numerical model developed and simulated showed that the magnitude of the EP strain increased with the number of passes. The EP strain was at its maximum at N6F4; and it was at its lowest at the N2F12. The strain homogeneity was found to be highly dependent on the feed length and slightly dependent on the number of passes. The highest homogeneity corresponded with the lowest CV and was achieved by the samples simulated at the F4 feed, followed by those simulated at the F6 and the F12 feeds respectively. The simulated results were validated with the experimental data. There was a direct correlation between the experimental and the simulation results on the yield stress and the hardness, which improved with the number of passes N2, N4, and N6, when compared with the AR samples. The experimental results showed a drop in the strength and the hardness at the N6 pass due to the hardening limit attained by the material. The model could not predict the material hardening limit and the onset of excessive yielding (necking) that occurred at N6 pass.

4.7 Summary

Chapter 4 has covered the detailed discussions on the results from the various tests that were performed. The tests were used to investigate quantitatively the effectiveness of the CBS technique to improve the microstructural, the hardness and the tensile strength of the Ti6Al4V alloy sheets. The results from the microstructural analysis, the hardness test, the tensile test, the numerical model simulation and the model validation were presented in

various forms; and then discussed in some depth. The microstructural analysis results showed that the CBS processed samples showed an improvement in the microstructural grain refinement when compared with the AR samples. The hardness test results showed that the micro hardness of the CBS processed samples improved significantly up to 24.4% as compared with those of the AR samples.

The tensile test results showed the maximum increase in the material ultimate tensile and the yield strengths of 29.3% and 33.5%, respectively. A numerical model was developed and simulated. The model results showed that a highest mean EP strain of 2.87 was achieved. The highest strain homogeneity that corresponded with the lowest value for the coefficient of strain variation (CV) of 18.9% was achieved. The results from all the tests showed that the microstructural properties, the magnitudes of the enhanced EP strain, the hardness and the tensile strength increased with the CBS number of passes at the reduced feed length. The homogeneity of the enhanced properties was directly dependent on the reduced feed length F; and it was slightly dependent on the number of passes N. The general conclusions from the study and the recommendations for future work will be given in Chapter 5.

CHAPTER FIVE: CONCLUSIONS AND RECOMMENDATIONS

5.1 Introduction

The main objective of this study was to investigate the mechanical and the microstructural properties of the Ti6Al4V alloy, processed by constrained bending and straightening (CBS) severe plastic deformation method. The CBS method was developed and aimed for a continuous process and enhance Ti6Al4V alloy sheets with improved magnitude and homogeneity of the strain, the tensile strength, the hardness and the microstructure. Both the experimental and the numerical approaches were used to achieve the study objectives. The CBS tool parts, materials and their respective dimensions were determined; thereafter, the tool was fabricated in the workshop.

The CBS process was performed on the Ti6Al4V alloy sheet samples at the selected combinations of the number of passes (N) and the feed lengths (F). These were denoted as: N2F6, N4F6, N6F6, N2F12, N4F12 and N6F12. The microstructural analysis, the hardness and the tensile tests were performed on the CBS processed samples. A numerical model for the CBS process was developed and simulated at N2F4, N4F4, N6F4, N2F6, N4F6, N6F6, N2F12, N4F12 and N6F12 passes (N)-feeds(F) combinations. The numerical model was used to predict the magnitude and the homogeneity of the effective plastic (EP) strain, the hardness and the yield tensile strength of the CBS processed samples. The model was then validated by the experimental data.

5.2 Conclusions

Microstructural analysis was done with the OPM and SEM; and the results showed that the CBS processed samples showed an improvement in the microstructural grain refinement, with an average alpha particle size of 3μm, with the formation of new elongated sub grains of alpha and beta particles as compared with the AR samples that had an average size of 10μm. The hardness test results showed that the CBS processed samples had a maximum increase in their micro hardness of 24.4% at N4F6, compared with that of the AR samples. The tensile test results showed that the maximum increase in the material tensile and yield strengths of 29.3% and 33.5%, respectively were achieved at N4F6.

The simulated results showed that the samples could achieve a maximum mean EP strain of 2.87, as well as the highest strain homogeneity (in this case the lowest coefficient of strain variation, CV of 18.9%) at N6F4. The experimental results showed that the microstructural grain refinement, the magnitude of the micro hardness and the tensile strength increased with the number of passes N2, N4, N6 as compared with those of the AR samples. The samples reached hardening and strengthening limits at N4 pass; and they started to yield at the N6 pass.

The simulated results showed that the magnitude values of the micro hardness and the tensile yield strength increased with the number of passes N2, N4, N6. The homogeneity of the enhanced properties directly depended on the reduced feed length F; and they slightly depended on the number of passes N. Both the experimental and the simulation results showed that the lower the feed length, the higher were the magnitude and the homogeneity of the induced properties. Therefore, the values for the micro hardness and the tensile strength at the F6 feed were higher than those at the F12 feed.

A comparison between the simulated and the experimental results showed a direct correlation at the N2 and N4 passes. At the N6 pass, the results showed an inverse correlation due to the saturation of material hardening. At this point, there could be a high rate of dislocations annihilation that resulted in the material softening. Both the experimental and the simulated results showed that the CBS was capable of the continuous process; and it enhanced the Ti6Al4V alloy, with improved homogeneity, as well as the magnitude of the EP strain, hardness and tensile strength.

However, a number of challenges that hindered the performance of this method were noted. The magnitude of the tensile strength, the hardness and the microstructural grain refinement enhanced by this process were relatively lower than those of some SPD methods, such as the ECAP and the HPT. The reason could be that the bending load

induced in the material by the CBS process was not entirely hydrostatic; as a result, the magnitudes of the enhanced properties were comparatively lower than those of the ECAP and the HPT.

The Ti6Al4V alloy is known to have a high bending resistance (known as the spring back effect) as compared with other metallic alloys. The high bending resistance of the Ti6Al4V alloy was a challenge to the bending of sheet samples with the dies, specifically at the room temperature.

In some cases, the brittle behaviour of the Ti6Al4V alloy at room temperature resulted in the formation of cracks, as well as the fracture of the CBS processed samples at the early passes. The CBS tool used in this study was manually operated; and therefore, the feeding of the sample and the bending force were manually applied. This could result in the inaccuracy of the feed length F, ultimately affecting the homogeneity and the magnitude of the enhanced microstructural and mechanical properties. The geometry and the sizes of the CBS die parts i.e. the width of the bender D1 and the die open width D2, could have affected the performance of the tool. However, based on the theory, it is anticipated that the smaller values of D1 and D2, would results in the higher homogeneity and the magnitudes of enhanced properties. This study has shown that the CBS process performed the intended purpose, however, it needs some improvement before it could be

fully viable as an alternative SPD method for the continuous processing of the titanium alloy sheets enhanced with homogeneous microstructural and mechanical properties.

5.3 Recommendations

In order to improve and optimize the performance of the CBS method, a number of recommendations were made for future work. There is a need to investigate the homogeneity, the microstructural grain refinement, the magnitude of the hardness and the tensile strength of the Ti6Al4V alloy processed by the CBS at elevated temperatures. More research needs to be done on the effect of the reduced sizes of the bender width D1, as well as the die width D2 on the optimal performance of the CBS process. The CBS process needs automation, whereby the selection and the control of both the motions and the forces for feeding, constraining, bending and straightening will be automated.

REFERENCES

[1] Y. Kirmanidou *et al.*, "New Ti-Alloys and Surface Modifications to Improve the Mechanical Properties and the Biological Response to Orthopedic and Dental Implants: A Review," *Biomed Res. Int.*, vol. 2016, pp. 1–22, Jan. 2016.

[2] G. Lütjering and J. C. Williams, *Titanium : Engineering Materials and Processes*, Second Edi. New York: Springer Berlin Heidelberg, 2007, pp.1-400.

[3] H. Fujii, K. Takahashi, and Y. Yamashita, "Application of titanium and its alloys for automobile parts," Tokyo, 2003, pp.70-74.

[4] L. Wagner and O. Schauerte, "Status of Titanium and Titanium Alloys in Automotive Applications," in *Ti-2007: Science and Technology*, 2007, vol. 2, pp. 1371–1378.

[5] H. Hermawan, D. Ramdan, and J. Djuansjah, "Metals for Biomedical Applications," in *Biomedical Engineering from Theory to Applications*, R. Fazel, Ed. InTechOpen, 2011, pp. 412–440.

[6] A. Thirugnanam, T. S. Sampath Kumar, and U. Chakkingal, "Tailoring the bioactivity of commercially pure titanium by grain refinement using groove pressing," *Mater. Sci. Eng. C*, vol. 30, no. 1, pp. 203–208, 2010.

[7] G. V. P. Kumar, G. G. Niranjan, and U. Chakkingal, "Grain Refinement in Commercial Purity Titanium Sheets by Constrained Groove Pressing," *Mater. Sci. Forum*, vol. 683, pp. 233–242, May 2011.

[8] W. M. Mwita and E. T. Akinlabi, “Numerical prediction of tensile yield strength and micro hardness of Ti6Al4V alloy processed by constrained bending and straightening severe plastic deformation,” *Mater. Res. Express*, vol. 6, no. 10, p. 106560, Aug. 2019. https://iopscience.iop.org/article/10.1088/2053-1591/ab39a9

[9] K. P. Sanosh, A. Balakrishnan, L. Francis, and T. N. Kim, “Vickers and knoop micro-hardness behavior of coarse-and ultrafine-grained titanium,” *J. Mater. Sci. Technol.*, 2010.

[10] J. Seo, J. W. Hu, and Kim.Kyoung-Hwan, “Analytical Investigation of the Cyclic Behavior of Smart Recentering T-Stub Components with Superelastic SMA Bolts,” *Metals (Basel).*, vol. 386, no. 7, pp. 1–20, 2017.

[11] C. N. Elias, M. A. Meyers, R. Z. Valiev, and S. N. Monteiro, “Ultrafine grained titanium for biomedical applications: An overview of performance,” *J. Mater. Res. Technol.*, vol. 2, no. 4, pp. 340–350, Nov. 2013.

[12] S. J. Li, M. Niinomi, T. Akahori, T. Kasuga, R. Yang, and Y. L. Hao, “Fatigue characteristics of bioactive glass-ceramic-coated Ti-29Nb-13Ta-4.6Zr for biomedical application,” *Biomaterials*, vol. 25, no. 17, pp. 3369–3378, Sep. 2004.

[13] C. Oldani and A. Dominguez, “Titanium as a Biomaterial for Implants,” in *Recent Advances in Arthroplasty*, S. K. Fokter, Ed. InTechOpen, 2012, pp. 150–162.

[14] L. Mishnaevsky *et al.*, “Nanostructured titanium-based materials for medical implants: Modeling and development,” *Mater. Sci. Eng. R Reports*, vol. 81, no. 1,

pp. 1–19, Jul. 2014.

[15] L. Petrini and F. Migliavacca, “Biomedical Applications of Shape Memory Alloys,” *J. Metall.*, vol. 2011, pp. 1–15, Jun. 2011.

[16] M. Niinomi, Y. Liu, M. Nakai, H. Liu, and H. Li, “Biomedical titanium alloys with Young’s moduli close to that of cortical bone,” *Regen. Biomater.*, vol. 3, no. 3, pp. 173–185, Sep. 2016.

[17] F. Schmidt and R. and Wood, “Heat treatment of titanium and titanium alloys,” Arsenal ALABAMA, 1966 https://ntrs.nasa.gov/search.jsp?R=19660015720 2017-08-21T12:20:08+00:00Z

[18] R. K. Gupta, V. A. Kumar, C. Mathew, and G. S. Rao, “Strain hardening of Titanium alloy Ti6Al4V sheets with prior heat treatment and cold working,” *Mater. Sci. Eng. A*, vol. 662, no. January 2018, pp. 537–550, Apr. 2016. http://dx.doi.org/10.1016/j.msea.2016.03.094

[19] M. T. Mohammed, “Mechanical and wear properties of HPT-biomedical titanium: A review,” *Biomater. Biomech. Bioeng.*, vol. 2, no. 3, pp. 185–196, Nov. 2015.

[20] R. Rajendran, M. Venkateshwarlu, V. Petley, and S. Verma, “Strain hardening exponents and strength coefficients for aeroengine isotropic metallic materials – a reverse engineering approach,” *J. Mech. Behav. Mater.*, vol. 23, no. 3–4, pp. 2–7, Sep. 2014 https://www.degruyter.com/view/j/jmbm.2014.23.issue-3-4/jmbm-2014-0012/jmbm-2014-0012.xml

[21] M. Gzyl, A. Rosochowski, S. Boczkal, L. Olejnik, and M. N. Katimon, "Producing High-Strength Metals by I-ECAP," *Adv. Eng. Mater.*, vol. 18, no. 2, pp. 219–223, May 2016.

[22] X. Zhang and H. Sehitoglu, "Crystallography of the B2 → R → B19′ phase transformations in NiTi," *Mater. Sci. Eng. A*, vol. 374, pp. 292–302, Jun. 2004.

[23] B. Kockar, I. Karaman, J. I. Kim, and Y. Chumlyakov, "A method to enhance cyclic reversibility of NiTiHf high temperature shape memory alloys," *Scr. Mater.*, vol. 54, no. 12, pp. 2203–2208, Jun. 2006.

[24] R. A. Coppeta, "Dislocation Modeling in III-Nitrides," Technischen Universität Wien, 2015 http://www.iue.tuwien.ac.at/phd/coppeta/DISS.html#DISSch1.html

[25] R. Z. Valiev, R. K. Islamgaliev, and I. V. Alexandrov, "Bulk nanostructured materials from severe plastic deformation," *Prog. Mater. Sci.*, vol. 45, no. 2, pp. 103–189, Jan. 2000.

[26] R. Z. Valiev *et al.*, "Fundamentals of Superior Properties in Bulk NanoSPD Materials," *Mater. Res. Lett.*, vol. 4, no. 1, pp. 1–22, Jun. 2016. https://doi.org/10.1080/21663831.2015.1060543

[27] H. Mecking and U. Kocks, "Kinetics of flow and strain-hardening," *Acta Metall.*, vol. 29, no. 11, pp. 1865–1875, Nov. 1981.

[28] Y. Estrin and L. Kubin, "Local strain hardening and nonuniformity of plastic deformationTitle," *Acta Metall.*, vol. 34, no. 12, pp. 2455–2464, Dec. 1986.

[29] Y. Estrin, L. Toth, A. Molinari, and Y. Brechet, “A Dislocation-Based Model for All Hardening Stages in Large Strain Deformation,” *Acta Mater.*, vol. 46, no. 15, pp. 5509–5522, 1998.

[30] X. Qiao, N. Gao, and M. Starink, “A model of grain refinement and strengthening of Al alloys due to cold severe plastic deformation Xiao,” *Philos. Mag.*, vol. 92, no. 4, pp. 446–470, Oct. 2012.

[31] M. Ashby, “The deformation of plastically non-homogeneous materials,” *Philos. Mag. A J. Theor. Exp. Appl. Phys.*, vol. 21, no. 170, pp. 399–424, May 1970.

[32] G. Taylor and FRS, “The Mechanism of Plastic Deformation of Crystals. Part1-Theoretical,” *Proc. R. Soc. A*, vol. 145, no. 855, pp. 362–387, Jul. 1934.

[33] L. S. Tóth, B. Beausir, C. F. Gu, Y. Estrin, N. Scheerbaum, and C. H. J. Davies, “Effect of grain refinement by severe plastic deformation on the next-neighbor misorientation distribution,” *Acta Mater.*, vol. 58, no. 20, pp. 6706–6716, Dec. 2010. https://linkinghub.elsevier.com/retrieve/pii/S1359645410005501

[34] Z. Jiang, J. Lian, and B. Baudelet, “A dislocation density approximation for the flow stress—grain size relation of polycrystals,” *Acta Metall. Mater.*, vol. 43, no. 9, pp. 3349–3360, Sep. 1995.

[35] S. To’th, Y. Estrin, and A. Molinari, “Strain Hardening at Large Strains as Predicted by Dislocation Based Polycrystal Plasticity Model,” *J. Eng. Mater. Technol*, vol. 24, no. 1, pp. 71–77, Jan. 2002.

[36] Y. Estrin and A. Vinogradov, “Extreme grain refinement by severe plastic deformation: A wealth of challenging science,” *Acta Mater.*, vol. 61, no. 3, pp. 782–817, Feb. 2013.

[37] T. Shanmugasundaram, M. Heilmaier, B. Murty, and S. Vadlamani, “On the Hall–Petch relationship in a nanostructured Al–Cu alloy,” *Mater. Sci. Eng. A*, vol. 527, no. 29, pp. 7821–7825, Nov. 2010.

[38] N. Lugo, N. Llorca, J. M. Cabrera, and Z. Horita, “Microstructures and mechanical properties of pure copper deformed severely by equal-channel angular pressing and high pressure torsion,” *Mater. Sci. Eng. A*, vol. 477, no. 1–2, pp. 366–371, Mar. 2008.

[39] J. Fu, H. Ding, Y. Huang, W. Zhang, and T. G. Langdon, “Influence of phase volume fraction on the grain refining of a Ti-6Al-4V alloy by high-pressure torsion,” *J. Mater. Res. Technol.*, vol. 4, no. 1, pp. 2–7, Jan. 2015. http://linkinghub.elsevier.com/retrieve/pii/S2238785414000957

[40] H. Shahmir, M. Nili-Ahmadabadi, Y. Huang, and T. G. Langdon, “Evolution of microstructure and hardness in NiTi shape memory alloys processed by high-pressure torsion,” *J. Mater. Sci.*, vol. 49, no. 8, pp. 2998–3009, Jan. 2014.

[41] R. Valiev and I. Smirnov, “Effect of high pressure torsion technical parameters on grain refinement in Ti-6Al-4V alloy,” *Mater. Sci. Eng.*, vol. 63, no. 012073, pp. 1–5, Jan. 2014.

[42] C. T. Wang, A. G. Fox, and T. G. Langdon, “An Investigation of Hardness Homogeneity and Microstructure in Pure Titanium Processed by High Pressure Torsion,” *Mater. Sci. Forum*, vol. 783–786, pp. 2701–2706, May 2014.

[43] Y. Todaka, M. Umemoto, A. Yamazaki, J. Sasaki, and K. Tsuchiya, “Effect of Strain Path in High-Pressure Torsion Process on Hardening in Commercial Purity Titanium,” *Mater. Trans.*, vol. 49, no. 1, pp. 47–53, Dec. 2008.

[44] M. Nie, C. T. Wang, M. Qu, N. Gao, J. A. Wharton, and T. G. Langdon, “The corrosion behaviour of commercial purity titanium processed by high-pressure torsion,” *J. Mater. Sci.*, vol. 49, no. 7, pp. 2824–2831, Apr. 2014.

[45] A. P. Zhilyaev, S. N. Sergeev, V. A. Popov, and A. V. Orlov, “Evolution of microstructure and microhardness in HPT titanium during annealing,” *Rev. Adv. Mater. Sci.*, vol. 39, no. 1, pp. 15–19, 2014.

[46] R. B. Figueiredo and T. G. Langdon, “Development of an ω-Phase in Grade 2 Titanium Processed by HPT at High Hydrostatic Pressure,” *Mater. Res.*, vol. 19, no.5,pp.1144–1148,2016. http://www.scielo.br/scielo.php?script=sci_arttext&pid=S1516-14392016000501144&lng=en&tlng=en

[47] K. Edalati, S. Lee, and Z. Horita, “Continuous high-pressure torsion using wires,” *J. Mater. Sci.*, vol. 47, no. 1, pp. 473–478, Jan. 2012.

[48] A. Hohenwarter, “Incremental high pressure torsion as a novel severe plastic

deformation process: Processing features and application to copper," *Mater. Sci. Eng. A*, vol. 626, pp. 80–85, Mar. 2015.

[49] R. G. Chembarisova, "Development and application of the dislocation model for analysis of the microstructure evolution and deformation behaviour of metals subjected to severe plastic deformation," *Rev.Adv.Mater.Sci*, vol. 16, pp. 51–72, 2007.http://www.ipme.ru/e-journals/RAMS/no_11607/alexandrov.pdf

[50] F. Djavanroodi, B. Omranpour, M. Ebrahimi, and M. Sedighi, "Designing of ECAP parameters based on strain distribution uniformity," *Prog. Nat. Sci. Mater. Int.*, vol. 22, no. 5, pp. 452–460, Oct. 2012.

[51] Y. Gu, A. Ma, J. Jiang, Y. Yuan, and H. Li, "Deformation structure and mechanical properties of pure titanium produced by rotary-die equal-channel angular pressing," *Metals (Basel).*, vol. 7, no. 297, pp. 1–10, Aug. 2017.

[52] K. Ivanov, "Comparative TEM study of microstructures of Ti-6Al-4V alloy processed by equal channel angular pressing and helical plus groove rolling," *Int. Conf. Adv. Mater. with Hierarchical Struct. New Technol. Reliab. Struct.*, vol. 1783, Nov. 2016, pp.020075-1-4.

[53] I. P. Semenova *et al.*, "Microstructural Features and Mechanical Properties of the Ti-6Al-4V ELI Alloy Processed by Severe Plastic Deformation," *Mater. Sci. Forum*, vol. 503–504, no. March 2016, pp. 757–762, Jan. 2006. http://link.springer.com/10.1007/1-4020-3923-9_33

[54] A. A. Mendes Filho, C. A. Rovere, S. E. Kuri, V. L. Sordi, and M. Ferrante, "A general study of commercially pure Ti subjected to severe plastic deformation: Microstructure, strength and corrosion resistance," *Rev. Mater.*, vol. 15, no. 2, pp. 254–259, 2010.

[55] M. Greger, L. Kander, V. Snášel, and Č. Martin, "Microstructure Evolution of Pure Titanium During Ecap," *Mater. Eng.*, vol. 18, pp. 97–104, Sep. 2011.

[56] A. V. Polyakov, I. P. Semenova, and R. Z. Valiev, "High fatigue strength and enhanced biocompatibility of UFG CP Ti for medical innovative applications," *IOP Conf. Ser. Mater. Sci. Eng.*, vol. 63, pp. 1–6, Aug. 2014.

[57] R. A. Parshikov, A. I. Rudskoy, A. M. Zolotov, and O. V Tolochko, "Technological Problems of Equal Channel Angular Pressing," *Rev. Adv. Mater. Sci.*, vol. 34, pp. 26–36, 2013. ww.ipme.ru/e-journals/RAMS/no_13413/04_13413_tolochko.pdf.

[58] W. M. Mwita, E. T. Akinlabi, and K. O. Sanusi, "Performance and Prospects of Severe Plastic Deformation for Effective Biomedical Titanium Alloys," *J. Mod. Mater.*, vol. 5, no. 1, pp. 8–23, Feb. 2018. doi.org/10.21467/jmm.5.1.8-23

[59] N. Tsuji, Y. Saito, S. H. Lee, and Y. Minamino, "ARB (accumulative roll-bonding) and other new techniques to produce bulk ultrafine grained materials," *Adv. Eng. Mater.*, vol. 5, no. 5, pp. 338–344, Feb. 2003.

[60] N. Tsuji, Y. Saito, H. Utsunomiya, and S. Tanigawa, "Ultra-fine grained bulk

steel produced by accumulative roll-bonding (ARB) process," *Scr. Mater.*, vol. 40, no. 7, pp. 795–800, Mar. 1999.

[61] B. Hai, L. Yu, C. Lu, A. K. Tieu, H. J. Li, and A. Godbole, "Special Rolling Techniques for Improvement of Mechanical Properties of Ultra fine-Grained Metal Sheets : a Review," *Adv. Eng. Mater.*, vol. 18, no. 5, pp. 754–769, May 2016.

[62] N. Tsuji, Y. Saito, H. Utsunomiya, and S. Tanigawa, "Ultra-fine grained bulk steel produced by accumulative roll-bonding (ARB) process," *Scr. Mater.*, vol. 40, no. 7, pp. 795–800, Mar. 1999.

[63] H. Sheikh and E. Paimozd, "Effect of Hot Accumulative Roll Bonding Process on the Mechanical Properties of AA5083," *Open J. Met.*, vol. 1, pp. 12–15, Sep. 2011.

[64] H. Kitahara *et al.*, "Fatigue Crack Propagation Behavior in Commercial Purity Ti Severely Deformed by Accumulative Roll Bonding Process," *Mater. Trans.*, vol. 49, no. 1, pp. 64–68, Jan. 2008.

[65] A. Fattah-alhosseini, A. Reza, Y. Mazaheri, and M. Karimi, "An Investigation of mechanical properties in accumulative roll bonded nano-grained pure titanium," *Mater. Sci. Eng. A*, vol. 688, pp. 218–224, Mar. 2017.

[66] J. Romberg *et al.*, "Ti/Al Multi-Layered Sheets: Accumulative Roll Bonding (Part A)," *Metals (Basel).*, vol. 6, no. 12, p. 30, Feb. 2016.

[67] G. Fan, Y. Du, T. Yu, N. Hansen, L. Geng, and X. Huang, “Laminated Ti-Al composites : Processing , structure and strength,” *Mater. Sci. Eng. A*, vol. 673, pp. 572–580, Jul. 2016.

[68] Y. C. and Y. Z. Jinfeng Nie , Mingxing Liu , Fang Wang , Yonghao Zhao , Yusheng Li, “Fabrication of Al / Mg / Al Composites via Accumulative Roll Bonding and Their Mechanical Properties,” *Materials (Basel).*, vol. 9, no. 11, pp. 1–14, 2016.

[69] T. Kunimine, T. Fujii, S. Onaka, N. Tsuji, and M. Kato, “Effects of Si addition on mechanical properties of copper severely deformed by accumulative roll-bonding,” *J. Mater. Sci.*, vol. 46, no. 12, pp. 4290–4295, Jun. 2011. http://link.springer.com/10.1007/s10853-010-5235-4

[70] W. Polkowski, “Differential Speed Rolling: A New Method for a Fabrication of Metallic Sheets with Enhanced Mechanical Properties,” in *Progress in Metallic Alloys*, V. Glebovsky, Ed. InTechOpen, 2016, pp. 111–126.

[71] R. Roumina and C. W. Sinclair, “Deformation geometry and through-thickness strain gradients in asymmetric rolling,” *Metall. Mater. Trans. A Phys. Metall. Mater. Sci.*, vol. 39, no. 10, pp. 1–9, Oct. 2008.

[72] Q. Chao, P. D. Hodgson, and H. Beladi, “Microstructure and Texture Evolution During Symmetric and Asymmetric Rolling of Martensitic Ti-6Al-4V alloy.,” *Metall. Mater. Trans. A*, vol. 47, no. 1, pp. 531–545, Jan. 2016.

[73] D. Tang, X. Liu, M. Song, and H. Yu, “Experimental and Theoretical Study on Minimum Achievable Foil Thickness during Asymmetric Rolling,” *PLoS One*, vol. 9, no. 9, pp. 1-12, Sep. 2014.

[74] S. H. Zhang, D. W. Zhao, C. R. Gao, and G. D. Wang, “Analysis of asymmetrical sheet rolling by slab method,” *Int. J. Mech. Sci.*, vol. 65, no. 1, pp. 168–176, 2012. http://dx.doi.org/10.1016/j.ijmecsci.2012.09.015

[75] Z. Li, A. Shan, and J. Jiang, “Improved Mechanical Properties of Nano-grained Ti Processed by Combination of Asymmetric and Symmetric Rolling.,” in *Shanghai International Nanotechnology Cooperation Symposium*, 2012, pp. 146–150.

[76] H. Yu, A. K. Tieu, C. Lu, and A. Godbole, “An Investigation of Interface Bonding of Bimetallic Foils by Combined Accumulative Roll Bonding and Asymmetric Rolling Techniques,” *Metall. Mater. Trans. A*, vol. 45, no. 9, pp. 4038–4045, Aug. 2014. http://link.springer.com/10.1007/s11661-014-2311-4

[77] V. Varyukhin, Y. Beygelzimer, R. Kulagin, O. Prokof, and A. Reshetov, “Twist Extrusion : Fundamentals and Applications,” *Mater. Sci. Forum*, vol. 667–669, pp. 31–37, Dec. 2011.

[78] A. Reshetov, R. Kulagin, A. Korshunov, and Y. Beygelzimer, “The Occurrence of Ideal Plastic State in CP Titanium Processed by Twist Extrusion,” *Adv. Eng. Mater.*, vol. 20, no. 5, pp. 1700899:1–9, Jan. 2018. http://doi.wiley.com/10.1002/adem.201700899

[79] V. V Stolyarov, Y. E. Beigel, D. V Orlov, and R. Z. Valiev, “Refinement of Microstructure and Mechanical Properties of Titanium Processed by Twist Extrusion and Subsequent Rolling,” *Phys. Met. Metallogr.*, vol. 99, no. 2, pp. 204–211, 2005.

[80] N. Kazantseva *et al.*, “Comparative analysis of the structure and internal stress in Ti-6Al-4V alloys manufactured by 3D printing and processing with screw extrusion,” *J. Phys. Conf. Ser.*, vol. 1115, pp. 1–7, Nov. 2018. http://stacks.iop.org/17426596/1115/i=4/a=042007?key=crossref.5b63320cb0436d5f8a8a294bc286ba23.

[81] A. Zavdoveev, S. Dobatkin, E. Pashinskaya, and A. Maksakova, “Structure and properties of low-carbon steel after twist extrusion,” *Emerg. Mater. Res.*, no. pp. 1-5, April 2015, 2014.

[82] Y. Beygelzimer, D. Orlov, and A. Korshunov, “Features of Twist Extrusion : Method , Structures & Material Properties,” *Solid State Phenom.*, vol. 114, no. June 2014, pp. 69–78, Jun. 2006.

[83] N. Shkatulyak, “Effect of twist extrusion and subsequent rolling on the texture and microstructure of aluminium alloy,” *Int. J. Adv. Mater. Sci. Eng.*, vol. 3, no. 1, pp. 15–25, Jan. 2014.

[84] M. I. Latypov, M.-G. Lee, Y. Beygelzimer, R. Kulagin, and H. S. Kim, “Simple shear model of twist extrusion and its deviations,” *Met. Mater. Int.*, vol. 21, no. 3,

pp. 569–579, May 2015. http://link.springer.com/10.1007/s12540-015-4387-9

[85] F. Djavanroodi, M. Ebrahimi, and J. F. Nayfeh, “Tribological and mechanical investigation of multi-directional forged nickel,” *Sci. Rep.*, vol. 9, no. 1, p. 241, Dec. 2019. http://www.nature.com/articles/s41598-018-36584-w.

[86] M. Kishchik, A. Mikhaylovskaya, A. Kotov, A. Mosleh, W. AbuShanab, and V. Portnoy, “Effect of Multidirectional Forging on the Grain Structure and Mechanical Properties of the Al–Mg–Mn Alloy,” *Materials (Basel).*, vol. 11, no. 11, p. 2166, Nov. 2018. http://www.mdpi.com/1996-1944/11/11/2166.

[87] A. Dashti, M. Shaeri, R. Taghiabadi, F. Djavanroodi, F. Vali Ghazvini, and H. Javadi, “Microstructure, Texture, Electrical and Mechanical Properties of AA-6063 Processed by Multi Directional Forging,” *Materials (Basel).*, vol. 11, no. 12, p. 2419, Nov. 2018. http://www.mdpi.com/1996-1944/11/12/2419.

[88] G. A. Salishchev, S. V. Zherebtsov, R. Galeyev, and K. Maekawa, “Mechanical Properties of Ti–6Al–4V Titanium Alloy with Submicrocrystalline Structure Produced by Severe Plastic Deformation,” *Mater. Trans.*, vol. 46, no. 9, pp. 2020–2025, Sep. 2005.

[89] I. Ansarian, M. H. Shaeri, M. Ebrahimi, P. Minárik, and K. Bartha, “Microstructure evolution and mechanical behaviour of severely deformed pure titanium through multi directional forging,” *J. Alloys Compd.*, vol. 776, no. 5, pp. 83–95,Mar.2019.https://linkinghub.elsevier.com/retrieve/pii/S0925838818338702

[90] H. Miura, M. Kobayashi, T. Aoba, H. Aoyama, and T. Benjanarasuth, "An approach for room-temperature multi-directional forging of pure titanium for strengthening," *Mater. Sci. Eng. A*, vol. 731, pp. 603–608, Jul. 2018. https://linkinghub.elsevier.com/retrieve/pii/S0921509318308542.

[91] Y. Zhu, J. Huang, H. Jiang, and T. Lowe, "Processing of Bulk Nano structured Copper by Repetitive Corrugation and Straightening (RCS)," Los Alamos, NM 87545, 2000. www.osti.gov/scitech/servlets/purl/765274-flO3cH/webviewable.

[92] N. Thangapandian, S. Balasivanandha Prabu, and K. A. Padmanabhan, "Effects of die profile on grain refinement in Al-Mg alloy processed by repetitive corrugation and straightening," *Mater. Sci. Eng. A*, vol. 649, pp. 229–238, Sep. 2016.

[93] M. S. Ghazani and A. Vajd, "Finite Element Analysis of the Groove Pressing of Aluminum Alloy," *Model. Numer. Simul. Mater. Sci.*, vol. 4, pp. 32–36, Jan. 2014.

[94] D. H. Shin, J. J. Park, Y. S. Kim, and K. T. Park, "Constrained groove pressing and its application to grain refinement of aluminum," *Mater. Sci. Eng. A*, vol. 328, no. 1, pp. 98–103, May 2002.

[95] S. Fong, A. Danno, M. J. Tan, and B. Wah Chua, "Effect of Deformation and Temperature Paths in Severe Plastic Deformation Using Groove Pressing on Microstructure, Texture, and Mechanical Properties of AZ31-O," *J. Manuf. Sci. Eng.*, vol. 137, no. 5, pp. 16–26, Feb. 2015.

[96] P. M. Bhovi and K. Venkateswarlu, “Influence of RCS on Al-3Mg and Al-3Mg-0.25Sc alloys,” *IOP Conf. Ser. Mater. Sci. Eng.*, vol. 114, no. 1, pp. 1–7, 2016.

[97] F. Khodabakhshi, M. Abbaszadeh, S. R. Mohebpour, and H. Eskandari, “3D finite element analysis and experimental validation of constrained groove pressing-cross route as an SPD process for sheet form metals,” *Int. J. Adv. Manuf. Technol.*, vol. 73, no. 9–12, pp. 1291–1305, May 2014.

[98] W. Mwita, E. Akinlabi, and K. Sanusi, “Constrained bending and straightening-a proposed method for severe plastic deformation of metals,” *IOP Conf. Ser. Mater. Sci. Eng.*, vol. 423, pp. 1–6, Nov. 2018. http://stacks.iop.org/1757-899X/423/i=1/a=012169?key=crossref.68eb86dd96cbb2244209a8481fe46839.

[99] W. M. Mwita and E. T. Akinlabi, “Bending Forces and Hardness Properties of Ti6Al4V Alloy Processed by Constrained Bending and Straightening Severe Plastic Deformation,” in *Advances in Material Sciences and Engineering.Lecture Notes in Mechanical Engineering.*, 1st ed., M. Awang, S. Emamian, and F. Yusof, Eds. Singapore: Springer-Singapore, 2020, pp. 389–398 http://link.springer.com/10.1007/978-981-13-8297-0_41.

[100] MacSteel, “STRUCTURAL STEEL CATALOGUE,” MaCSteel, Johannesburg, pp. 7-19, 2016. www.Macsteel.co.za.

[101] Kaizenha, “Manufacturing Lecture,” *Kaizenha*, 2015. http://kaizenha.com/cdn/files/Manufacturing 1/Lecture 15.pdf. [Accessed: 01-

Apr-2019].

[102] E. ToolBox, "Metric Steel Bolts - Grades and Property Classes," *Engineering ToolBox*, 2008. https://www.engineeringtoolbox.com/steel-bolts-metric-grades-d_1428.html. [Accessed: 01-Mar-2019].

[103] R. J. Roark, W. C. Young, and R. G. Budynas, *Roark's Formulas for Stress and Strain*, 7th ed. New York: McGraw-Hill, 2002. http://materiales.azc.uam.mx/gjl/Clases/MA10_I/Roark's formulas for stress and strain.pdf.

[104] A. W. (AWC) Council, *Beam Design Formulas with Shear and Moment Diagrams*, 2005th ed. Washington DC: American Forest & Paper Association, pp.16, 2007.

[105] T. S. C. Institute, *Handbook of Structural Steelwork Eurocode Edition Handbook of Structural Steelwork*, EuroCode., no. 55. London: The British Constructional Steelwork Association, pp. 210-258, 2013. www.steelconstruction.info.

[106] E. Oberg, F. D. Jones, H. L. Horton, and H. H. Ryffel, *Machinery ' s Handbook*, 26th ed. New York: Industrial Press INC, pp. 1521-1539, 2000.

[107] R. G. Budynas and J. Nisbett, *Shigley's Mechanical Engineering Design*, 10th ed. New York: McGraw-Hill, pp. 414-436, 2015.

[108] ASTM -E8, *Standard Test Methods for Tension Testing of Metallic Materials 1*. West Conshohocken PA USA: Astm International, pp.1-25, 2008. www.astm.org,

[109] ASTM-E3, *Standard Practice for Preparation of Metallographic Specimens*, vol. 82, no. C. West Conshohocken PA USA: ASME Internationsl, pp. 1-7, 1995 .http://www.astm.org/cgi-bin/resolver.cgi?E140%0Ahttp://www.astm.org/Standards/E8.htm.

[110] ASTM-E92, *Standard Test Method for Vickers Hardness of Metallic Materials1*, vol. 82, no. Reapproved. West Conshohocken PA USA: Astm International, pp. 1-9, 1997.

[111] ASTM-E407, *Standard Practice for Microetching Metals and Alloys-1*. West Conshohocken PA USA: Astm International, pp. 1-21, 2007.

[112] L. Wojnar, "Application of ASTM standards in quantitative microstructure evaluation," *Czas. Tech. Mech.*, vol. Y. 113, pp. 1–6, 2016. http://yadda.icm.edu.pl/yadda/element/bwmeta1.element.baztech-4ae89280-280f-431e-a1cc-1fd278fee678

[113] K. Venkateswarlu, M. Sandhyarani, T. A. Nellaippan, and N. Rameshbabu, "Estimation of Crystallite Size, Lattice Strain and Dislocation Density of Nanocrystalline Carbonate Substituted Hydroxyapatite by X-ray Peak Variance Analysis," *Procedia Mater. Sci.*, vol. 5, pp. 212–221, 2014.

[114] G. K. Williamson and W. H. Hall, "X-Ray broadening from filed aluminium and wolfram," *Acta Metall.*, vol. 1, pp. 22–31, 1953. http://www.xray.cz/xray/csca/kol2011/kurs/dalsi-cteni/clanky/Williamson-

ActaMet-1953-1-22-WH-Plot.pdf.

[115] S. K. Mishra, H. Roy, A. K. Lohar, S. K. Samanta, S. Tiwari, and K. Dutta, "A comparative assessment of crystallite size and lattice strain in differently cast A356 aluminium alloy," *IOP Conf. Ser. Mater. Sci. Eng.*, vol. 75, no. 1, 2015.

[116] Z. E and B. H, "Comparing Plastic Deformations Produced by HPT and ECAP Processes Using the Finite Element Analysis Method," *Int. J. Mech. Appl.*, vol. 2, no. 1, pp. 20–24, 2012.

[117] N. Solhjoei, A. R. Varposhty, H. Mokhtarian, and A. Manian, "A Comparative Study To Evaluate the Efficiency of RCS and CGP Processes," *Indian J.Sci.Res*, vol. 1, no. 2, pp. 563–572, 2014.

[118] F. Javanroodi, A. Sajadi, and M. Borhani, "Experimental and Numerical Investigation of Groove Pressed UFG Pure Aluminum," *Int. J. Adv. Des. Manuf. Technol.*, vol. 5, no. 2, pp. 1–5, Mar. 2012.

[119] W. Ramberg and W. R. Osgood, *Description of stress-strain curves by three parameters*. Washington DC USA: National National Advisory Committee of Aeronautics, Technical Note 902Bureau of Standards, 1943.

[120] H. Lan and T. A. Venkatesh, "On the relationships between hardness and the elastic and plastic properties of isotropic power-law hardening materials," *Philos. Mag.*,vol.94,no.1,pp.35–55,Sep.2014.
http://www.tandfonline.com/doi/abs/10.1080/14786435.2013.839889

[121] M. Ashida, P. Chen, H. Doi, Y. Tsutsumi, T. Hanawa, and Z. Horita, "Microstructures and mechanical properties of Ti-6Al-7Nb processed by high-pressure torsion," *Procedia Eng.*, vol. 81, no. October, pp. 1523–1528, Oct. 2014.

[122] G. Kulkarni, V. Hiwarkar, J. Patil, and R. Singh, "Microstructural Behavior of Ti6Al4V during Room Temperature Deformation," *J. Nanosci. Nanotechnol. Res.*, vol. 2, no. 1:1, pp. 1–4, Apr. 2018. http://www.imedpub.com/journal-nanoscience-nanotechnology-research.

[123] X. Ma, F. Li, X. Mao, S. Yuan, and J. Wang, "Effect of strain reversal on microstructure and mechanical properties of Ti-6Al-4V alloy under cyclic torsion deformation," *Procedia Eng.*, vol. 207, pp. 1469–1474, Sep. 2017. https://doi.org/10.1016/j.proeng.2017.10.915

APPENDICES

A: Engineering drawings

B: Microstructural analysis results

C: Experimental results

D: Equipment

E: Cost estimates for the CBS process tool

A: ENGINEERING DRAWINGS

A1: Tensile test specimen

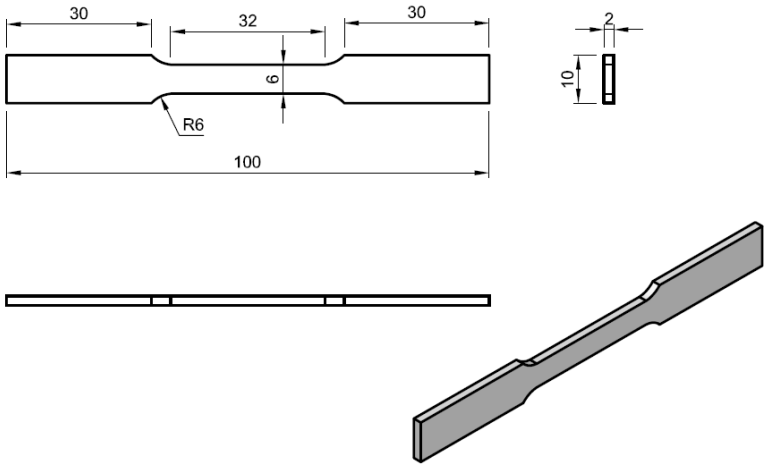

	TENSILE TEST SAMPLE	ASTM-E8-E8M	TI6AI4V	16
NO	NAME	STD / SPECIFICATION	MATERIAL	QTY
	SCALE: 1:1	DRAWN: WMM	REMARKS	
	DIMENSION: MM	GROUP: PGS - MATERIALS		
	DATE: 06-09-2017	CHECKED: ETA		
UNIVERSITY OF JOHANNESBURG	TENSILE TEST		DRW NO 01	SHEET A4

A2: Bender

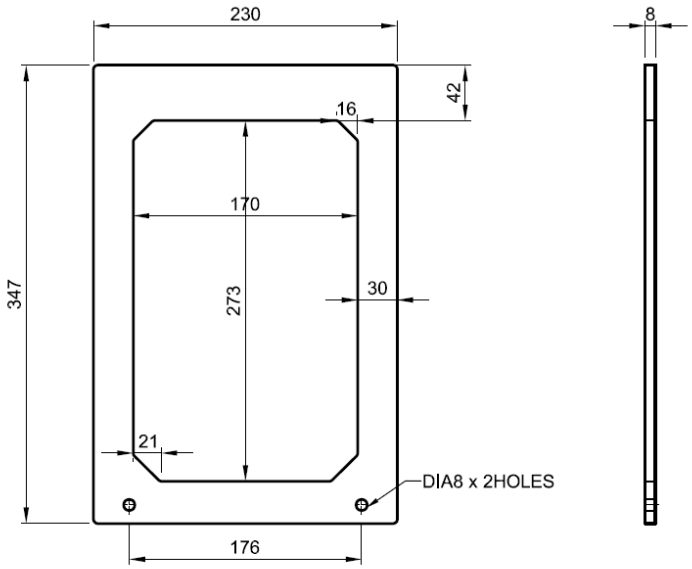

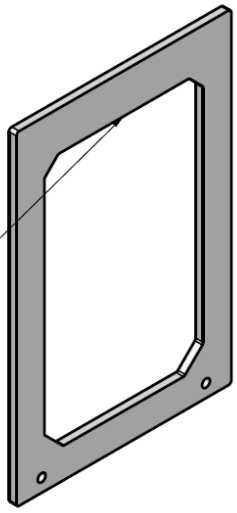

BENDING FACE AND ALL CORNERS
MADE WITH R2 FILLETS

SURFACE ROUGHNESS

	BENDER	FLAT DIE	MILD STEEL	1
NO	NAME	STD / SPECIFICATION	MATERIAL	QTY
	SCALE: 1:4	DRAWN: WMM	REMARKS	
	DIMENSION: MM	GROUP: PGS - MATERIALS		
	DATE: 08-09-2017	CHECKED: ETA		
UNIVERSITY OF JOHANNESBURG	CBS-BENDER		DRW NO 02	SHEET A4

A3: Straightener

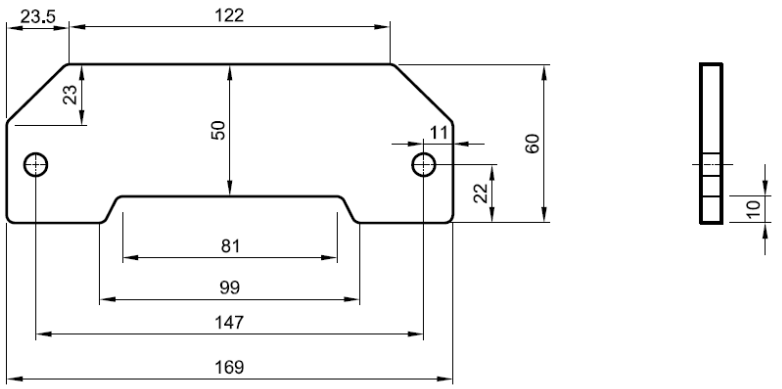

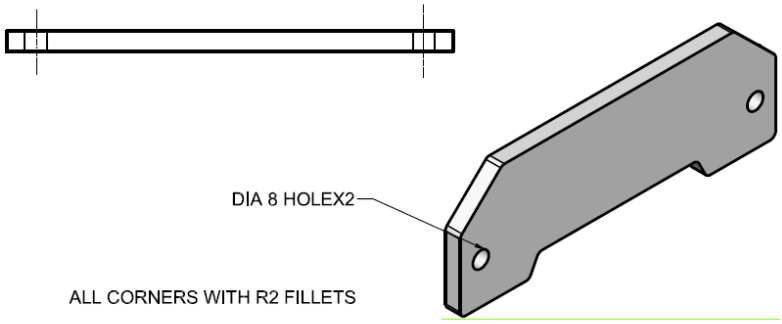

SURFACE ROUGHNESS

	STRAIGHTENER	FLAT DIE	MILD STEEL	1
NO	NAME	STD / SPECIFICATION	MATERIAL	QTY
	SCALE: 1:2	DRAWN: WMM	REMARKS	
	DIMENSION: MM	GROUP: PGS - MATERIALS		
	DATE: 09-09-2017	CHECKED: ETA		
UNIVERSITY OF JOHANNESBURG	CBS-STRAIGHTENER		DRW NO 03	SHEET A4

A4: Upper constraining bracket

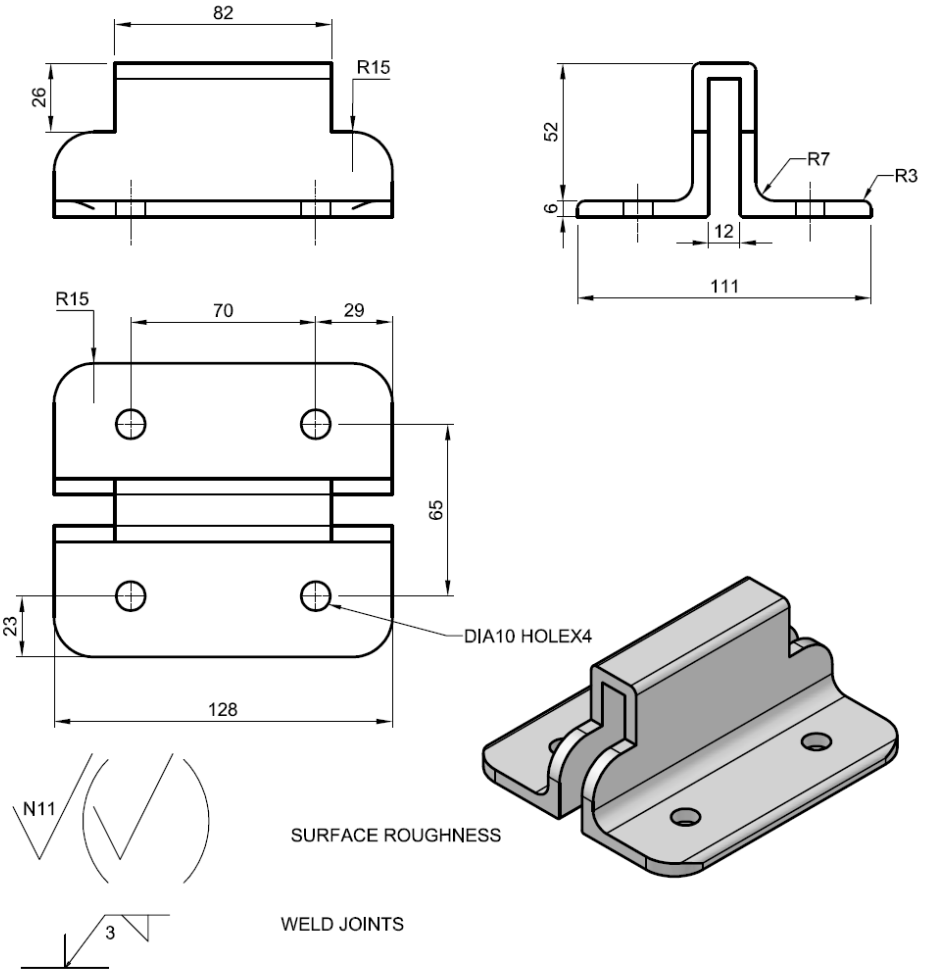

	UPPER CONSTR. BRACKET	2 JOINED 50X50X6 ANGLE SECTION	MILD STEEL	1
NO	NAME	STD / SPECIFICATION	MATERIAL	QTY
	SCALE: 1:2	DRAWN: WMM	REMARKS	
	DIMENSION: MM	GROUP: PGS - MATERIALS		
	DATE: 05-10-2017	CHECKED: ETA		
UNIVERSITY OF JOHANNESBURG	CBS-CONSTRAINING BRACKETS		DRW NO 04	SHEET A4

A5: Upper jack supporter

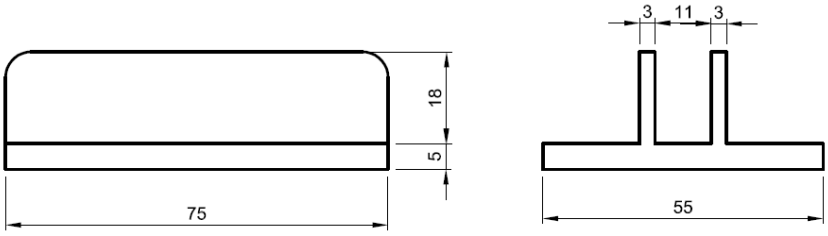

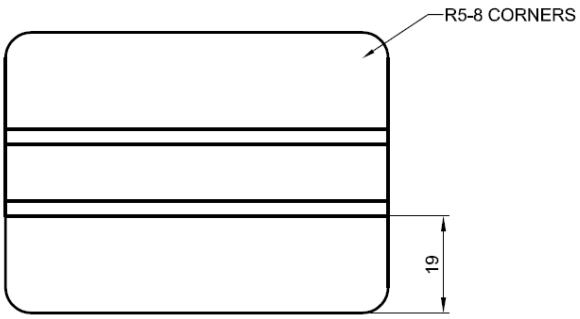

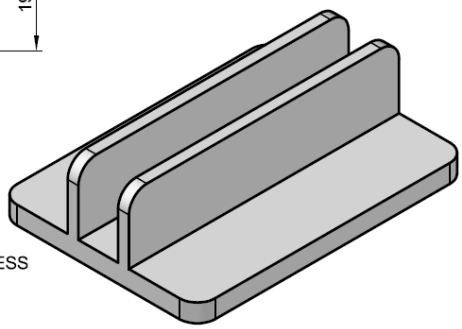

SURFACE ROUGHNESS

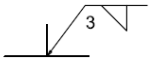

WELD JOINTS

	UPPER JACK SUPPORTER	50X5 AND 20X3 FLAT BARS	MILD STEEL	1
NO	NAME	STD / SPECIFICATION	MATERIAL	QTY
	SCALE: 1:1	DRAWN: WMM	REMARKS	
	DIMENSION: MM	GROUP: PGS - MATERIALS		
	DATE: 08-10-2017	CHECKED: ETA		
UNIVERSITY OF JOHANNESBURG	CBS-JACK SUPPORTERS		DRW NO 05	SHEET A4

A6: Lower jack supporter

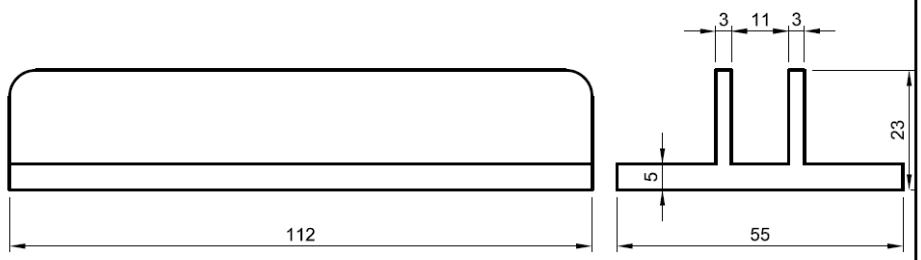

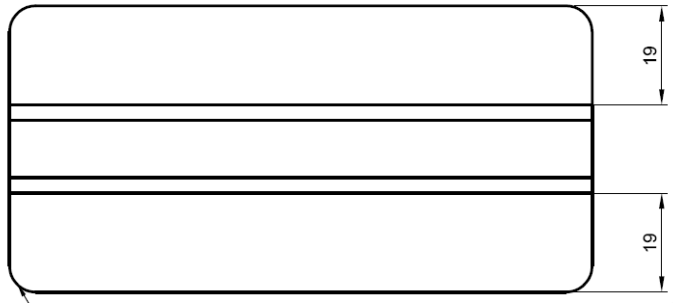

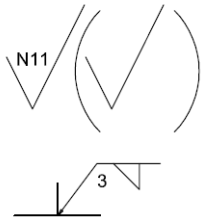

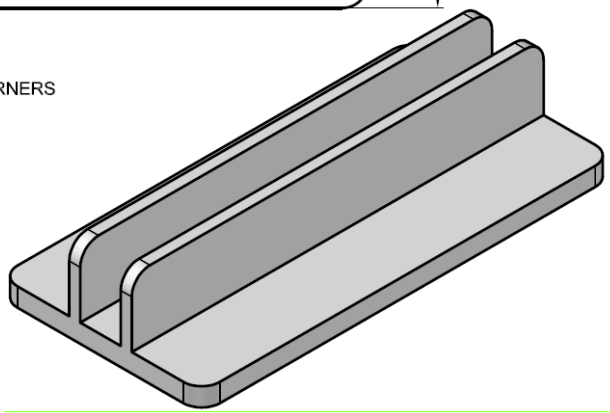

	LOWER JACK SUPPORTER	50X5 AND 20X3 FLAT BARS	MILD STEEL	1
NO	NAME	STD / SPECIFICATION	MATERIAL	QTY
	SCALE: 1:1	DRAWN: WMM	REMARKS	
	DIMENSION: MM	GROUP: PGS - MATERIALS		
	DATE: 08-10-2017	CHECKED: ETA		
UNIVERSITY OF JOHANNESBURG	CBS-JACK SUPPORTERS		DRW NO 06	SHEET A4

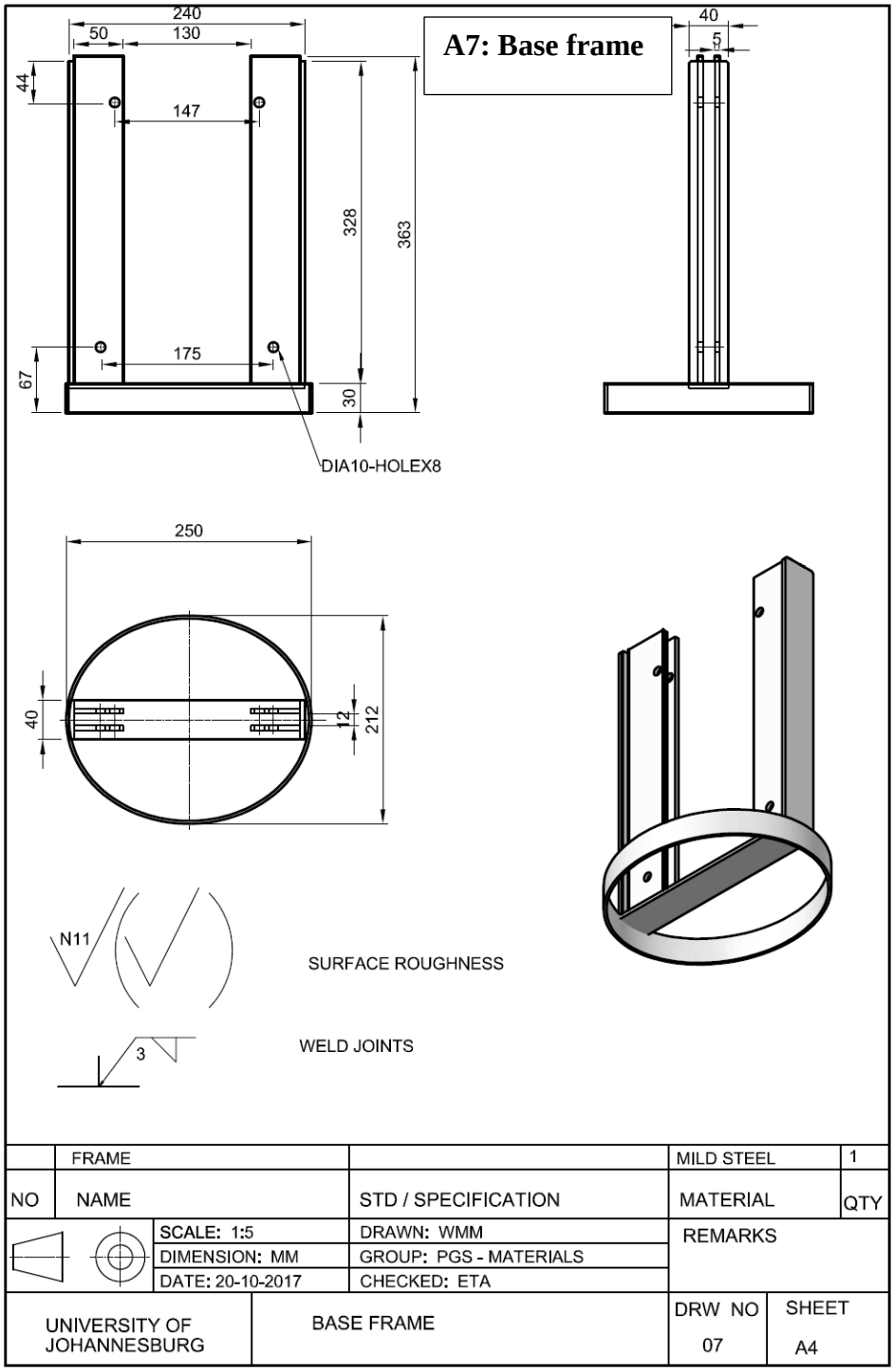
A7: Base frame
240
50
130
44
147
328
363
175
67
30
DIA10-HOLEX8
40
5
250
40
12
212
N11
SURFACE ROUGHNESS
3
WELD JOINTS
FRAME
MILD STEEL
1
NO
NAME
STD / SPECIFICATION
MATERIAL
QTY
SCALE: 1:5
DRAWN: WMM
REMARKS
DIMENSION: MM
GROUP: PGS - MATERIALS
DATE: 20-10-2017
CHECKED: ETA
UNIVERSITY OF JOHANNESBURG
BASE FRAME
DRW NO
07
SHEET
A4

A8: Lower constraining bracket

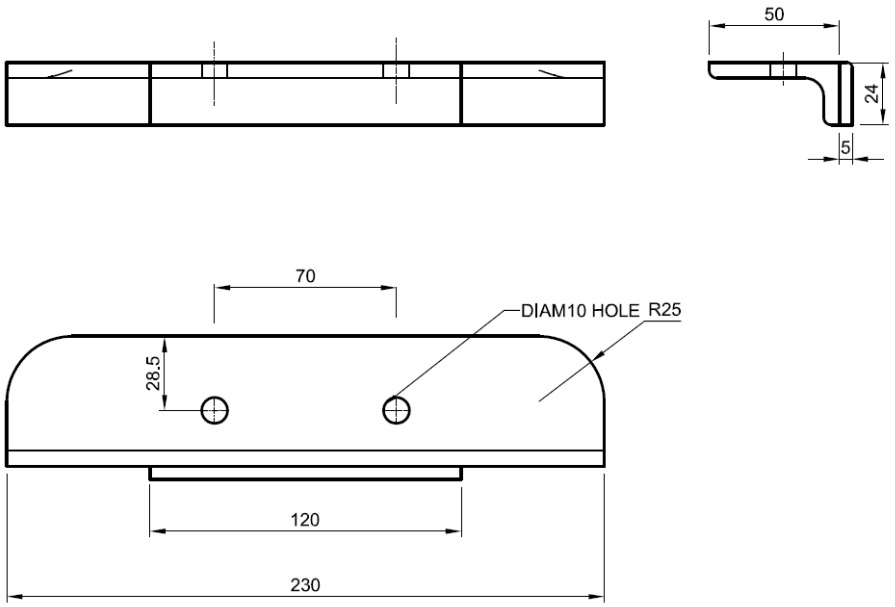

SURFACE ROUGHNESS

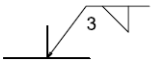

WELD JOINTS

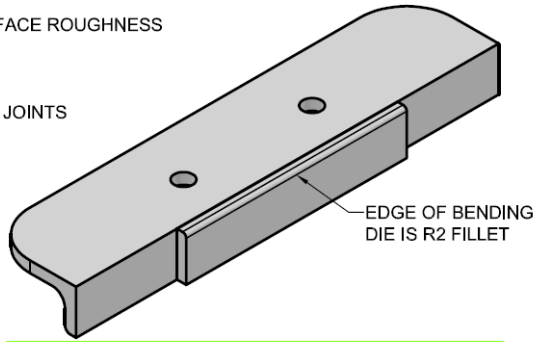

	LOWER CONST BRACKET	50X50X6 ANGLE, 25X5 FLAT BAR	MILD STEEL	2
NO	NAME	STD / SPECIFICATION	MATERIAL	QTY
	SCALE: 1:2	DRAWN: WMM	REMARKS	
	DIMENSION: MM	GROUP: PGS - MATERIALS		
	DATE: 08-12-2017	CHECKED: ETA		
UNIVERSITY OF JOHANNESBURG	CBS-CONSTRAINING BRACKETS		DRW NO 08	SHEET A4

A9: Lock pin

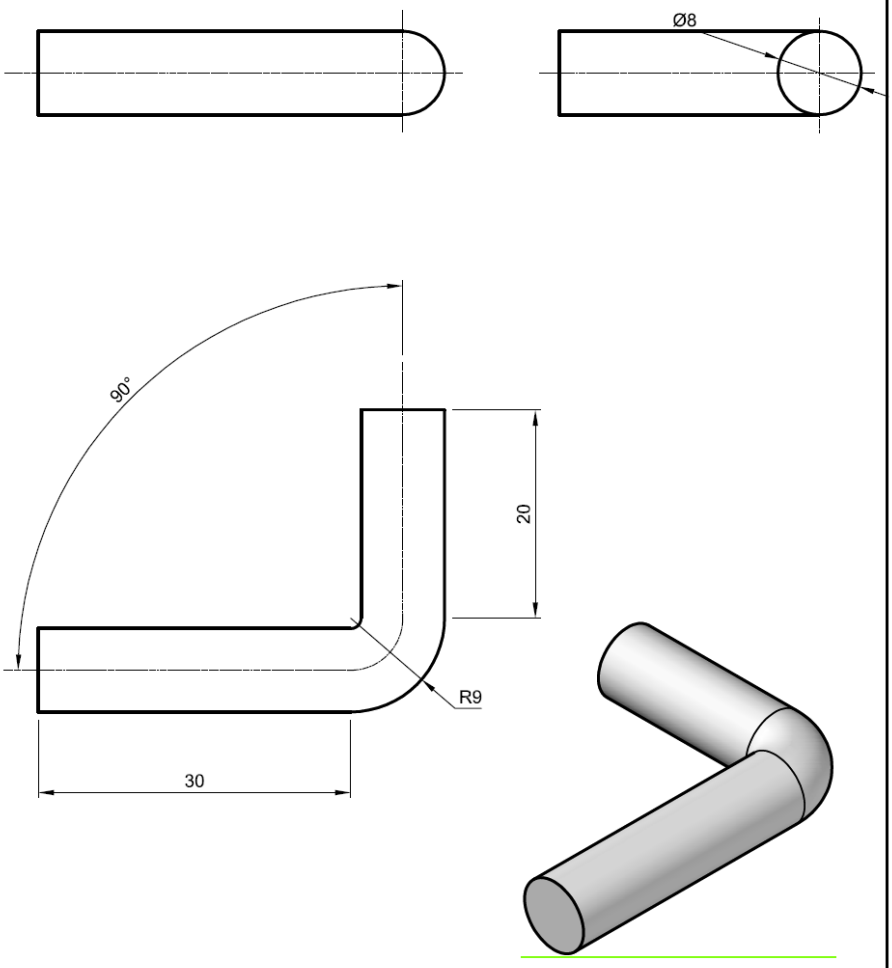

	LOCK PIN	DIA 8MM ROUND BAR	MILD STEEL	4
NO	NAME	STD / SPECIFICATION	MATERIAL	QTY
	SCALE: 2:1	DRAWN: WMM	REMARKS	
	DIMENSION: MM	GROUP: PGS - MATERIALS		
	DATE: 01-11-2017	CHECKED: ETA		
UNIVERSITY OF JOHANNESBURG	CBS-LOCK PIN		DRW NO 09	SHEET A4

A10: Bolt and nut

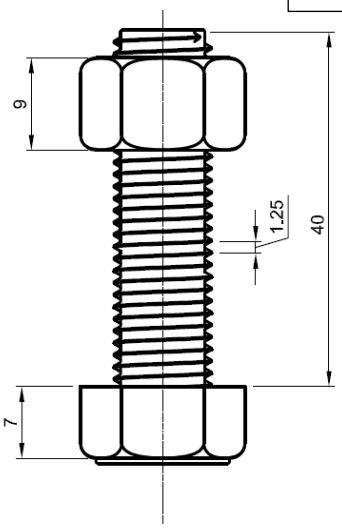

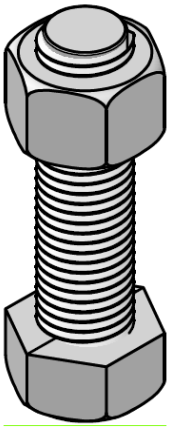

	BOLT AND NUT	M10X40X1.25	STEEL	4
NO	NAME	STD / SPECIFICATION	MATERIAL	QTY
	SCALE: 2:1	DRAWN: WMM	REMARKS	
	DIMENSION: MM	GROUP: PGS - MATERIALS		
	DATE: 09-12-2017	CHECKED: ETA		
UNIVERSITY OF JOHANNESBURG	CBS- BOLTS AND NUTS		DRW NO 10	SHEET A4

A11: Sub assembly of the CBS tool

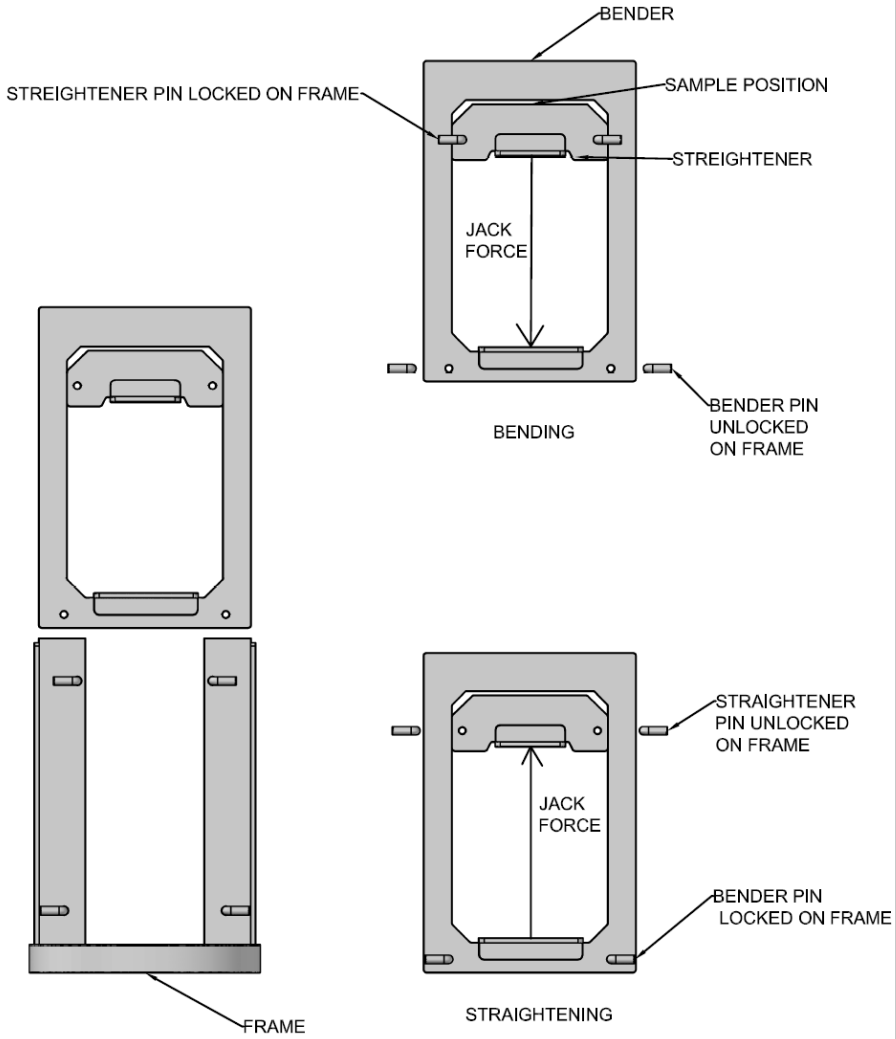

NO	NAME	STD / SPECIFICATION	MATERIAL	QTY
	SCALE: 1:5	DRAWN: WMM	REMARKS	
	DIMENSION: MM	GROUP: PGS - MATERIALS		
	DATE: 14-12-2017	CHECKED: ETA		
UNIVERSITY OF JOHANNESBURG	SUB ASSEMBLY OF BENDER, STREIGHTENER AND FRAME		DRW NO 11	SHEET A4

A12-1: Main assembly of the CBS tool

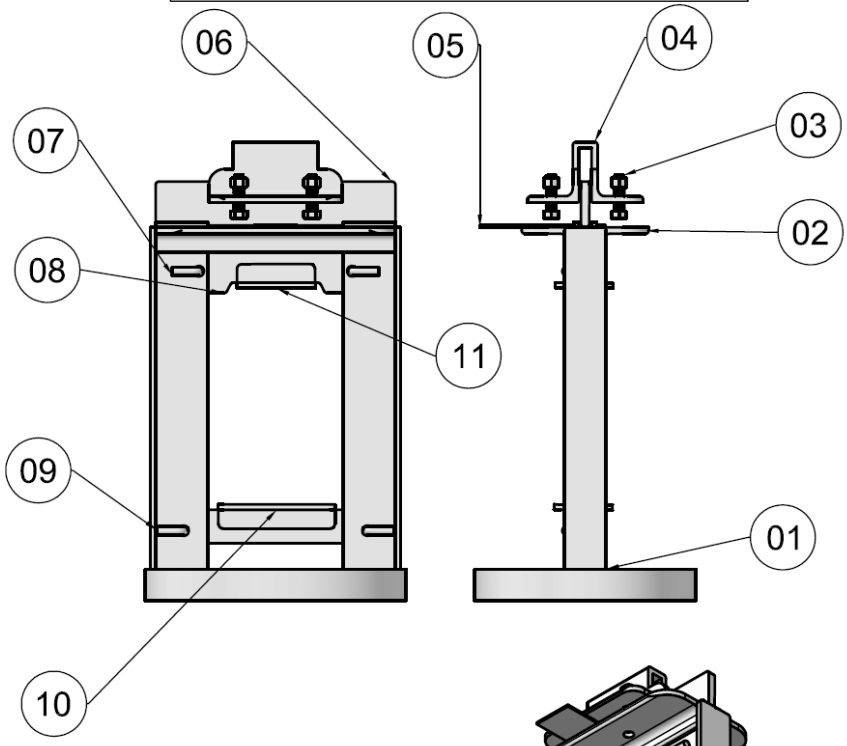

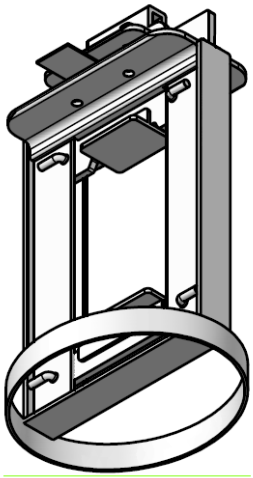

NO	NAME	STD / SPECIFICATION	MATERIAL	QTY
	SCALE: 1:5	DRAWN: WMM	REMARKS	
	DIMENSION: MM	GROUP: PGS - MATERIALS		
	DATE: 15-12-2017	CHECKED: ETA		
UNIVERSITY OF JOHANNESBURG	CBS TOOL MAIN ASSEMBLY PART LIST IS GIVEN ON SEPARATE PAGE		DRW NO 12-1	SHEET A4

A12-2: Part list for main assembly of the CBS

NO	NAME	STD / SPECIFICATION	MATERIAL	QTY
11	UPPER JACK SUPPORTER	50X5, 20X3 FLAT BARS	MILD STEEL	01
10	LOWER JACK SUPPORTER	50X5, 20X3 FLAT BARS	MILD STEEL	01
09	BENDER LOCK PIN	DIA 8MM ROUND BAR	MILD STEEL	02
08	STRAIGHTENER	8MM THICK PLATE	MILD STEEL	01
07	STRAIGHTENER LOCK PIN	DIA 8MM ROUND BAR	MILD STEEL	02
06	BENDER	8MM THICK PLATE	MILD STEEL	01
05	SAMPLE	TI6AI4V- GRADE5	TITANIUM	15
04	UPPER CONSTRAIN BRACKET	50X50X6 ANGLE SECTION-DOUBLED	MILD STEEL	01
03	BOLT AND NUT	M10X40MMX1.25MM	STEEL	04
02	LOWER CONSTRAIN BRACKET	50X50X6 ANGLE SECTION	MILD STEEL	02
01	FRAME	50X50X6 ANGLE SECTION-DOUBLED	MILD STEEL	01

SCALE: 1:5	DRAWN: WMM	REMARKS
DIMENSION: MM	GROUP: PGS - MATERIALS	
DATE: 15-12-2017	CHECKED: ETA	

UNIVERSITY OF JOHANNESBURG	CBS TOOL MAIN ASSEMBLY PART LIST	DRW NO 12-2	SHEET A4

A13: Picture of the CBS process tool

B: MICROSTRUCTURAL RESULTS

B1: Optical Microscope (OPM) images

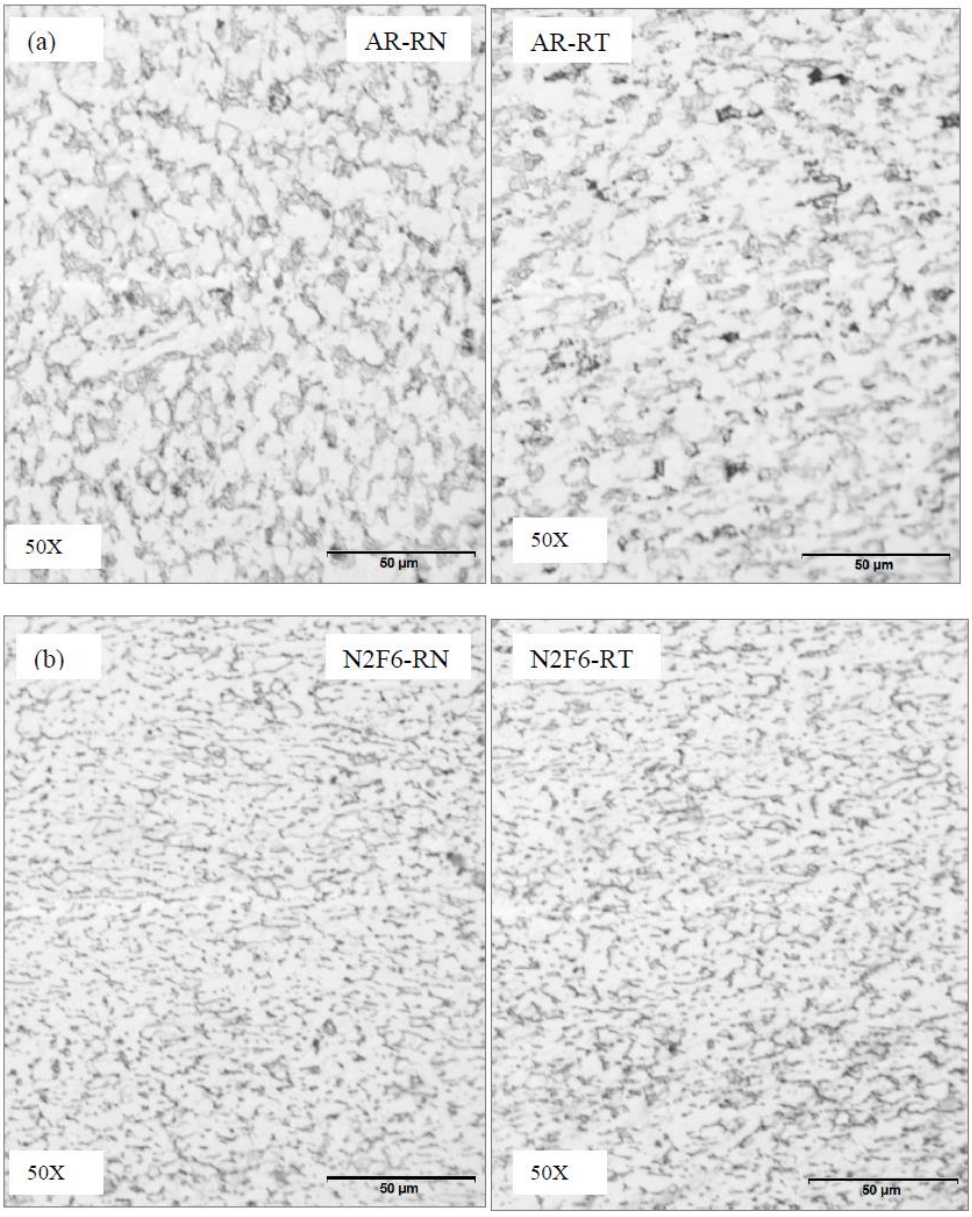

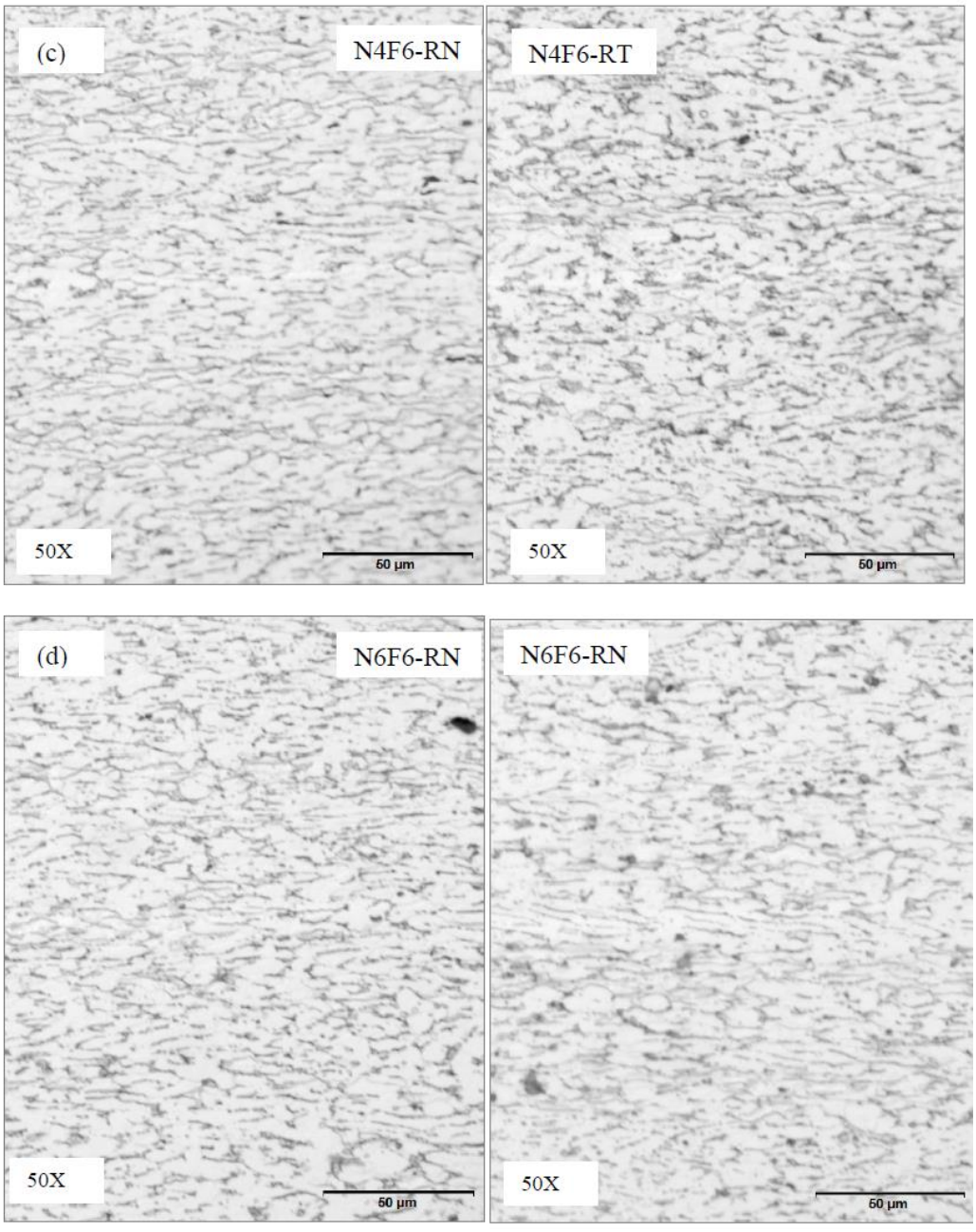
(c)
N4F6-RN
50X
50 µm
N4F6-RT
50X
50 µm
(d)
N6F6-RN
50X
50 µm
N6F6-RN
50X
50 µm

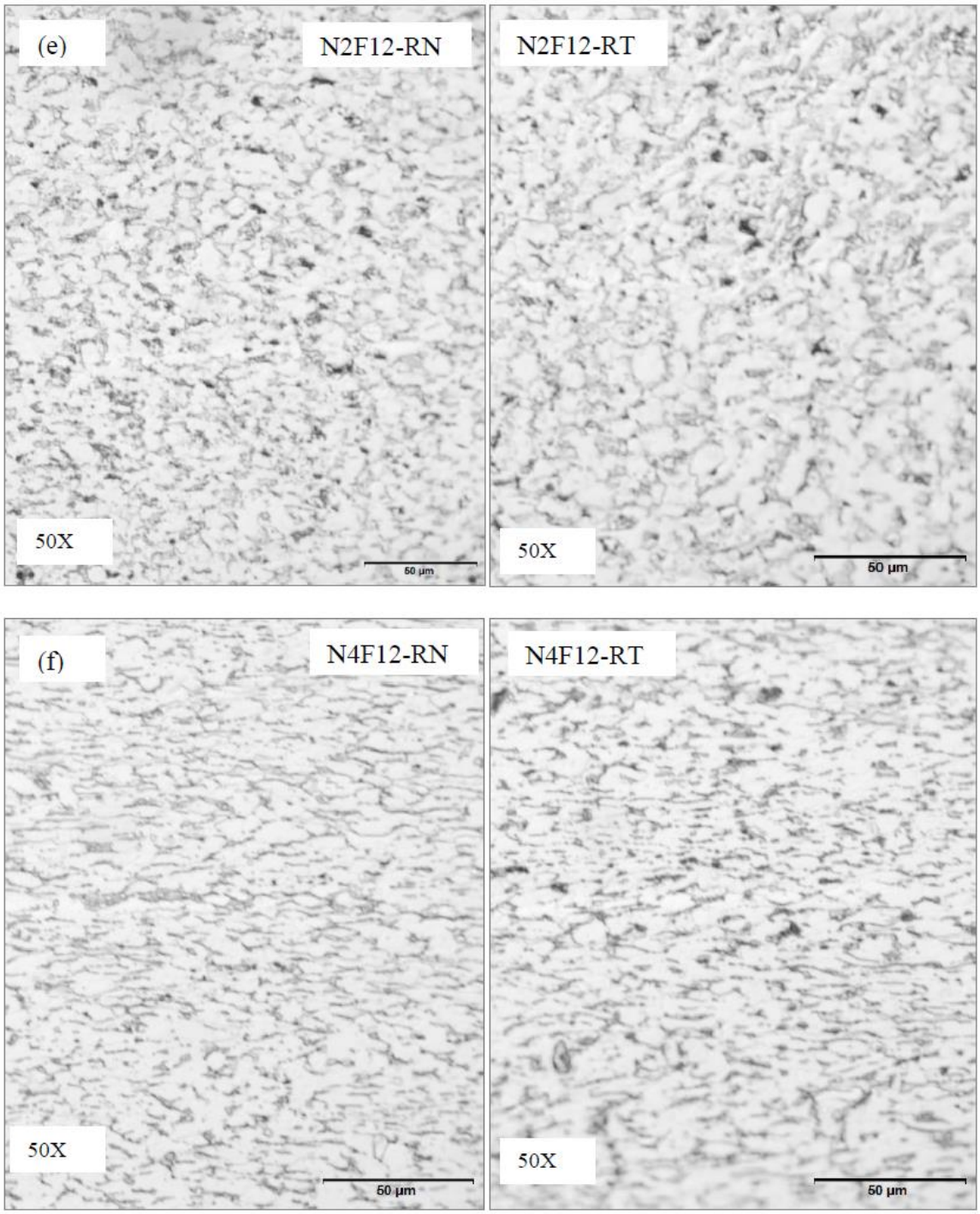
(e)
N2F12-RN
50X
50 µm
N2F12-RT
50X
50 µm
(f)
N4F12-RN
50X
50 µm
N4F12-RT
50X
50 µm

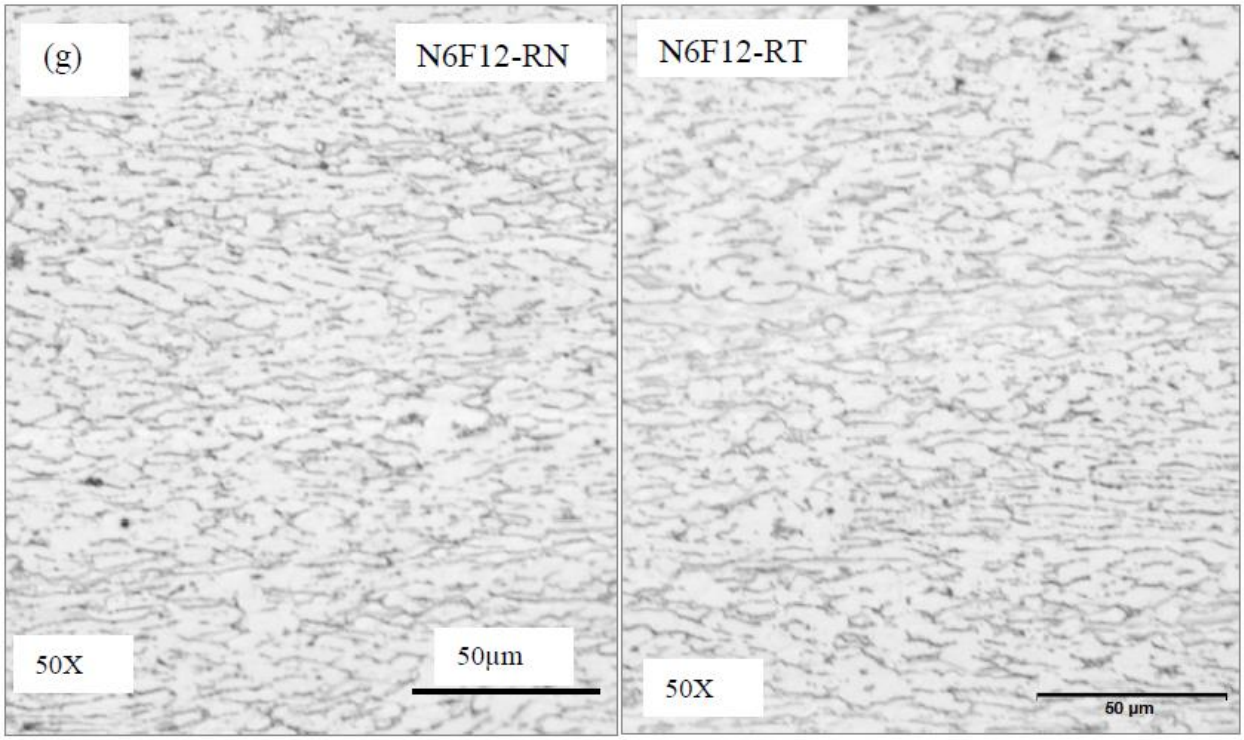
(g)
N6F12-RN
50X
50µm
N6F12-RT
50X
50 µm

Scanning Electron Microscope (SEM) images

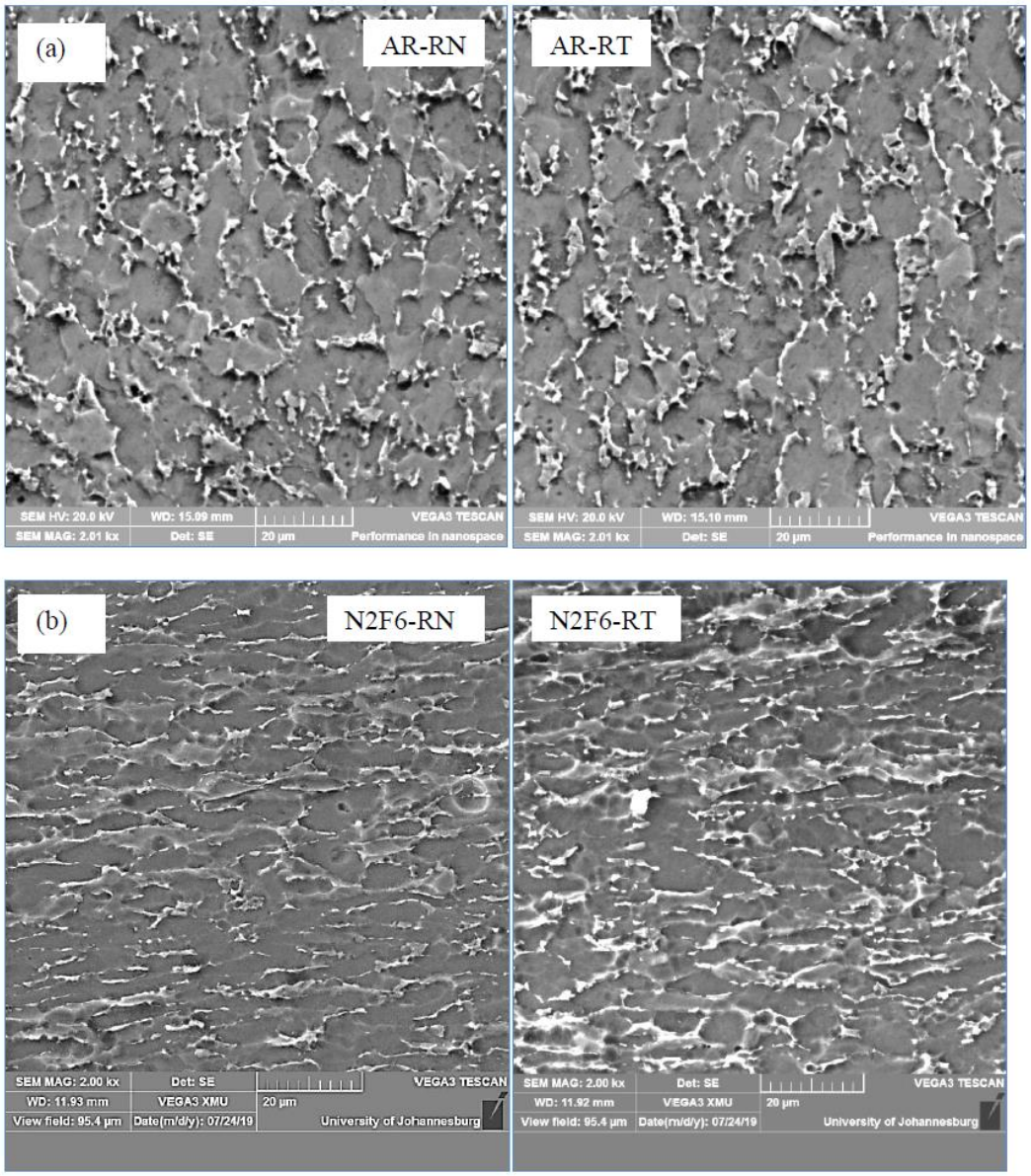

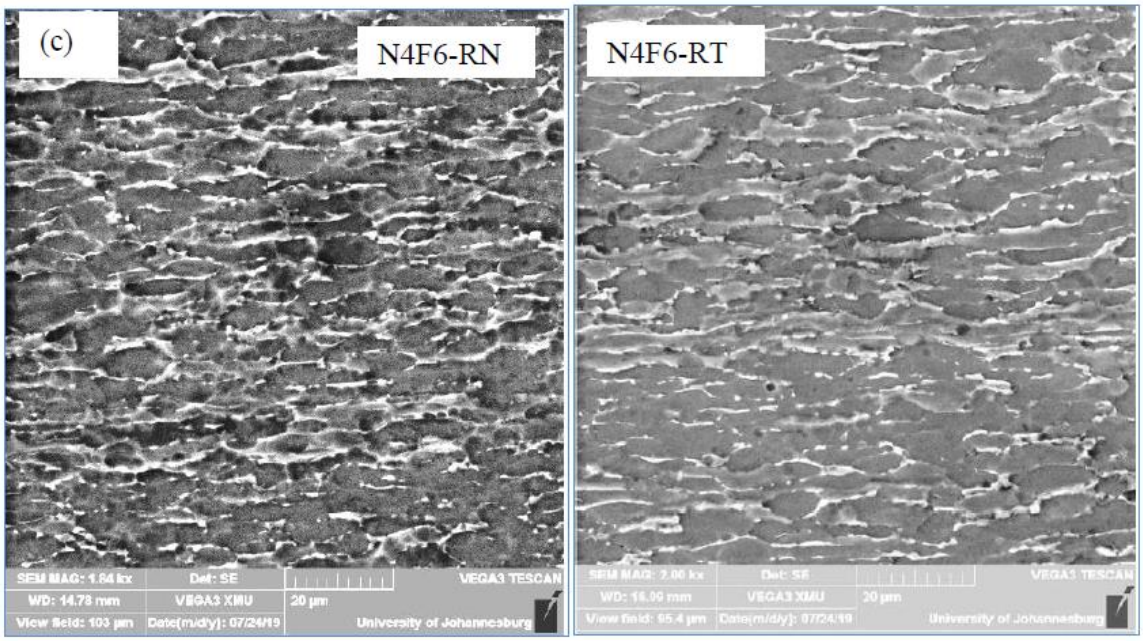
(c)
N4F6-RN
SEM MAG: 1.84 kx
Det: SE
VEGA3 TESCAN
WD: 14.78 mm
VEGA3 XMU
20 µm
View field: 103 µm
Date(m/d/y): 07/24/19
University of Johannesburg

N4F6-RT
SEM MAG: 2.00 kx
Det: SE
VEGA3 TESCAN
WD: 16.09 mm
VEGA3 XMU
20 µm
View field: 95.4 µm
Date(m/d/y): 07/24/19
University of Johannesburg

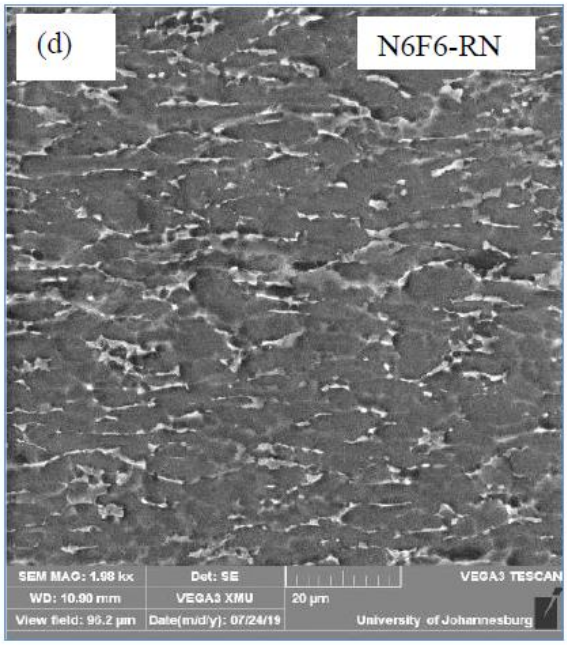
(d)
N6F6-RN
SEM MAG: 1.98 kx
Det: SE
VEGA3 TESCAN
WD: 10.90 mm
VEGA3 XMU
20 µm
View field: 96.2 µm
Date(m/d/y): 07/24/19
University of Johannesburg

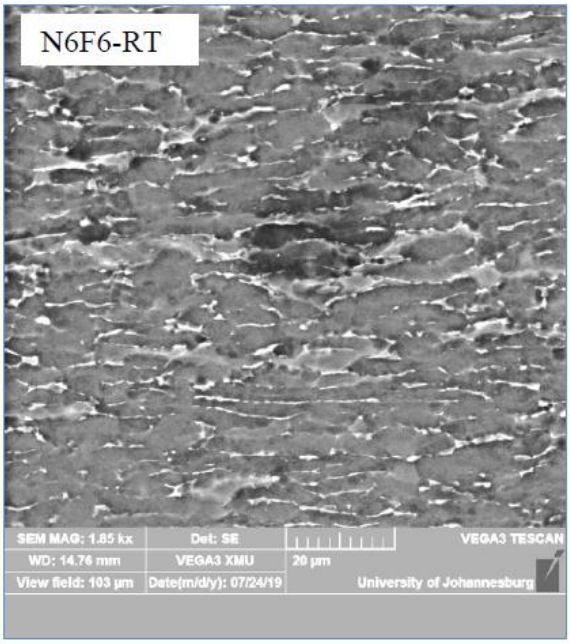
N6F6-RT
SEM MAG: 1.85 kx
Det: SE
VEGA3 TESCAN
WD: 14.76 mm
VEGA3 XMU
20 µm
View field: 103 µm
Date(m/d/y): 07/24/19
University of Johannesburg

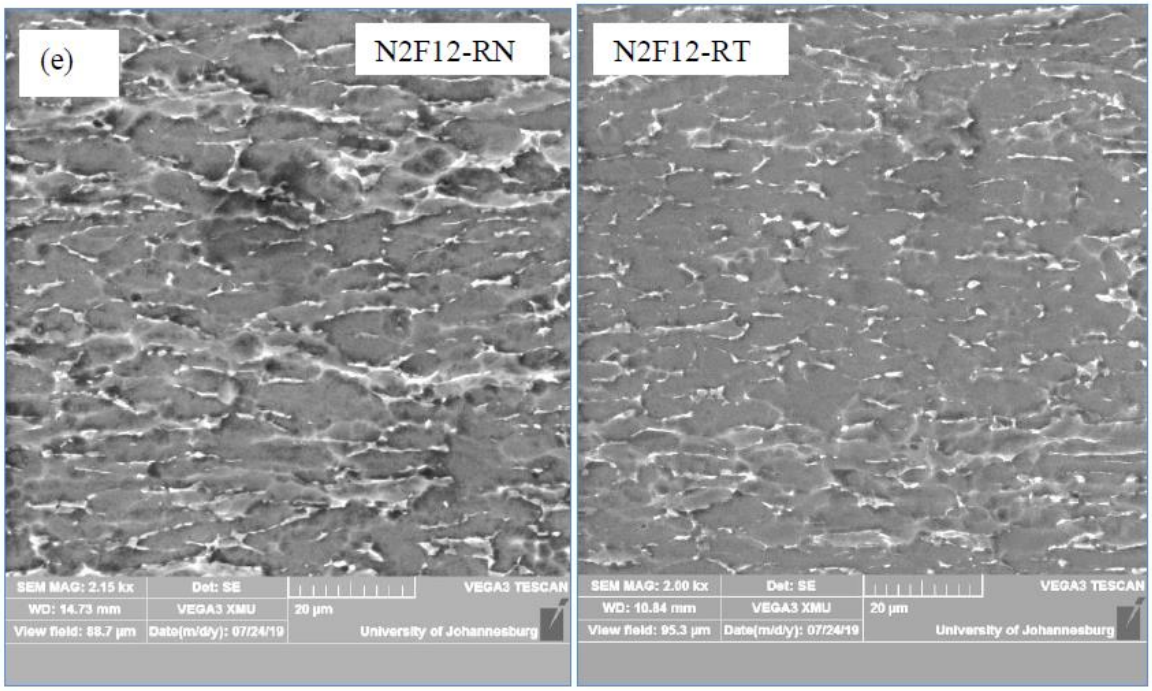
(e)
N2F12-RN
SEM MAG: 2.15 kx
Det: SE
VEGA3 TESCAN
WD: 14.73 mm
VEGA3 XMU
20 µm
View field: 88.7 µm
Date(m/d/y): 07/24/19
University of Johannesburg

N2F12-RT
SEM MAG: 2.00 kx
Det: SE
VEGA3 TESCAN
WD: 10.84 mm
VEGA3 XMU
20 µm
View field: 95.3 µm
Date(m/d/y): 07/24/19
University of Johannesburg

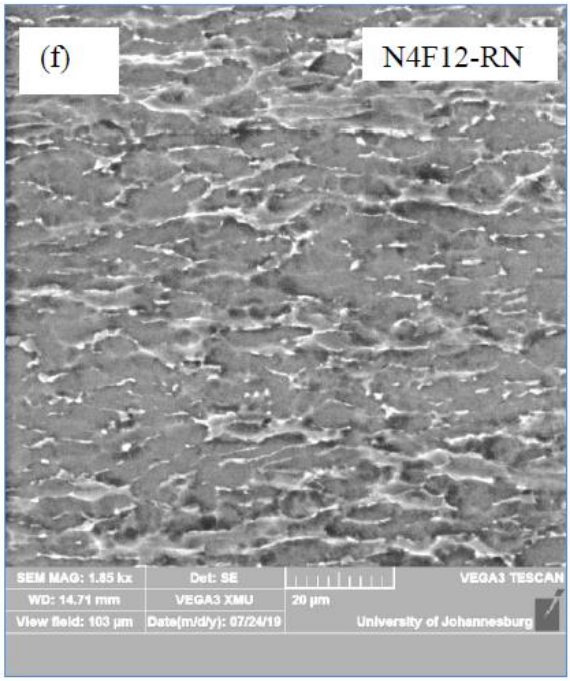
(f)
N4F12-RN
SEM MAG: 1.85 kx
Det: SE
VEGA3 TESCAN
WD: 14.71 mm
VEGA3 XMU
20 µm
View field: 103 µm
Date(m/d/y): 07/24/19
University of Johannesburg

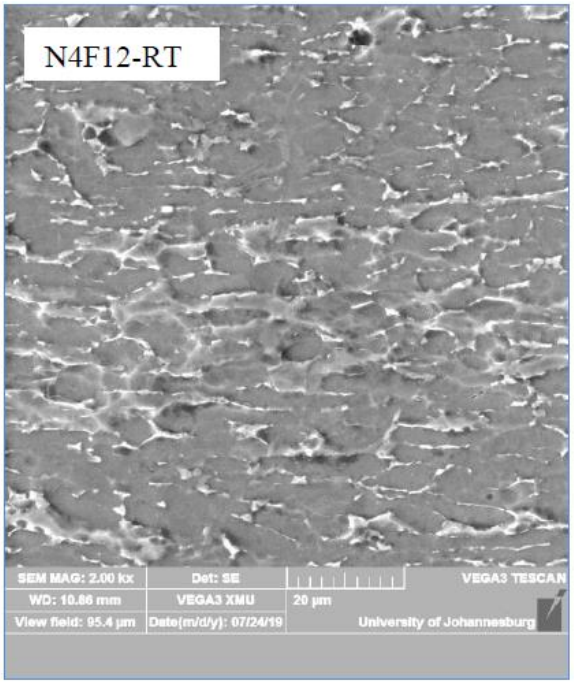
N4F12-RT
SEM MAG: 2.00 kx
Det: SE
VEGA3 TESCAN
WD: 10.86 mm
VEGA3 XMU
20 µm
View field: 95.4 µm
Date(m/d/y): 07/24/19
University of Johannesburg

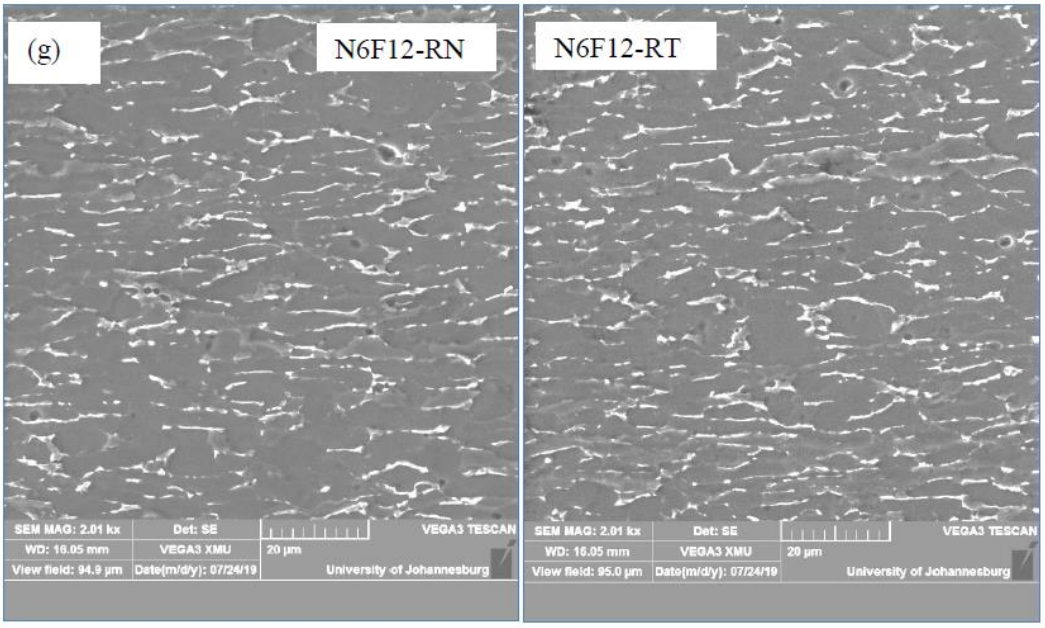
(g)
N6F12-RN
SEM MAG: 2.01 kx
Det: SE
VEGA3 TESCAN
WD: 16.05 mm
VEGA3 XMU
20 µm
View field: 94.9 µm
Date(m/d/y): 07/24/19
University of Johannesburg
N6F12-RT
SEM MAG: 2.01 kx
Det: SE
VEGA3 TESCAN
WD: 16.05 mm
VEGA3 XMU
20 µm
View field: 95.0 µm
Date(m/d/y): 07/24/19
University of Johannesburg

C: EXPERIMENTAL RESULTS

C1: Average engineering tensile stress, strain and hardness test results for the Ti6Al4V sheets versus pass-feed (NF)

Samples Category	Tensile strength ST(MPa)	Yield Strength SY(MPa)	Fracture Stress SF(MPa)	Elongation EP (%)	Elongation at Fracture EF (%)	Hardness (HV)
AR	946.9	890	780	10.9	14.8	322
N2F6	1153	1085.7	1113.6	7.9	10.7	372
N4F6	1223.9	1188	1194.5	6.5	8.1	400.1
N6F6	1172.5	1093.4	1141	6.8	9.2	379.9
N2F12	1028.6	941.2	970.3	9.3	12.5	344.5
N4F12	1090.0	1015	1033.7	8.3	11.1	357.7
N6f12	1056.9	986	1005	8.5	11.4	352

C2: Hardness test results for Ti6Al4Vsamples versus pass-feed (NF)

Sample plane	Hardness (HV) Measured at interval of 1mm on 15mm sample length										Average Hardness (HV)
AR-RN	318.5	324.8	318.5	317.9	325.4	319.9	322.1	324.8	320.2	325.3	321.5
AR-RT	324.3	325.5	321.3	320.2	319.3	325.5	317.9	326.0	326.2	321.8	322.8
N2F6-RN	370.6	370.9	367.7	376.7	369.6	375.8	377.3	369.9	373.3	367.9	372.0
N2F6-RT	380.9	374.0	374.9	378.3	379.2	383.2	373.3	369.7	378.8	373.2	376.6
N4F6-RN	402.8	400.3	393.4	403.6	393.4	405.1	398.9	403.3	397.5	402.1	400.1
N4F6-RT	404.3	395.3	404.9	401.2	404.5	407.8	401.6	409.1	398.8	404.9	403.3
N6F6-RN	381.5	374.4	378.8	386.9	377.9	381.6	376.6	381.6	377.2	379.8	379.6
N6F6-RT	386.9	383.6	385.5	387.3	384.4	375.7	387.2	383.3	386.4	383.0	384.3
N2F12-RN	348.8	352.4	336.7	352.6	341.4	353.2	335.6	332.9	353.3	338.4	344.5
N2F12-RT	356.6	341.5	357.7	358.9	340.6	345.4	360.9	342.9	341.2	352.7	349.8
N4F12-RN	362.7	350.7	363.9	355.6	351.2	355.4	364.9	353.2	363.9	354.9	357.7
N4F12-RT	358.4	361.6	352.8	370.8	366.6	370.1	355.9	364.0	366.2	360.9	362.7
N6F12-RN	351.0	357.8	350.7	351.6	355.8	358.5	348.6	357.2	345.5	352.3	352.9
N6F12-RT	357.7	352.8	346.6	353.1	357.2	350.9	359.1	358.2	349.7	346.8	353.2

C3: Tensile stress-strain curves for 3 samples (T1, T2, and T3) of Ti6Al4V alloy versus pass-feed (NF)

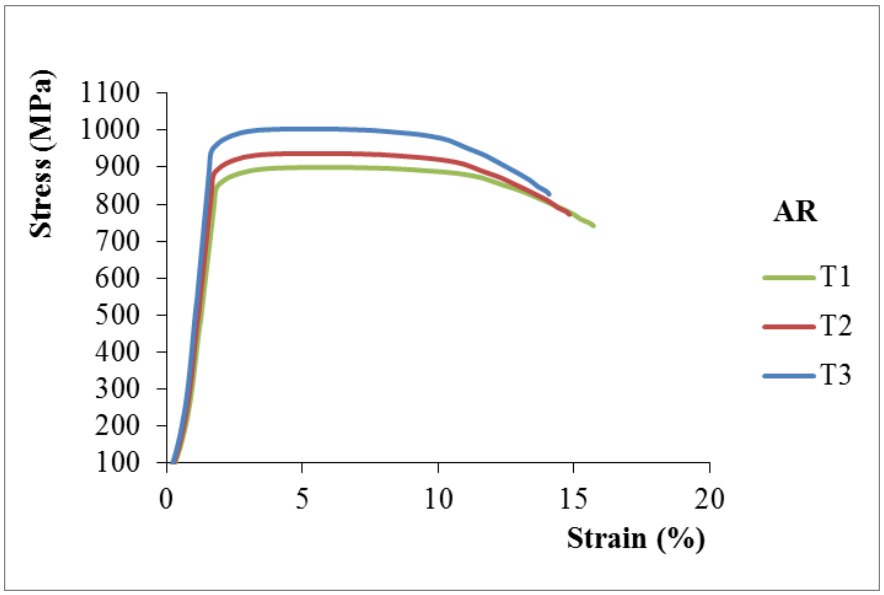

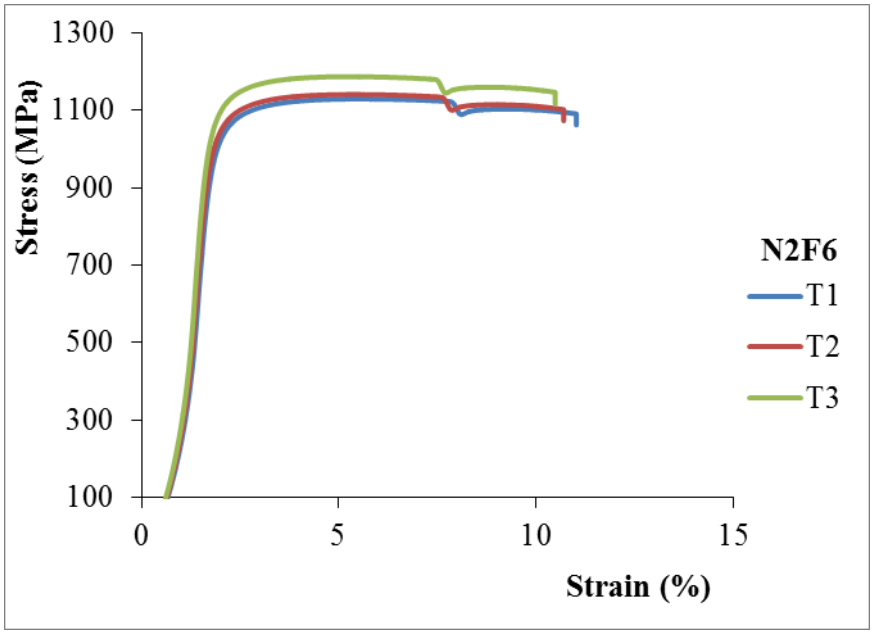

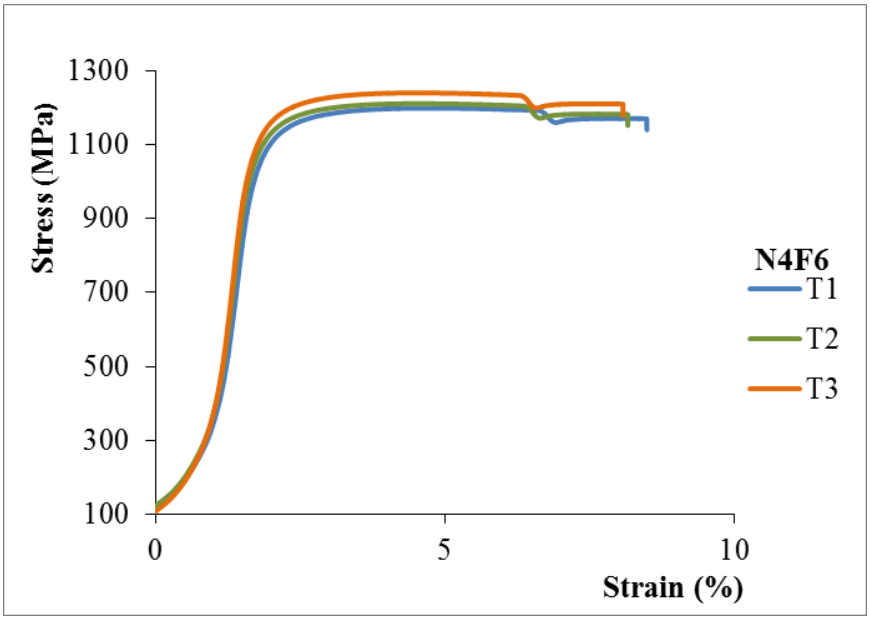
Stress (MPa)
1300
1100
900
700
500
300
100
0
5
10
Strain (%)
N4F6
T1
T2
T3

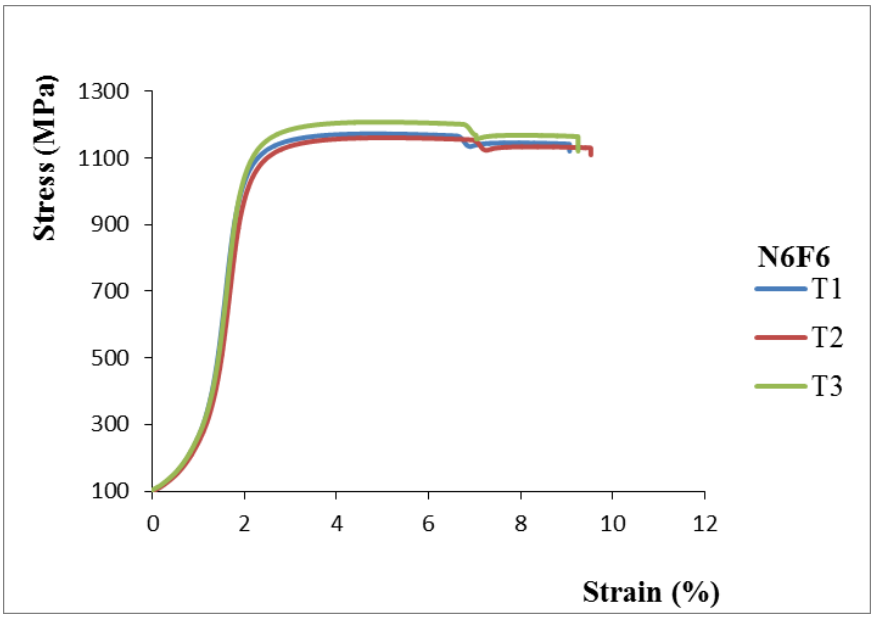
Stress (MPa)
1300
1100
900
700
500
300
100
0
2
4
6
8
10
12
Strain (%)
N6F6
T1
T2
T3

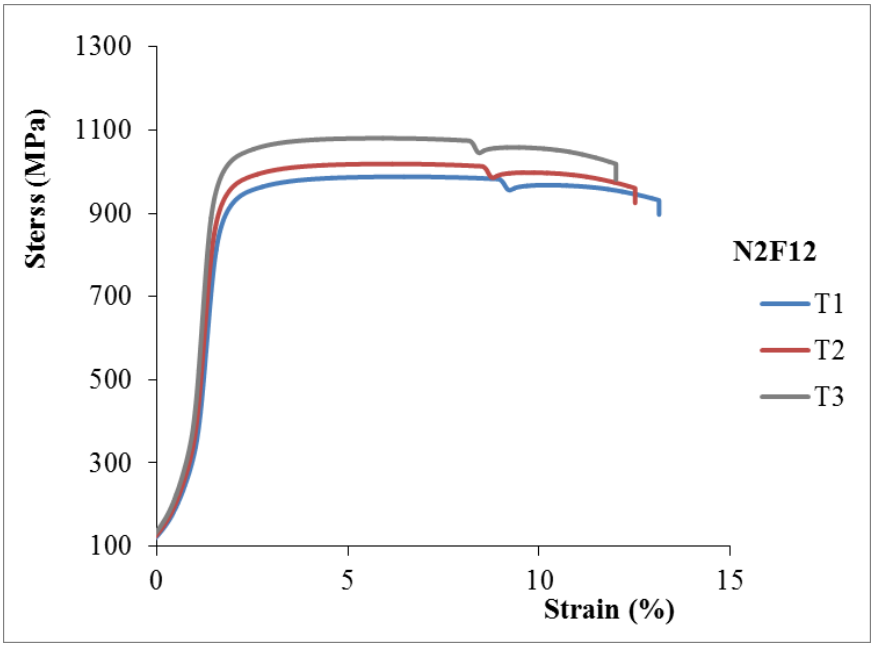
1300
1100
900
700
500
300
100
Sterss (MPa)
0
5
10
15
Strain (%)
N2F12
T1
T2
T3

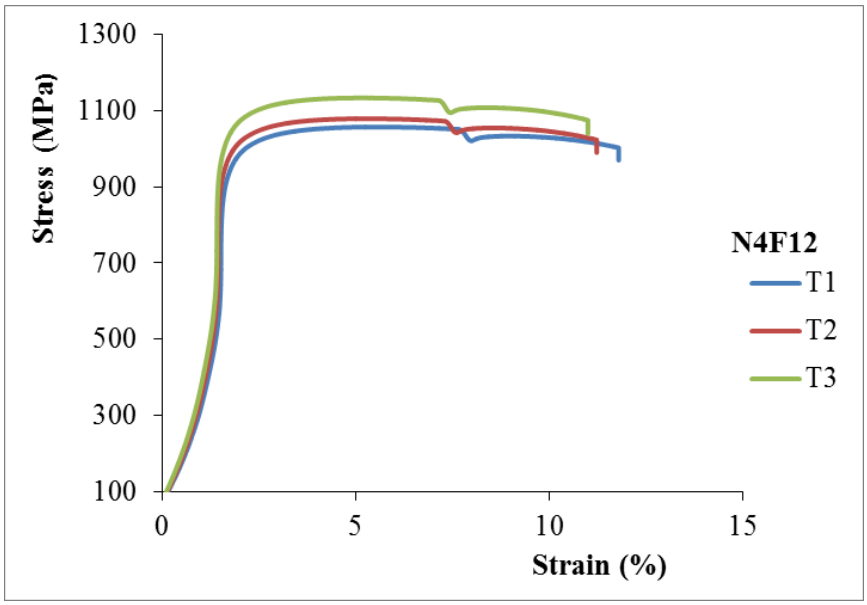
1300
1100
900
700
500
300
100
Stress (MPa)
0
5
10
15
Strain (%)
N4F12
T1
T2
T3

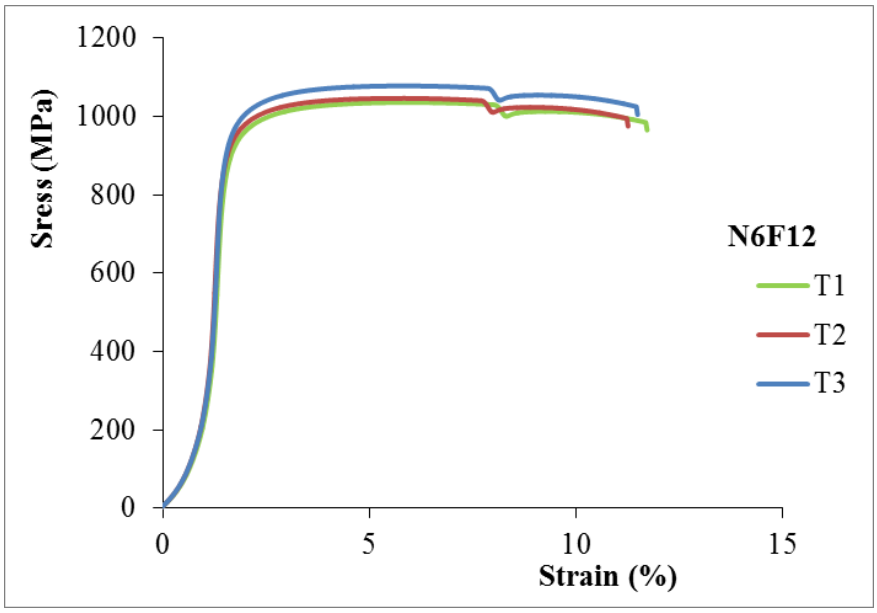
1200
1000
800
600
400
200
0
Sress (MPa)
0
5
10
15
Strain (%)
N6F12
T1
T2
T3

D: EQUIPMENTS

D1: Cutoff machine

D2: Mounting machine

D3: Grinding and polishing machine

D4: Micro hardness tester

D5: Optical Microscope (OPM)

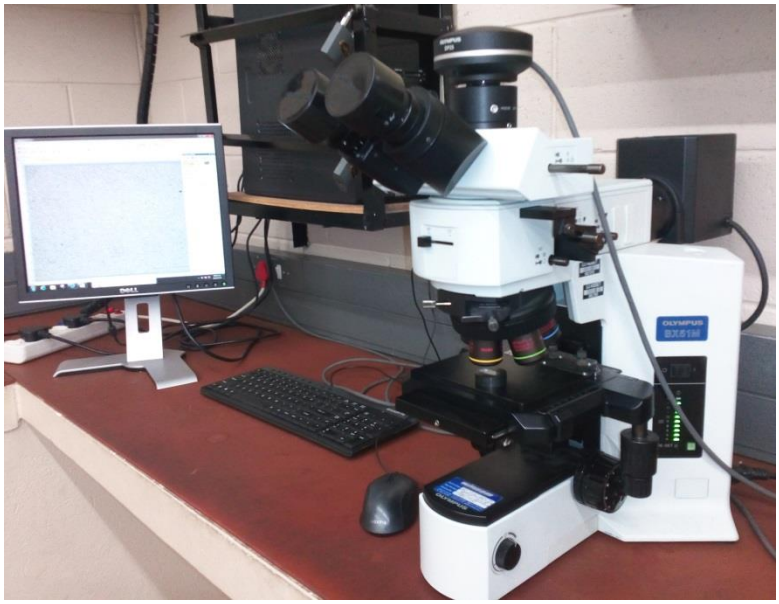

D6: Scanning Electron Microscope (SEM)

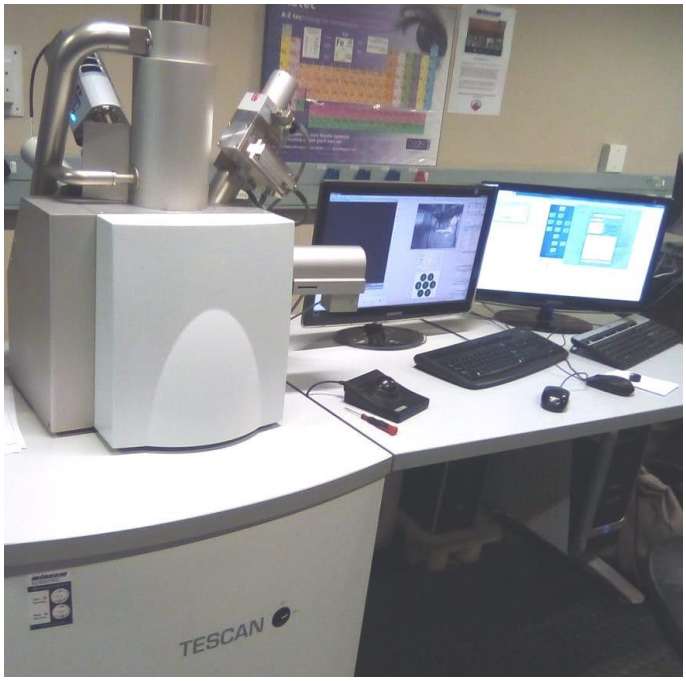

D7: Tensile test machine

E: COST ESTIMATES FOR THE CBS PROCESS TOOL

COST ESTIMATES FOR THE CBS PROCESS TOOL						
No	**Part**	**Standard/ Geometry**	**Material**	**Quantity /total size**	**Unit Cost (ZAR)**	**Total Cost (ZAR)**
1	Bender	Plate 8 mm T	Steel EN10025-S275JR[	1/ A = 0. 1 m^2	1394.75	139.60
2	Straightener	Plate 8 mm T	Steel EN10025-S275JR	1/ A = 0.01 m^2	1394.75	13.96
3	Constraining Brackets	Angle section 2",6mm T	Steel EN10025-S355JR[	2/ L = 0.8 m	63.00	50.40
4	Frame	Plate 5 mm T	Steel EN10025-S355JR[	1/ A = 0.12 m^2	1238.00	149.00
5	Jack Supporters	5mm T	Steel EN10025-S355JR[	2/ A = 0.015 m^2	1238.00	18.57
6	Welding rods	E6013 2.5 mm Dia		2 kg	22.50	45.00
7	Lock pins	8 mm T Dia	Steel EN10025-S355JR	4	2.50	10.00
8	Bolts and Nut	Grade 8.8 M10x40mm x1.25	Steel	4	6.00	24.00
9	Spanner	Size 17 For M10 bolt and nut	Chrome Vanadium Steel	4	135.00	540.00
10	Hydraulic Jack	10Tons		1	245.00	245.00
11	Hydraulic Pressure Gauge	Model No:G2517L		1	2000.00	2000.00
12	Thread Tap	N410-3 NPT¼		1	860.00	860.00
13	Labour charge					1200.00
14	**GrandTotal**					**5295.53**